Faculty of Science and Engineering

Department of Applied Geology

Thermochronological record of tectonic events in central and southeastern South China since the Mesozoic

Ni Tao

This thesis is presented for the Degree of

Doctor of Philosophy

of

Curtin University

December 2014

Declaration

To the best of my knowledge and belief this thesis contains no material previously published by any other person except where due acknowledgment has been made.

This thesis contains no material which has been accepted for the award of any other degree or diploma in any university.

Signature: .....

Date: 03/09/15

Acknowledgements

I would like to express my sincere thanks to those who helped me during my PhD study.

First and foremost, I would like to thank my supervisors, Professor Zheng-Xiang Li, Associate Professor Noreen Evans, and Dr. Martin Danišík. I thank Professor Zheng-Xiang Li for offering me the opportunities to conduct this project. I appreciate that he trained me on how to conduct fieldwork and how to think through geological questions. I thank him for the fortnightly discussions and for providing me the opportunities to be familiar with a range of techniques and instruments. I am grateful to Associate Professor Noreen Evans. I thank her for teaching me (U-Th)/He dating and for editing my manuscripts. Her coordination of workflow and efficiency smoothed the development of my project. I thank her for guiding me through many difficult situations, in research and in life. I sincerely thank Dr. Martin Danišík for training me on thermochronological theory and laboratory skills, for helping with data generation and for constructive scientific discussions. I greatly appreciate his invaluable advice and encouragement during the preparation of my thesis and paper. I thank him and his wife for their help when I visited Waikato University in New Zealand.

Professor Wu-Xian Li is thanked for his help with field trip organization, for offering accommodation when I was conducting vitrinite reflectance analysis in Guangzhou and for scientific discussions. I thank Dr. Chong-Jin Pang for sharing his sample collection and stratigraphic study results.

The staff from the following laboratories are acknowledged for their support: Western Australian Argon Isotope Facility (Associate Professor Fred Jourdan, Mr. Adam Frew, Mrs. Celia Mayers), GeoHistory Facility (Mr. Brad McDonald) and SHRIMP Facility (Dr. Allen Kennedy, Mr. Hao Gao) at Curtin University, Australia; State Key laboratory of Organic Geochemistry at Guangzhou Institute of Geochemistry, Chinese academy of Sciences (Professor De-Han Liu, Mr. Jia-Gui Shen, Professor Xian-Ming Xiao and the postgraduates in the group); fission track laboratory (Professor Peter Kamp, Dr. Gan-Qing Xu) at University of Waikato (New

Zealand).

I thank all the staffs and postgraduate students in the Department of Applied Geology, Curtin University, for their varied and much appreciated help during my study.

I thank friends in Australia and China who helped and supported me during my PhD.

This PhD project was supported by the Australian Research Council Discovery Project (DP110104799), the Chinese Academy of Sciences (Grant KZCX1-YW-15-2), and National Natural Science Foundation of China (Grant 41173039). My study at Curtin University was supported by the Curtin International Postgraduate Research Scholarship (CIPRS) and the Institute for Geoscience Research Award.

This thesis is dedicated to my dear parents, Qing and Yin.

Abstract

The South China Block (SCB) constitutes a major continental block in southeastern Asia, which is characterized by a complex geotectonic evolution. This study is focused on the central and southeastern SCB, hereafter referred to as the SE SCB. Given its established relationship with the subducting Pacific oceanic plate, this area is located in a key strategic position for geodynamic reconstruction of the Asia-Pacific region. Li and Li (2007) reported the first evidence of Mesozoic flat-slab subduction along the West Pacific margin and the impact of this tectonic process on the Mesozoic SE SCB. The SE SCB experienced significant vertical movement since the Mesozoic, with sequential development of a Triassic orogeny, Late Triassic–Early Jurassic shallow marine basin, and Middle–Late Jurassic magmatic province. This sequence of uplifting and subsidence likely reflects the underlying lithospheric dynamics and this study uses Mesozoic–Cenozoic thermal record of the SE SCB to reconstruct the regional thermal history. The aim of the study is to test the new conceptual hypothesis that flat-subduction and its associated mineral phase changes and eventual oceanic plateau delamination can cause multiple, significant vertical tectonic movements on the overriding continent.

One regional traverse was constructed in the SE SCB and comprised four strategically selected key study areas—Meizhou, Daxi, Shaoguan-Longnan and Hunan from the southeast to the northwest—encompassing both the predicted margin and centre of the Late Triassic–Early Jurassic basin. Along the traverse, pre-Cenozoic magmatic and sedimentary rocks (mainly granites and sandstones) were collected. Zircon from the magmatic samples were analysed by U-Pb dating methods in order to constrain the high temperature spectrum (1000–800°C) of the thermal history. Apatite and zircon were analysed by (U-Th-Sm)/He and fission track methods to reconstruct the thermal history within the lower temperature range of 270–40°C. $^{40}Ar/^{39}Ar$ analysis of muscovite and biotite (400–300°C) and K-feldspar (350–150°C) were performed to elucidate the magmatic cooling and reheating of granites. Permian–Mesozoic coal seams were also sampled for vitrinite reflectance measurements in order to determine the maximum post-depositional temperature.

Muscovite and biotite $^{40}Ar/^{39}Ar$ ages cluster at Late Triassic (220–200 Ma) in

the northwest inland area and at Late Jurassic (165–155 Ma) in the southeastern regions. Zircon fission track and (U-Th-Sm)/He ages range from 341 Ma to 70 Ma with most ages spanning from Late Jurassic (150 Ma) to Late Cretaceous (70 Ma). Apatite fission track and (U-Th-Sm)/He ages form a relatively tight Late Cretaceous–Eocene cluster from 70 to 30 Ma. Vitrinite reflectance data vary from 1.3% to 4.2%. Forward and inverse modelling of the multi-thermochronological dataset, together with other geological, stratigraphical, petrographic evidence, reveals the following major thermal event in the SE SCB: Late Triassic cooling; Late Triassic–Early Jurassic heating; Middle–Late Jurassic thermal peak; Cretaceous slow cooling and Late Cretaceous–Eocene rapid cooling. The thermal evolution is consistent with the flat-subduction model. The Late Triassic cooling is interpreted to be related to orogenic uplift during the approach of the flat-subducted paleo-Pacific oceanic plateau and the Late Triassic–Early Jurassic heating resulted from burial in a sagging basin formed by the gravitational pull of the metamorphosed oceanic flat slab. The Middle–Late Jurassic thermal peak is related to Jurassic granitic intrusions resulting from delamination and break-up of the Paleo-Pacific flat-slab. Slow Cretaceous cooling is consistent with lithospheric rebound due to foundering and roll-back of the subducted Paleo-Pacific plate. Rapid exhumation-driven cooling during the latest Cretaceous–Eocene coincides with continental rifting in SE SCB, and may be linked to a late episode of roll-back of the Paleo-Pacific plate in the lead-up to the opening of the South China Sea.

Overall, this study applies a multi-chronological approach to reveal a complete thermal history (from emplacement/deposition to final exhumation) of pre-, syn- and post-Triassic orogenic sedimentary and magmatic rocks in the SE SCB, and allows quantitative magmatic-tectono-thermal constraints to be placed on this large, geodynamically important and until now under-investigated area. The reported major thermal events in the SE SCB are important references for considering the Mesozoic–Cenozoic geotectonic evolution of the SE SCB. The dataset verifies the validity of the flat-subduction model and links the model-proposed dynamic process with existing thermochronological data. This study provides a way to examine how horizontal tectonics led to continental-scale vertical movements and basin formation, with implications for a number of enigmatic broad mountain belts and magmatic

provinces in the global geological record.

Table of Contents

List of Figures

List of Tables

Chapter 1 Introduction

1.1 Background

The South China Block constitutes a major continental segment in southeastern Asia, separated from the Indochina Block to the southwest by the Red River Fault, from the Songpan-Ganzi Terrane to the northwest by the Longmenshan Fault, from the North China Craton to the north by the Qinling-Dabie Orogen, and bordered by the South China Sea (SCS) and the Pacific Ocean to the south and east, respectively (**Figure 1.1**). Southeast South China Block (SE SCB) is defined as the area that was affected by an Early Mesozoic orogeny (**Section 2.3.1**). In the Mesozoic–Cenozoic a transition of the SE SCB plate boundary from an Andean-type to a Western Pacific-type occurred (Charvet et al., 1994; Li et al., 2012). Because of its relationships with the western Pacific oceanic plates that are currently subducting beneath its southeastern margin, SE SCB is in a key position to shed light on the geodynamic reconstruction of the Asia-Pacific region.

The SE SCB is of notable economic value as well. It is rich in a wide range of base and precious metal deposits, such as copper, tungsten, tin, lead, zinc, iron, molybdenum, nickel, sulphide, gold, silver, platinum etc. (Wang et al., 2006; Gu et al., 2007; Jiang et al., 2007; Zaw et al., 2007; Zhou et al., 2007; Mao et al., 2011; Hu and Zhou, 2012; Mao et al., 2013b). A significant amount of mineralization is hosted in granitoids resulting in the formation and distribution of mineralization being related to a few major tectonothermal phases, including those in the Proterozoic, the Paleozoic, and especially the Mesozoic when massive granitoids were generated (Zaw et al., 2007; Hu and Zhou, 2012).

This projects aims to use a combination of thermochronometers to establish a comprehensive low temperature thermal history for the SE SCB. There are a number of thermochronometers that are relatively well studied and widely applied. These include apatite and zircon (U-Th-Sm)/He and fission track dating, and muscovite, biotite and K-feldspar $^{40}Ar/^{39}Ar$ dating, with each age reflecting closure of the respective system to thermal influences at different temperatures (400–40°C;

Chapter 3).

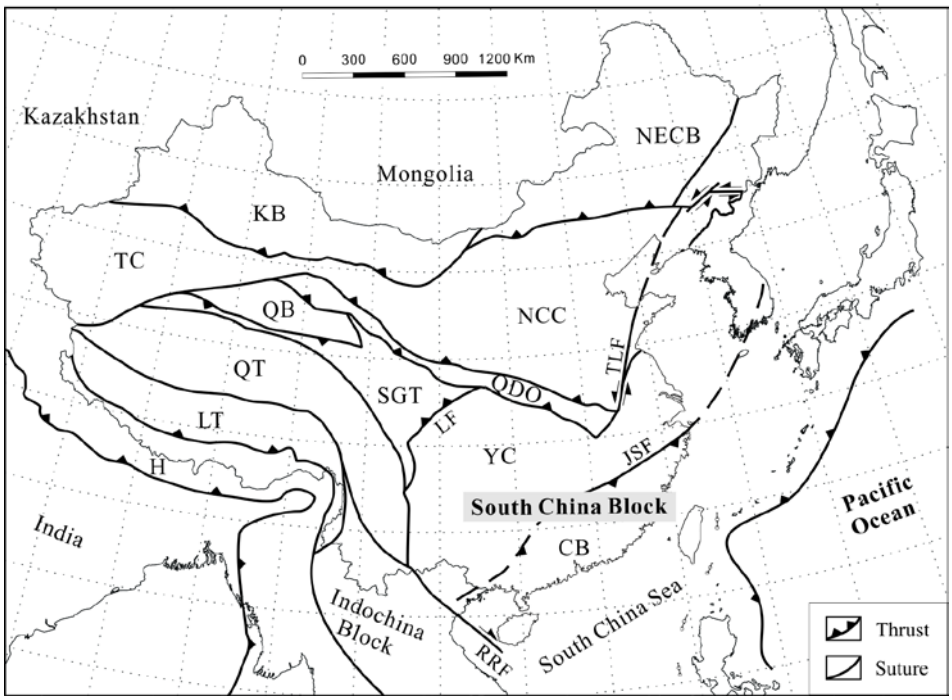

Figure 1.1 Simplified map of major blocks and orogenic belts in China and surrounding areas showing position of the South China Block, modified after Ji et al. (2009).
CB=Cathaysia Block; H=Himalaya; JSF=Jiangshan-Shaoxing Fault; KB=Kazakhstan Block; LF=Longmenshan Fault; LT=Lhasa Terrane; NCC=North China Craton; NECB=Northeast China Block; QB=Qaidam Basin; QDO=Qinling-Dabie Orogen; QT=Qiangtang Terrane; RRF=Red River Fault; SGT=Songpan-Ganzi Terrane; TC=Tarim Craton; YC=Yangtze Craton. Dashed line illustrates the possible extension of a fault or a suture.

1.2 Project design

The SE SCB is a geotectonically complex region where Mesozoic tectonothermal events once caused large-scale vertical crustal movements (Cui and Li, 1983; Goodell et al., 1991; Ren, 1991; Zhou and Li, 2000; Zhou et al., 2006; Li and Li, 2007; Xu et al., 2007; Jiang et al., 2009; Shu et al., 2009; Metcalfe, 2011; Li et al., 2012; Charvet, 2013; Wang et al., 2013; Li et al., 2014a). Extensively exposed Mesozoic granitoids suggest that the overlying rocks have been removed. A shallow-marine basin once existed in the SE SCB in early Mesozoic (Figure 1.2; Liu and Xu, 1994). Reconstructed paleo-geographic map of the SE SCB presents clear marine-

terrestrial facies alternations with vertical movements resulting in exhumation in mountain ranges and subsidence in sedimentary basins during the Mesozoic. Hence, the exhumation/subsidence history of pre-Cenozoic sedimentary strata and magmatic rocks in the SE SCB is fundamental for unrevealing the regional tectonothermal history. Until now, little has been done on the thermal history of the SE SCB, resulting in the poor understanding of the Mesozoic exhumation and burial processes and the tectonic evolution of the SE SCB.

Li and Li (2007) proposed a flat-slab subduction model to explain the tectonic and geological framework in the SE SCB from the Middle Permian to the Cretaceous. Although comprehensive, this model remains controversial, with alternative hypotheses favouring later initiation of Paleo-Pacific plate subduction in either the Late Triassic (Wang et al., 2013) or the Middle Jurassic (Zhou et al., 2006; Jiang et al., 2009; Shu et al., 2009), or attributing a significant role to the Indo-Asia collision (Flower et al., 2001; Wang et al., 2007; Chen et al., 2008; Lin et al., 2008). Although each model is arguably consistent with certain aspects of regional geology, these models do predict distinct exhumation history for the region, a hitherto under-constrained aspect of the regional geological history (Wang et al., 1994; Li et al., 2005a; Zhou et al., 2005; Yan et al., 2009a).

Herein, a multi-chronometer approach is applied in order to assess the thermal history of the SE SCB. This insight will allow us to refine our understanding of the tectonothermal evolution of the SE SCB since the Mesozoic, and provide the basis to more effectively examine the flat-subduction model.

1.2.1 Objectives

The objectives of this study are:

1. To establish complete thermal histories of pre-, syn- and post-Triassic orogenic sedimentary and magmatic rocks in key localities in order to quantify the timing, rate and spatial distribution of multiple exhumation/burial phases in the continental crust.

2. To possibly constrain the underlying dynamic processes by integrating thermal history of key areas in the SE SCB.

3. To evaluate the flat-subduction model proposed for the SE SCB.

1.2.2 Approach

Four study areas were strategically selected for this project, forming a SE-NW traverse across the Early Mesozoic basin in SE SCB (**Figure 1.2**). Meizhou area (*A* in **Figure 1.2**) is near the east edge of the basin, recording the youngest post-orogenic magmatic activities. Daxi area (*B* in **Figure 1.2**) and Shaoguan-Longnan area (*C* in **Figure 1.2**) fall within the depocentre of the basin. Central Hunan (*D* in **Figure 1.2**) locates at the northwest edge of the basin.

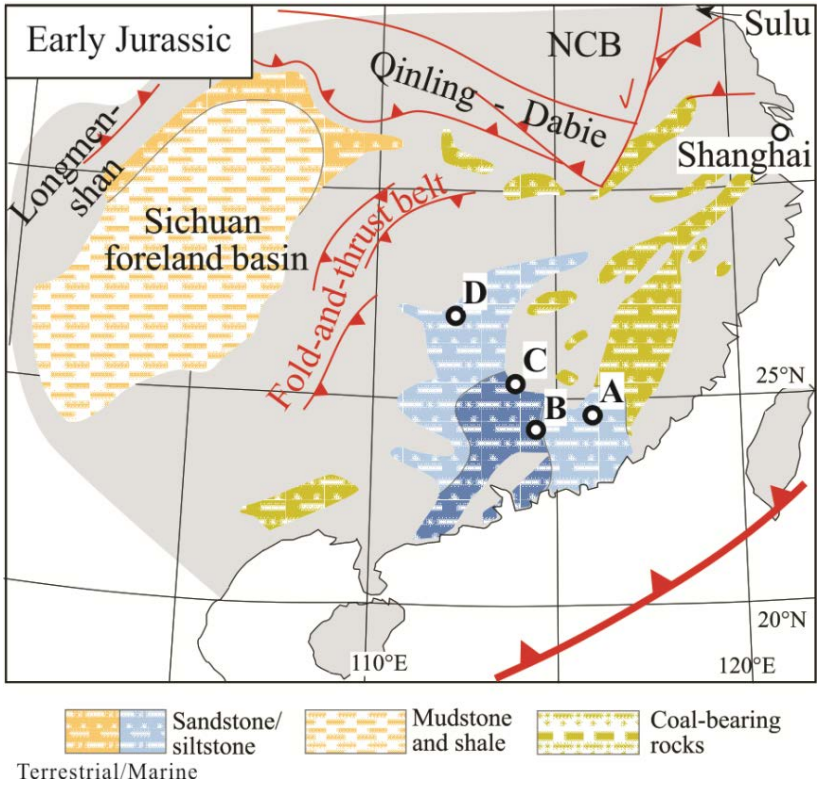

Figure 1.2 Paleo-geographic map SE SCB showing four strategically-selected study areas in this project, modified from Liu and Xu (1994) and Li and Li (2007).
A, B, C, and D represent locations of the Meizhou, Daxi, Shaoguan-Longnan, and central Hunan, respectively.

Sample collection and detailed examination of outcrops and structures were followed by geochronological and thermochronological data collection. The dating encompasses zircon U-Pb geochronology along with comprehensive thermochronology of both granitic and sedimentary rocks, including (U-Th-Sm)/He and fission track dating of apatite and zircon, and $^{40}Ar/^{39}Ar$ dating of K-feldspar, biotite and muscovite. Interpretation of low-temperature thermochronological data was combined with forward and inverse modelling procedures. Local geological observations, stratigraphic, petrographic, geochemistry and geophysical results, along with previously published thermochronological data from samples in the SE SCB are combined with the new data to formulate discussions on the regional tectonic setting.

1.2.3 Significance

This study generates the first systematic thermochronological dataset for the SE SCB. In addition, the work provides a way to examine how horizontal tectonics led to continental-scale vertical movements and basin formation, and how this may be responsible for enigmatic broad mountain belts and magmatic provinces.

1.3 Thesis layout

This thesis consists of eight chapters that are presented as follows:

Chapter 1 begins by clarifying what scientific problems will be addressed in this study, how they were examined and why they are important. **Chapter 2** briefly reviews the geotectonic evolution of the SE SCB, from the Archean to the Cenozoic. **Chapter 3** introduces the analytical methods utilized in this study. **Chapters 4–7** present thermochronological data and tectonothermal histories for the four key study areas; Meizhou, Daxi, Shaoguan-Longnan, and Hunan. **Chapter 8** summarizes the thermochronological data generated from this study and documents the thermochronological and tectonic history of the SE SCB since the Mesozoic.

Chapter 2 Geotectonic context

In this Chapter, the geological background of the SE SCB is introduced in the order of time: early Neoproterozoic amalgamation of two discrete continental terranes (the Yangtze and Cathaysia blocks; **Figure 2.1**; see **Section 2.1**), followed by two orogenic events and one stage of extension since the Paleozoic (**Figure 2.1**).

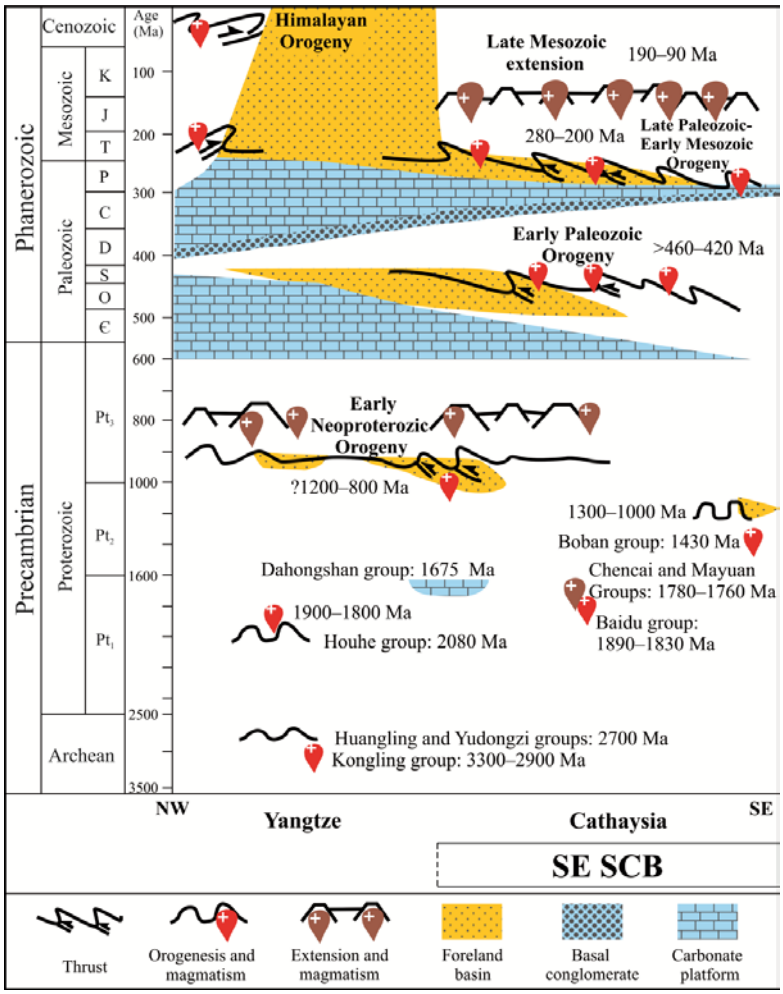

Figure 2.1 Schematic diagram demonstrating major Neoproterozoic and Phanerozoic tectonic events in the SCB, modified from Li et al. (2014d).
Geochronological ages are from (otherwise stated in **Sections 2.2–2.4** or in the caption of **Figure 2.2**): Baidu Group (Wang et al., 2008a; Xiang et al., 2008; Yu et al., 2009; Xia et al., 2012); Boban group (Li et al., 2008c); Chencai group (Li et al., 2010); Dahongshan group (Greentree and Li, 2008); Houhe group (Wu et al., 2012); Huangtuling group (Sun et al., 2008; Wu et al., 2008); Mayuan Group (Li et al., 1998); Yudongzi group (Zhang et al., 2001).

2.1 Precambrian evolution

The SCB was formed when the Yangtze Block and the Cathaysia Block (**Figure 2.2**) amalgamated through a Neoproterozoic orogenic belt (Shu and Charvet, 1996; Zhao and Cawood, 1999; Li et al., 2002b; Zhao and Cawood, 2012; Zhai, 2013; Zheng et al., 2013), named the Sibao Orogen (Li, 1998).

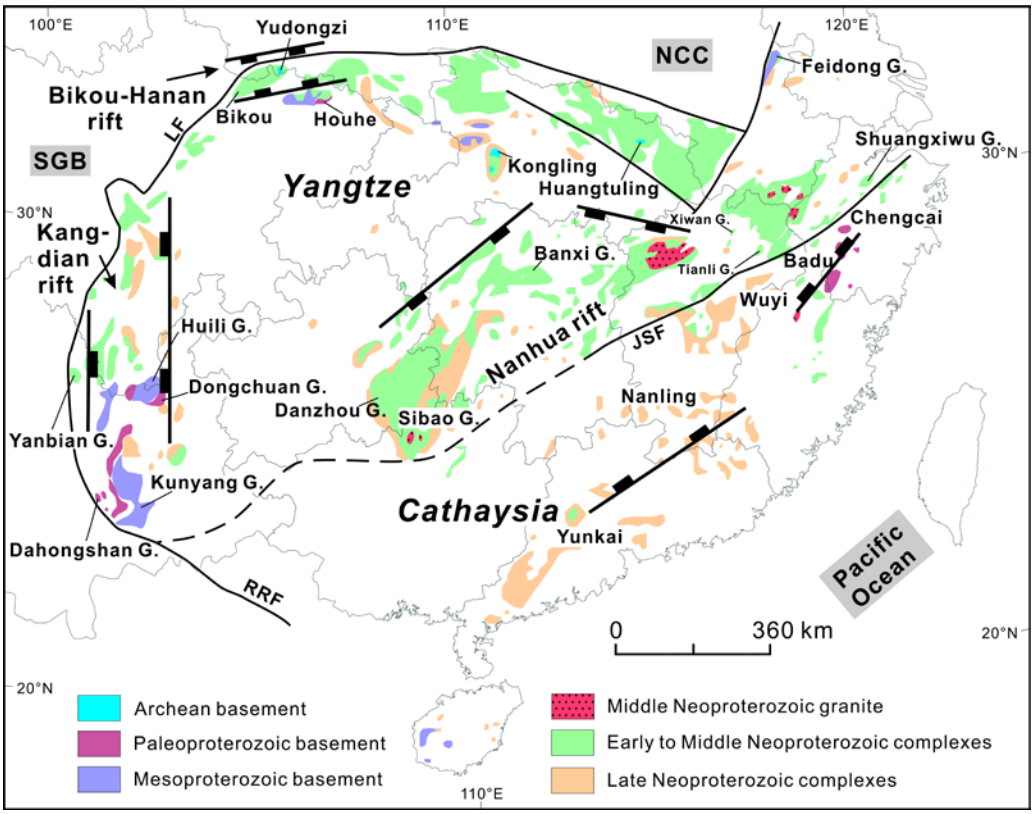

Figure 2.2 Geological map showing the distribution of Precambrian rocks and the Neoproterozoic continental rift systems in the SCB, modified afterLi et al. (1999) and Zhao and Cawood (2012).

JSF=Jiangshan-Shaoxing Fault; NCC=North China Craton; RRF=Red River Fault; SGT=Songpan-Ganzi Terrane. Geochronological ages are from (otherwise stated in **Sections 2.2–2.4** or in the caption of **Figure 2.1**): Kangdian Group (Li et al., 2002a; Li et al., 2005b); Shuangxiwu group (Li et al., 2009a); Tianli schists (Li et al., 2007b); Xiwan group (Li and Li, 2003; Li et al., 2008a).

The cratonization record in the Yangtze Block dates back to the Archean and the oldest basement rock in the Cathaysia Block can be dated back to late Paleoproterozoic (**Figures 2.1** and **2.2**). The oldest crystalline basement in the

Yangtze Block is the Kongling Complex (ca. 3.30–2.87 Ga) (Gao and Zhang, 1990; Qiu et al., 2000; Jiao et al., 2009). The Mesoproterozoic and Lower Neoproterozoic strata (e.g. the Shuangxiwu/Sibao Group; Zhao and Cawood, 2012) were deformed by greenschist-facies metamorphism and were unconformably overlain by younger Neoproterozoic strata (e.g. Banxi Group and its equivalents; Figure 2.2; Wang and Li, 2003; Wang et al., 2011; Zhao and Cawood, 2012). No Archean rock have been identified within the Cathaysia Block, in spite of Archean-age detrital zircons being reported (Li et al., 1998; Xu et al., 2005; Xu et al., 2007; Wan et al., 2010; Zheng et al., 2011; Yu et al., 2012). Precambrian metamorphic basement rocks of the Cathaysia Block are dominated by Neoproterozoic volcaniclastic rocks and mafic intrusions (**Figure 2.2**), with minor Mesoproterozoic granites and meta-volcaniclastic rocks (Li et al., 2002b; Li et al., 2008c) and Upper Paleoproterozoic granitoids and meta-gabbroic rocks (Li, 1997; Li et al., 1998; Wang et al., 2008a; Xiang et al., 2008; Yu et al., 2009; Li et al., 2010).

The present boundary between the Yangtze and Cathaysia blocks in the east is the northeast-orientated Jiangshan-Shaoxing (Jiang-Shao) fault (*JSF* in **Figure 2.2**) (Zhang et al., 2005). The southwest extension of the boundary (dashed extension of *JSF* in **Figure 2.2**) is unclear due to sedimentary cover and tectonothermal reworking since the Neoproterozoic (**Sections 2.2–2.4**) (Li et al., 2014b).

Neoproterozoic continental rift systems developed in the SCB after the Sibao orogeny (**Figure 2.2**) (Li et al., 1999; Wang and Li, 2003; Wang et al., 2011). The Neoproterozoic intercontinental rifting in SCB and its accompanying large mafic-ultramafic igneous provinces have be linked to the break-up of the Rodinia supercontinent (Li et al., 1999; Li et al., 2002b; Li et al., 2008b; Wang et al., 2011). The dominant tectonic setting of the SE SCB transformed from rifting to basin sagging (Wang and Li, 2003) during late Neoproterozoic (Zhang et al., 2008) with the sagging lasted until the Early Paleozoic (**Figure 2.1**).

2.2 Paleozoic evolution

2.2.1 Early Paleozoic Wuyi-Yunkai orogeny

The Early Paleozoic orogeny in SCB was named as the Wuyi-Yunkai orogeny (Li et al., 2010) based on the fact that the greenschist to amphibolite-facies metamorphic core of the orogen is found in the Wuyi Mountain and the Yunkai Mountain regions (Figure 2.3). The Wuyi-Yunkai orogeny is characterized by peak metamorphism during 460–440 Ma (Li et al., 2010), syn-to late orogenic magmatism at 440–415 Ma (Figure 2.4) and retrograde metamorphism at no later than ca. 420 Ma (Li et al., 2010). The orogeny produced a regional angular unconformity between the strongly deformed pre-Devonian sequences and the post-Silurian rocks (Ren, 1991; Zhao et al., 2013).

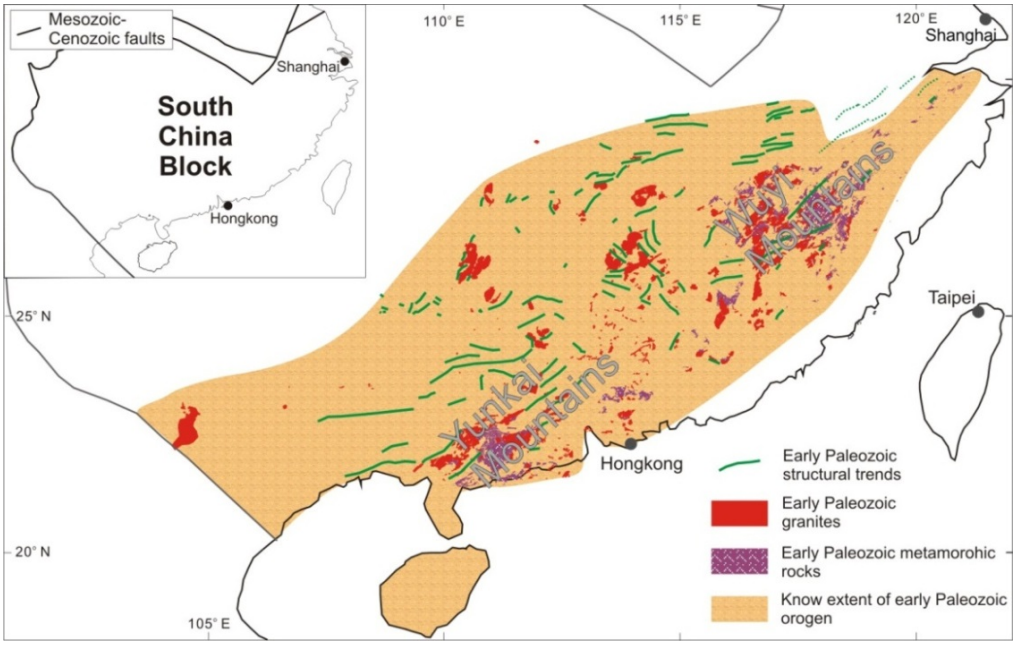

Figure 2.3 Simplified geological map showing the regional extent of the early Paleozoic Wuyi-Yunkai orogeny, from Li et al. (2010).

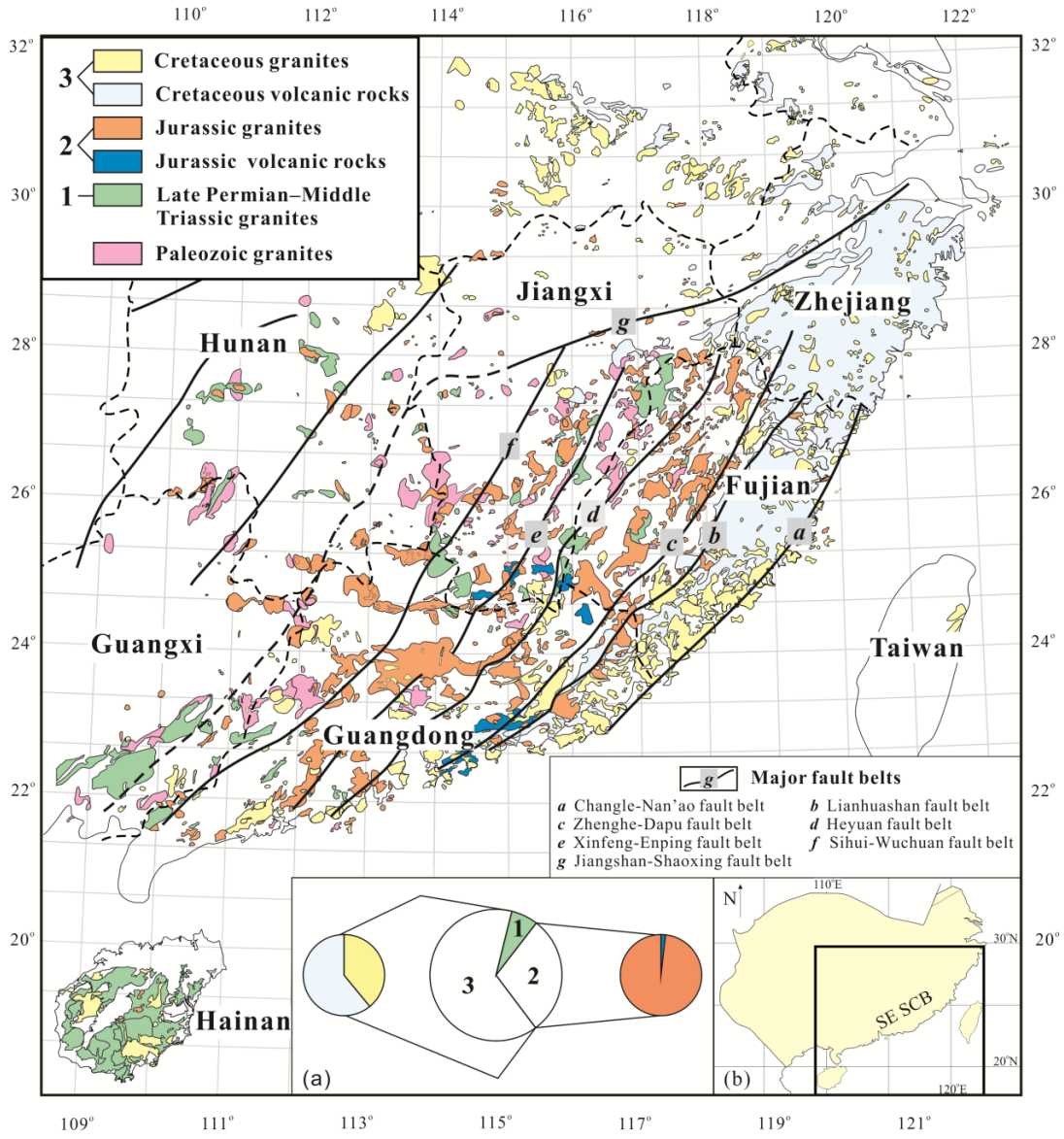

Figure 2.4 Distribution of Paleozoic and Mesozoic granitic and volcanic rocks in SE SCB (modified after Sun, 2006) and major NE-striking faults in SE SCB (modified after Figure 317 in GDBGMR (1988); Yang et al. (2010); Wang et al. (2013)).

(a) Pie-charts show relative outcrop areas of the Late Permian–Middle Triassic, Jurassic and Cretaceous magmatic rocks and the proportions of granitic and volcanic rocks within latter two stages. 1–Late Permian–Middle Triassic granites (green); 2–Jurassic granites (orange) and volcanic rocks (blue); 3–Cretaceous granites (yellow) and volcanic rocks (light blue). (b) Carton showing the location of the SE SCB.

2.2.2 Devonian to Early Permian records

Following the Wuyi-Yunkai orogeny, a Devonian to Carboniferous marine transgression occurred in the SE SCB (**Figure 2.1**). The transgression started from

the southwest in the Early Devonian and extended during Middle–Late Devonian, when carbonate deposits were formed over most regions of the SE SCB (Liu and Xu, 1994). A passive margin is considered to have remained along the southeast rim of the SCB until Permian (**Figure 2.5A**) (Li et al., 2014d).

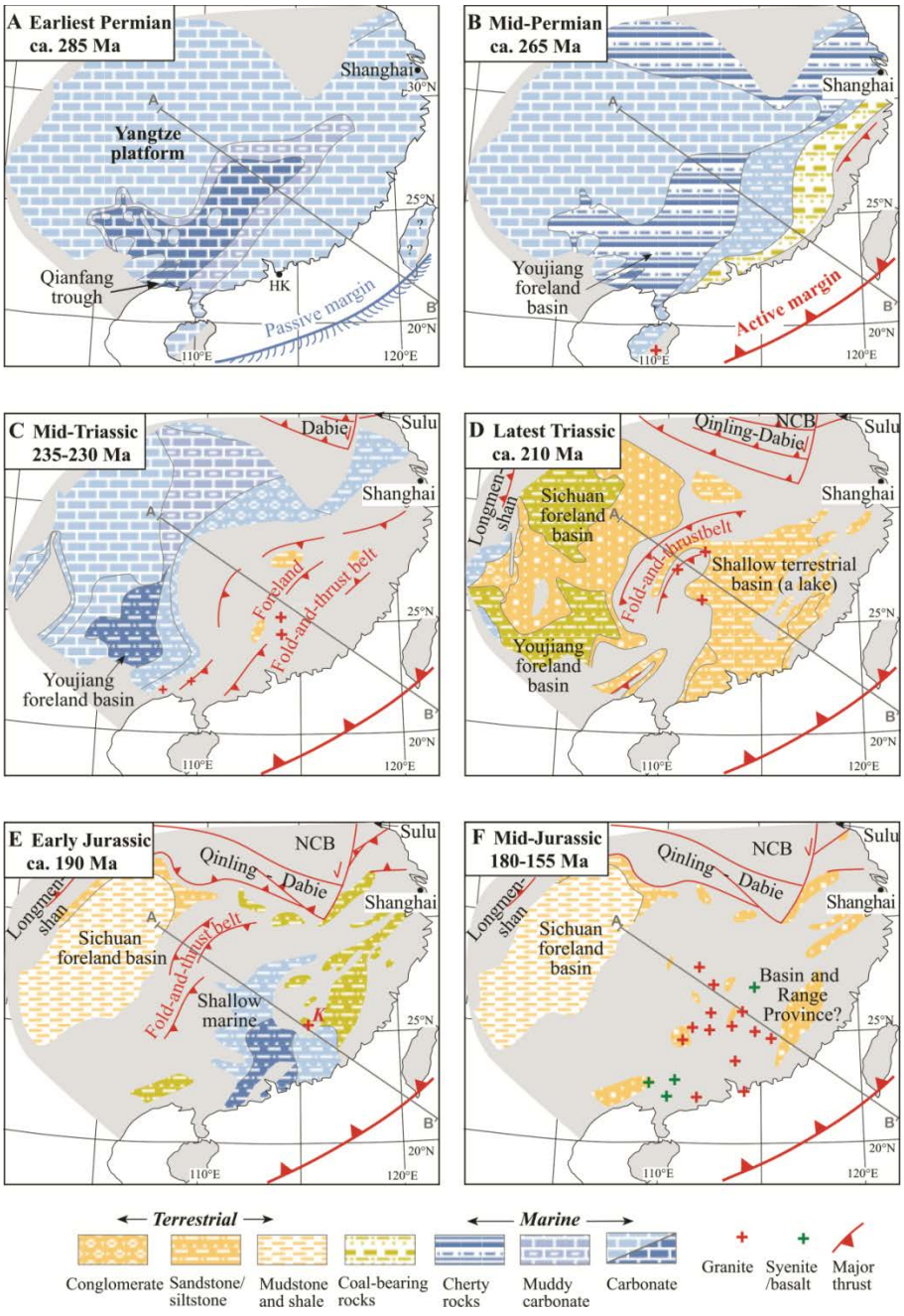

Figure 2.5 Paleo-geographic evolution of the SCB during Permian–Jurassic time, from Li and Li (2007).
NCB=North China Block.

2.3 Mesozoic evolution

2.3.1 Early Mesozoic orogeny

An Early Mesozoic orogen stretches northeastward with a width of ca. 1300 km from the coast to the craton interior and a length of ca. 2000 km (**Figure 2.6**). The distribution of major thrust faults and metamorphism belts displays an inland-younging age pattern (ca. 255–195 Ma) across the Early Mesozoic orogen (Figure 2 in Li and Li, 2007). The age distribution of syn-orogenic magmatism shows the similar inland-younging trend (Li and Li, 2007). Subduction-related magmatism of Middle–Late Permian ages were identified at the continual margin of the SE SCB (Wang et al., 2005; Li et al., 2006). Early Triassic granites occurred sporadically and were primarily on the southern margin of the SE SCB (ca. 251-234 Ma; Peng et al., 2006; Zhou et al., 2006). Late Triassic plutons are confined to only the central interior regions of the SE SCB (**Figure 2.4**) (Zhou et al., 2006; Meng et al., 2012).

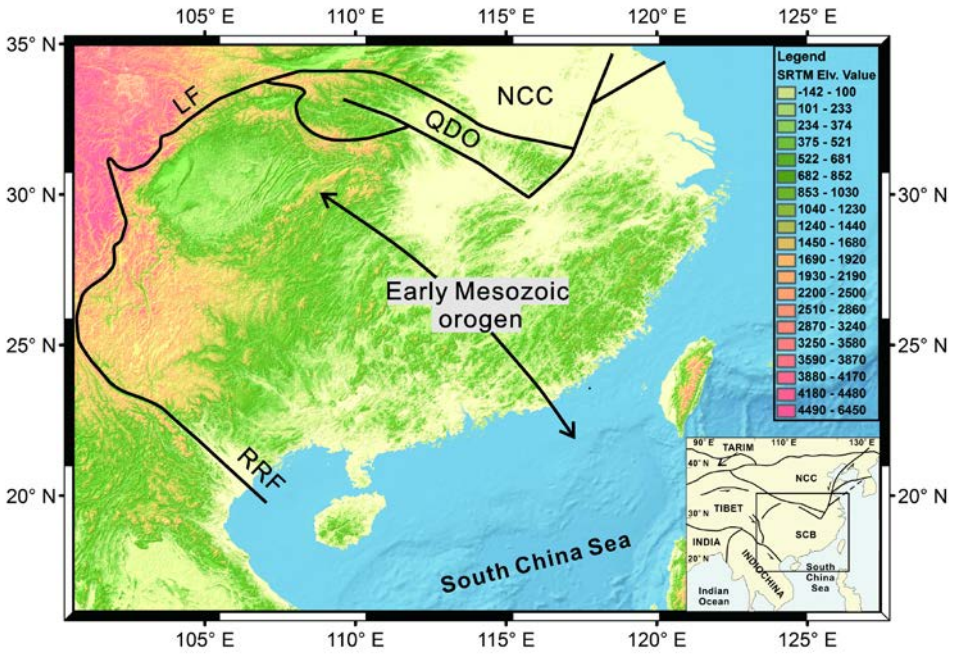

Figure 2.6 Digital topography map of the SCB, showing the scale of the Early Mesozoic orogen modified after Li and Li (2007).

LF=Longmenshan Fault; NCC=North China Craton; QDO=Qinling-Dabie Orogen; RRF=Red River Fault.

Marine regression was first noticed in the coast of SE SCB during the Late Permian (**Figure 2.5B**), and by Middle Triassic the majority of the SE SCB, from the SE to the NW, had been elevated above sea level (**Figure 2.5C**). An regional unconformity between the Lower and Upper Triassic sequences (JXBGMR, 1984; FJBGMR, 1985; GDBGMR, 1988) was produced after the Early Mesozoic orogeny.

Upper Triassic–Lower Jurassic strata continuously deposited within the SE SCB. A shallow terrestrial basin first appeared inland in the early Late Triassic, receiving Upper Triassic coal-bearing lacustrine-facies deposits (Qian et al., 1987; Pang et al., 2014). The terrestrial basin gradually enlarged to cover the central region of the SE SCB (**Figure 2.5D**). During the Early Jurassic, the basin had developed into a broader shallow-marine basin with fine-grained sandstone and siltstone (**Figure 2.5E**) (Liu and Xu, 1994; Pang et al., 2014).

2.3.2 Late Mesozoic extension

The Late Mesozoic extensional tectonics was manifested in the development of a series of NE-trending fault-controlled terrestrial basins from the Middle Jurassic (**Figure 2.5F**), filled with coarse volcaniclastic sediments (Chan et al., 2010; Shi and Li, 2012). In addition, prominent Jurassic intrusions and extensive Cretaceous bimodal volcanisms and intrusions characterized the Late Mesozoic magmatism (Chen et al., 2002b; Li et al., 2003; Wang et al., 2003; Deng et al., 2004; Li et al., 2004a; Li et al., 2004b; Zhou et al., 2006; Chen et al., 2008; Shu et al., 2008; Wang et al., 2008b; He et al., 2010; Yu et al., 2010; Wang et al., 2013). Distribution of magmatism in SE SCB migrated from the central area (i.e. Daxi) towards the coast from the Jurassic to the Cretaceous (**Figure 2.4**). Limited amount of Lower Jurassic volcanic rocks (ca. 195–170 Ma age) constitute a bimodal assemblage in the inland SE SCB, with the OIB-like basaltic components (Zhou et al., 2006; Meng et al., 2012), whereas Cretaceous bimodal volcanism is characterized by arc geochemical signatures (Wang et al., 2008a; Meng et al., 2012). Continental extension in SE SCB was considered to be associated with the retreat of the paleo-Pacific subduction zone in the Late Mesozoic (Li et al., 2012; Shi and Li, 2012). Back-arc marginal basins,

i.e. the proto-South China Sea, began to open in the Late Cretaceous (Seton et al., 2012).

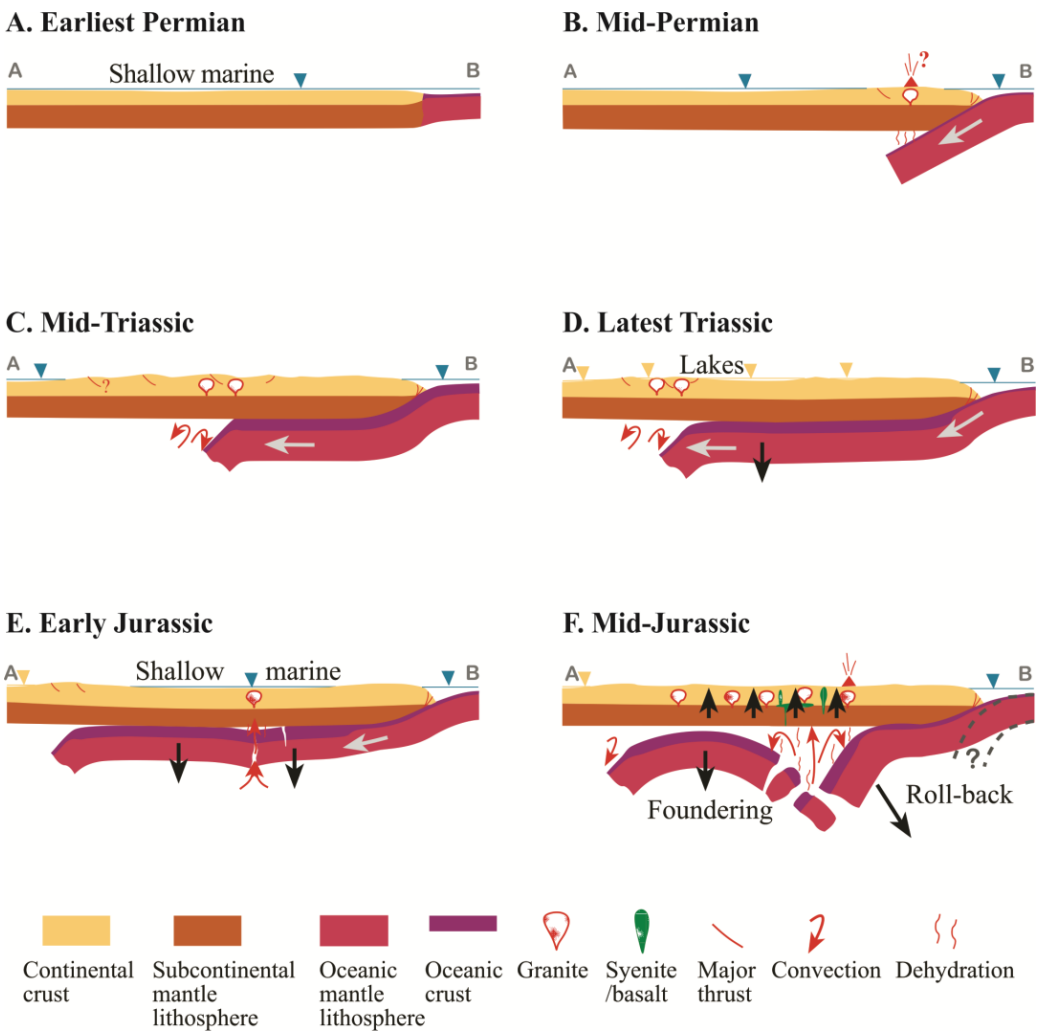

Figure 2.7 Cartoon showing the flat-slab subduction model from Li and Li (2007).

The NE-striking regional fault belts in the SE SCB not only control the distribution of Late Mesozoic basins, but also associate with Mesozoic metamorphic belts (**Figure 2.4**). The Changle-Nan'ao fault belt (***a*** in **Figure 2.4**) likely initiated during the Jurassic with peak activity in the Late Jurassic–Early Cretaceous (GDBGMR, 1988). The fault belt consists of parallel thrust belts, metamorphic belts and migmatization belts (GDBGMR, 1988). The Lianhuashan fault belt (***b*** in **Figure 2.4**) is considered to have formed since the Early Paleozoic (GDBGMR, 1988). This

fault belt controls a Jurassic low-to-medium degree metamorphic belt (GDBGMR, 1988). The Zhenghe-Dapu fault belt (***c* in Figure 2.4**) bounds the Cretaceous volcanic eruptions and granitic intrusions to its east (FJBGMR, 1985). Other major fault belts, extending hundreds of kilometres in a parallel direction, include the Heyuan, Xinfeng-Enping, Sihui-Wuchuan fault belts (***d*, *e* and *f* in Figure 2.4**, respectively).

The geodynamic mechanisms operating in the SE SCB during the mid-Permian and the Mesozoic have been interpreted by a flat-slab model (Li and Li, 2007). The Early Mesozoic orogeny is attributed to subduction of the paleo-Pacific oceanic plates (**Figure 2.7B**). The subducting buoyant oceanic slab and its coupling with the overriding SE SCB provide an explanation for the craton-ward advancement of the mountain front, its foreland basin and the propagation of thrusting and metamorphic belts during the orogeny (**Figure 2.7C**). Once the subduction continued to a critical extent, a gentle depression formed within the metamorphosed flat slab, accompanied by sagging on the continental lithosphere (**Figure 2.7 D** and **E)**. Burial stopped and was replaced by extensive volcanic upwelling when oceanic slab break-off occurred in the mid-Jurassic (**Figure 2.7F)**.

2.4 Cenozoic evolution

A few arid continental basins with fine-grained sandstone, mudstone and gypsum layers were deposited during the Paleogene, while weathering and erosion are the dominant processes in the Neogene in the SE SCB (Ma et al., 2007).

The Cenozoic basaltic volcanism of the SE SCB manifests as widely-distributed small eruptions (**Figure 2.8**) (Fan and Hooper, 1991; Sun, 1991; Zhu et al., 1991; Chung et al., 1997; Zhu et al., 2004). Eruption of Paleocene–Eocene basalts probably signals the initiation of rifting in the SE SCB (Chung et al., 1997; Wang et al., 2012; Huang et al., 2013). Zhou et al. (1995) distinguished episodic rifting in a broad area covering the SE SCB and the continental slope of the SCS. The rifting started onshore in early Cenozoic and propagated to the south until the Oligocene at earliest (Zhou et al., 1995; Shi et al., 2011). The continental rifting was followed by opening

of the SCS during the Oligocene to Miocene (ca. 30–16 Ma; Taylor and Hayes, 1983; Cande and Kent, 1992; Zhou et al., 2009). Miocene basalts show OIB affinity (Huang et al., 2013; Gong and Chen, 2014), consistent with the marginal sea environment in the SCS during the late Cenozoic.

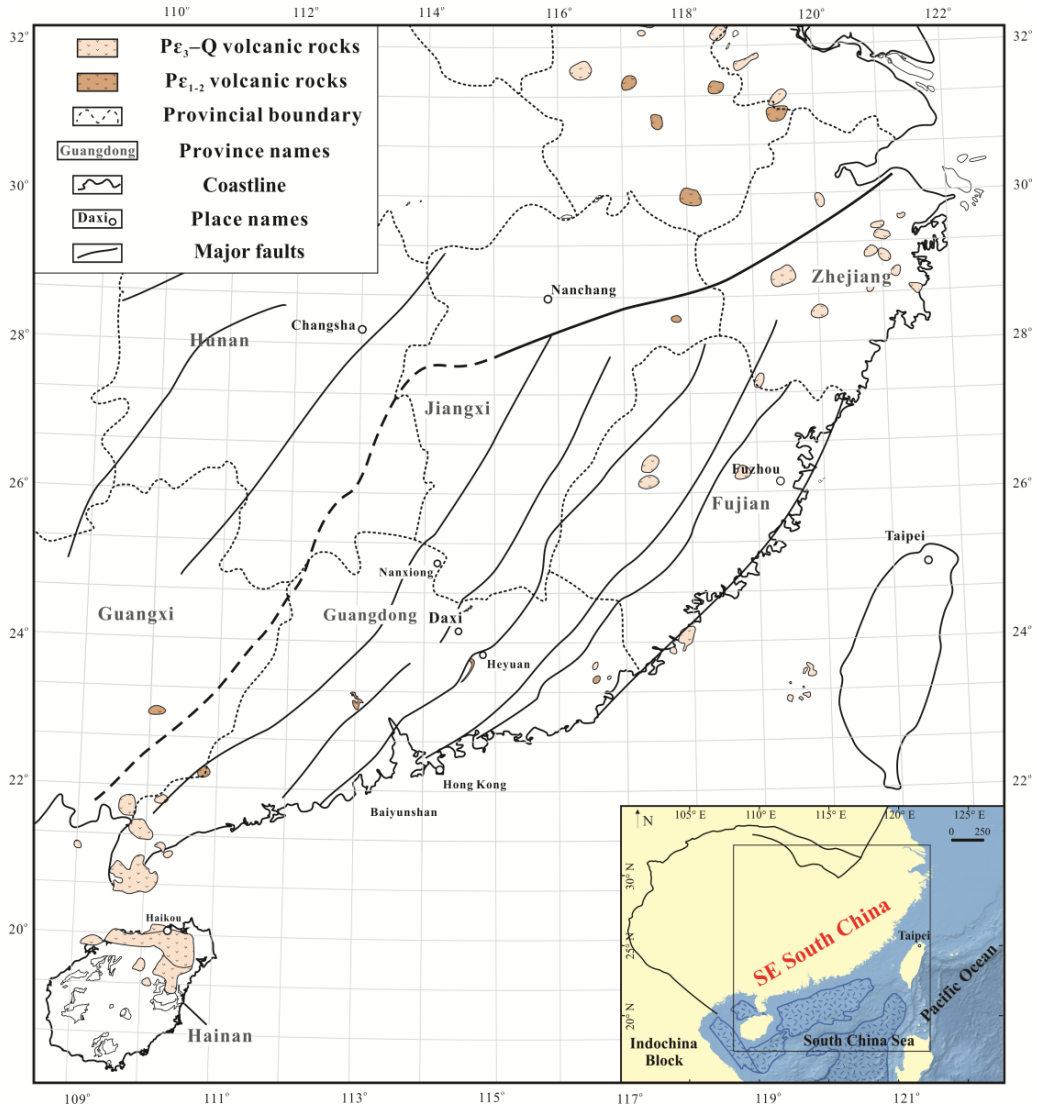

Figure 2.8 Distribution of Cenozoic volcanic rocks in the SE SCB, modified after Gong and Chen (2014).

2.5 Previous thermochronological studies

Thermochronological data have been accumulated mainly in southern SE SCB,

i.e. the Guangdong province (**Figure 2.9 insert**). Previous studies focused on zircon and apatite fission track dating of granitic and metamorphic rocks, with ages clusters at Early Cretaceous and Late Cretaceous–Eocene, respectively (**Table 2.1**) (Wang et al., 1994; Li et al., 2005a; Zhou et al., 2005; Yan et al., 2009a; Shi et al., 2013; Tang et al., 2014; Wang et al., 2015). Biotite $^{40}Ar/^{39}Ar$ ages clearly show two populations, ca. 155 Ma and ca. 90 Ma (Yue et al., 1998; Chen et al., 2002b; Yang et al., 2010). The available data, in general, are consistent with each other.

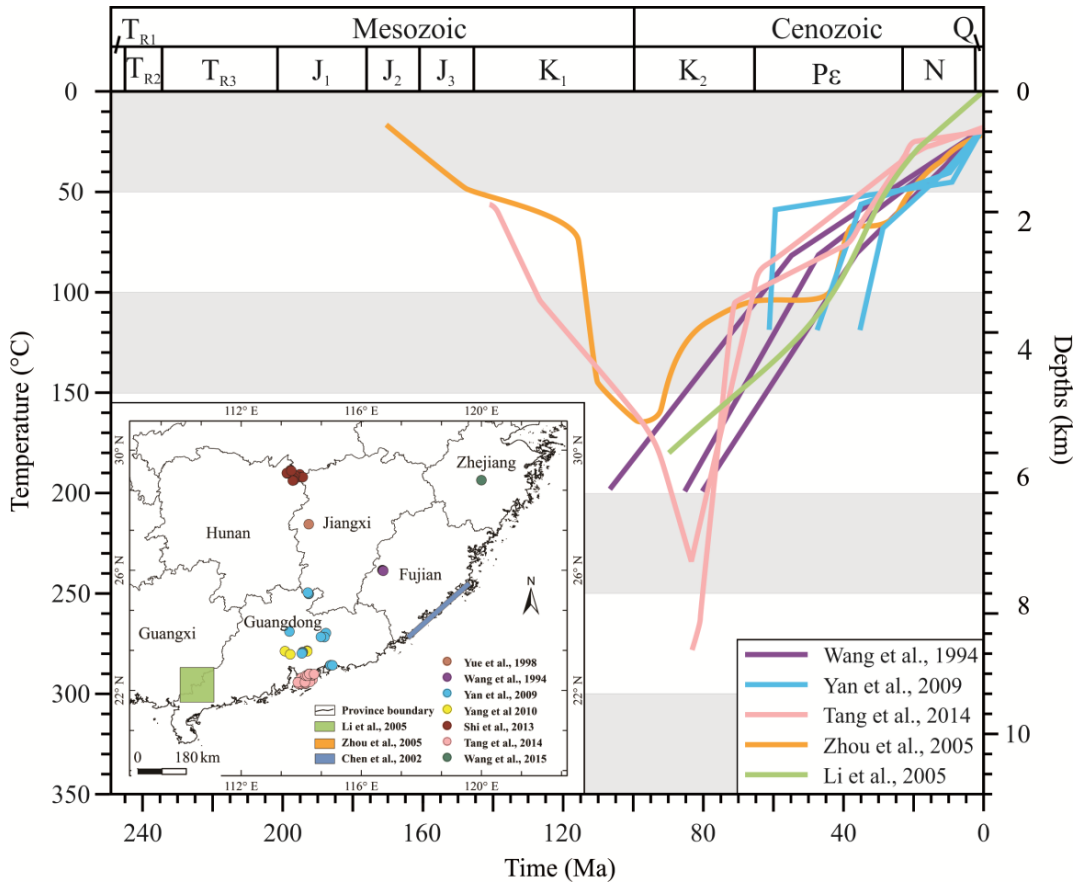

Figure 2.9 Summary of published forward or inversing modelling curves.
Insert: sample locations (circles) or study areas (rectangles) of previous thermochronology studies in the SE SCB. T_R=Triassic, J=Jurassic, K=Cretaceous, Pε=Paleogene, Q=Quaternary.

Late Cretaceous cooling from ~200°C to <100°C is observed in granitic and magmatic rocks (**Figure 2.9**). A decrease in the cooling rate after the Late Cretaceous is shown by most the results of most studies. Variations in the cooling rates from

different studies during the Late Cretaceous is observed but have not been discussed. Lower Paleozoic sandstones in west Jiangxi and lower Mesozoic sandstones in the coast (Hong Kong) experienced heating in the mid-Cretaceous before joining a similar cooling history of other granitic samples (**Figure 2.9**). The coastal samples seem to have experienced higher thermal maximum temperatures than samples from the inland. If true, what caused the different thermal conditions? Are those thermal peaks in mid-Cretaceous the maximum paleo-temperature experienced by the sedimentary samples? These confusions could not be resolved by present datasets mainly because the interpretation of low-temperature thermochronological data were not brought together with high-temperature thermochronometers, like the muscovite and biotite $^{40}Ar/^{39}Ar$ systems. In addition, pre-Cretaceous history has hardly been touched in previous studies. A systematic thermochronological study covering both the coast and the inland regions of the SE SCB, and employing multi-thermochronometries, is therefore urgently needed to facilitate comparison and correlation of the thermal histories of different areas within the SE SCB and a better-understood thermal evolution of the SE SCB.

Table 2.1 Summary of published thermochronological data in SE SCB.

Rock	Thermochronological ages (Ma)					Track length (μm)	Reference
	$^{40}Ar/^{39}Ar$	ZFT	ZHe	AFT	AHe		
Devonian mylonites; Triassic gneisses and granites		133–89		79–35		13.95–13.26	Wang et al. (1994)
Lower Jurassic granite	152 (biotite) 83 (K-feldspar)			42			Yue et al. (1998)
Pingtan-Dongshan metamorphic rocks	132–82 (various minerals)						(Chen et al., 2002b)
Permian–Lower Cretaceous sandstones		unrest; 165		95–50		13.61–12.26	Zhou et al. (2005)
mylonites, migmatites and granites		133–97		68–43		14.36–12.60	Li et al. (2005a)
Middle Jurassic–Lower Cretaceous granites		117–87		61–37	48–15	13.95–13.26	Yan et al. (2009a)
Upper Ordovician and Lower Silurian gneiss	155 (hornblende) 153 (biotite) 98–94 (biotite)						Yang et al. (2010)
Jurassic–Early Cretaceous granitic rocks			131–74	71–24	44–33		(Shi et al., 2013)
Lower Mesozoic magmatic rocks		140–60		83–43		14.60–12.33	Tang et al. (2014)
Upper Mesozoic Sedimentary rocks		90–75					
Precambrian diorite, gneiss and mylonite	431–386 (biotite)	144–103		66–41			(Wang et al., 2015)

ZFT=zircon fission track; ZHe=zircon (U-Th-Sm)/He; AFT=apatite fission track; AHe=apatite (U-Th-Sm)/He.

Chapter 3 Methodology

This chapter outlines the background, theory and techniques for the analytical methods adopted in this study (**Figure 3.1**). More details are provided for low-temperature thermochronology including (U-Th-Sm)/He and fission track dating methods because these are the primary methods employed.

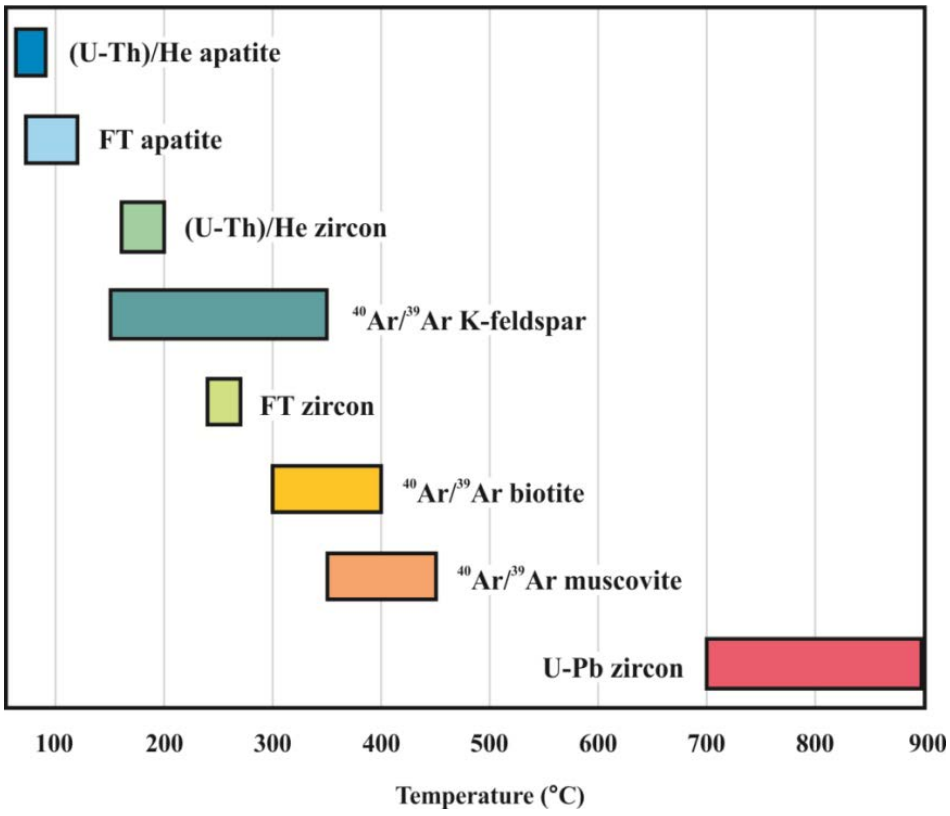

Figure 3.1 Geo-/thermo-chronometers and associated closure temperatures (adapted from http://su-thermochronology.syr.edu/).

3.1 (U-Th-Sm)/He dating

The (U-Th-Sm)/He dating method is based on the spontaneous alpha (α) decay of U, Th and Sm series isotopes, where the α-particles (^{4}He atoms) are then trapped

in the mineral structure after cooling below the mineral's He closure temperature. The method was first proposed in the early 1900s but it yielded unexpectedly young ages (Rutherford, 1905), and was practically abandoned for almost 90 years. The revival of the (U-Th-Sm)/He dating method started with the paper by Zeitler et al. (1987), who correctly interpreted (U-Th-Sm)/He ages as recording the time of cooling rather than the time of mineral formation. Apatite and zircon (U-Th-Sm)/He thermochronometers (AHe and ZHe) with closure temperatures (T_c) of ~70°C (Wolf et al., 1998; Farley, 2000) and ~180°C (Reiners et al., 2004; Guenthner et al., 2013), respectively, provide valuable tools for dating geological processes at shallow crustal depths (~2–6 km).

3.1.1 He ingrowth

(U-Th-Sm)/He ages can be calculated from the content of parent and daughter isotopes and by applying known decay constants. The decay equations for helium production are:

$$^{238}U \rightarrow {}^{206}Pb+8\alpha+\gamma \quad (1)$$

$$^{235}U \rightarrow {}^{207}Pb+7\alpha+\gamma \quad (2)$$

$$^{232}Th \rightarrow {}^{208}Pb+6\alpha+\gamma+\beta \quad (3)$$

$$^{147}Sm \rightarrow {}^{143}Nd+\alpha+\gamma \quad (4)$$

Based on the above, the He ingrowth equation can be given as:

$$^{4}He=8^{238}U[\exp(\lambda_{238}t)-1]+7^{235}U[\exp(\lambda_{235}t)-1]+6^{232}Th[\exp(\lambda_{232}t)-1]+ {}^{147}Sm[\exp(\lambda_{147}t)-1] \quad (5)$$

where ^{4}He, ^{238}U, ^{235}U, ^{232}Th, ^{147}Sm refer to the present-day measured parent isotopes, t is the α-accumulation time ((U-Th-Sm)/He age), and λ^{238} (1.551×10^{-10} yr^{-1}), λ^{235} (9.849×10^{-10} yr^{-1}), λ^{232} (4.948×10^{-11} yr^{-1}), λ^{147} (6.538×10^{-12} yr^{-1}) are α-decay constants for ^{238}U, ^{235}U, ^{232}Th and ^{147}Sm, respectively (Farley, 2002). Two assumptions must be satisfied for **Equation 5** to be valid: (i) secular equilibrium must exist among all radionuclides, which is guaranteed for crystals formed >~1 Myr

before the start of He accumulation, and (ii) no initial ^{4}He can be present in dated grains (Farley, 2002). This latter condition may not be met if the mineral hosts fluid inclusions that contain excess helium. An additional complication is introduced from mineral inclusions, such as zircon, monazite, or allanite, that can frequently occur within other minerals and may bias He measurements if they are not fully dissolved during parent element analysis, leading to anomalously old He ages (so called "parentless daughter") (House et al., 1997; Farley, 2002; Ehlers and Farley, 2003).

3.1.2 Alpha ejection and F_T correction

Alpha particles are formed and released with high kinetic energy (~4–8 MeV) allowing them to travel a certain "stopping distance" in the host mineral lattice before returning to a static state when their energy has been exhausted (Farley et al., 1996). The stopping distance depends on the source of α-decay, the decay energy and the density of the travelling medium (Farley et al., 1996). Stopping distances of ^{4}He from parent apatite (Ap) and zircon (Zr) nuclides are given in **Table 3.1**.

Table 3.1 Stopping distances of ^{4}He in apatite and zircon in micrometres (μm).

	Apatite	Zircon
^{238}U	19.68	16.97
^{235}U	22.83	19.64
^{232}Th	22.46	19.32
Average	~22	~19

Data for apatite are from Farley et al. (1996) and for zircon are from Farley et al. (1996) and Hourigan et al. (2005).

The effect of α-release is characterized by the relationship between the ejection radius (R, R_{max}= one stopping distance) and the distance (L) from the site of a parent atom to the nearside physical boundary of its host mineral grain (Farley, 2002). Specifically, if L > R_{max}, α-particles will be completely retained within the host mineral and no ejection occurs (the probability of ejection is 0%); if L< R_{max}, the

parent nuclei is closer to the rim, fewer α-particles are retained and more will be ejected from the grain (Farley, 2002). The probability of ejection increases to up to 50% when α-decay occurs along the grain edge (assuming the edge of the grain is a flat surface) (Farley, 2002). Due to the loss of daughter particles, the measured helium age would be erroneously young.

Farley et al. (1996) proposed a quantitative α-ejection correction model (F_T correction) to account for the younger age caused by α-ejection, calculated as:

$$F_T=1+a_1\beta+ a_2\beta^2 \quad (6)$$

where a_1 and a_2 are fit parameters incorporating the stopping distance and density of the stopping medium and β is the surface area to volume ratio (**Table 3.2**) (Farley, 2002). As crystal width decreases below a level (e.g., 75 μm), F_T values become sensitive to grain size and errors in F_T correction will become increasingly large. Therefore, sufficiently large grain diameter (typically >60 μm) is one of the key criteria for grain selection as larger grains have more accurate (and lower) F_T corrections.

Table 3.2 Geometry and mineral-specific fit parameters and surface to volume ratio for F_T calculation (Farley, 2002).

Geometry	Mineral	Decay series	Fit parameters		Equation for β calculation	Parameter remarks
			a_1	a_2		
hexagonal prism	Apatite	^{238}U	-5.13	6.78	(2.31L+2R)/(RL)	R is half the distance between the opposed apices and L is the length
		^{232}Th	-5.90	8.99		
tetragonal prism	Zircon	^{238}U	-4.31	4.92	(4L+2W)/(LW)	L is the length and W is the width of the prism
		^{232}Th	-5.00	6.80		

The ^{238}U series has a lower mean energy of α-decay than the ^{232}Th series

(Farley, 2002). To compensate for this difference, a weighted mean F_T for U and Th is utilized which takes into account the fraction of ^{4}He derived from each decay series (Farley, 2002):

$$^{\text{Mean}}F_T = a_{238} \cdot {}^{238}U F_T + (1 - a_{238}) \cdot {}^{232}Th F_T \quad (7)$$

The corrected helium age is then calculated as:

$$\text{Corrected Age} = \frac{\text{Measured Age}}{^{\text{Mean}}F_T} \quad (8)$$

Two assumptions need attention when applying the correction. One is the lack of ^{4}He implantation from the matrix (or neighbouring minerals), which should be valid for most applications given the relatively high U/Th concentration of analysed minerals compared with host rock, although, exceptions may be apatite with extremely poor U-Th content (Farley, 2002; Spiegel et al., 2009). Additionally, homogeneous U, Th and Sm distribution throughout the mineral is also assumed, which may not be always valid for natural samples (Reiners et al., 2004; Hourigan et al., 2005).

3.1.3 Diffusion

Helium derivation adheres to fundamental molecular motion laws and He can undergo thermally controlled, diffusive post in-growth behaviour. The present-day He content in a mineral is the result of the competing effects of α-ingrowth and He-diffusion. In-vacuum, cycled step-heating diffusion experiments on a variety of apatite samples, including the Durango apatite standard (McDowell et al., 2005), obey an Arrhenius relationship (**Equation 9**), suggesting that He diffusion from apatite is a single-mechanism thermally activated volume-diffusion process, at least at temperatures <300°C (Farley, 2002).

$$\frac{D}{a^2} = \left(\frac{D_0}{a^2}\right) \cdot e^{-\frac{E_a}{RT}} \quad (9)$$

where D is the diffusivity, D_o is the diffusivity at infinitely high temperature, E_a is the activation energy, R is the gas constant, T is Kelvin temperature and a is the

diffusion domain radius (Farley, 2000).

Helium diffusion data for the Durango apatite standard yields a He T_c of 75 ± 7°C for grains with a radius of ~70–90 μm, activation energies between ~32–38 kacl/mol and a cooling rate of 10°C/Ma (Wolf et al., 1996). The D/a^2 values of Durango apatite vary with grain size, indicating that the grain itself is the diffusion domain (Farley, 2002).

The He partial retention zone (PRZ) is the region where helium retentivity is most sensitive to temperature. For apatite, the PRZ extends from about 40°C to 80°C (Wolf et al., 1998; Farley, 2000). Factors that may affect the temperature range of the PRZ include radiation damage (Shuster et al., 2006; Flowers et al., 2009; Gautheron et al., 2009; Shuster and Farley, 2009), chemical composition (Gautheron et al., 2013), grain size (Reiners and Farley, 2001), and crystal breakage (Brown et al., 2013).

Laboratory diffusion experiments (Reiners et al., 2002; Reiners et al., 2004), empirical studies on exhumed fault blocks (Reiners et al., 2002) and on high-density bore-hole samples (Wolfe and Stockli, 2010) suggest that zircon PRZ is 180 ± 20°C. Guenthner et al. (2013) showed that radiation damage can change the closure temperature of zircon (U-Th-Sm)/He system causing it varying from 140°C to 220°C.

3.1.4 Analytical procedures

The analytical flowchart is shown in **Figure 3.2**. It essentially involves grain selection and size measurement, laser gas extraction for acquisition of He, isotope dilution ICP-MS for U-Th-Sm concentration and application of any necessary F_T correction before final age calculation.

(U-Th-Sm)/He analyses in this study were conducted at the GeoHistory Facility in the John de Laeter Centre, Curtin University and at the helium facility at The University of Waikato.

Ideal crystals for (U-Th-Sm)/He thermochronology are euhedral, transparent, defect-free, colourless and large (ideally, the shortest axis should be >70 μm to maximum helium gas abundances and minimize the F_T correction). In this study, grains were carefully examined and selected under both binocular and petrographic microscopes and those with cracks or impurities that may release excess helium were excluded (**Section 3.1.1**). Unwanted inclusions were often not visible under the microscope due to their small size (often <1 μm), the presence of pervasive internal reflections or non-transparent crystals. These inclusions later reveal themselves during gas re-extracts (see below) or when irreproducible ages are obtained during replicate measurements (Ehlers and Farley, 2003). Digital images of selected grains were taken and size measurements were recorded for F_T calculation (**Section 3.1.2**). Single crystals of zircon and apatite were loaded into Nb and Pt micro-crucibles, respectively.

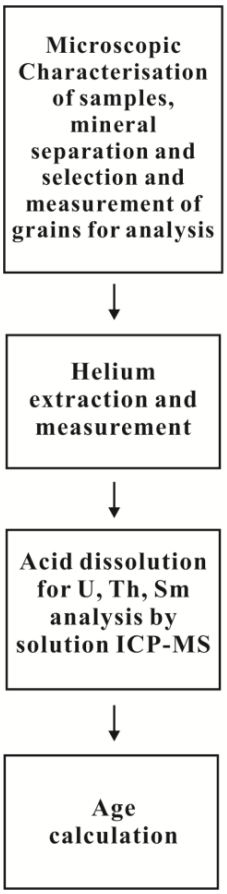

Figure 3.2 Flow chart showing the analytical procedures of (U-Th-Sm)/He dating.

Helium gas was extracted from single mineral crystals using laser heating. Packages (mineral + micro-crucible) were heated by a diode laser (~1200°C for zircon and ~950°C for apatite). ^{4}He gas content was measured by isotope dilution with regularly calibrated a ^{3}He spike (Evans et al., 2005b). Each grain was heated twice (re-extract) in order to assess the presence of undetected inclusions and verify that total gas extraction was achieved. If background gas values were not obtained during the second heating, undetected mineral inclusions were assumed and sample was excluded from further consideration. Prior to U, Th and Sm measurements, the degassed grains were dissolved without being removed from the Pt or Nb packet following the procedures of Evans et al. (2005a). U and Th concentrations were determined using isotope dilution using either an Agilent 7500CS ICP-MS at TSW Analytical™ or a PerkinElmer SCIEX ELAN DRC II ICP-MS at the University of Waikato. Sm concentration was measured by external calibration only at the Waikato lab.

3.1.5 Age calculation, accuracy and precision

Raw (U-Th-Sm)/He age data were corrected for ^{4}He ejection by applying the geometrical F_T correction, calculated for individual grains based on 3-dimension geometry calculation after Farley et al. (1996). Replicates overlapping within 2σ error ranges were combined to determine a weighted-mean (U-Th-Sm)/He age using Isoplot 4.15 (Ludwig, 2012).

Precision of (U-Th-Sm)/He ages was assessed by analysis of 3 or more individual grain replicates for each sample. Replicate analyses of Durango apatite standards and Fish Canyon zircon standards gave weighted-mean ages that are consistent with the published values of 31.13 ± 1.01 Ma for Durango apatite (McDowell et al., 2005) and 28.294 ± 0.036 Ma for Fish Canyon zircon (Renne et al., 2011).

3.2 Fission track dating

In the late 1950s, using transmission electron microscopy (TEM), it was discovered that heavy charged particles passing through insulating materials can leave trails of radiation damage (Silk and Barnes, 1959). Soon afterwards, damage trails were demonstrated to be fixed and enlarged by a simple process of chemical etching, which made them visible under an ordinary optical microscope (Price and Walker, 1962a). These discoveries led to development of fission track (FT) dating. Tracks formed over geological time by the spontaneous fission of ^{238}U were first observed in natural micas by Price and Walker (1962b), and these two physicians firstly proposed that FT could be used as a geological dating method (Price and Walker, 1963). Since then, FT dating has become a robust dating tool that has been successfully applied in various disciplines of geosciences (Dunkl et al., 2001; Donelick et al., 2005; Tagami, 2005; Danišík et al., 2012).

3.2.1 Track formation

The FT dating is based on spontaneous fission decay of a parent isotope (^{238}U) and analysis of the accumulation of physical damage to the crystal structure due to fission (Gallagher et al., 1998). On geological timescales, the spontaneous fission of ^{238}U (with a half-life of 8.2×10^{15} years) is the major reaction accounting for accumulation of fission tracks (Gallagher et al., 1998). Only about one in two million ^{238}U decay events occurs by spontaneous fission decay (Gallagher et al., 1998). Each fission event produces a single straight 'fission track' when the two fragments, formed by the sub-equal halves of the original ^{238}U nuclei, fly apart in opposite directions, leaving behind a continuous, up to 20 μm long liner defect (**Figure 3.3**). High-resolution TEM images of nuclear tracks show that the core of fission track is approximately 10 nm in diameter and consists of a region of amorphous material that has an abrupt transition to a normal undamaged crystal lattice (Gaiduk et al., 2000). This amorphous material is essentially glass that is much more chemically reactive than the surrounding undamaged lattice (Brenier et al., 1999). This property is critically important as it provides the possibility of distinguishing latent tracks from

the host mineral using chemical etching. Each fossil fission track represents one ^{238}U nucleus that conducted spontaneous fission, so the number of spontaneous tracks within a crystal represents the number of fission process (Gleadow, 2007).

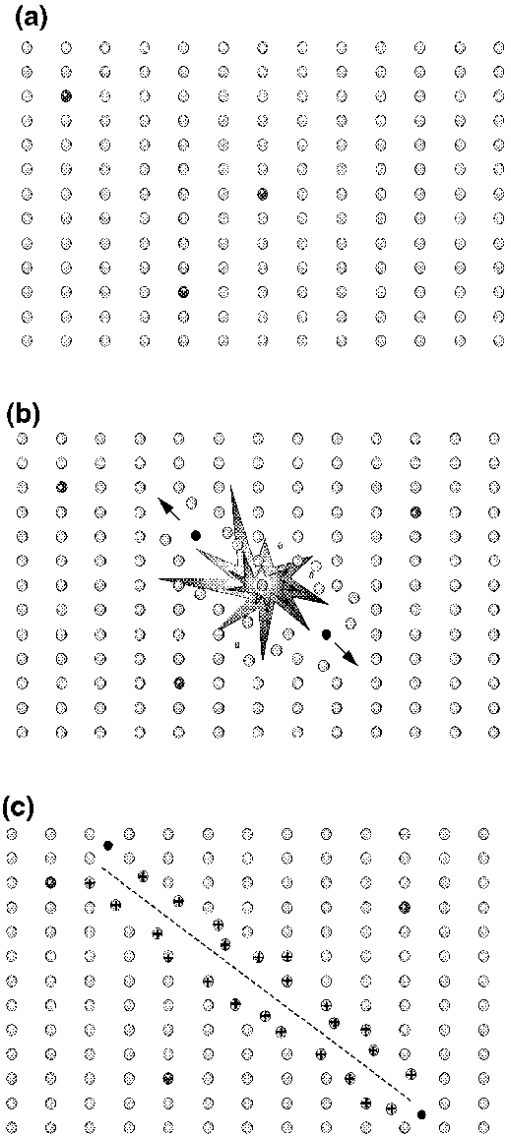

Figure 3.3 Formation of fission tracks (Fleischer et al., 1975).

3.2.2 Track etching

Since latent fission track are generally only 3–14 nm wide and can only be observed under a TEM, an etching process is used to reveal the tracks and make them visible under optical microscopes with high magnification (i.e. 1200 x) (Gallagher et

al., 1998). It should be noted that not every feature in an etched mount is a fission track. To distinguish fission tracks from spurious features of other origins is of critical importance, and some useful principles for distinguishing fission tracks are summarized in Fleischer and Price (1964) and Gleadow (2007).

3.2.3 Track annealing

Fission tracks are metastable features, which will fade with increasing temperature. This phenomenon is called fission track annealing and represents the major strength of the method. For example, for minerals analysed from a drill hole with a downward increase in temperature, FT lengths will shorten irreversibly and the number of tracks will decrease with increasing depth in the hole (Green et al., 1989). Consequently, fewer tracks will be counted and the age estimate becomes younger in deeper samples. (Green et al., 1986).

The partial annealing zone (PAZ), proposed by Wagner (1979) as the "partial stability zone", is a temperature range located above the total annealing zone (where there is no track retention), and below the total retention zone (where negligible annealing occur and fission tracks are stable). The temperature of the apatite PAZ ranges from 60°C to 120°C as determined from several natural examples and laboratory experiments (Gleadow and Duddy, 1981; Green et al., 1986; Laslett et al., 1987; Duddy et al., 1988; Green et al., 1989; Wagner et al., 1994). Annealing experiments (Hasebe et al., 1994; Yamada et al., 1995; Tagami et al., 1998) and extrapolations to geological time scales (Tagami et al., 1996; Tagami and Shimada, 1996) constrained the zircon PAZ to 230°C–330°C, with the range of 240 ± 30°C applicable for most natural zircon samples (Hurford, 1986; Brandon et al., 1998).

The range of temperatures when annealing occurs varies for different minerals as well as being dependent on other factors. Earlier studies have pointed out that the chemical composition of apatite, especially the chlorine content, has critical influence on fission track annealing and therefore effects the FT age (Laslett et al., 1987; Carlson, 1990; Crowley et al., 1991; Laslett and Galbraith, 1996; Barbarand et al., 2003).

The FT closure temperature for F-apatite is ~110°C (Gleadow and Duddy, 1981; Brandon et al., 1998), ~240°C for radiation damaged zircon (Hurford, 1986; Brandon et al., 1998) and ~>300°C for zircon with low to zero radiation damage (Yamada et al., 1995; Rahn et al., 2004).

3.2.4 External detector method

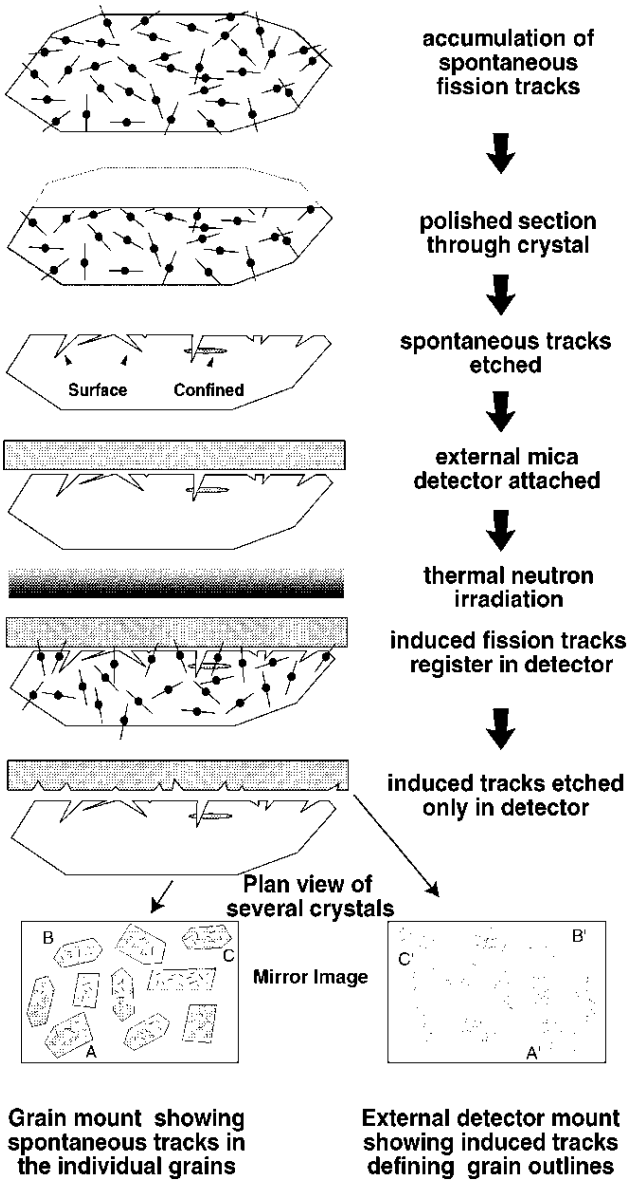

Figure 3.4 The sequence of steps involved in the external detector method of fission track dating (Gallagher et al., 1998).

3.2.5 Age calculation

The general age equation of radiometric dating is:

$$t = \frac{1}{\lambda}\ln\left(\frac{N_P}{N_d}\right) \quad (10)$$

where t=decay time; λ=decay constant; N_p=content of parent isotope; N_d=content of daughter products.

The fission track age equation is a modified form of the above equation (Price and Walker, 1963; Naeser, 1969; Donelick et al., 2005):

$$t = \frac{1}{\lambda_D}\ln\left(1 + \frac{\lambda_D \Phi \sigma I g}{\lambda_f}\frac{\rho_s}{\rho_i}\right) \quad (11)$$

where t=FT age of a grain, λ_D=total decay constant of ^{238}U, 1.55125 x10^{-10} yr^{-1}, Φ=thermal neutron fluence, σ=thermal neutron cross-section for ^{235}U, 580.2 x10^{-24} cm^2, I=isotopic ratio $^{235}U/^{238}U$, 7.2527 x10^{-3}, g=geometry factor for spontaneous FT registration, λ_f=spontaneous fission decay constant of ^{238}U, ρ_s=spontaneous FT density for grain which equals (N_S/A_S) where Ns is the number spontaneous FT counted over area A_S, ρ_i=induced FT density for grain which equals (N_i/A_i) where Ni is the number induced FT counted over area A_i (Gleadow, 2007).

Φ has positive correlation with ρ_d (FT density induced by neutron irradiation for a standard glass dosimeter) is (Tagami and O'Sullivan, 2005):

$$\Phi = B\rho_d \quad (12)$$

where the constant B is a calibration factor and its value is determined by an assumed value of λ_f (Gleadow, 2007). However, there have been different opinions regarding the value of λ_f (Fleischer et al., 1975; Hurford and Green, 1982, 1983; Wagner and Van den Haute, 1992). The zeta (ζ) age calibration method (Hurford and Green, 1983) was applied to calculate fission track age, which allows circumvention of the still significant difficulties in determining Φ and the precise value of λ_f and B separately (Hurford and Green, 1982, 1983; Hurford, 1990b, a). In the ζ approach, mineral age standards with independently determined ages are irradiated together with unknown samples. This calibration and determination of ζ -factor by an operator

avoids the problematic uncertainties inherent in λ_f and B.

$$\zeta = \frac{\sigma IB}{\lambda_f} = \frac{e^{\lambda D t_{STD}} - 1}{\lambda_D (\rho_S/\rho_i)_{STD} \rho_d} \quad (13)$$

Then the FT age equation becomes (Donelick et al., 2005):

$$t = \frac{1}{\lambda_D} \ln(1 + \lambda_D \zeta g \frac{\rho_S}{\rho_i} \rho_d) \quad (14)$$

The symmetrical error of the FT single-grain age determined using the EDM is given by (Donelick et al., 2005):

$$\sigma = [\frac{1}{N_s} + \frac{1}{N_i} + \frac{1}{N_d} + \left(\frac{\sigma_\zeta}{\zeta}\right)^2]^{\frac{1}{2}} \quad (15)$$

where N_d = number of induced FT over the standard glass counted to determine ρ_d, σ_ζ is error of ζ (Donelick et al., 2005). Typical error of FT ages is 10% (1σ).

Three commonly-used "average" age estimates are the pooled, mean, and central age (Gallagher et al., 1998). The assumed distribution of variation of single-grain ages (in a form of ρ_s/ρ_i) is Poisson distribution (Gallagher et al., 1998). Whether a practical case satisfies this premise can be examined by a determination of Chi-square (χ^2) (Green, 1981). When the value of probability of χ^2 ($P\chi^2$) is >5%, all dated grains are related to a single age and the variation of ρ_s/ρ_i fits within a Poisson distribution, and the three age estimates are considered the same. A pooled age can be calculated as (Gleadow, 2007):

$$\frac{\rho_S}{\rho_d} = \frac{\frac{\sum_{j=1}^{n} N_{sj}}{\sum_{j=1}^{n} A_{sj}}}{\frac{\sum_{j=1}^{n} N_{ij}}{\sum_{j=1}^{n} A_{ij}}} \quad (16)$$

If the value of χ^2 probability is <5%, representing multiple age populations (the variation in ρ_s/ρ_i will be greater than expected for a Poisson distribution), a mean age is suggested should be adopted (Green, 1981; Gleadow, 2007):

$$[\frac{\rho_S}{\rho_i}] = \sum_{j=1}^{n} \frac{[\frac{\rho_S}{\rho_i}]_j}{n} \quad (17)$$

3.2.6 Track length measurement

The conventional protocol for fission-track length measurement is to measure the length of horizontal confined fission tracks (Bhandari et al., 1971; Gallagher et al., 1998). Confined tracks must be completely preserved in the crystal and should be oriented parallel to the c-axis (Gallagher et al., 1998). Confined tracks can be divided into three types: track in track (TINT) and track in cleavage (TINCLE) (Lal et al., 1969), and a recently-proposed type, track in defect or fluid or soluble mineral inclusion (TINDEF) (Donelick et al., 2005) (**Figure 3.5**). An integrated record of measurable parameters regarding a confined track include its complete length, its angle relative to the crystallographic *c*-axis, the type of the track and the D_{par} (Burtner et al., 1994).

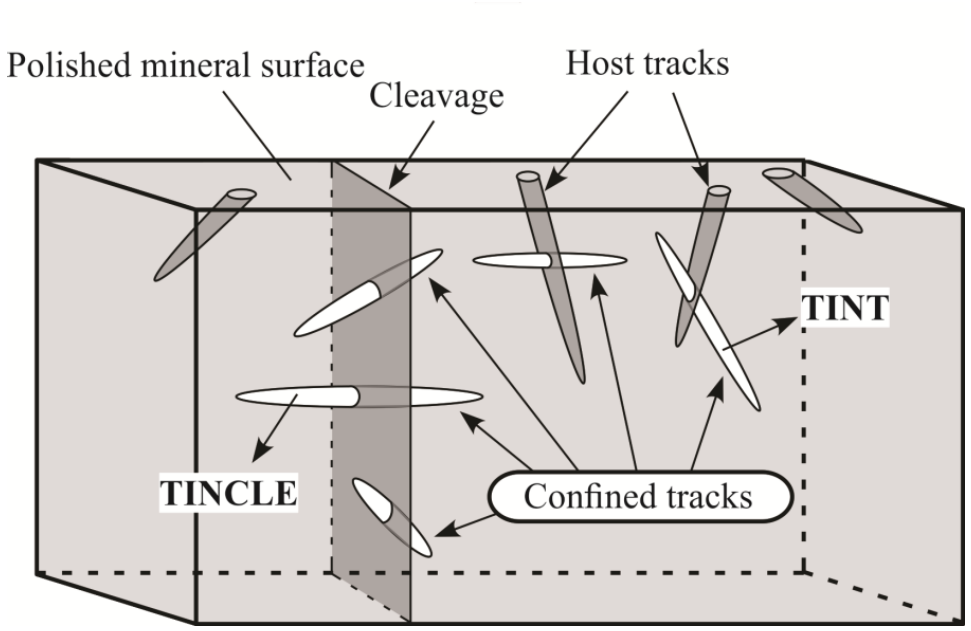

Figure 3.5 A schematic cartoon showing different confined tracks, from Peter and Todd (2005). TINCLE=tracks-in-cleavage; TINT=tracks-in-track.

Grains record heating and cooling events by track length shortening and growth, generating responses in FT ages. Then, distinguishing and comparing the characters of different confined-track length distributions will illustrate related

thermal history scenarios the host rock experienced (**Figure 3.6**).

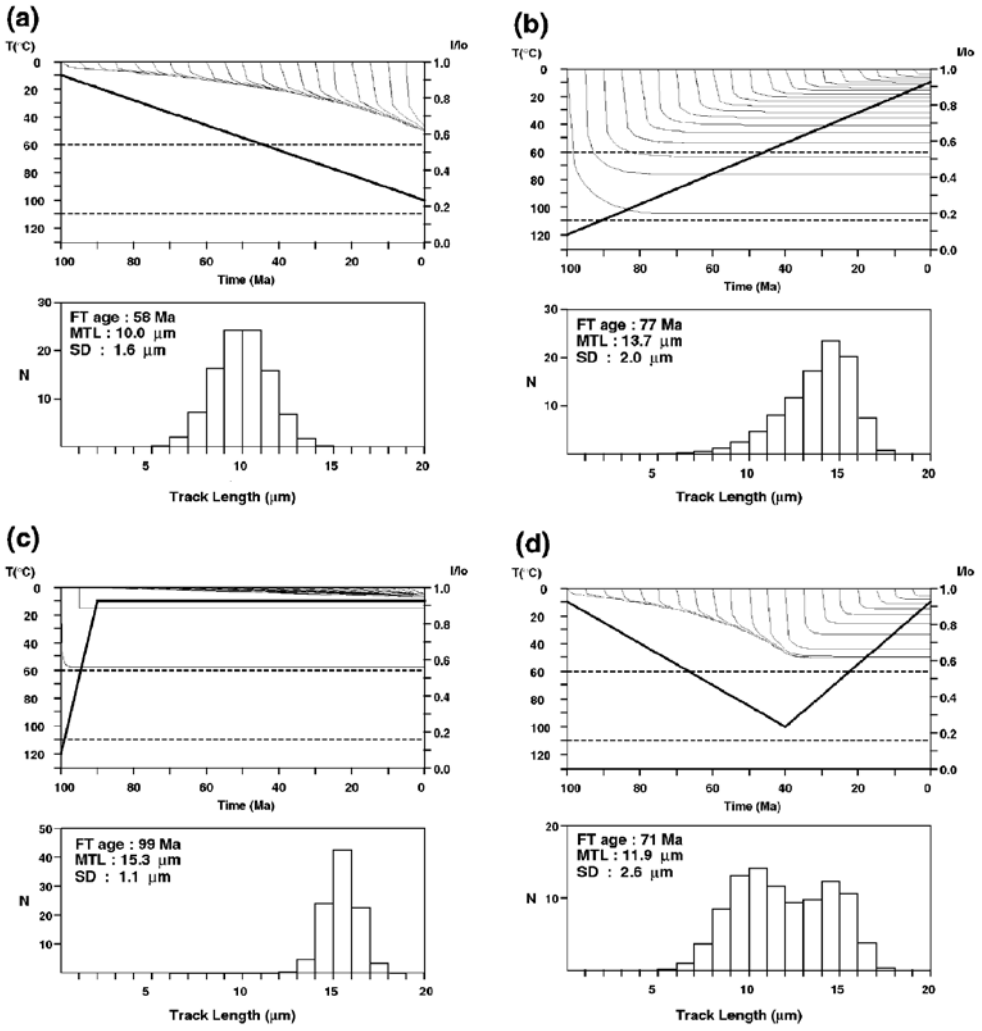

Figure 3.6 Thermal histories (upper panels) and the predicted track length distributions (lower panels) of Durango apatite (Gallagher et al., 1998).

3.2.7 Analytical procedures

Apatite and zircon fission track (AFT and ZFT) analysis using the external detector method (**Section 3.2.4**) and zeta calibration approach (**Section 3.2.5**) was conducted at the University of Waikato (New Zealand) following the methods reported by Danišık et al. (2007). Apatite fission track analysis of sample 04GD43 was assessed at the University of Melbourne following the experimental procedures

documented in Kohn et al. (1995). Sample 04GD43 was irradiated at X-1 facility of the HIFAR; all other samples were irradiated at Oregon State University.

Here I briefly outline the steps involved in the EDM as shown in **Figure 3.4**.

a. Mounting. Mount Ap and Zr crystals in epoxy resin and Teflon™, respectively.

b. Grinding and polishing. Keep the exposure gradual when grinding. The aim of this step is to obtain a perfectly flat polished surface.

c. Etching of spontaneous tracks. In this project, apatite samples were etched in 5.5 M HNO_3 at 21°C for 20 seconds (Donelick et al., 1999). Zircon samples were etched in KOH:NaOH eutectic melt at 215°C for 2–16 hours (Zaun and Wagner, 1982).

d. Attaching mica external detector and irradiation.

e. Counting using microscope.

Central ages and errors were determined using TrackKey program (Dunkl, 2002). The lengths of horizontal confined tracks were measured on surfaces that are parallel to the c-axis, and the measurements were normalized for crystallographic angle adopting the c-axis projection approach (Donelick et al., 1999; Ketcham et al., 2007). The annealing properties of apatite analysed in the Waikato lab were assessed by measuring D_{par} (Crowley et al., 1991; Naeser, 1992; Burtner et al., 1994). The Popshare program (Dunkl and Székely, 2003) was used for age component analysis.

3.3 $^{40}Ar/^{39}Ar$ dating

The $^{40}Ar/^{39}Ar$ dating method can be applied to any rocks and minerals that contain potassium (e.g. micas and feldspars) and is used in the determination of a broad age spectrum when geological processes occurred (Renne et al., 1997; Swindle et al., 2009).

3.3.1 $^{40}Ar/^{39}Ar$ principles

Principles of the $^{40}Ar/^{39}Ar$ method were first proposed by Merrihue and Turner (1966). The $^{40}Ar/^{39}Ar$ method acquires its potassium concentration via neutron-activated conversion of ^{39}K to ^{39}Ar.

$$^{39}_{19}K + ^{1}_{0}n \rightarrow ^{39}_{18}Ar + ^{1}_{1}p \quad (18)$$

The radioactive half-life of ^{39}Ar is 269 yr., therefore, in geological time scale all measured ^{39}Ar can reasonably be ascribed to ^{39}K (Renne, 2006). As the $^{39}K/^{40}K$ ratio is homogeneous in terrestrial materials (Humayun and Clayton, 1995), ^{40}K can be determined with known extent of the neutron conversion. The amount of ^{39}Ar produced from a neutron-irradiated sample is (McDougall and Harrison, 1999; Renne, 2006):

$$^{39}Ar = {}^{39}K\ \Delta \int \sigma(\varepsilon)\ \Phi(\varepsilon)\ d\varepsilon \quad (19)$$

where ^{39}K=the amount of ^{39}K; Δ=the duration of the irradiation; σ=the probability of the reaction; ε=neutron energy; Φ=the neutron flux (Renne, 2006).

The age equation for the $^{40}Ar/^{39}Ar$ method is (McDougall and Harrison, 1999):

$$t = \frac{1}{\lambda}\ln[1 + J \cdot (\frac{^{40}Ar^{*}}{^{39}Ar})] \quad (20)$$

A parameter J is defined as (McDougall and Harrison, 1999):

$$J = (\frac{^{39}K}{^{40}K}) \cdot (\frac{\lambda}{\lambda_e}) \cdot \Delta \cdot \int \sigma(\varepsilon)\Phi(\varepsilon)d\varepsilon \quad (21)$$

Age standards are irradiated in the same condition of unknowns. In this case, J value derived from the standards can be applied to unknowns by assuming that they have experienced the same neutron flux during the same time period (Renne, 2006).

The $^{40}Ar/^{39}Ar$ closure temperature for muscovite (MsAr), biotite (BtAr) and K-feldspar (KfsAr) is 350 ± 50°C (Hames and Bowring, 1994), 300 ± 50°C (Harrison et al., 1985) and 150–350°C (Lovera et al., 1989).

3.3.2 Laboratory procedures

$^{40}Ar/^{39}Ar$ analyses were performed at the Western Australian Argon Isotope Facility in the John de Laeter Centre at Curtin University, Australia, following the protocols of Jourdan et al. (2011). Prior to separation, a suitable sample was selected on the basis of petrographic thin-sections, excluding potential samples where target minerals were intergrown with other Ar-bearing mineral phases. Unaltered mineral separates were hand-picked from the 500–800 μm-size fractions and thoroughly and ultrasonically rinsed with distilled water. Unknown samples were loaded into one well within an aluminium disc. The unknown wells were set near wells containing Fish Canyon sanidine (FCs) (Renne et al., 2011) or Hb3gr hornblende (Jourdan et al., 2006) standards that monitored the neutron flux during the irradiation. Aluminium discs were Cd-shielded in order to minimize nuclear interference reactions (Tetley et al., 1980; Jourdan et al., 2014).

Sample 08FG-1 and 04GD43 were irradiated for 25 hours at McMASTER Nuclear Reactor, and all the other samples were irradiated for 40 hours at the USGS TRIGA Reactor. Flux densities were calculated and recorded for comparison with standards. After irradiation, samples were allowed to cool for 2 to 3 weeks in order to achieve a low radioactive background for safe handling. The J-values were calculated from standard grains from each pit, and the mean J-values were computed as the mean of J-values of the all wells from all irradiation discs (Dalrymple et al., 1981). The uncertainty of the mean J-value was determined as the standard deviation of J-values of the wells within disc. An automated air pipette with a mean value of 1.006 (± 0.35%) per dalton was used for controlling mass discrimination. Irradiated samples were either wrapped in zero-blank niobium foil and incrementally heated by a 110 W Spectron laser, or wrapped in copper foil and heated by an automated Pond-Engineering low-blank furnace. Argon isotopes were measured by a MAP 215-50 mass spectrometer through 10 cycles of peak scanning. The mass spectrometer was run under a static mode and was attached with a Balzers SEV 217 electron multiplier. One laser blank was analysed every three or four unknowns, with normal ^{40}Ar blanks ranging from 1×10^{-16} to 2×10^{-16} mol.

Data reduction were performed with the ArArCALC program (Koppers, 2002).

Age calculation adopted the decay constants reported by Renne et al. (2011) and incorporated all sources of uncertainties. Plateau ages were calculated as the error-weighted mean of all plateau steps, and are reported at the 2σ level. Adjacent heating steps within a age plateau must agree within a 95% confidence level, satisfy a probability of fit of no less than 5%, and include at least 70% of the released ^{39}Ar (or, for a mini plateau, 50–70%). Where no plateau age was identified, a weighted-mean age or qualitative information (e.g. maximum age or minimum age) is provided.

3.4 SHRIMP zircon U-Pb dating

3.4.1 SHRIMP U-Pb zircon geochronology

U-Pb geochronology exploits two completely independent decay schemes, ^{235}U to ^{207}Pb and ^{238}U to ^{206}Pb with precisely calibrated decay constants (Jaffey et al., 1971; Bowring et al., 2006). The main application of the Sensitive High Resolution Ion Microprobe (SHRIMP), which is a large-radius secondary ion mass spectrometer, is U-Pb dating of zircon from geological samples. It achieves both high mass resolution and high abundance sensitivity with *in-situ* age dating at a 5–25 µm spatial resolution (Ireland and Williams, 2003; Parrish and Noble, 2003).

Zircon U-Pb measurements constrain the high temperature spectrum (800 ± 100°C) (Cherniak and Watson, 2003) of the thermal history of samples and provide a 'birth certificate' for the mineral analysed.

3.4.2 SHRIMP analytical techniques

U-Pb analysis was carried out at the SHRIMP lab at the John de Laeter Centre, Curtin University, following procedures described by Williams (1998) and Nelson (2001).

Sample mounts were made by embedding zircon unknown grains and multigrain zircon standards in epoxy, which were then polished until a suitable surface was achieved. All SHRIMP mounts were ultrasonically rinsed and gold

coated. Transmitted and reflected light images of mounted grains were taken. The cathodoluminescence (CL) images of mounted grains were taken at the Microscopy and Microanalysis Facility, John de Laeter Centre, Curtin University. Both optical photomicrographs and CL images were used to characterize zoning structure and U/Th concentration of zircon crystals and were used for selection of analysis spots.

To acquire the magmatic ages of the granitic samples, analysis spots were placed at the outer rim of zircon grains. The primary O_2-beam produced positive secondary ions and generated elliptical spots approximately 20-30 μm in size. Data were acquired over 6 cycles of peak scanning. Operating at a mass resolution of >5000 at 1% peak height was prompted to minimize spectral interferences (Compston et al., 1984). A raster (surface cleaning) time of 2.5–3 minutes was used. U-Th-Pb ratios of unknowns were measured by referring to that of the TEMORA 2 standard (Black et al., 2004) or Plešovice (Sláma et al., 2008). U and Th abundances were calibrated to the BR266 (Stern, 2001) or M257 (Nasdala et al., 2008). Raw SHRIMP data were processed using Squid 2.5 (Ludwig, 2009) and plotted by Isoplot 4.15 (Ludwig, 2012).

3.5 Vitrinite reflectance thermometry

The first reported modelling results on vitrinite maturation in the 1980s marked the initiation of utilising vitrinite reflectance (VR) as an thermal indicator (Waples, 1980). VR has become a widely used tool in oil and gas exploration as well as for estimating maximum temperature attained by sedimentary rocks in hydrothermal environment. In this study, VR of representative coal and shale samples was conducted to define the maximum post-depositional temperatures.

3.5.1 Organic matter in sediments

Organic matter in sediments is derived from the thermal alteration of plants over geologic time. Vitrinite is a common maceral in coals, shales or other organic source rocks. As the maturity of organic source rock increases, the chemical

composition of the vitrinite changes accordingly, resulting in the increases of the reflectance of vitrinite. Therefore, vitrinite reflectance is a function of the organic component maturity (Mukhopadhyay and Dow, 1994). VR measurements assess the percentage of light reflected from the sample.

3.5.2 VR and maximum paleo-temperature

Waples (1980) conducted VR modelling based on a simple assumption that the rate of maturation of vitrinite doubles when the temperature increases by 10°C. This simple simulation works quite well but lacks theoretical basis (Sweeney and Burnham, 1990). One group of models suggests that increasing duration at maximum temperature has little influence on thermal maturation (Price, 1983; Barker and Pawlewicz, 1986; Barker, 1989). Another group of models correlated VR with Arrhenius first-order chemical reactions with a with a single activation energy (Middleton, 1982; Lerche et al., 1984; Ritter, 1984; Antia, 1986; Wood, 1988; Armagnac et al., 1989), but such single reaction fails to account for complex case cover a wide range of heating rates and temperatures (Sweeney and Burnham, 1990; Laughland and Underwood, 1993). Larter (1988) proposed a Gaussian distribution of activation energies, but the model is only valid for VR values between 0.5%–1.3% (Sweeney and Burnham, 1990).

Easy%R_o model calibrates the correlation between measured composition and measured coal VR values (R_o) by adopting H/C and O/C atomic ratios for composition calculations (Burnham and Sweeney, 1989). In Easy%R_o, R_o is determined from:

$$\%\mathrm{Ro} = exp(-1.6 + 3.7F) \qquad 22$$

where F is the extent of reaction ranging from 0–0.85 (Sweeney and Burnham, 1990).

Easy%R_o model stands over a range of VR values, from 0.3% to 4.7%, as well as heating rates, from 1°C/week to 1°C/10 Myr (Sweeney and Burnham, 1990).

3.5.3 VR measurements

VR analysis in this study was conducted in State Key laboratory of Organic Geochemistry at Guangzhou Institute of Geochemistry, Chinese academy of Sciences, Guangzhou, China. Analytical procedures are described below.

a. Crush Bulk samples (coal/shale) and separate and disaggregate organic matter (including vitrinite).

b. Mount organic matter (e.g. **Figure 3.7a**).

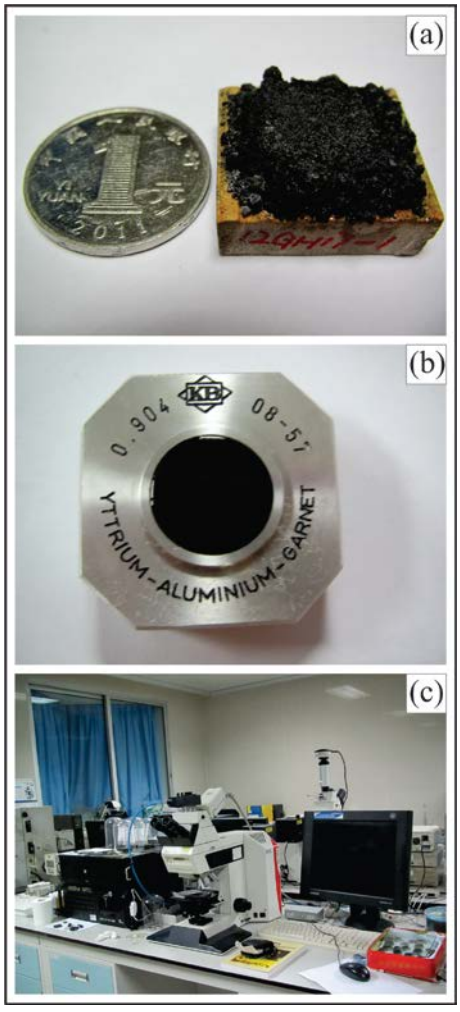

Figure 3.7 One mounted sample and key facilities for VR measurement.
(a) A coal sample fragments mounted on a flat ceramic plate by adhesive. (b) Yttrium-Aluminium garnet standard with a reflectance of 0.904 used in this study. (c) A photo of the VR lab, equipped with light source, micro-photometer and microscope.

c. Polish.

d. Measurement. Source light (λ=546 nm) was transferred through an optical fibre to produce a faculae ~0.06 mm in diameter. The micro-photometer was a 3YMSP LEICA DMR XP (UV-VIS 2000). Standards with VR values of 0.904% and 3.11% were adopted given their similar reflectance values to the measured samples. Prior to analysis, a drop of Leitz fluorescence microscopy immersion oil (with a reflectance of 1.5180) was placed onto the analysed unknown/standard to create an oil immersion environment. The oil objective lens was 50x magnification and eyepiece was 10x. Sample analysis began once an accurate and precise measurement of the standard was achieved. The standard was measured during and at the end of sample analysis to keep good measurement reproducibility.

3.6 Modelling of thermal history using HeFTy program

HeFTy is a commonly used computer program for the forward and inverse modelling of low-temperature thermochronological data (apatite and zircon (U-Th-Sm)/He and fission track) and vitrinite reflectance data and was adopted in this work. Ketcham (2005) comprehensively reviewed the theoretical aspects and practical operation of the HeFTy program, which evolved from an earlier version known as AFTSolve (Ketcham et al., 2000).

If given one or more measured data and assumed starting conditions, HeFTy conducts inverse modelling of thermal history by finding the intervening time–temperature paths using constrained Monte Carlo simulations. The user specifies time–temperature region(s) through which each model path must pass, and the complexity of the paths between these regions (Ketcham, 2005; Ketcham et al., 2009). Generally, because of the limited constraints from measured data and other geological information and the lack of system uniqueness, an inverse model solution usually ends up with more than one thermal histories that are consistent with the measured data (Ketcham, 2005). HeFTy has the capacity to offer the best-fitting model path and weighted mean path (weights based on goodness of fit statistics) options (Ketcham, 2014).

How well the measured data (age or track length) and model results match with each other is evaluated by the statistic—goodness-of-fit (GOF) in HeFTy (Ketcham et al., 2000; Ketcham, 2005). The track length GOF is acquired by adopting either Kuiper's Statistic (used in this study) or Kolmogorov-Smirnov tests and comparing fission-track length distribution to the track length distribution predicted by the model (Ketcham, 2014). The age GOF is the goodness-of-fit between the age data and the age predicted by the model (Ketcham, 2014). A "good" fit between the measured data and model result corresponds to a GOF value of 0.5 or higher, which is the expected value when the time-temperature model path and kinetic model are correct (Ketcham et al., 2009; Ketcham, 2014). An "acceptable" fit corresponds to a GOF value of 0.05 or higher, which indicates that the model has not failed the null hypothesis test that forms the basis of these statistics at the 95% confidence level (Ketcham et al., 2009; Ketcham, 2014). A model is considered "good" if first, the mean GOF value must be at least 0.5, and second, the minimum GOF value is greater than 1/(N+1), where N is the number of GOF tests that were run (Ketcham et al., 2009; Ketcham, 2014).

In this study, HeFTy pre-filling input data included the AFT, ZHe, and AHe ages and AFT track length if available. Annealing and diffusion kinetic models used were from Farley (2000) for AHe, Reiners et al. (2004) for ZHe and Ketcham et al. (2007) for AFT. The MsAr, BtAr, or ZFT data were manually added as a constraint when available. The modelling starting points for sedimentary samples were the assumed annual mean temperature (20 ± 3°C) at the time of deposition. For granitic samples, modelling started at the MsAr or BtAr closure temperature and age, or at a point 20 Ma older and 50°C hotter than the ZFT or ZHe thermochronometer to ensure an initial condition where no daughter products were retained. The modelling ending point was 20 ± 3°C at present. Model settings included monotonic variable path between two constraints, paths halves 2 times, episodic randomizer, and no imposed maximum cooling rate. Inversions were run until 100 "good" fits were obtained. If, after running a huge number of modelling paths (~10 million), the model paths contain no "good" path, inversions were run until 100 "acceptable" fits were obtained.

Chapter 4 Thermochronological record of tectonic events in the Meizhou area

4.1 Geological setting

The Meizhou area, in the coastal margin of the SE SCB (**Figure 4.1a**), falls between the Heyuan fault zone and the Zhenghe-Dapu fault zone (**Figure 4.1b**). Jurassic sedimentary and magmatic rocks are widely exposed in the Meizhou area, whereas Triassic and Cretaceous magmatic rock are rarely exposed (**Figure 4.1b**) in the area.

In the study area, the pre-Middle Triassic strata is deformed and overlain by Upper Triassic–Middle Jurassic strata (GDBGMR, 1971; Pang, 2014). The Upper Triassic delta facies strata (~235–201 Ma), consisting of conglomerate, sandstone and mudstone (GDBGMR, 1970, 1971), is unconformably overlain by Lower Jurassic strata comprising fluvial to shallow-marine conglomerate, sandstone mudstone and shale, with tuff and volcanic rocks in the lower (~201–199 Ma), and sandstone and mudstone in the middle part (~199–182 Ma) (GDBGMR, 1971; Pang, 2014). Tuffaceous siliciclastic deposits in the upper part of the Lower Jurassic sequences (~182–174 Ma) continue into the Middle Jurassic (~164 Ma) (GDBGMR, 1971; Shu et al., 2009; Pang, 2014). An unconformity exists between the Upper Jurassic strata and the Lower–Middle Jurassic strata, accompanied with a change in lithology. The Upper Jurassic strata contains volcaniclastics and volcanic rocks (GDBGMR, 1988; Pang, 2014) while the Lower Cretaceous comglomerate, sandstone, siltstone, and tuffaceous comglomerate and sandstone, overlie the Upper Jurassic unconformably (GDBGMR, 1971). Disconformably or uncomforably overlying the Lower Cretaceous strata, the Upper Cretaceous rocks manly comprise comglomerate, glutenite, sandstone, and tuffaceous glutenite with acid volcanic rock interlays in the lower part, and rhyolitic prophry, rhyolitic tuff and tuff breccia intercallations in the upper part (GDBGMR, 1970, 1971). Very limited outcrops of Eocene conglomerate, glutenite, sandstone and siltstone unconformably overlie the Upper Cretaceous volcanic sequence, and are uncomformably overlain by

Quaternary sediments (GDBGMR, 1970, 1971).

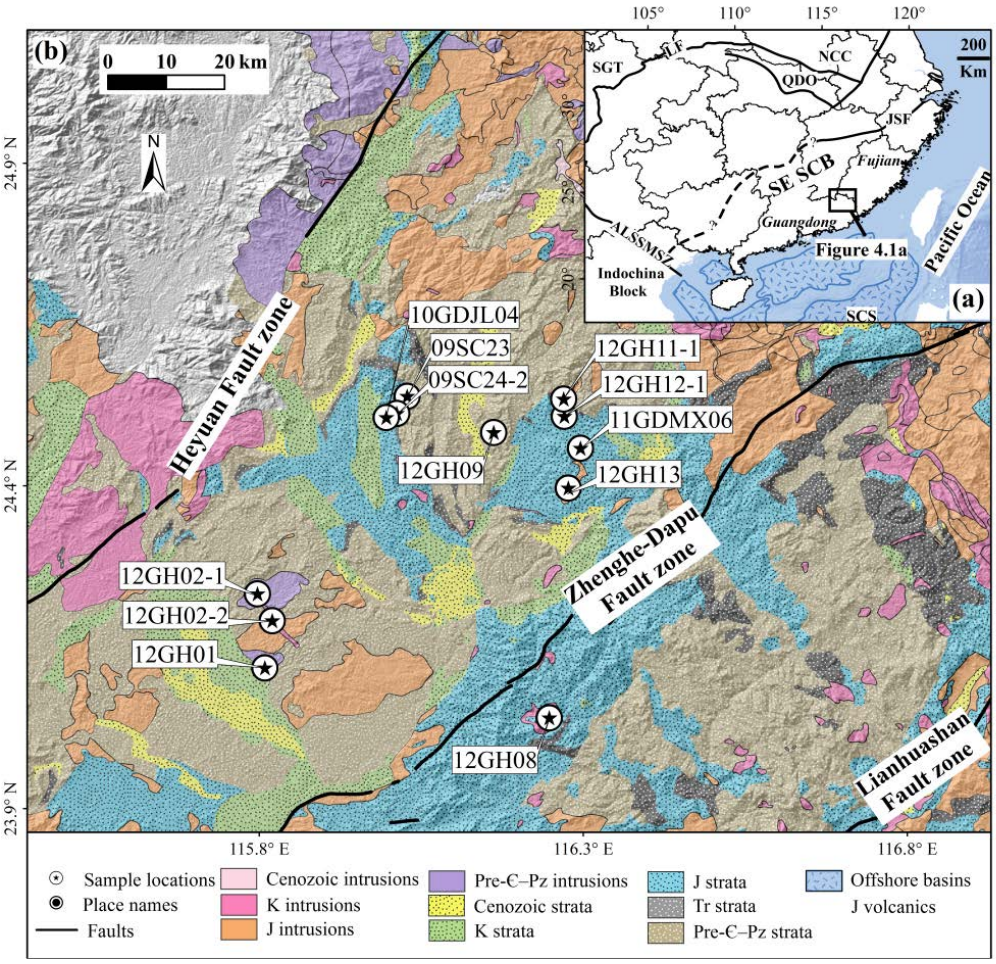

Figure 4.1 Simplified geological map of Meizhou area, showing sample names and locations, compiled from GDBGMR (1970, 1971).

Areas out of the Guangdong and Fujian provinces are only shown with digital elevation model data (NASA EODIS database). Divisions of geologic time are after Walker et al. (2012) and symbols of geologic periods are after GNCUSGS (2010). **Figure 4.1a**: Tectonic map of SCB-West Pacific region showing the extent of **Figure 4.1b**.

Late Jurassic (160–150 Ma) Cu-Fe-W-Sn-Mo polymetallic ore deposits and Cretaceous (135–80 Ma) porphyry Cu–Au–Ag-Mo deposits, with a peak of mineralization age of 110–90 Ma, are developed in the study area (Huang and Liao, 2008; Mao et al., 2011; Mao et al., 2013b; Zeng et al., 2013). The two episodes of mineralization distinctively well correspond with the Late Jurassic and Cretaceous granitic magmatism in SE SCB (Li, 2000; Zhou and Li, 2000; Chen et al., 2002a; Li et al., 2003; Chen et al., 2005; Zhou et al., 2006; Li et al., 2007a; Wong et al., 2009;

He et al., 2010). In addition, Sb-Cu deposits distributed in NE-direction (Huang and Liao, 2008), parallel to the trending of Late Mesozoic magmatic belts and volcaniclastic pull-apart basins. The metallogenesis of Late Jurassic and Cretaceous mineralization is attributed to regional lithospheric extensional thinning and thermal erosion in SE SCB related to the subduction of paleo-Pacific plates (Mao et al., 2011; Mao et al., 2013b; Zeng et al., 2013).

4.2 Sampling

Seven sedimentary and five granitic samples from the Meizhou area (**Figure 4.1**) were obtained.

One Middle Permian shale sample (12GH09) and one Lower Jurassic shale sample (12GH12-1) were collected for VR measurement in order to ascertain the maximum paleo-temperature since the deposition. Sample 12GH09 was collected from a large carbonaceous shale quarry (**Figure 4.2d**). Upper Triassic–Middle Jurassic tuff and sandstones (09SC23, 09SC24-2, 10GDJL04, 12GH11-1 and 11GDMX06) were collected for evaluation of the post-Middle Triassic orogenic thermal history (**Table A1**).

Five granitoids were collected for complimentary geo-/thermo-chronological investigations (**Figure 4.1**). Only two Triassic granitic or granodioritic intrusions have been mapped in the Meizhou area and neither has yielded reliable magmatic age (GDBGMR, 1970), so one sample was taken from each of the intrusions (12GH01 and 12GH02-1, **Figure 4.1 and 4.2**) for magmatic age determination and for thermochronological investigation if they were of Triassic age or older. The mid-Cretaceous porphyritic belt (12GH02-2; 120–90 Ma) that transects the “Triassic” granite was also sampled in order to distinguish thermal reheating from magmatic cooling (**Figure 4.2b**). Both geo- and thermo-chronology investigation of the Cretaceous granite (12GH08) and Jurassic porphyry (12GH13) were undertaken in order to distinguish thermal reheating from magmatic cooling.

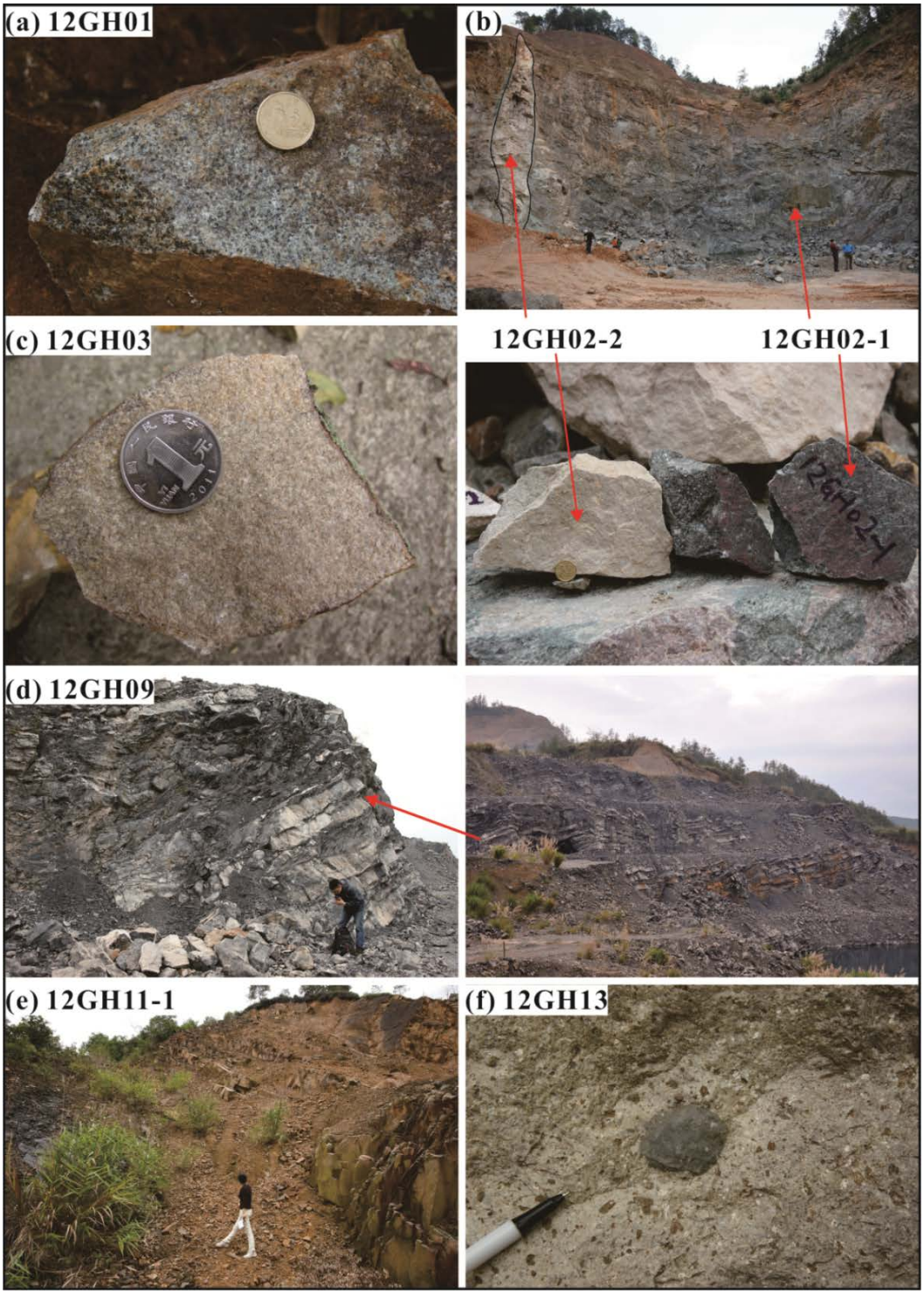

Figure 4.2 Photos of key localities and samples from the Meizhou area.

4.3 Results and interpretation

4.3.1 U-Pb age

Samples 12GH01 and 12GH02-1 had zircon U-Pb ages of ca. 435 Ma. The U concentration of 12GH02-1 ranged from 151–569 ppm while most 12GH01 zircon were more enriched in U (> 500 ppm), which was also demonstrated by their lower reluctant CL images (**Figure 4.3a**). Concentric oscillatory zoning of magmatic origin was observed in the CL images of both samples (**Figure 4.3 a and b**). Fourteen spot analyses for 12GH01 yielded a weighted mean $^{206}Pb/^{238}U$ age of 437.9 ±4.2 Ma (MSWD=1.7; P=0.0.6; 2σ; **Figure 4.3a**). Seventeen spots analysed for 12GH02-1 yielded a well-defined concordia age of 434.3 ± 4.8 Ma (MSWD=0.76; P=0.38, 2σ; **Table A2**), and an indistinguishable weighted mean $^{206}Pb/^{238}U$ age of 434.2 ± 5.0 Ma (MSWD=1.7; P=0.0.6; 2σ; **Figure 4.3b**). The new zircon U-Pb ages for sample 12GH01 and 12GH02-1 provide an Early Silurian magmatic age for the two intrusions, which is different from the Triassic age previously proposed (GDBGMR, 1970).

Zircons from the 12GH13 are euhedral to sub-euhedral. Concentric oscillatory zoning, typical of magmatic zircons, was observed in the CL images (**Figure 4.3c**). The magmatic origin was also suggested by Th/U ratios of 0.26–0.94 (Wu and Zheng, 2004) (**Table A2**). A total of eighteen spots were analysed on different magmatic zircon grains, yielding a weighted mean $^{206}Pb/^{238}U$ age of 146.8 ± 1.8 Ma (MSWD=0.44; P=0.98; 2σ; **Figure 4.3c**). The results suggest a Late Jurassic crystallization age for this porphyry.

Zircons from the granite 12GH08 are euhedral and broken crystals are commonly seen (**Figure 4.3d**). Well-developed concentric oscillatory zoning suggests a magmatic-origin for the zircons (**Figure 4.3d**). Twenty analysed spots gave a well-defined concordia age of 138.2 ± 1.6 Ma (MSWD=0.49; P=0.48; 2σ; **Table A2**), and an identical weighted mean $^{206}Pb/^{238}U$ age of 138.3 ± 1.6 Ma (MSWD=0.61; P=0.90; 2σ; **Figure 4.3d**). The results constrain an Early Cretaceous magmatic age for the granite.

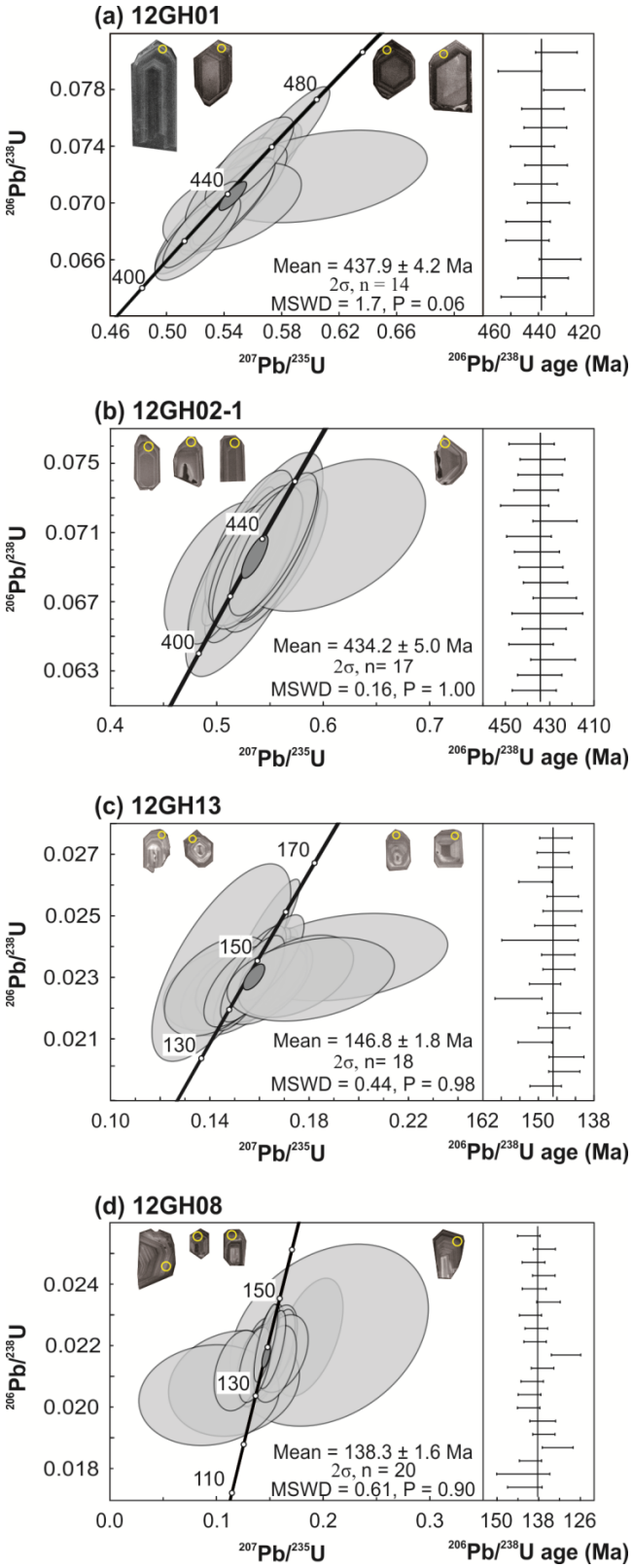

Figure 4.3 Zircon U-Pb concordia diagrams and weighted-mean plots.
Analysed spots of ~30 μm diameter are shown as yellow circles on the CL images. Error ellipses in the concordia diagrams and dashes in the weighted-mean plots are displayed at the 2σ confidence interval. MSWD=mean square of weighted deviates. n=number of analysed spots.

4.3.2 $^{40}Ar/^{39}Ar$ ages

A K-feldspar multi-grain package from the Lower Cretaceous granite (12GH08) was analysed by laser step-heating in order to ascertain the timing of closure of the KfsAr system. In total, 20 heating steps were conducted in two sessions (**Table A3**). The last eight steps from the first session and all five steps in the second session yielded a weighted plateau age of 82.78 ± 0.56 Ma (MSWD=1.12; P=0.34; 2σ; **Figure 4.4**), representing an Early Cretaceous closure of the KfsAr system (150–350 °C; Lovera et al., 1989).

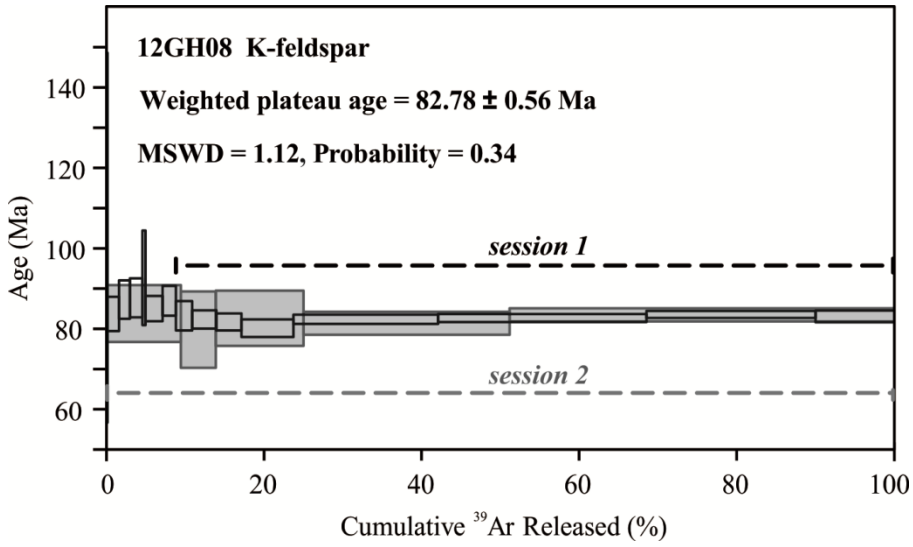

Figure 4.4 K-feldspar $^{40}Ar/^{39}Ar$ age spectra showing weighted plateau age of sample 12GH08. MSWD=mean square of weighted deviates. Step-heating data bars are displayed at the 2σ confidence interval.

4.3.3 ZHe ages

Early Cretaceous (141–121 Ma) ZHe ages were given by four Upper Triassic–Middle Jurassic sandstones and one Lower Jurassic tuff, indicating that all ages were reset (**Table 4.1; Table A4**). For the intrusive samples, Late Jurassic, Early Cretaceous and Late Cretaceous ZHe ages were obtained (**Table 4.1**). The Lower Silurian granodiorite (12GH01) gave the oldest ZHe age at 151 Ma whereas, about 10 km north, the other Lower Silurian granodioritic sample (12GH02-1) that is

intruded by mid-Cretaceous porphyry (12GH02-2), yielded a 20 Myr younger ZHe age of 129 Ma (**Table 4.1**). A similar result (128 Ma) was obtained from the Lower Cretaceous porphyry (12GH13; **Table 4.1**). Mid- and Lower Cretaceous porphyry and granite (12GH02-2 and 12GH08) gave young Late Cretaceous ages (100 Ma and 84 Ma; **Table 4.1**).

Table 4.1 Table showing all new data from Meizhou.

Sample #.	Lithology	Age ± 2σ (Ma)					VR
		Stratigraphic or U/Pb	$^{40}Ar/^{39}Ar$	ZHe	AFT	AHe	(%)
11GDMX06	sandstone	J_2		141.0 ± 9.2	55.3 ± 7.0	41 ± 5	
12GH11-1	sandstone	T_3		136.7 ± 9.0			
10GDJL04	tuff	199.5± 1.3[a]; J_1		131 ± 12			
09SC24-2	sandstone	T_3		121.2 ± 8.2	34.3 ± 4.8	31.9 ± 8.8	
09SC23	sandstone	T_3		138 ± 12	41.4 ± 4.4		
12GH02-2	porphyry	K_{1-2}		99.8 ± 6.5			
12GH08	granite	138.3 ± 1.6; K_1	82.8 ± 0.6 (Kfs)	83.7 ± 5.2	63.5 ± 11.2		
12GH13	porphyry	146.8 ± 1.8; J_3		127.5 ± 7.9			
12GH02-1	granodiorite	434.2 ± 5.0; S_1		129.3 ± 9.8	70.8 ± 9.0	35.4 ± 1.8	
12GH01	granodiorite	437.9 ± 4.2; S_1		151 ± 13	45.5 ± 5.4	37.8 ± 2.2	
12GH12-1	shale	J_1					4.219
12GH09	shale	P_2					2.296

[a]Data from Pang (2014). Data supporting Figures 4.2–4 and Table 4.1 are available in Appendices Tables A2–6.

4.3.4 AFT data

Eocene AFT ages of 34 Ma, 46 Ma and 55 Ma were yielded by the Lower Triassic sandstone (09SC24-2), Lower Silurian granodiorite (12GH01), and Middle Jurassic sandstone (11GDMX06), respectively (**Figure 4.5a, c and g**). A slightly older Paleocene AFT age was given by the Lower Cretaceous granite 12GH08 (ca.

64 Ma; **Figure 4.5e**). In contrast to the samples discussed above, sample 12GH02-1 failed the Chi-square test (**Table A5**). Component analysis by using Popshare (Dunkl and Székely, 2003), suggested two age components of 52.7±4.0 (9%) and 78.3±28.3 (91%) (mean age±standard deviation) (**Figure 4.5f**).

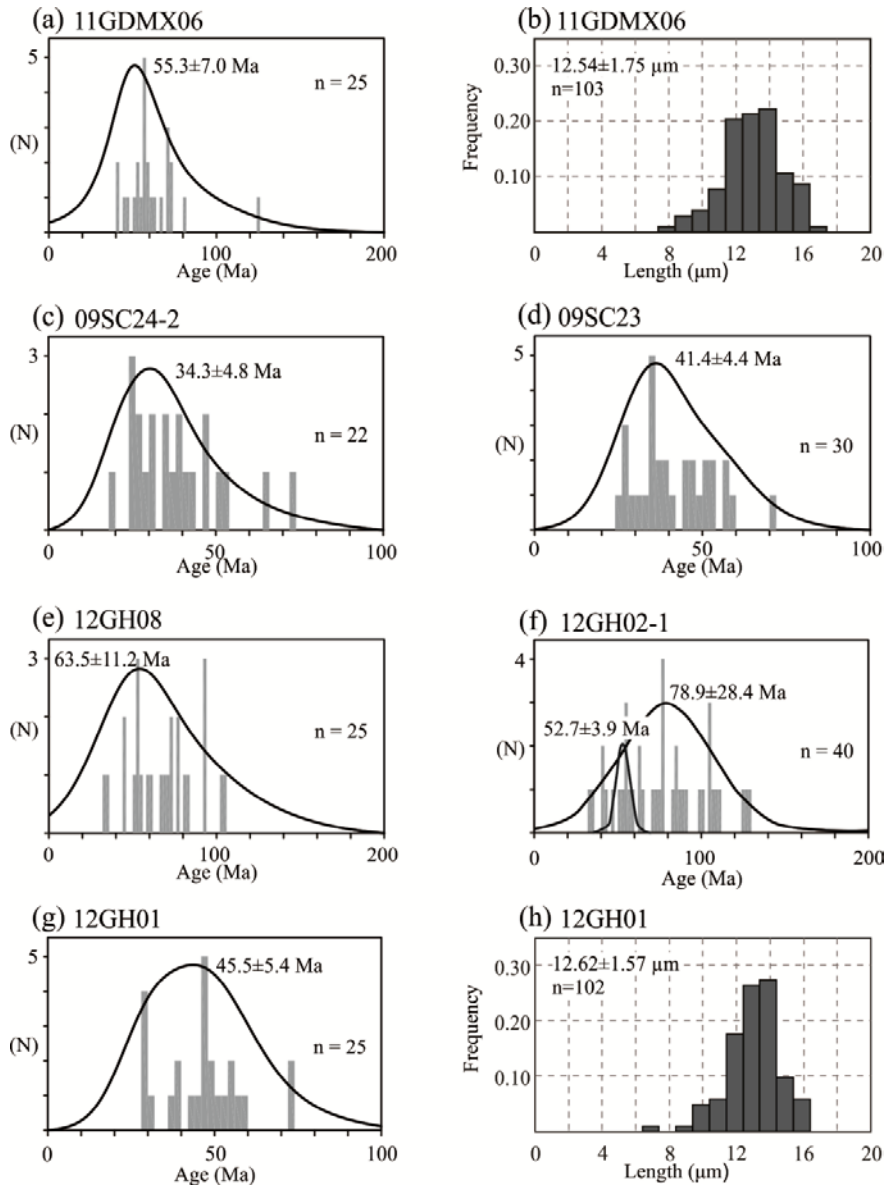

Figure 4.5 Apatite fission track single-grain age and track length distribution histograms. Single-grain age histograms: y-axis shows number of grains; x-axis shows age in Ma; black curve shows the linear age spectrum with AFT age ± 2σ error labelled next to it; middle right is the number of counted grains. Fission track length distribution histograms (b and h): y-axis shows frequency of tracks; x-axis shows length in µm; top left are mean track length ± standard deviation and number of measured tracks.

Samples 11GDMX06 and 12GH01 were suitable for AFT track length measurement. Track lengths from 11GDMX06 gave a mean of 12.54 μm with a standard deviation of 1.75 μm (**Figure 4.5b**). The mean track length of 12GH02-1 (12.62 ± 1.57 μm) was almost identical to that of 11GDMX06 (**Figure 4.5h**). A unimodal distribution of track lengths was obtained in both samples, although a higher proportion of 12GH02-1 track lengths fell into the middle range of 12–14 μm (**Figure 4.5b and h**). The relatively short mean track lengths (12.6 μm) are an indication of thermal annealing of initially longer tracks (~16 μm).

4.3.5 AHe ages

Thirty AHe single-grain ages ranged from 20–80 Ma (**Figure 4.6; Table 4.1**). The dominant age population is Late Eocene (36.9 ± 1.16 Ma, 2σ), shared by 80% of total analysed grains (**Figure 4.6)**.

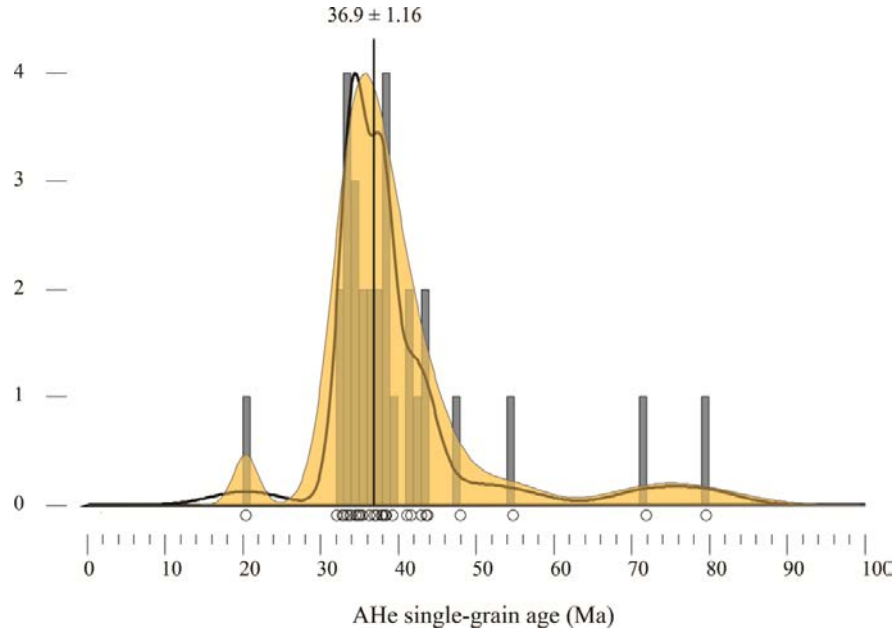

Figure 4.6 Distribution of 30 single-grain apatite (U-Th-Sm)/He ages shown by histogram, density plot and kernel density estimation.
The black line is the kernel density estimation (KDE), filled yellow curve is density plot and histogram is shown with grey bars. The bin size of histogram is 1 Myr and the bandwidth of KDE is 2 Myr. Major age components (± 2σ) were calculated with DensityPlotter (Vermeesch, 2012). Black circles display the data points. Plotted data are available in **Table A6**.

4.3.6 VR data

For the Middle Permian black shale (12GH09), fewer vitrinite macerals were suitable for measurement because of the common occurrence of impurities (**Figure 4.7a**). Reflectance values of eleven vitrinite macerals were measured and the values ranged from 2.276% to 3.561%, with a mean value and a standard deviation of 2.696% and 0.473%, respectively (**Table A7**). Both the maximum and minimum VR values and the mean were considered for forward modelling using the Easy%R_o model (Sweeney and Burnham, 1990) and the HeFTy modelling program (Ketcham, 2005), suggesting maximum post-depositional temperature of 220 ± 20°C.

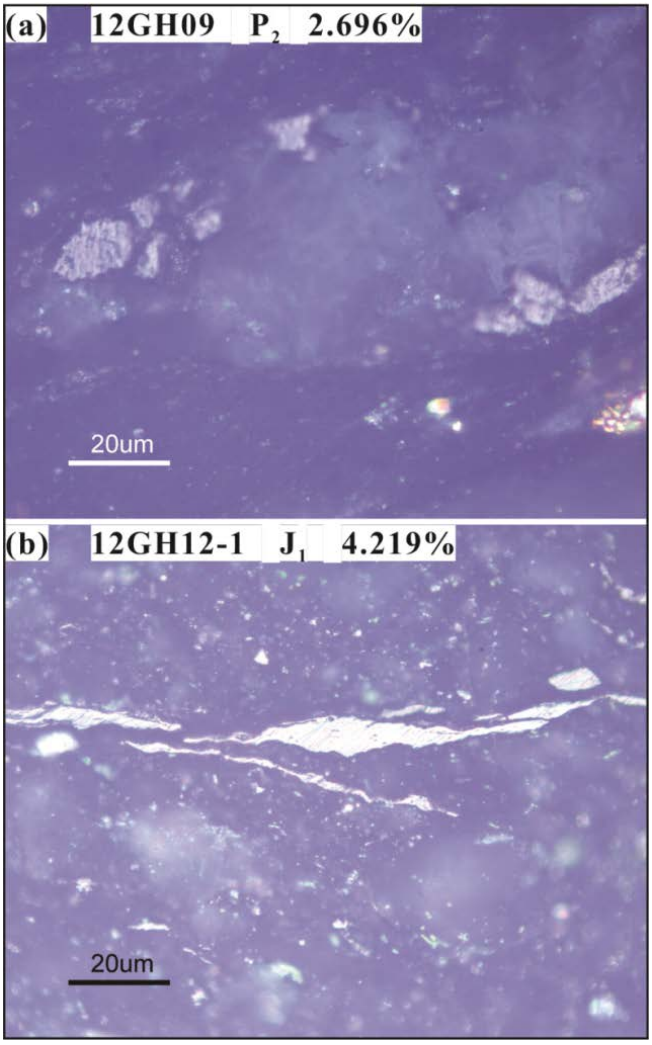

Figure 4.7 Microscopic reflected light photo of vitrinite macerals from two shale samples.

Twenty VR measurements of Lower Jurassic shale (12GH12-1) ranged from 3.871% to 4.712%, with a mean value of 4.219% and a standard deviation of 0.249% (**Table A7**). Brighter vitrinite macerals from sample 12GH12-1 observed under microscope suggest a higher VR value than 12GH09 (**Figure 4.7**). The maximum post-depositional temperature was constrained to 280 ± 20°C.

4.3.7 Modelling of thermal history

The thicknesses of 0.7–2 km, 1.6–3.6 km and 0.6–1 km, between the Upper Triassic, Lower Jurassic and Middle Jurassic strata, and their the respective unconformity formed underneath Upper Jurassic Stata were extracted from local 1:20,000 geological maps (GDBGMR, 1971). The minimum burial thicknesses were converted into temperature constraints with an assumed typical continental geothermal gradient of 30°C/km and were compiled into modelling, shown as green boxes (**Figure 4.8**).

The modelled time-temperature paths showed a similar cooling pattern of Pre-Lower Cretaceous samples that all cooled below 150°C at ca. 130 Ma, followed by a plateau over 70 Myr (**Figure 4.8a–e** and **g**). Rather than a prolonged plateau, two Lower Cretaceous intrusions stood out with a Late Cretaceous cooling (**Figure 4.8 f** and **h**). The Upper Triassic sandstone (09SC23) and Lower Jurassic tuff (10GDJL04) showed a very rapid heating from ~170°C to >300°C in the Late Jurassic after post-depositional heating at an intermediate rate (**Figure 4.8 a** and **c**). The Middle Jurassic (10GDJL04) sedimentary sample only showed the rapid Late Jurassic heating (**Figure 4.8e**). From 150–130 Ma, the three pre-Lower Cretaceous sedimentary samples started a fast cooling and similar rapid cooling paths were yielded from three pre-Lower Cretaceous intrusions (**Figure 4.8 b, d** and **g**).

Modelling of AFT and AHe data showed an increase of rate in cooling from ca. 70 Ma (**Figure 4.8 b** and **f**) to 40 Ma (**Figure 4.8 a, b ,d** and **e),** irrespective of lithology and magmatic/stratigraphic ages.

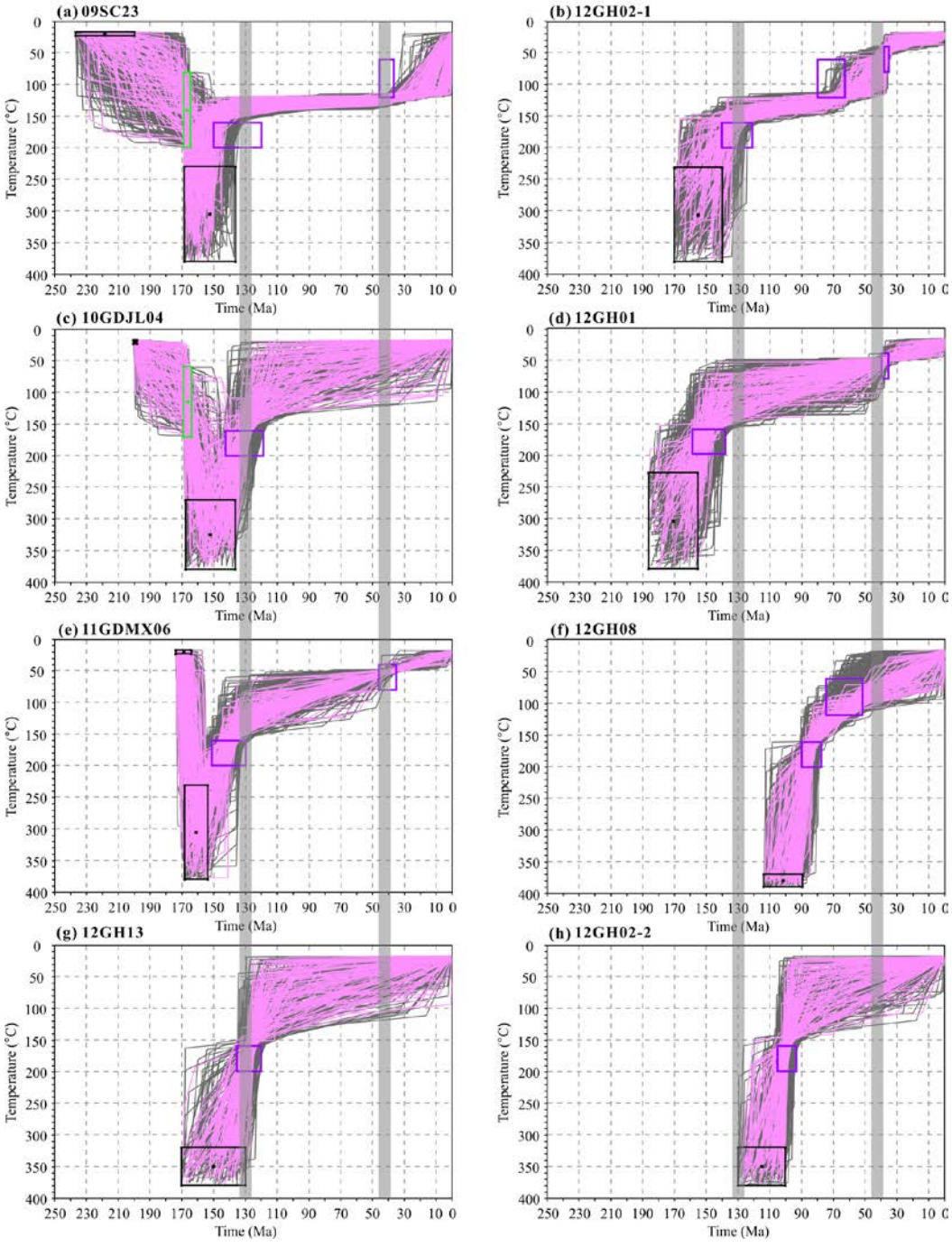

Figure 4.8 Results of the modelling of the thermal histories of selected samples from Meizhou region.

Black boxes represent the modelling starting points for sedimentary and granitic samples. Input data included the AFT, ZHe, and AHe ages, shown as purple boxes. Good fits were shown as pink curves and acceptable fits were shown as grey curves.

4.4 Discussion

4.4.1 Late Jurassic thermal maximum

Simplified time-temperature trajectories were plotted by correlating the thermochronological ages and respective closure temperatures of each sample (**Figure 4.9**).

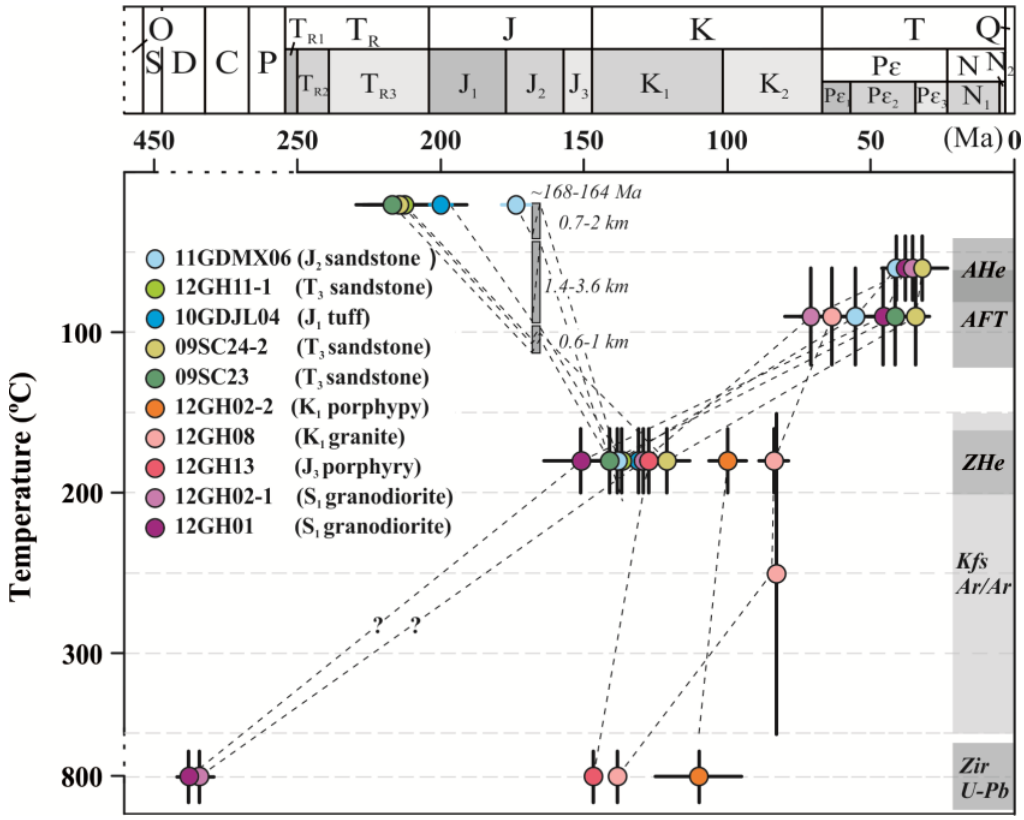

Figure 4.9 Time-temperature trajectories constructed with data generated in this study.
The trajectories of sedimentary samples start at the depositional ages at the assumed annual mean temperature of 20 ± 3°C, and those of granites start at the time defined by zircon U-Pb ages at 800 ± 100°C. All trajectories end at 0 Ma and 20 ± 3°C. The y-axis (temperature) of curves is determined by the characteristic closure temperature of each thermometer. The x-axis (time) is controlled by measured AHe, AFT, ZHe, KfsAr, and U-Pb ages. Data-point error bars are displayed at 2σ confidence interval.

It is noted that the Upper Triassic–Middle Jurassic sedimentary samples experienced heating after deposition to Late Jurassic time without any significant change in rate (**Figure 4.9**). Whereas from the inverse modelling paths, faster heating

rates are clearly presented in the Late Jurassic relative to the Late Triassic–Middle Jurassic (**Figure 4.8**). The significant increase in heating rate coincides with a change of sedimentation type from clastic-dominated to volcanic-dominated across the unconformity between Upper Jurassic strata and younger sequences (GDBGMR, 1988). Thicker than 4 km of volcanic and volcaniclastic rocks were deposited during the Late Jurassic in the study area (GDBGMR, 1971).

The Meizhou area is located in a zone that is thermally overprinted by Late Jurassic magmatism (**Figure 4.10**). After the Middle Triassic depositional hiatus, the 2.7–6.6 km-thick Upper Triassic–Middle Jurassic clastic strata with minor volcanic interlays could have induced an elevated paleo-thermal gradient and raised the temperature to ~150°C (**Figure 4.8**). Late Jurassic volcanism and granitic intrusions (e.g. 12GH13) increased temperatures further (up to ~300°C) in a reasonably short period of time (~5 Ma) (**Figure 4.8**). The ~300°C thermal maximum is consistent with the VR data from the Lower Jurassic shale (12GH12-1) that suggests a maximum paleo-temperature up to ~300°C after deposition. The Middle Permian black shale (12GH09) seems to have experienced a lower maximum paleo-temperature of 220 ± 20°C, probably resulting from its relative isolation from Jurassic intrusions and lack of direct contact with Jurassic volcanic strata (**Figure 4.1**).

After the Late Jurassic thermal maximum, Upper Triassic–Middle Jurassic sedimentary samples (**Figure 4.8a, c, and e**) displayed a fast cooling from 300°C to 150°C. The cooling pattern is very similar to the post-magmatic cooling of the Upper Jurassic porphyry sample (**Figure 4.8g**), indicating that the older sedimentary samples began to share a similar cooling history as the Upper Jurassic intrusions. Comparably, Lower Silurian granitic samples also show rapid cooling in the Lower Jurassic (**Figure 4.8b and d**). Due to the lack of observed contact relationships between the Lower Silurian granitic samples and Jurassic strata, there is no direct evidence that the Silurian rocks (12GH01 and 12GH02-1; **Figure 4.1**) were exhumed to surface before being heated to ~300°C in the Late Jurassic. However, since the same Late Jurassic thermal history was detected in the Upper Triassic–Middle Jurassic sedimentary samples (**Figure 4.8**) and the adjacent Jurassic intrusion

(**Figure 4.1**), it is reasonable to assume that the Late Jurassic heating event affected the Lower Silurian intrusions (**Figure 4.9**).

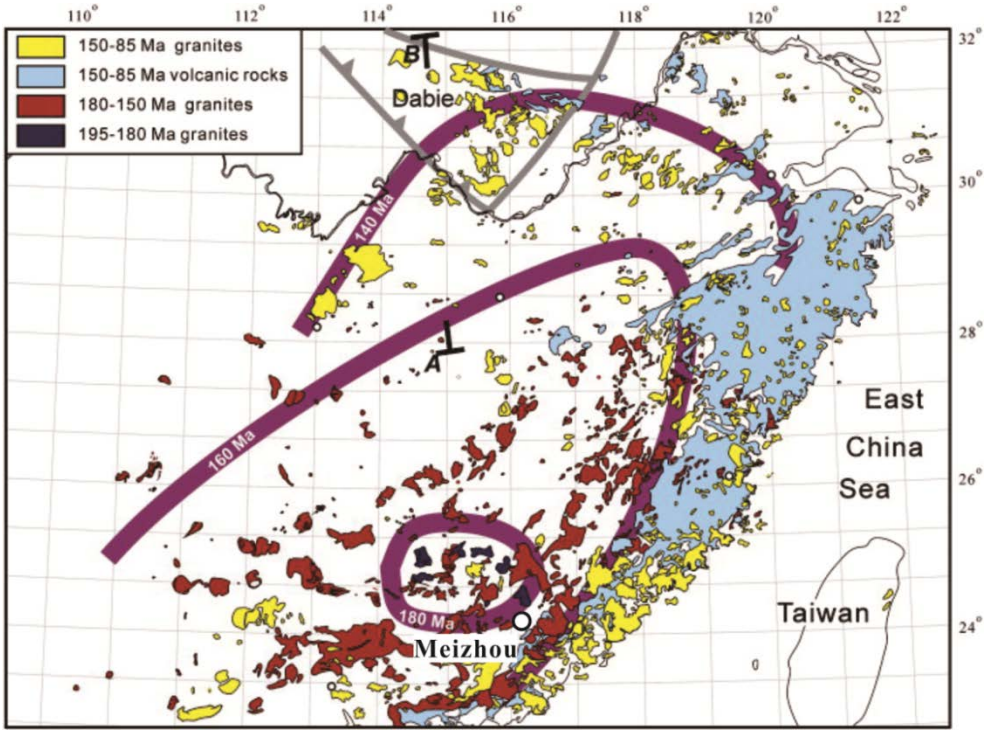

Figure 4.10 Temporal and spatial distribution of the Jurassic and Cretaceous magmatism in SE SCB (from Li et al. (2013)), with the location of Meizhou plotted.

To sum up, pre-Upper Jurassic rocks in the Meizhou area reached a ~300°C thermal maximum in the Late Jurassic, with heat sources from both sedimentary burial and magmatism. The Late Jurassic magmatism has been proposed to be generated by delamination and foundering of the flat-subducted paleo-Pacific plates beneath the SE SCB (Li and Li, 2007).

4.4.2 Post-emplacement reheating in the mid-Cretaceous

Overlapping of inverse modelling paths based on thermochronological data alone present thermal plateaus during Cretaceous time for all pre-Cretaceous samples (**Figure 4.8)**. The temperatures of the Cretaceous plateaus are, however, not well

constrained, because the plateaus cover a wide temperature range from near surface temperatures of 20°C (e.g. **Figure 4.8c**) to ~150°C (e.g. **Figure 4.8b**). In the study area, both Lower Cretaceous and Upper Cretaceous strata overly the underlying strata unconformably (**Figure 4.11a**). In some areas, Upper Cretaceous strata directly overlies Lower Paleozoic strata over an unconformity (**Figure 4.11b**), indicating more intensive Early Cretaceous exhumation and erosion. *In-situ* mid-Cretaceous magmatism (e.g. 12GH02-2), a potential compensatory thermal impact relative to exhumation, could make the Cretaceous thermal evolution of the Meizhou area more complex than a thermal plateau in **Figure 4.8a–g**. To further investigate the extent of the Early Cretaceous exhumation and the influence of the Early Cretaceous magmatism, two extra constraints were enforced on the inverse modelling of sample 12GH02-1 (**Figure 4.1; Figure 4.11**). The first constraint allocated an Early Cretaceous exhumation to below <150°C to near surface temperatures based on the existence of an erosion surface during this period (the second black box in **Figure 4.12b**). To introduce intrusion of the mid-Cretaceous age, the second constraint was placed at a higher temperature range between 120 Ma and 90 Ma (the third black box in **Figure 4.12b**).

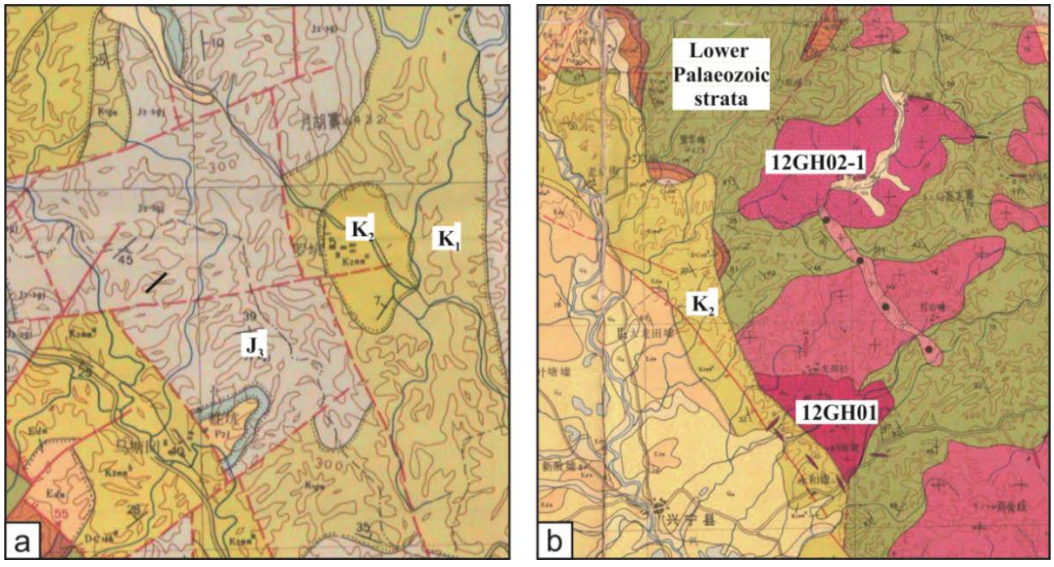

Figure 4.11 Geological map showing (a)the unconformity between the Upper Cretaceous strata and the Lower Paleozoic strata, and (b) the unconformity between the Upper and Lower Cretaceous strata, and the unconformity between the Lower Cretaceous and the Upper Jurassic strata, after GDBGMR (1970, 1971).

Modelled paths with GOF larger than 0.5 and 0.05 were shown as pink and grey curves respectively in **Figure 4.12 a** and **c**, and the constrained points of the paths were shown as pink and grey points in **Figure 4.12 b** and **d**. Both the thermal plateau and magmatic reheating scenarios were statically supported by measured AFT, ZHe, and AHe ages. In comparison, modelling statistics were better in the magmatic reheating scenario, with higher GOF between measured and modelled AFT, ZHe, and AHe ages (**Figure 4.12 b** and **d**). In this case, the sample cooled to shallow temperatures soon after the Late Jurassic thermal maximum and was reheated to ~150°C in the mid-Cretaceous (**Figure 4.12b**), rather than following a monotonic plateau (**Figure 4.12a**). By mapping the constrained points of the inversed-modelled paths, the temperature of the mid-Cretaceous magmatic reheating is very well constrained to 150 ± 30°C, although the Early Cretaceous cooling is relatively loosely constrained (20–180°C; **Figure 4.12d**). The reheating temperature (150 ± 30°C) overlapped with the higher boundary of the AFT closure temperature (90 ± 30°C), so the mid-Cretaceous magmatism could have partially reset the AFT data. Our AFT age and length data support this speculation. The AFT age of sample 12GH02-1 failed the Chi-square test with two populations distinguished. The older population (78.9 ± 28.4 Ma) ranged from mid-Cretaceous to Cenozoic. Short track length (12.62 ± 1.57 μm) is given by a sample nearby (12GH01; **Figure 4.1**). With comprehensive analysis and modelling of stratigraphic information, the magmatic record and thermochronological data, it can be concluded that after an Early Jurassic exhumation, a mid-Cretaceous magmatic reheating to 150 ± 20°C resulted from contemporary magmatism occurring in the Meizhou area. Mid-Cretaceous intrusion-related reheating was also proposed in Hong Kong (Tang et al., 2014). The alternating basin formation and uplift with coexisting magmatism in SE SCB during the Cretaceous (Charvet et al., 1996; Zhou and Li, 2000; Zhou et al., 2006; Jiang et al., 2009; Wang et al., 2013) has been recognized as basin-and-range tectonics (Gilder et al., 1991; Li and Li, 2007), related to roll-back of the paleo-Pacific oceanic plates (Li and Li, 2007).

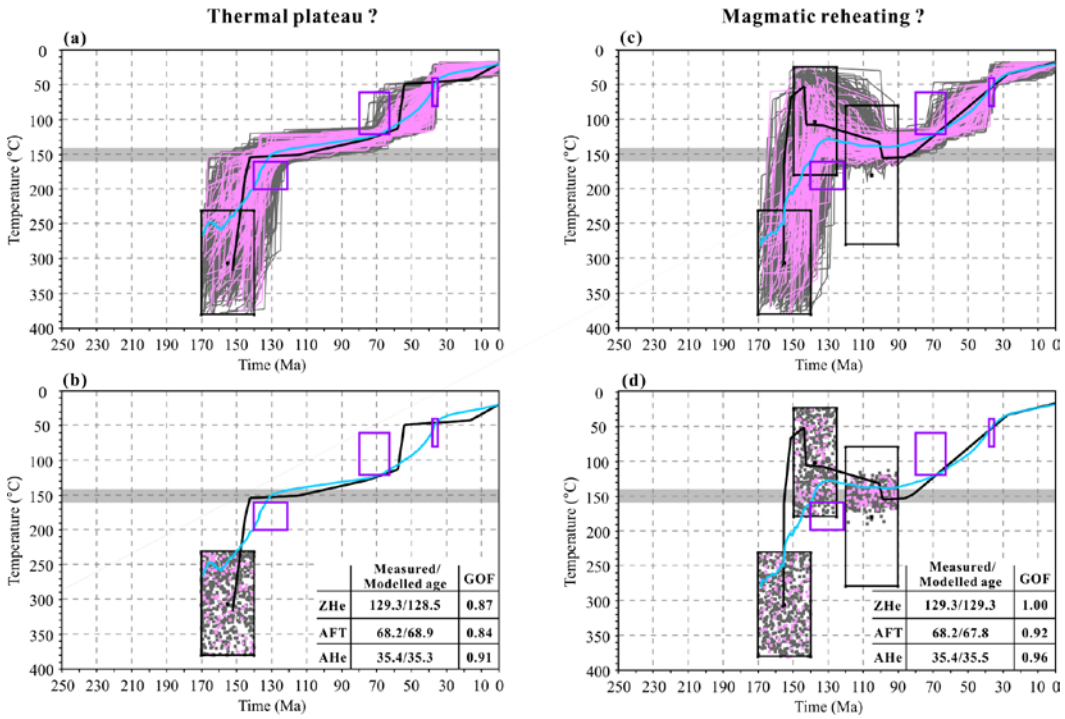

Figure 4.12 Inverse modelling results of the Early Cretaceous cooling and the magmatic reheating scenarios.

4.4.3 Early Tertiary cooling

Early Tertiary AFT and AHe, and much younger than Cretaceous ZHe ages, signify a rapid cooling in the Early Cenozoic (**Table 4.1**). Inverse modelling of samples with AFT and AHe data confirmed the ca. 40 Ma cooling (**Figure 4.8 a, b, d** and **e**). Lower Tertiary strata is almost absent in the study area, apart from limited belt-shape Eocene clastics deposited at the margin of fault-controlled basins (GDBGMR, 1971). The regional erosion in Meizhou is consistent with rifting tectonics in SE SCB in the Early Tertiary (**Section 2.4**). The rifting eventually led to the sea-floor spreading of the South China Sea from ca. 30 to ca. 16 Ma (Taylor and Hayes, 1983; Cande and Kent, 1992; Zhou et al., 2009).

4.5 Conclusions

This study presents a detailed investigation of the Mesozoic–Cenozoic thermal

history of the Meizhou area using low-temperature thermochronological techniques and U-Pb geochronological dating methods.

The major conclusions are:

(1) ZHe ages of the Lower Silurian granodiorites and Upper Triassic–mid-Cretaceous sedimentary and magmatic rocks range between 140 and 85 Ma, with most between c. 140 and 120 Ma. AFT ages range between 64 and 34 Ma, with an outlier at 71 Ma. AHe ages range between 41 and 32 Ma. The results show that the ZHe, AFT and AHe systems all have been reset. Inverse modelling shows that that pre-Late Jurassic sedimentary and granitic samples experienced post-depositional and post-magmatic heating to temperature of ~300°C, interpreted to be a combined result of heating from both sedimentary burial and the Late Jurassic magmatism in the area.

(2) Inverse modelling of ZHe, AFT and AHe ages supports a mid-Cretaceous thermal reheating to >150°C ages, consistent with the geological setting. The reheating accounts for a bimodal distribution of AFT ages and short mean track length. The mid-Cretaceous magmatism and Cretaceous basins with discontinuous deposition is linked to a basin-and-range setting formed by roll-back of the paleo-Pacific oceanic plates.

(3) Eocene cooling revealed by AFT and AHe ages is consistent with the rifting environment in SE SCB, prior to the final opening of the South China Sea in the Oligocene–Neogene.

Chapter 5 Thermochronological record of tectonic events in Daxi: from Late Jurassic magmatic reheating to Eocene rift-related rapid cooling

5.1 Geological setting

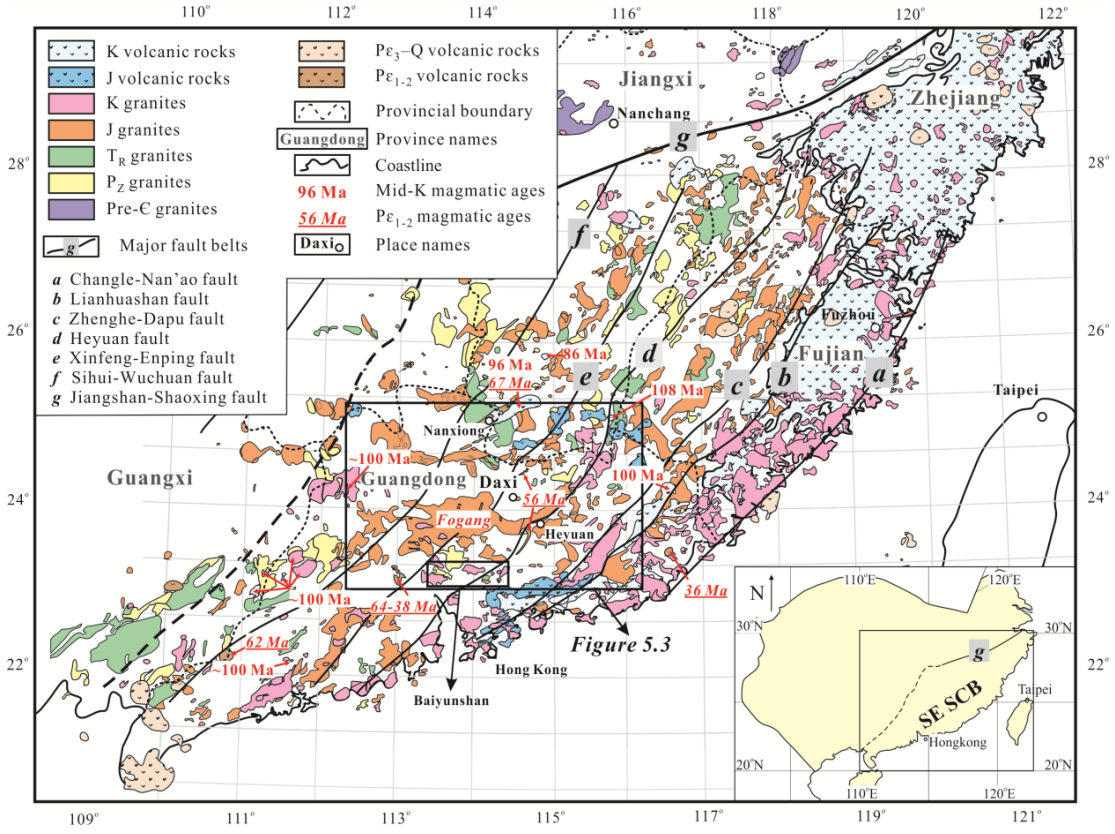

Figure 5.1 Geological map showing the distribution of Precambrian to Cenozoic magmatic rocks and major fault belts in SE SCB, and reported ages of Middle Cretaceous–Eocene magmatism. Radiometric ages were from Zhu et al. (1991); Chung et al. (1997); Shu et al. (2004); Geng et al. (2006); Sun (2006); Zhou et al. (2009); Wang et al. (2011); Meng et al. (2012); Gong and Chen (2014); Li et al. (2014c). Divisions of geologic time are after Walker et al. (2012) and symbols of geologic periods are after GNCUSGS (2010). Pre-Є=Precambrian, P_Z=Paleozoic, $P\varepsilon_{1-2}$=Paleocene–Eocene, $P\varepsilon_3$=Oligocene. Insert: Tectonic map of SCB-West Pacific region showing the extent of **Figure 5.1**.

The SE SCB (**Figure 5.1**) is characterized by the formation of an

intracontinental basin in the Late Triassic–Early Jurassic (**Figure 5.2**) (Liu and Xu, 1994; Li and Li, 2007) and the Daxi region is close to the depocentre of this broad basin (**Figure 5.2**) (Li and Li, 2007; Pang et al., 2014). Exhumation of the Late Triassic–Early Jurassic basin is indicated by a depositional gap occurring during the Middle Jurassic (Pang et al., 2014). The change in vertical crustal movement from basin subsidence to basin inversion coincides with the occurrence of anorogenic magmatism in the Daxi region in the Early–Middle Jurassic (Table 3 in Pang et al., 2014). The original intracontinental basin was broken up into NE-trending extensional (half-)graben basins later in the Jurassic–Cretaceous (Gilder et al., 1991; Li and Li, 2007). This was accompanied by a progressive evolution from intraplate bimodal volcanism and A-type intrusion (195–170 Ma), to widespread granitic intrusion (165–150 Ma) (Li, 2000; Chen et al., 2002a; Li et al., 2003; Chen et al., 2005; Zhou et al., 2006; Li et al., 2007a; He et al., 2010; Yu et al., 2010; Ye et al., 2013), and finally voluminous 140–90 Ma intraplate rhyolitic and basaltic volcanism accompanied by I- and A-type granitic intrusions (Li, 2000; Zhou and Li, 2000; Wong et al., 2009; Meng et al., 2012) in the coastal region bounded by the Zhenghe-Dapu fault and Changle-Nan'ao fault (**Figure 5.1**).

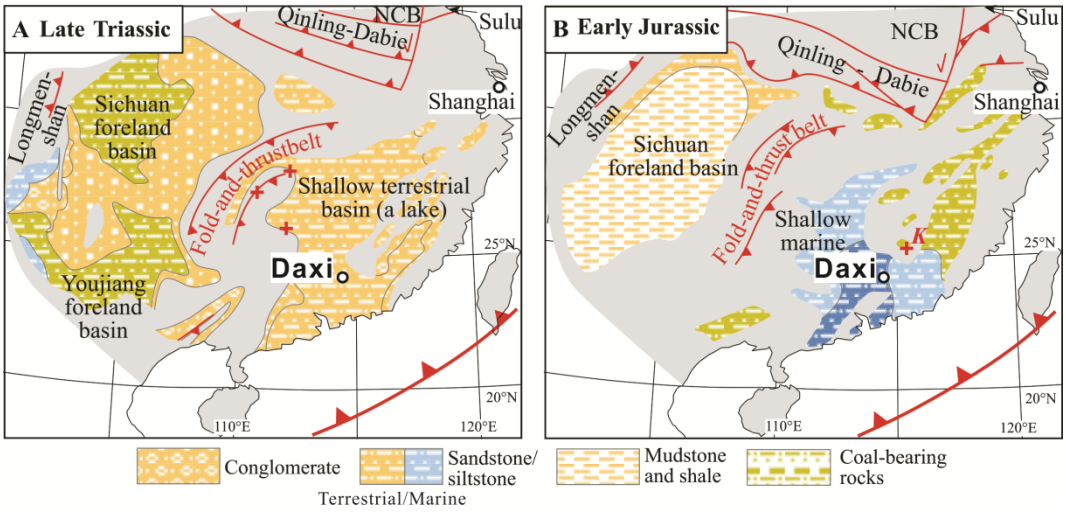

Figure 5.2 Paleo-geographic evolution of SCB during the Late Triassic and Early Jurassic, modified after Liu and Xu (1994) and Li and Li (2007).

There are a series of regional NE-striking faults in SE SCB (**Figure 5.1**). The Daxi region is now bounded by the Sihui-Wuchuan Fault and the Heyuan Fault (*f* and *d* in **Figure 5.1**, respectively) and cut by the Xinfeng-Enping fault (*e* in **Figure 5.1**). Sihui-Wuchuan Fault belt is located in the western and northern portions of the Guangdong province. This fault could have been established since the Ordovician (GDBGMR, 1988) and was influenced by Early Paleozoic and Mesozoic tectonothermal events, and intruded by Lower Paleozoic to Mesozoic granites (GDBGMR, 1988). The Heyuan fault belt preserves granitic intrusions from the Triassic to Cretaceous while Upper Jurassic and Lower Cretaceous volcaniclasts are mainly found to the east of the fault belt (GDBGMR, 1988). Mesozoic–Cenozoic continental basins are distributed linearly within the fault belt. The Xinfeng-Enping fault belt (as *e* in **Figure 5.1**) probably formed in the Early Paleozoic (GDBGMR, 1988) and was strongly overprinted by later magmatism, especially in the Jurassic.

5.2 Sampling

Table 5.1 Daxi sample information.

Sample No.	Lithology	Stratigraphic/ Formation Age (Ma)	References	Location	Latitude N (°)[a]	Longitude E (°)[a]
10GDDX34	sandstone	K_1: 125-100	GDBGMR (1988); Pang et al. (2014)	Daxi	24.119	114.477
10GDDX32-	sandstone	J_1: 185–174			24.122	114.480
09DX08	sandstone	J_1: 201–185			24.133	114.496
09DX02	sandstone	T_3: 220–201			24.157	114.502
10GDDX01-	sandstone	T_3: 220			24.168	114.511
12GH20	sandstone	C_1: 359–323			24.168	114.510
08FG-1	granite	J_{2-3}: 162	Li et al. (2007a)	Fogang	23.413	113.363
09SC11-1	granite				24.121	114.196
12GH19-1	granite	J_1: 193 Ma	This study	Shibei	24.135	114.555
09SC02-1	granite	T_{2-3}: 236 Ma	Xu et al. (2005)	Xiazhuang	24.578	114.215
11GG10-1	granite	T_{2-3}: 236 Ma	Tao (2012)	Longyuanba	24.895	114.399
12GH14	granite	O_3–S_1: 441 Ma	This study	Heping	24.454	114.919

[a]Coordinate system: WGS84.

Six sedimentary rock samples were collected from the Daxi section (**Table 5.1**;

Figure 5.3), consisting of five Upper Triassic–Lower Cretaceous sandstones (for evaluation of the post-Middle Triassic orogeny thermal history), and one Lower Carboniferous sandstone (included to quantify the magnitude and timing of post-depositional reheating). Six granitoids were collected for complimentary geo-/thermo-chronological investigations (**Table 5.1**; **Figure 5.3)**, covering the major intrusive episodes experienced in SE SCB during the Late Ordovician–Early Silurian, the Middle–Late Triassic, the Early Jurassic, and the Middle–Late Jurassic.

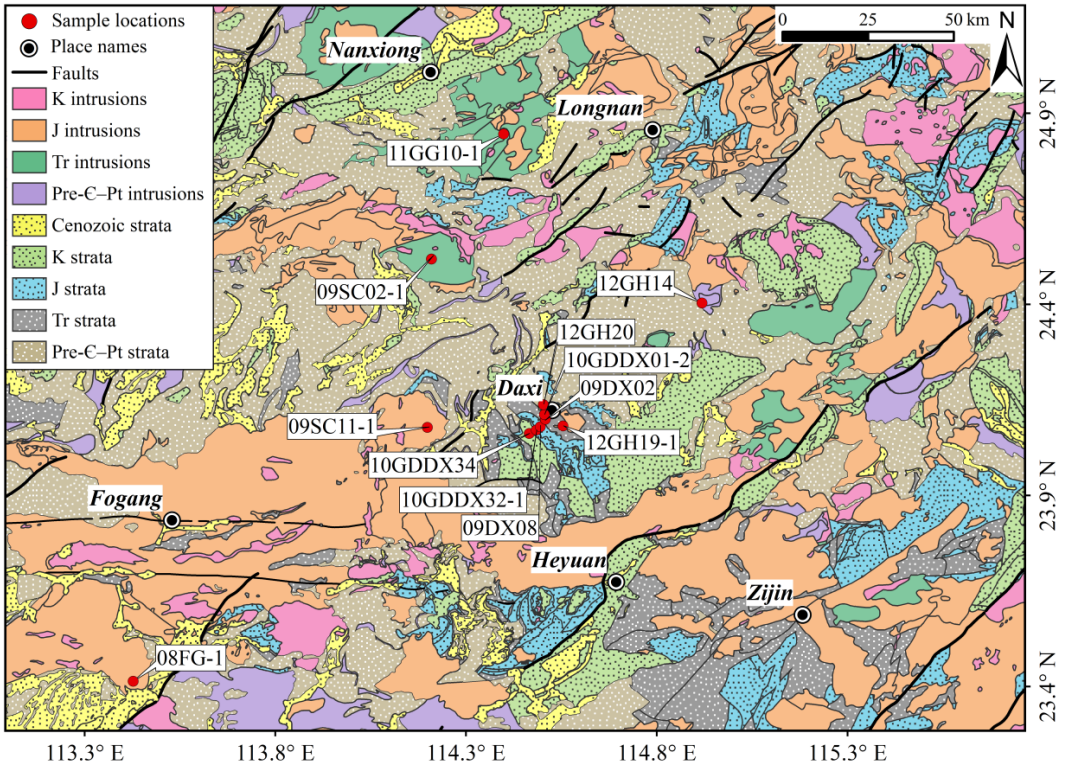

Figure 5.3 Simplified geological map of the Daxi region, showing sample names and locations, compiled from GDBGMR (1962, 1965, 1966, 1969b, 1969a, 1970a, 1970b) and JXBGMR (1970, 1973).

5.3 Results and interpretation

5.3.1 U-Pb age

Zircons from the Heping granite were euhedral to sub-euhedral, with grain lengths ranging from 180 to 330 μm, and length-width ratios from 1.5 to 2.5. The

majority of the crystals were transparent, and colourless to light brown and concentric oscillatory zoning of magmatic origin was observed in the CL images of most crystals (**Figure 5.4a**). A total of eighteen spots were analysed on different magmatic zircon grains, yielding Th/U ratios of 0.49–0.70, and U and Th concentrations from 541 to 1530 pm and 310 to 892 ppm, respectively. The uncertainties on individual analyses were reported at the 1σ level, and the concordia age and weighted-mean $^{206}Pb/^{238}U$ age at the 2σ confidence level (**Table B1**; **Figure 5.4**). The analyses form a single, concordant group yielding a well-defined concordia age of 441± 4 Ma (MSWD=1.7; P=0.19), and a weighted mean $^{206}Pb/^{238}U$ age of 442 ± 5 Ma (MSWD=0.44; P=0.98) (**Figure 5.4**). The results suggest a Late Ordovician–Early Silurian crystallization age for the Heping granite.

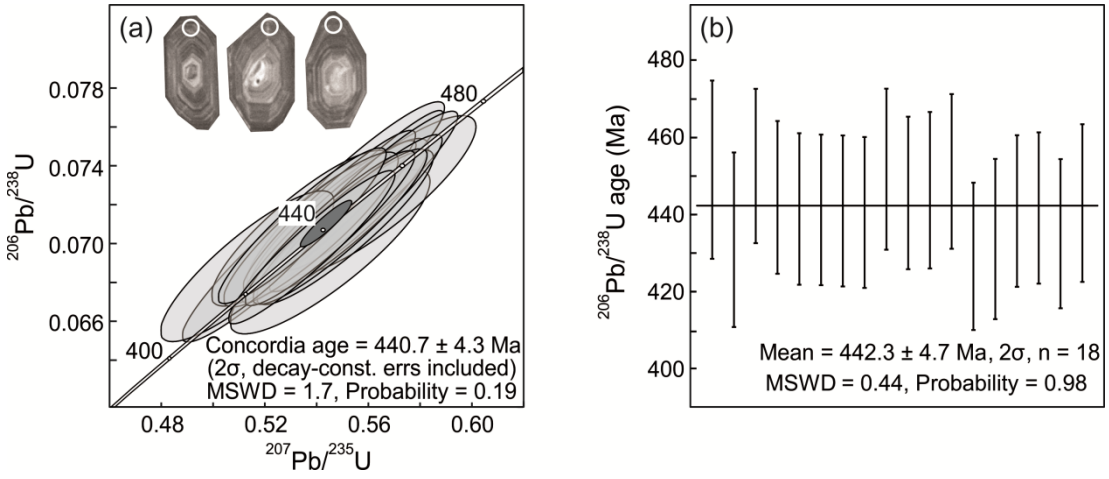

Figure 5.4 (a) Zircon U-Pb concordia diagram and (b) weighted-mean plot of Heping granite (12GH14).

Analysed spots of ~30 μm diameter are shown as white circles on the CL images in **Figure 5.4a**. Error ellipses (**Figure 5.4a**) and dashes (**Figure 5.4b**) are displayed at the 2σ confidence interval. MSWD=mean square of weighted deviates. n=number of analysed spots.

5.3.2 $^{40}Ar/^{39}Ar$ ages

A single muscovite grain from the Longyuanba granite (11GG10-1) was used for $^{40}Ar/^{39}Ar$ dating. The last three incremental heating steps contributed 81% of released ^{39}Ar and defined a plateau age of 166.7 ± 1.6 Ma (MSWD = 1.61; P = 0.20)

(**Figure 5.5a**, **Table B2**), representing a Middle Jurassic closure of the MsAr system (350 ± 50 °C; Hames and Bowring, 1994). A single muscovite crystal from the Triassic Xiazhuang granite (09SC02-1) yielded a decreasing staircase spectrum (**Figure 5.5b**), with an initial age maximum of ~273 Ma progressively falling away to ~169 Ma during incremental heating. Although the degassing behaviour potentially masked excess argon contamination, the age spectrum provided an upper bound of 169 Ma for the timing of MsAr isotopic closure for this sample, which is notably consistent with the MsAr age of the Longyuanba granite (11GG10-1; **Figure 5.5a**).

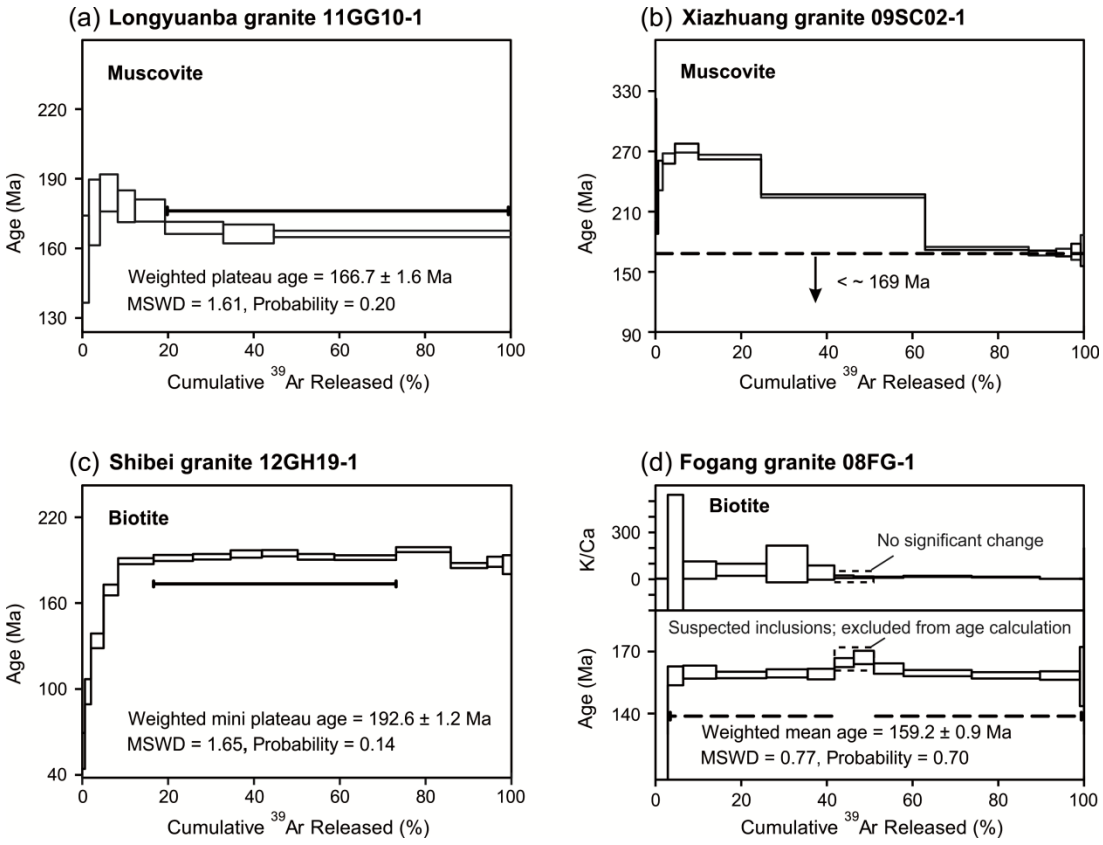

Figure 5.5 Biotite and muscovite $^{40}Ar/^{39}Ar$ age spectra showing plateau or weighted-mean ages and K/Ca ratios.
MSWD=mean square of weighted deviates. Step-heating data bars are displayed at the 2σ confidence interval.

Analysis of a single biotite grain from the Lower Jurassic Shibei granite

(12GH19-1) gave consistent ages across 57% of total ^{39}Ar released and defined a mini plateau age of 192.6 ± 1.2 Ma (MSWD=1.65; P=0.14) (**Figure 5.5c**, **Table B2**). The BtAr age of the Shibei granite is synchronous with its magmatic age. Magmatic cooling through the BtAr closure temperature is interpreted to have occurred at ca. 193 Ma.

A biotite multi-grain analysis from the Upper Jurassic Fogang granite (08FG-01) yielded an age spectrum that included mostly concordant steps (91% of total ^{39}Ar released, **Table B2**) with the exception of two slightly older steps in the middle of the spectrum (**Figure 5.5d**). The two anomalous steps were not associated with any variation in K/Ca ratio (**Figure 5.5d**) and seemed to be only related to an isolated increase of ^{40}Ar*. The most reasonable explanation is considered to be the opening of fluid inclusions, releasing minor quantities of excess Ar in the middle of the analysis. Strictly speaking, this sample did not form a plateau age, but the behaviour of the two steps did not seem to affect the rest of the age spectrum. As such, the weighted-mean age of 159.2 ± 0.9 Ma (MSWD=0.77; P=0.70) given by the majority concordant steps, is interpreted to be an accurate age for cooling through the BtAr closure temperature. The zircon U-Pb ages of the Fogang granitic body, 159 ± 3 Ma to 165 ± 2 Ma, gave estimates of the crystallization age of the intrusion (Li et al., 2007a). Our BtAr age is very close to the zircon U-Pb ages data within error, therefore illustrating a magmatic cooling.

5.3.3 ZFT and ZHe ages

ZFT ages were determined for two sandstones and three granites. All samples passed the chi-square test with a probability of greater than 5% (**Table B3**), with each thus comprising a single age population (**Figure 5.6**). Lower Paleozoic–Upper Jurassic samples gave Early to Late Cretaceous ZFT ages (**Figure 5.7**), indicating a post-depositional reset of ZFT system.

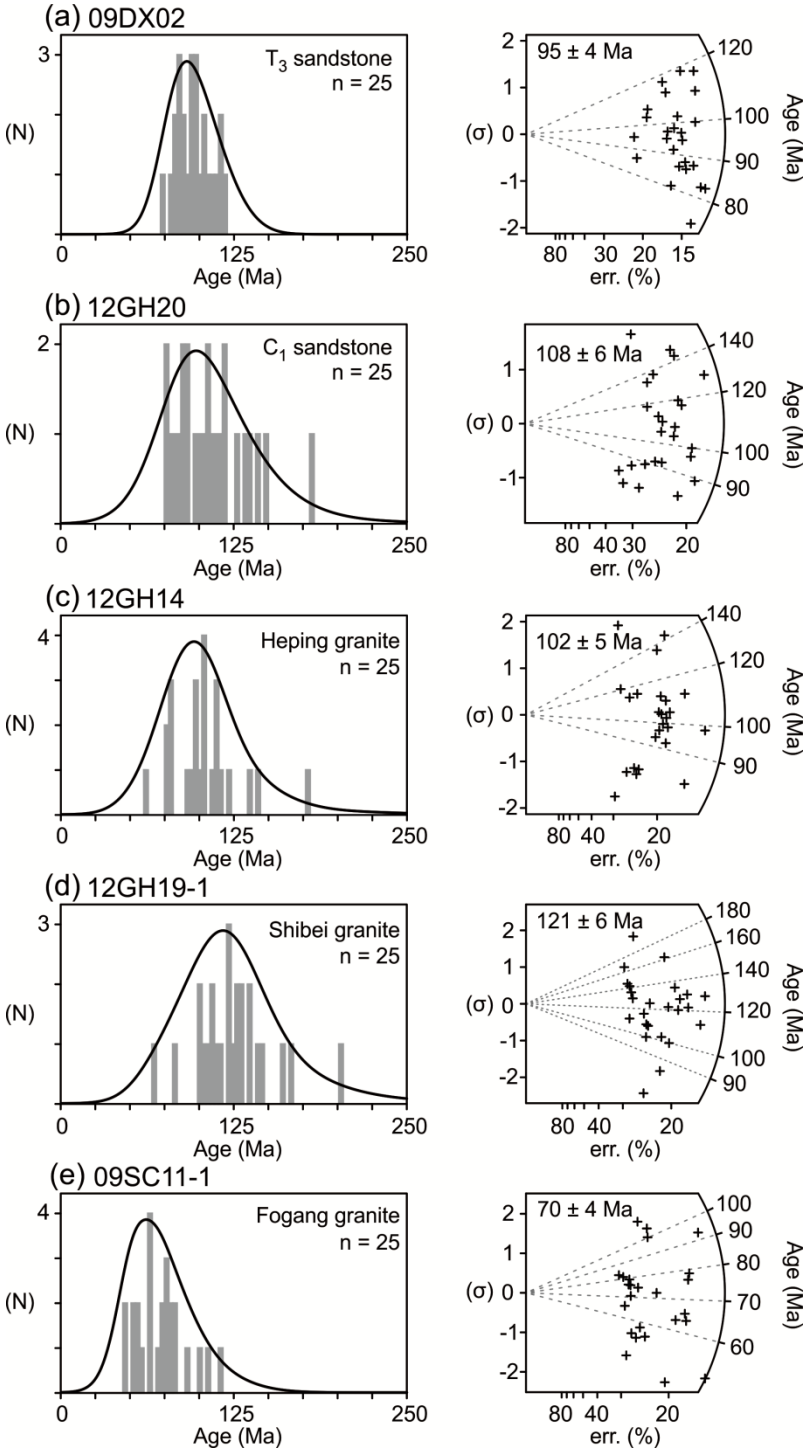

Figure 5.6 Zircon fission track single-grain age histograms and radial plots.

To the left are single-grain age histograms (y-axis: number of grains, x-axis: age in Ma, top right are sample description and the total number of dated zircon grains, the black curve represents one identified age group). To the right are radial plots (left-hand-axis: σ error, bottom axis: relative error in %, right-hand axis: age in Ma, top left: zircon fission track central age ± 1σ error).

Similarly to ZFT ages, ZHe ages (138–75 Ma) were reset in all measure samples, except that in sample 10GDDX34 (**Figure 5.7; Table B4**). The Lower Cretaceous sandstone (10GDDX34) yielded a Late Jurassic ZHe age (147 Ma), indicating that post-depositional temperatures were not high enough to fully reset the ZHe system. Therefore, this age may represent the cooling age of the source area or a partially reset age caused by a subsequent thermal event.

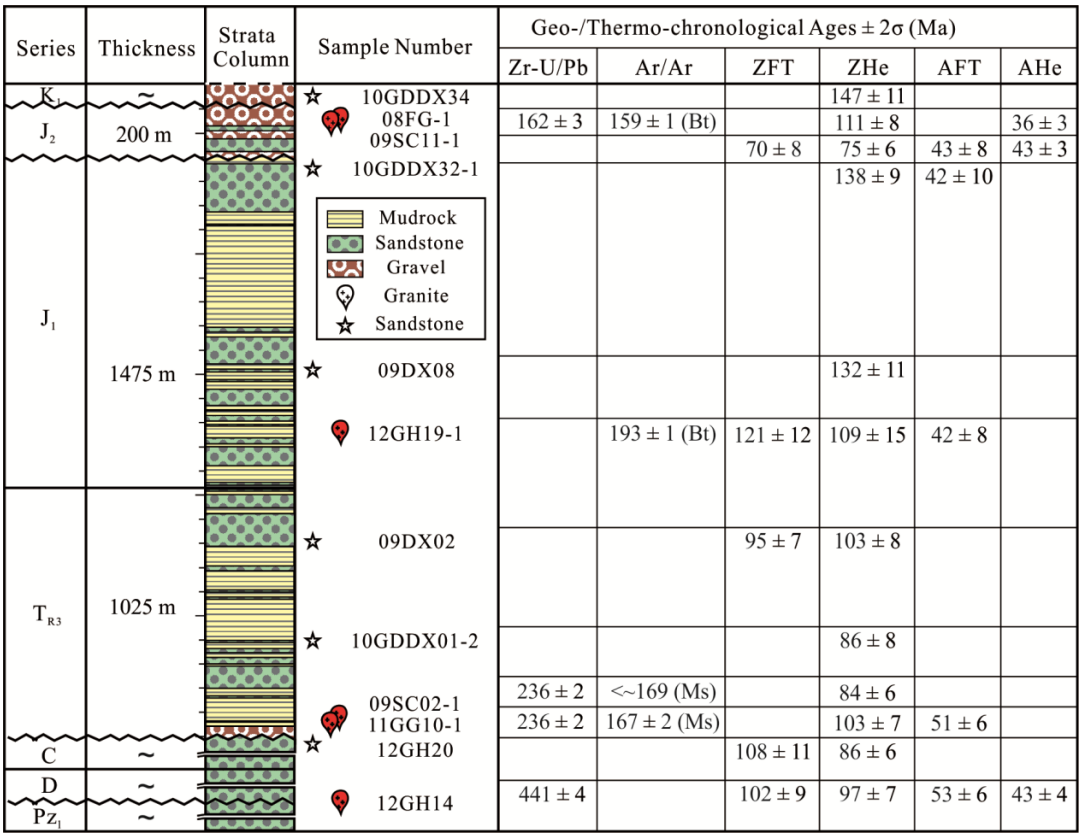

Series	Thickness	Strata Column	Sample Number	Geo-/Thermo-chronological Ages ± 2σ (Ma)					
				Zr-U/Pb	Ar/Ar	ZFT	ZHe	AFT	AHe
K_1	~		10GDDX34				147 ± 11		
J_2	200 m		08FG-1 09SC11-1	162 ± 3	159 ± 1 (Bt)		111 ± 8		36 ± 3
						70 ± 8	75 ± 6	43 ± 8	43 ± 3
			10GDDX32-1				138 ± 9	42 ± 10	
J_1	1475 m		09DX08				132 ± 11		
			12GH19-1		193 ± 1 (Bt)	121 ± 12	109 ± 15	42 ± 8	
			09DX02			95 ± 7	103 ± 8		
T_{R3}	1025 m		10GDDX01-2				86 ± 8		
			09SC02-1	236 ± 2	<~169 (Ms)		84 ± 6		
			11GG10-1	236 ± 2	167 ± 2 (Ms)		103 ± 7	51 ± 6	
C	~		12GH20			108 ± 11	86 ± 6		
D	~								
Pz_1	~		12GH14	441 ± 4		102 ± 9	97 ± 7	53 ± 6	43 ± 4

Figure 5.7 Stratigraphic column and all new data of the Daxi region.
The stratigraphic column was modified after Figure 1c in Pang et al. (2014). The stratigraphic positions of sedimentary samples are shown as stars to the right the stratigraphic column. The magmatic age of granitic samples are marked with respect to the age column. Age data in this table are available in **Tables B1–4**.

To estimate the range of PRZ, ZHe ages were plotted as a function of depth, by converting strata thickness in **Figure 5.7,** and assuming a surface temperate of 20°C and a assumed typical continental geothermal gradient of 30°C/km. ZHe ages of the

Daxi basin exhibited a systematic decrease with increasing paleo depth, as is typical for an exhumed zircon PRZ (**Figure 5.8**). The data reflected incomplete resetting of the zircon Helium system within the PRZ before exhumation began. Sample 10GDDX34, at the shallowest depth, might be at the upper level of the exhumed zircon PRZ or it might record an older cooling event unrelated to the Cretaceous exhumation. At greater depths, samples with similar young apparent ages indicated a completely reset ZHe thermochronometer at >200°C prior to exhumation and cooling through the zircon PRZ.

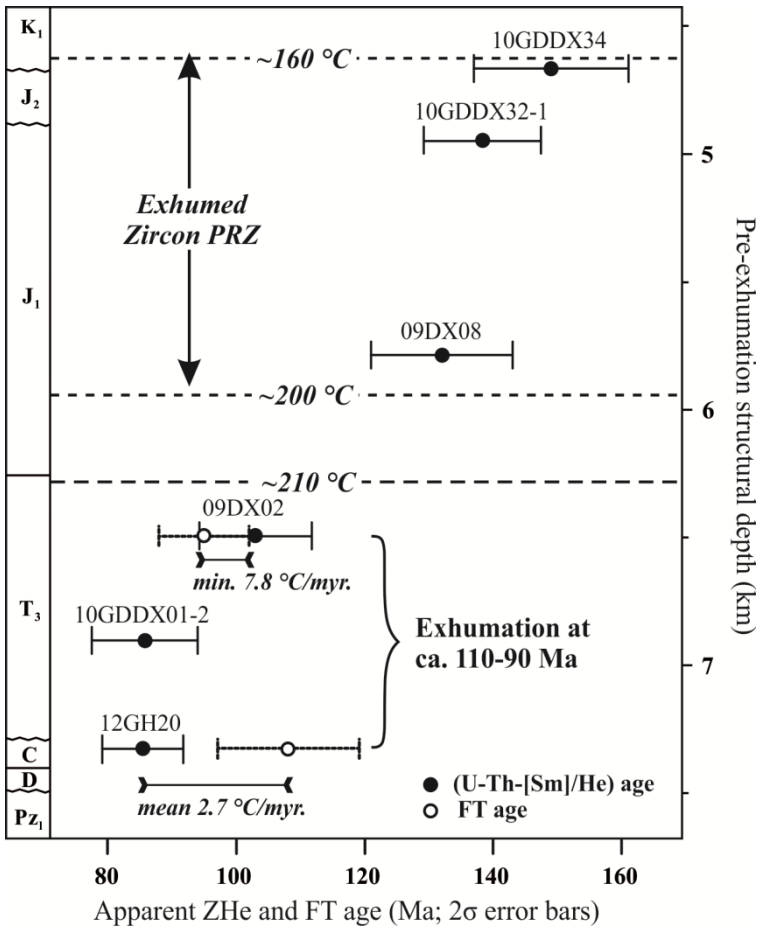

Figure 5.8 Zircon (U-Th-Sm)/He mean ages plotted with pre-exhumation depths.

5.3.4 AFT and AHe data

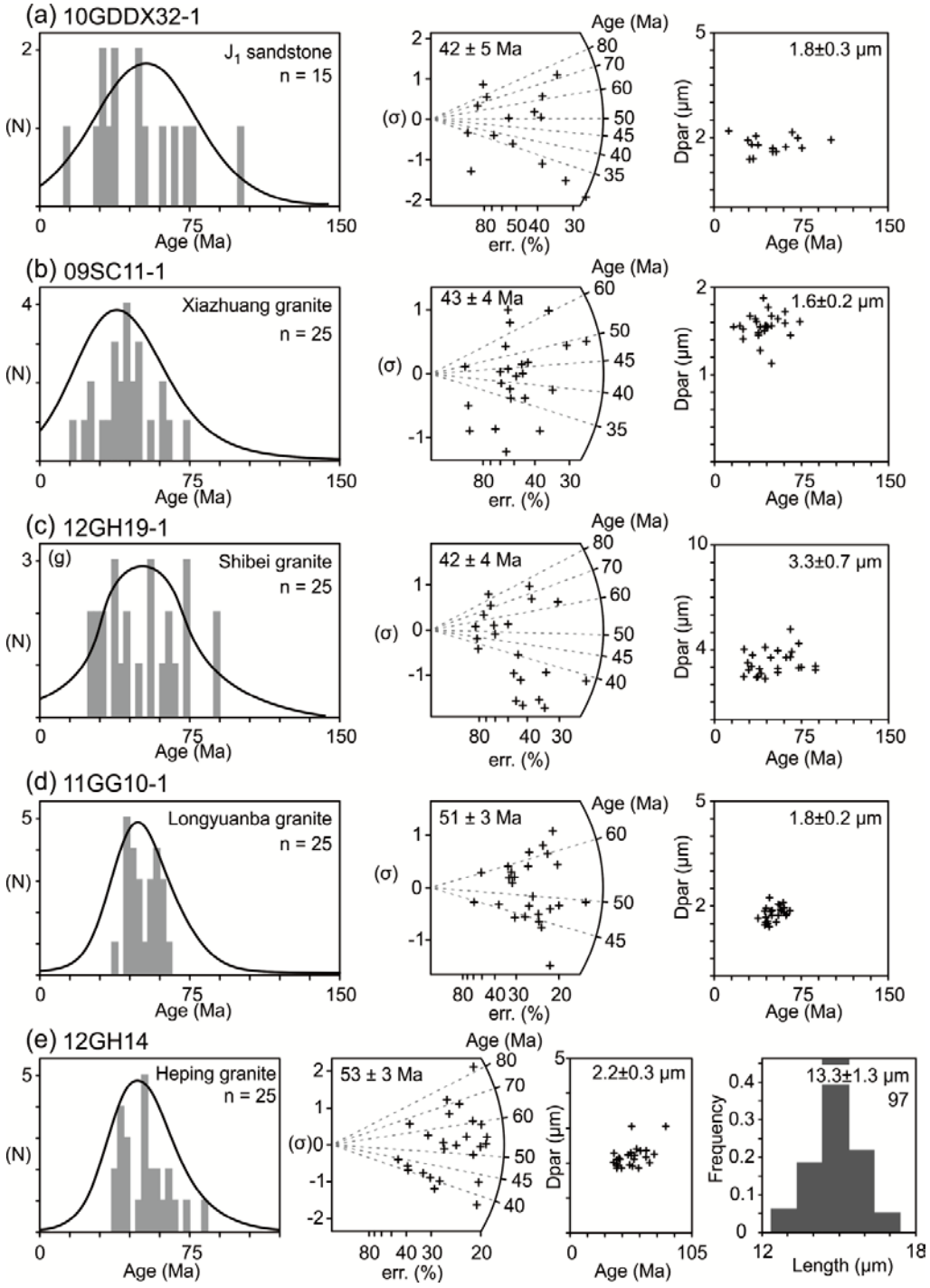

Figure 5.9 Apatite fission track single-grain age histograms, radial plots, AFT age vs. D_{par} plots of all analysed samples and track length distribution histogram of Heping granite.

Single-grain age histograms (y-axis: number of grains, x-axis: age in Ma). Radial plots (left-hand-axis: σ error, bottom axis: relative error in %, right-hand axis: age in Ma, top right are sample description and the total number of dated apatite grains, the black curve represents the age distribution of the identified age group, top left are apatite fission track central age ± 1σ error). D_{par} plots (y-axis: D_{par} values in μm, x-axis: age in Ma, top right are mean D_{par} value ± standard deviation). Fission track length distribution histogram (y-axis: frequency of tracks, x-axis: length in μm, top right are mean track length ± standard deviation and number of measured tracks).

AFT ages were obtained from one sedimentary sample (10GDDX32-1) and four granitic samples (12GH14, 11GG10-1, 12GH19-1 and 09SC11-1). The five sample passed the chi-square test and each comprised a single age population with an Eocene central age (53–42 Ma) (**Figure 5.7; Figure 5.9**). The apatite sample from the Heping granite (12GH14) contained sufficient horizontal confined tracks for track length measurement, yielding a mean track lengths of 13.3 ±1.3 μm (**Figure 5.9**). This unimodal track length distribution suggested a single phase of relatively rapid cooling through the apatite PAZ.

AHe ages (43–36 Ma) were measured on three granites (**Figure 5.7; Table B4**). The tight AHe age cluster for each of these samples dated the timing of the passage through the apatite PRZ.

5.4 Discussion

5.4.1 Middle–Late Jurassic thermal resetting

The Middle Jurassic MsAr ages of the Middle–Upper Triassic granites (11GG10-1; 09SC02-1) record cooling after a Middle–Late Jurassic thermal resetting. This interpretation is supported by the fact that the granites are unconformably overlain by the Lower Jurassic strata (**Figure 5.10a**). Therefore, the Longyuanba granite had exhumed to the surface in the Early Jurassic with temperature below the closure temperature of the MsAr system (**Figure 5.11**). The Heping granite (12GH14) was intruded by an Upper Jurassic granitic body and the Upper Jurassic granite also intruded the Lower Jurassic strata (**Figure 5.10b**). A fault contact relationship has not been observed between the Heping granite, the Lower Jurassic strata and the Upper Jurassic granite (**Figure 5.10b**). In this case, the Heping granite should be at a similar shallow depth as the Lower Jurassic strata in the Early Jurassic. In addition, the Lower Jurassic Shibei granite (12GH19-1) intruded into the Upper Triassic strata (**Figure 5.3**), which is around 1 km thick and was conformably overlain by the Lower Jurassic strata (**Figure 5.7**). Thus, the Shibei granite was emplaced at shallow depth (<1 km from the surface) in the Early Jurassic. In the case of such a shallow-emplacement, the Shibei granite is expected to cool to low

temperatures reasonably soon after the Early Jurassic. Therefore, it can be concluded that pre-Jurassic granites were exhumed to a shallow positon in the Early Jurassic.

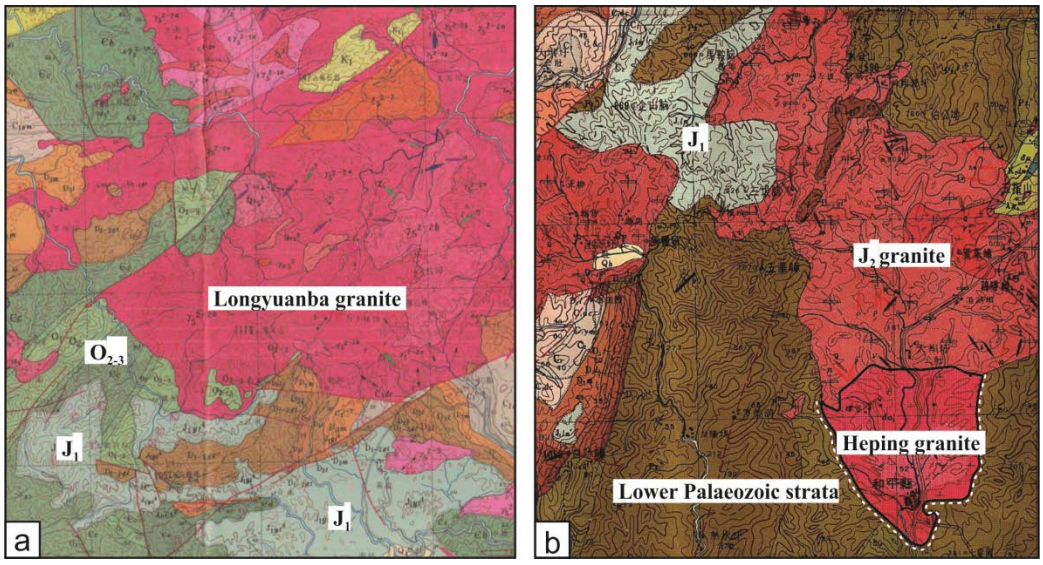

Figure 5.10 Geological maps showing (a) the Longyuanba granite and (b) the Heping granite and surrounding strata, from GDBGMR (1965) and JXBGMR (1970).
The Lower Paleozoic Heping granite is unconformably overlain by the Lower Paleozoic strata, indicating a surface exposure soon after its emplacement (**Figure 5.11**).

Heating to ~350°C is required in order to fully reset the MsAr system (**Figure 5.11**). The heat source can be either burial or magmatic heating. Burial heating is unlikely because the Lower Jurassic strata in the Daxi area is of insufficient thickness (<1.5 km thick, **Figure 5.7**), assuming an average gradient of 30°C/km. Magmatic heating in the Jurassic, therefore contributed to the heat budget required to reset the MsAr system. Early–Middle Jurassic granitic intrusions and basalts in the study are evidence of a thermal anomaly in the region (**Table 5.2**). In particular, Middle Jurassic intrusions could directly provide the heat (i.e. Dafengnao syenite intrusion of the Longyuanba granite in **Table 5.2**), while the Late Jurassic intrusions represent a continued phase of igneous activity and heat after the Middle Jurassic thermal resetting (ca. 156 Ma; Tao et al., 2013). To reset MsAr ages, a greenschist facies overprint should be visible in sediments and granites of pre-Middle Jurassic ages. Thin section observation of samples in Daxi validates this argument (**Figure 5.12**). In the Upper Carboniferous sandstone (12GH20), typical greenschist mineral epidote

was observed (**Figure 5.12a**). Other metamorphic features observed in the sample included quartz and biotite undulating extinction (**Figure 5.12 b** and **c**) and recrystallization of quartz (**Figure 5.12d**). In the Middle–Upper Triassic granite (09SC02-1), chlorite and bending of polysynthetic twins in plagioclase were observed (**Figure 5.12 f** and **h**), apart from biotite and quartz undulating extinction (**Figure 5.12 e** and **g**). In the Lower Jurassic granite (12GH19-1), epidote, orientated hornblende and calcite were observed (**Figure 5.12 i** and **j**). In general, a mineral assemblage of quartz ± epidote ± chlorite ± plagioclase ± K-mica ± calcite was presented in samples from Daxi, which is a most common greenschist to epidote-amphibolite facies metamorphic assemblage at temperatures of ≥300° C (Muffler and White, 1969; Winter, 2010).

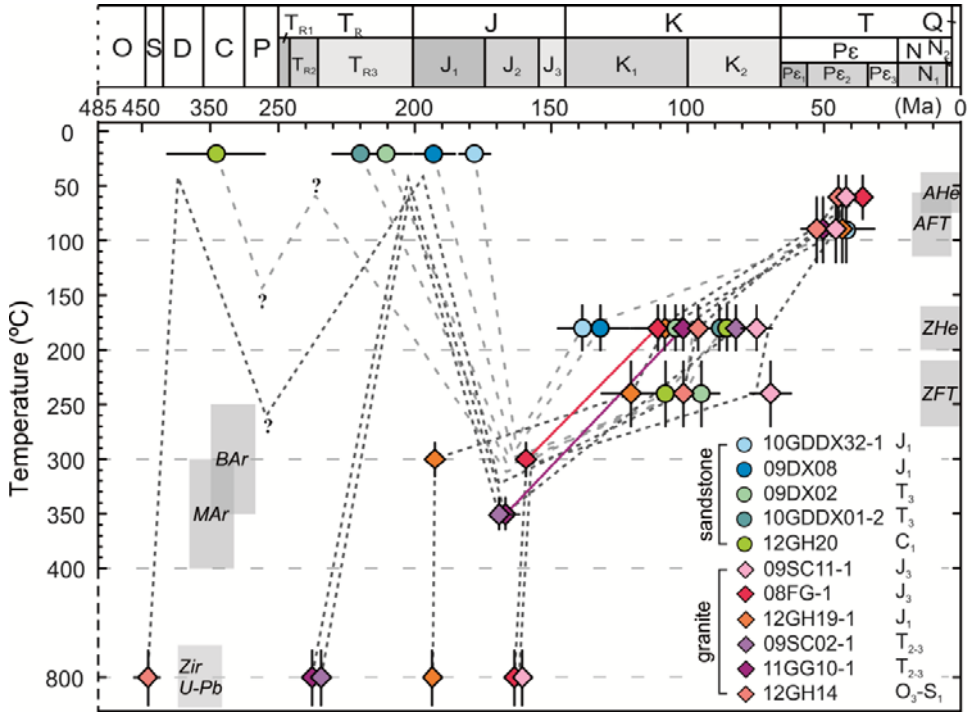

Figure 5.11 Time-temperature trajectories constructed with data generated in this study.
The trajectories of sedimentary samples start at the depositional ages at the assumed annual mean temperature of 20 ± 3°C, and those of granites start at the time defined by zircon U-Pb ages at 800 ± 100°C. All trajectories end at 0 Ma and 20 ± 3°C. The pre-Jurassic time-temperature curve of the Lower Carboniferous sandstone is further constrained by strata thickness and strata-unconformity thickness estimated from the local geological report and the 1:200,000 geological maps. The y-axis (temperature) of curves is determined by the characteristic closure temperature of each thermometer. The x-axis (time) is controlled by measured AHe, AFT, ZHe, ZFT, BtAr, and MsAr ages. Data-point error bars are displayed at 2σ confidence interval.

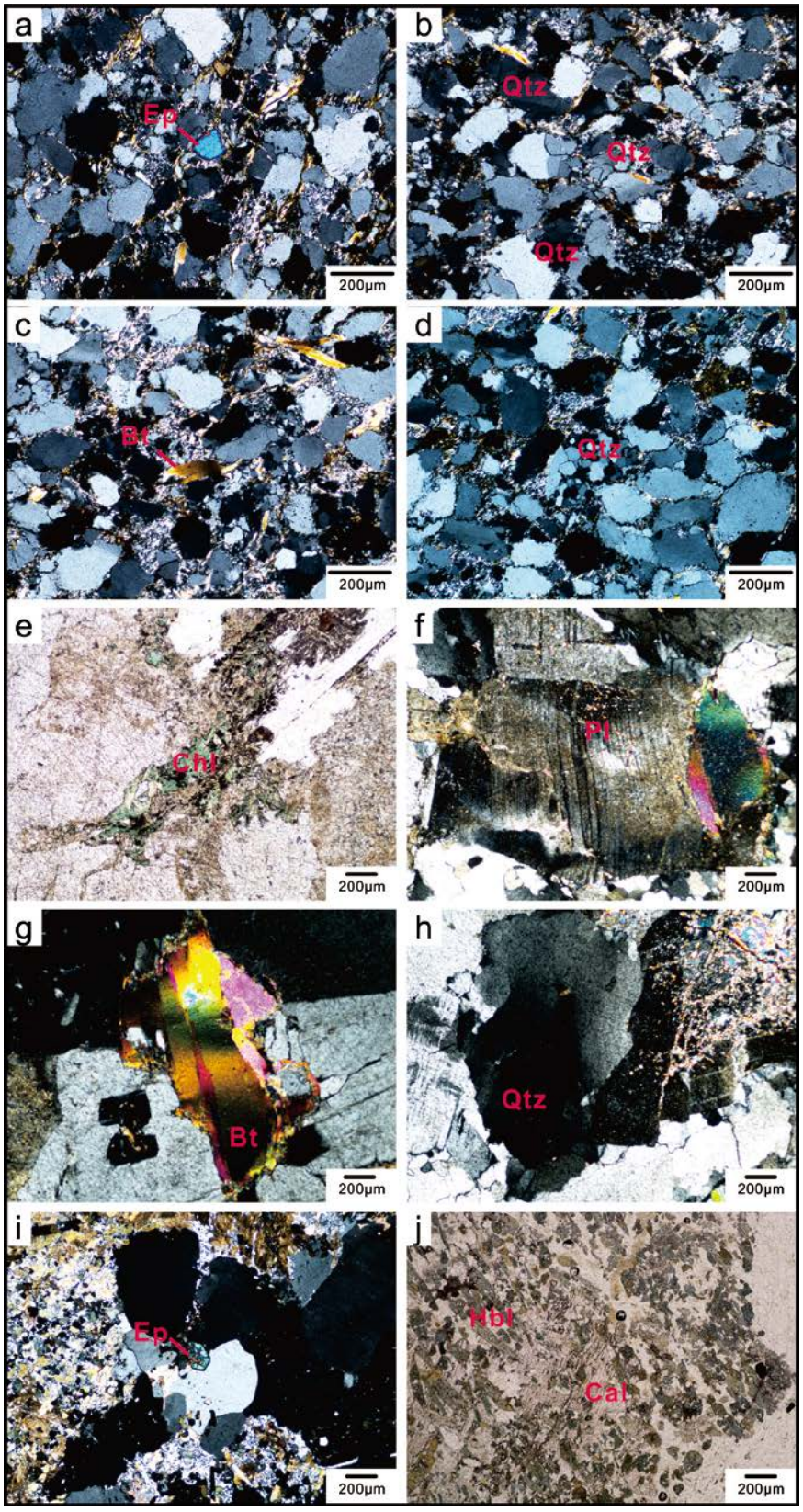

Figure 5.12 Microphotographs photos showing greenschist facies metamorphism of pre-Middle Jurassic rocks in Daxi area.

Bt=biotite; Cal=calcite; Chl= chlorite; EP=epidote; Hbl=hornblende; Pl=plagioclase Qtz=quartz.

The prominent Jurassic A-type granites and mafic intrusions in the Daxi region and areas nearby suggest an extensional tectonic setting (Li, 2000; Li et al., 2000; Chen et al., 2002a; Li et al., 2003; Chen et al., 2005; Zhou et al., 2006; Li et al., 2007a; Li and Li, 2007; He et al., 2010; Yu et al., 2010; Ye et al., 2013), and have been described as elements of magmatism produced by mantle upwelling due to oceanic lithosphere delamination in the Mesozoic flat-slab subduction model of Li and Li (2007).

Table 5.2 List of representative Early–Middle Jurassic magmatism in Daxi region.

Lithology	Age (Ma)	Dating Method	Reference
Shibei granite	193 ± 1	BtAr	[this study]
Keshubei A-type granite	189 ± 3	zircon U-Pb	(Li and Li, 2007)
Pitou A-type granite	179 ± 2	zircon U-Pb	(He et al., 2010)
Zhaibei A-type granite	172 ± 5	zircon U-Pb	(Li et al., 2003)
Mashan shoshonitic granoiorite	164 ± 2	hornblende $^{40}Ar/^{39}Ar$	(Li et al., 2000)
Xialan gabbro	195 ± 1	zircon U-Pb	(Yu et al., 2010)
Chebu gabbro	176 ± 2	zircon U-Pb	(He et al., 2010)
Chenglong gabbro	182 ± 1	zircon U-Pb	(He et al., 2010)
Taibei shoshonitic syenite	178 ± 3	zircon U-Pb	(He et al., 2010)
Huangbu syenite	179 ± 1	zircon U-Pb	(He et al., 2010)
Dafengnao syenite	166 ± 1	zircon U-Pb	(He et al., 2010)
Baimianshan basalt	173 ± 3	K-Ar	(Wang et al., 2003)
Heyuan andesitic porphyries	Lower Jurassic	stratigrapic constrained	(GDBGMR, 1988)

5.4.2 Cretaceous exhumation cooling

With the Middle Jurassic reheating established, the Cretaceous ZFT/ZHe ages are interpreted as the results of a cooling following either the Middle Jurassic thermal resetting or a younger thermal resetting. We interpret ZFT and ZHe ages of both granitic and sedimentary samples as recording a progressive cooling after the Middle–Late Jurassic thermal resetting during the Cretaceous. This is because, firstly, ZHe datasets can best be explained by a prolonged stay in the PRZ (i.e. as a

result of slow exhumation) rather than by a complete rapid resetting. Secondly, the heat source for a younger Cretaceous heating is challenging to identify. Only a few small ca. 100 Ma volcanic outcrops with reliable ages have been found around the margin of Daxi region (**Figure 5.1**) and Cretaceous granitic intrusions are generally 50 km away from the Daxi basin (**Figure 5.3)**. The vast majority of Cretaceous magmatism occurred in the coastal areas bounded by regional Changle-Nan'ao and Zhenghe-Dapu faults (***a*** and ***c*** in **Figure 5.1**) (GDBGMR, 1988; Zhou and Li, 2000; Wang et al., 2003; Shu et al., 2004; Wang et al., 2008b; Jiang et al., 2009; Li et al., 2014a; Li et al., 2014c). Therefore, even if there was a thermal anomaly in the mid-Cretaceous caused by contemporaneous magmatism (Li et al., 2000), we suggest that its thermal influence would be more traceable in coastal areas (**Chapter 4**(Yang et al., 2010; Tang et al., 2014).

Prolonged Cretaceous cooling is consistent with extensional exhumation in the Daxi region. The Ejinao alkali syenite that intruded the Fogang granite at ca. 145 Ma (Xu et al., 2012) implies the involvement of mantle materials (Bao et al., 2000), which is considered as evidence for lithosphere thinning and crustal extension. To the north of Daxi, normal fault in Nanxiong County (**Figure 5.1**) started in the Early Cretaceous (ca. 117 Ma), with strong extensional ductile shearing developed in the early Late Cretaceous (ca. 95 Ma) (Li and Zou, 2011), providing more evidence for Cretaceous lithospheric extension. The extension in the Daxi region could, therefore, have developed soon after the Middle–Late Jurassic thermal resetting, and continued to the Cretaceous. Our mica $^{40}Ar/^{39}Ar$ and ZHe ages for the Longyuanba (11GG10-1) and Fogang (08FG-1) granites (linked by a purple and a red line respectively in **Figure 5.11**), define a Late Jurassic–Early Cretaceous cooling of 2–4°C/Myr, suggesting a stable exhumation over this interval.

In SE SCB, the coexistence of basaltic rocks and northeast-southwest striking extensional basins, and extensive A- and I-type granitoids in the coastal region during the Cretaceous strongly imply an extensional tectonic setting (Gilder et al., 1991; Charvet et al., 1996; Zhou and Li, 2000; Zhou et al., 2006; Li and Li, 2007; Jiang et al., 2009; Wang et al., 2013). Such apparent coupling of magmatism and extensional basin developed in SCB (Gilder et al., 1991; Li, 2000; Li and Li, 2007)

was also noted for the Basin and Range system in the western US (Zoback and Thompson, 1978; Eaton, 1982), particularly in its early stage (e.g. 45–30 Ma; Zoback et al., 1981). At present, both SE SCB and the western US Basin and Range province have thin average crust thicknesses of ~30 km (Jones et al., 1992; Hearn et al., 2004). Subduction and roll-back of the Pacific oceanic plates has been closely linked with the development of extensional tectonics in both regions. Pacific flat-slab foundering and consequent rebounding of the overriding SCB during the Cretaceous would have generated intraplate lithospheric extension (Li and Li, 2007), providing a coherent explanation for the protracted slow cooling observed in Daxi. The Pacific subduction zone and its related arc retreated southeastward during this period (Li et al., 2012), and had migrated to the south of the present continental margin of SCB by ~90 Ma (Lapierre et al., 1997), accounting for the movement of intensive Late Cretaceous volcanic activity (Meng et al., 2012) into coastal areas of the SCB at this time.

5.4.3 Paleogene–Eocene rapid cooling

The AFT (ca. 53–42 Ma) and AHe (ca. 43–36 Ma) ages in our dataset point to relatively rapid cooling from the apatite fission-track closure temperature (~110 °C) to surface temperature (~20°C) during the Eocene (**Figures 5.11** and **5.13**). This cooling is likely a natural continuation of long-term Cretaceous exhumation cooling, because heating in the Late Cretaceous–Eocene is not supported by inverse modelling. Inversing modelling results present an increase in cool rate in the Eocene (**Figure 5.13**), implying a pronounced Paleogene–Eocene fast cooling. The timing of the cooling coincides with a recognized episode of rifting in inland SCB (Ren et al., 2002; Zhu et al., 2004; Yan et al., 2009b; Zhou et al., 2009). In the Daxi region, substantial basaltic and rhyolitic lavas of corresponding ages have been recognised (i.e. ca. 67 Ma basalts in Nanxiong and ca. 56 Ma basalts in Lianping and Heyuan; **Figure 5.1).** Paleogene sediments are notably absent from the Daxi region and generally from inland SE SCB, implying that the area could have represented a domain of relative uplift during this period, as might be expected for a shoulder setting relative to rifting activity.

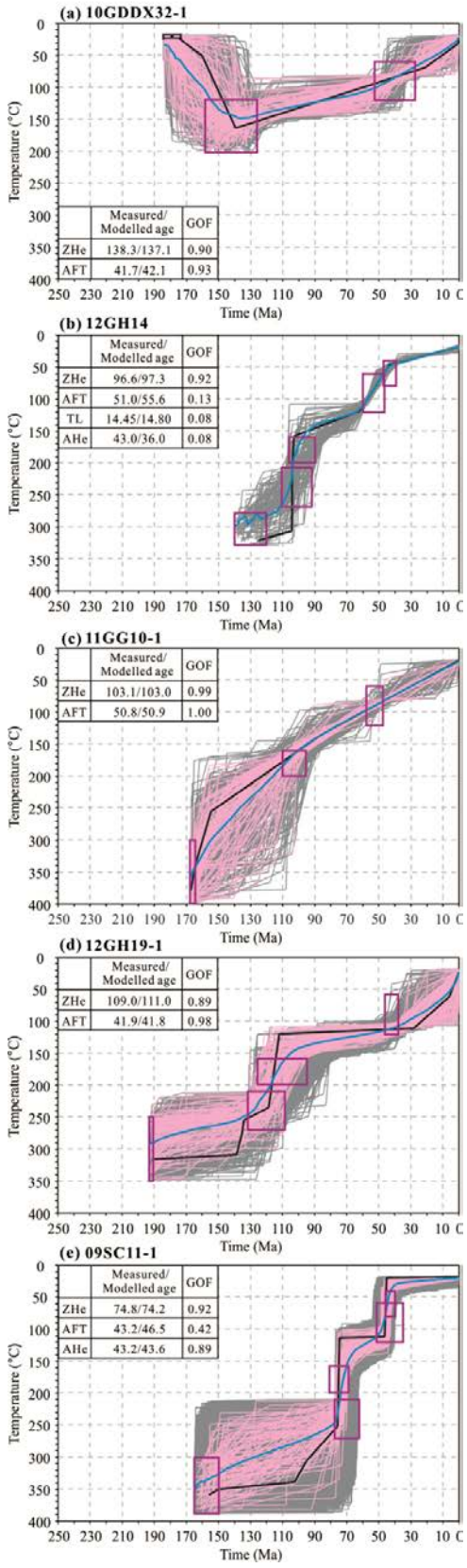

Figure 5.13 Results of the modelling of the thermal histories of selected samples from Daxi region.

The Early Cenozoic rifting in SE SCB has been linked to the rollback of the subducting western Pacific oceanic plates (Northrup et al., 1995; Li et al., 2012). The geochemistry and Sr-Nd isotopic composition of the Cenozoic basalts suggested an intraplate back-arc setting for SE SCB at this time (Yu et al., 2003), consistent with subduction zone retreat towards the ocean (Li et al., 2012). Subduction-induced mantle upwelling in a back-arc setting is also consistent with the noted low-velocity mantle structure of SCB (Hearn et al., 2004; Liu et al., 2004). Alternatively, eastward lateral mantle extrusion driven by the Indo-Asian collision (since ~50 Ma; Molnar and Tapponnier, 1975) has been argued to account for geochemical and geochronological records of Cenozoic rifting in SCB (Flower et al., 2001; Zhu et al., 2004), and is consistent with inversion modelling of geophysical data (Liu et al., 2004). This model, however, is inconsistent with the fact that Early Cenozoic rifting along the continental margin of SCB predates the Indo–Asia collision at ~50 Ma (Ye et al., 1987; Yan et al., 2009b). The most recent demonstrable cooling is bounded by the youngest AHe mean age of 36 Ma (08FG-1). The youngest volcanism in inland SCB is near-contemporaneous with this age at 38 Ma (Zhu et al., 2004; Gong and Chen, 2014). Sea-floor spreading of the South China Sea begun by 30 Ma (Zhou et al., 2009) and continued until 16 Ma (Taylor and Hayes, 1983; Cande and Kent, 1992). Rift-related extension in Daxi thus seems to finish synchronously with the establishment of drift in the SCS. This apparent rift-drift transition probably implies that the Cretaceous extension and Early Cenozoic rifting observed in inland region was intimately associated with, and ultimately led to the opening of the South China Sea in the Late Eocene–Neogene time.

5.5 Conclusions

Middle–Late mica $^{40}Ar/^{39}Ar$ ages, revealed for two granites of Middle–Late Triassic magmatic age, record a Middle–Late Jurassic thermal event related to Jurassic granitic intrusions resulting from the delamination and break-up of the Paleo-Pacific plate, subducted at a low angle beneath SE SCB. Zircon fission track and (U-Th-Sm)/He ages from Lower Carboniferous–Lower Jurassic sandstones range from 140 to 70 Ma, recording slow Cretaceous cooling. This cooling

represents post-intrusion exhumation in an extensional setting, consistent with lithospheric rebound due to foundering and roll-back of the subducted Paleo-Pacific plate. Apatite fission track and (U-Th-Sm)/He ages of 53–36 Ma record rapid exhumation-driven cooling during the Eocene. This cooling phase coincides with continental rifting in SE SCB, and may be linked to a late episode of roll-back of the Paleo-Pacific plate leading to the opening of the South China Sea.

Chapter 6 Mesozoic and Cenozoic thermochronological record of the Shaoguan-Longnan region

6.1 Geological setting

The Shaoguan-Longnan region is located in the northern Guangdong and southern Jiangxi provinces, slightly north of the Daxi region (**Chapter 5; Figure 6.1**). It is in the central SE SCB, between the Xinfeng-Enping fault zone to the southeast and the Sihui-Wuchuan fault zone to the northwest (**Figure 6.1a**). The Shaoguan-Longnan region experienced multi-stage thermal events, as indicated by lower Mesozoic coal seams and late Mesozoic magmatism. The exact Mesozoic thermal history in this region, however, is still poorly understood. In this study, a comprehensive thermochronological investigation was conducted in the Shaoguan-Longnan region in order to decode the thermal history in the central SCB since the Mesozoic.

In Shaoguan, the Ordovician to Silurian strata are missing. The Devonian to the Lower(–Middle?) Triassic strata unconformably overlay the Cambrian and Precambrian sequences (GDBGMR, 1962). Upper Triassic to Lower Jurassic sandstone and shale with coal seam interlayers are unconformably deposited between Lower (to Middle?) Triassic and Middle Jurassic sandstones (GDBGMR, 1962). Lower Cretaceous purple conglomerates and sandstones are unconformably deposited between Middle Jurassic sandstones and Eocene sandstones (GDBGMR, 1962) or between Lower Triassic and Middle Cretaceous sandstones (JXBGMR, 1969). Quaternary sediments are unconformably deposited on Eocene or Middle Cretaceous strata (GDBGMR, 1962; JXBGMR, 1969). Similar stratigraphy is observed in Longnan. Two regional unconformities are found beneath the Lower or Middle Devonian and beneath the Lower Jurassic strata (GDBGMR, 1965; JXBGMR, 1970, 1973). Middle Jurassic (limited outcrops), Upper Jurassic, Lower Cretaceous, Upper Cretaceous and Eocene strata unconformably overlay the underlying strata (GDBGMR, 1965; JXBGMR, 1970, 1973) and Neogene strata are rarely observed (GDBGMR, 1965). Quaternary sediments are unconformably

deposited directly upon Tertiary (mostly Eocene) strata (GDBGMR, 1965; JXBGMR, 1970, 1973).

Granitoids of Early Paleozoic to Cretaceous ages are widely distributed in the study area (**Figure 6.1**) while Jurassic granitoids have the largest exposure area (**Figure 6.1**). The Zhuguangshan complex is one of the major granitic complexes in the SE SCB, consisting of Paleozoic, Triassic, Jurassic and Cretaceous intrusions (**Figure 6.1**). Volcanic rocks of Late Cretaceous and Eocene ages are reported in the study area (Shu et al., 2004).

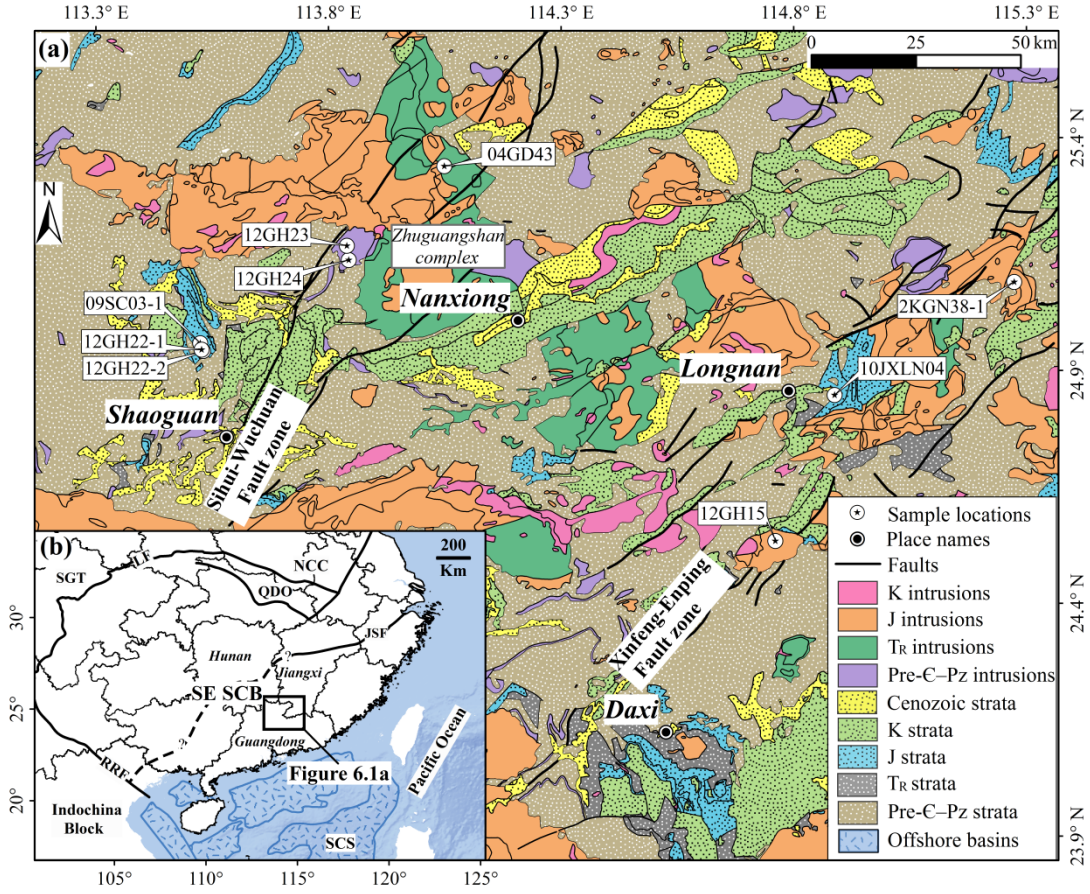

Figure 6.1 (a) Simplified geological map of the Shaoguan-Longnan area, showing sample names and locations, compiled from , GDBGMR (1962, 1965); JXBGMR (1969, 1970), and Deng et al. (2012). (b) Tectonic map of SCB-West Pacific region showing the major units that compose the region and provinces in SE SCB.

In **Figure 6.1b**, Black frame represents the extent of **Figure 6.1a.** LF—Longmenshan Fault, JSF—Jiang-Shao Fault, NCC—North China Craton, QDO—Qinling-Dabie Orogen, RRF—Red River Fault, SCS—South China Sea, SGT—Songpan-Ganzi Terrane.

6.2 Sampling

Four sandstones and five granitoids were collected from the Shaoguan-Longnan area (**Table 6.1**). Lower Jurassic sandstone samples were collected from basins in Shaoguan (09SC03-1 and 12GH22-1) and Longnan (10JXLN04) (**Figure 6.1**). Lower Jurassic strata in Shaoguan developed coal seams and one coal sample (12GH22-2) was collected for vitrinite reflectance measurement with the aim to reveal the maximum paleo-temperature since the Early Jurassic. Granitic samples were taken from the Fuxi body (12GH23 and 12GH24) and the Late Triassic Mengdong body (04GD43) within the Zhuguangshan complex (**Figure 6.1**), and from the Lower Jurassic Keshubei (2KGN38-1) and Liyuan granites (12GH15). The Liyuan granite was considered to have intruded in the Jurassic (GDBGMR, 1965) but no precise magmatic age has been reported. There is no reliable magmatic age for the Fuxi granite either, although a wide spectrum of ages were reported (i.e. 548 Ma, 399 Ma and 203 Ma; Deng, 1987). Therefore, in addition to thermochronological dating, high precision SHRIMP U-Pb dating on the Liyuan and Fuxi granites has been conducted in this study.

Table 6.1 Shaoguan-Longnan sample information

Sample #.	Lithology	Stratigraphic / Formation age	Location	Latitude N (°)	Longitude E (°)	Elevation (m)
10JXLN04	sandstone	J_1 Qiaoyuan Fm. 185-174 Ma[a]	Longnan	24.899	114.888	232
12GH22-1	sandstone	J_1 Jinji Fm. 201-185 Ma[a]	Shaoguan	25.002	113.524	191
12GH22-2	coal			25.002	113.524	191
09SC03-1	sandstone	J1 Jinji Fm. 201-185 Ma[a]		25.004	113.522	181
12GH23	granite	438.1 ± 2.1[b]	Fuxi	25.218	113.840	184
12GH24	granite	442.1 ± 2.8[b]	Fuxi	25.183	113.844	275
04GD43	granite	230.7 ± 3.4[c]	Mengdong	25.387	114.039	486
2KGN38-1	granite	188.7 ± 2.8[c]	Keshubei	25.141	115.274	303
12GH15	granite	162.1 ± 2.7[b]	Liyuan	24.585	114.761	373

[a]Stratigraphic ages are based on strata correlation with the T_3–J_1 Daxi basin (Pang et al., 2014).

[b]SHRIMP Zircon U-Pb ages of Fuxi granites and Liyuan granite are from this study.

[c]SHRIMP Zircon U-Pb ages of Mengdong and Keshubei granites published by Li and Li (2007).

6.3 Results and interpretation

6.3.1 U-Pb ages

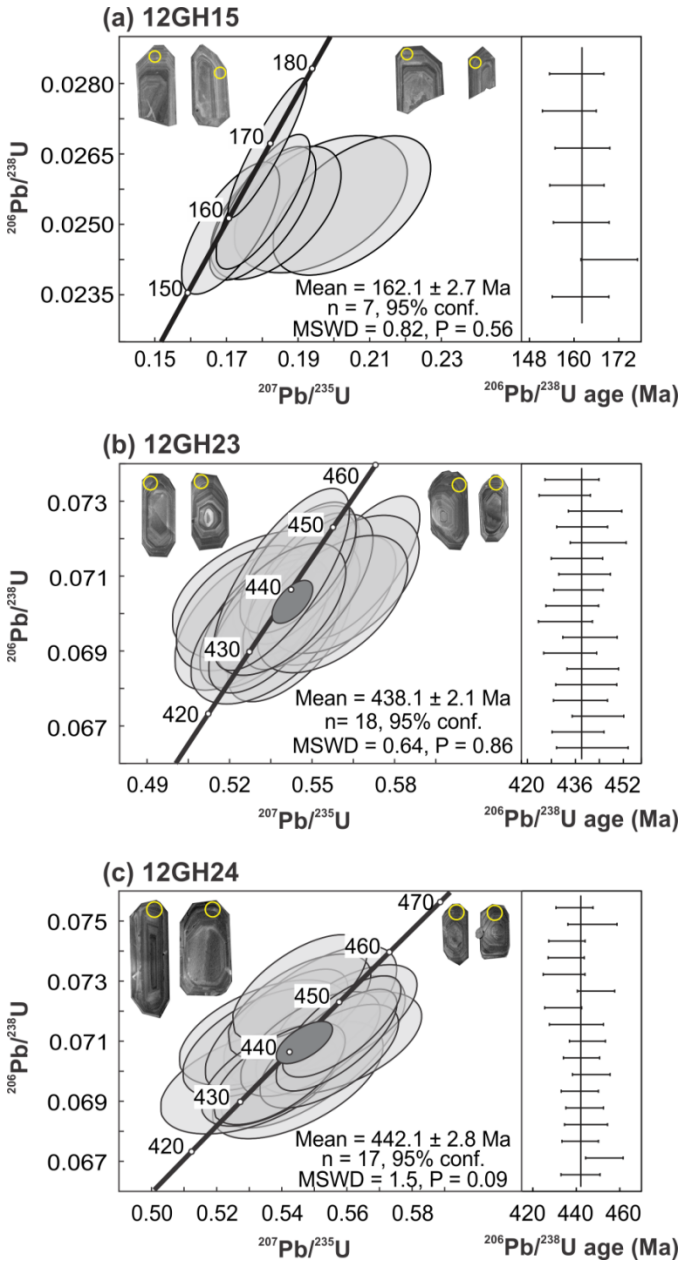

Figure 6.2 Zircon U-Pb concordia diagrams and weighted-mean plots.
Analysed spots that were ~30 μm in diameter are shown as yellow circles on the CL images. Error ellipses and dashes are displayed at the 2σ confidence interval. Dark grey ellipses in **Figure 6.2b** and **c** represent concordia ages. Mean—weighted-mean $^{206}Pb/^{238}U$ age. MSWD—mean square of weighted deviates. n—number of analysed spots. P—probability value for a chi-square test at N degrees of freedom (N=number of analyses-1).

Zircons from the Liyuan granite (12GH15) were euhedral with grain lengths ranging from 130 to 400 μm, and length-width ratios ranged from 6:1 to 2:1. The majority of the crystals showed a milky interior with inclusions and cracks. Most were light-dark brown, although some were transparent and colourless with negligible impurities. CL images of zircon separates showed the concentric oscillatory zoning typical of magmatic zircons (**Figure 6.2a**). The weighted mean ^{204}Pb-corrected ^{206}Pb/^{238}U age of the analysed spots on the TEMORA 2 standard zircon was 420.2 ± 3.3 Ma (95% conf.), within error of the accepted ^{206}Pb/^{238}U age of 417 Ma (Black et al., 2004). Absolute abundances of U and Th were calibrated to the BR266 standard which has U and Th concentrations of 909 and 201 ppm (Stern, 2001), respectively. BR266 was also used as a secondary age standard (559 Ma, Stern, 2001), yielding a weighted mean ^{204}Pb-corrected ^{206}Pb/^{238}U age of 563.5 ± 11.4 Ma (95% conf.), consistent with the standard value within error. Seven spots on different zircon grains were analysed for the Liyuan granite and yielded a weighted mean ^{204}Pb-corrected ^{206}Pb/^{238}U age of 162.1 ± 2.7 Ma (MSWD=0.82; P=0.56; 95% conf.; **Table C1; Figure 6.2a**). The weighted mean age represents the Late Jurassic crystallization age of the Liyuan granite.

Zircons from two Fuxi granite samples (12GH23 and 12GH24) were euhedral to sub-euhedral (**Figure 6.2 b** and **c**). The grain lengths ranged from 100 to 300 μm, with most crystals longer than 120 μm. The majority of the crystals were transparent and colourless to brown. Concentric oscillatory zoning suggesting a magmatic origin was observed in the CL images of most crystals (**Figure 6.2 b** and **c**). Plešovice was used as the primary age standard for U-Th-Pb ratio calibration. The weighted mean ^{204}Pb-corrected ^{206}Pb/^{238}U age of the analysed spots on Plešovice was 336.9 ± 1.8 Ma (95% conf.), indistinguishable from the published ^{206}Pb/^{238}U age of 337.1 ± 0.4 Ma (Sláma et al., 2008; Li et al., 2009b). Absolute abundances of U and Th were calibrated to the M257 standard which has a U concentration of 840 ppm and Th/U ratio of 0.27 (Nasdala et al., 2008). M257 was also used as a secondary age standard (561 Ma, Nasdala et al., 2008) and repeated analyses yielded a weighted mean ^{204}Pb-corrected ^{206}Pb/^{238}U age of 562.5 ± 3.2 Ma (95% conf.), consistent with the standard value within error. A total of 18 spots on different zircon grains were analysed on 12GH23 yielding a weighted mean ^{204}Pb-corrected ^{206}Pb/^{238}U age of 438.1 ± 2.1 Ma

(95% conf.; MSWD=0.64; P=0.86; **Figure 6.2b**). A concordia age of 438.3 ± 2.4 Ma (95% conf.; MSWD of concordance=3.0; P of concordance=0.08) was calculated. A total of 17 spots on different zircon grains were analysed for 12GH24 with a weighted mean ^{204}Pb-corrected ^{206}Pb/^{238}U age of 442.1 ± 2.8 Ma (95% conf.; MSWD=1.5; P=0.09; **Figure 6.2c**). A concordia age of 442.1 ± 2.8 Ma (95% conf.; MSWD=0.65; P of concordance=0.42) was calculated for this sample. The results suggest an Early Silurian crystallization age for the Fuxi granite.

6.3.2 ^{40}Ar/^{39}Ar ages

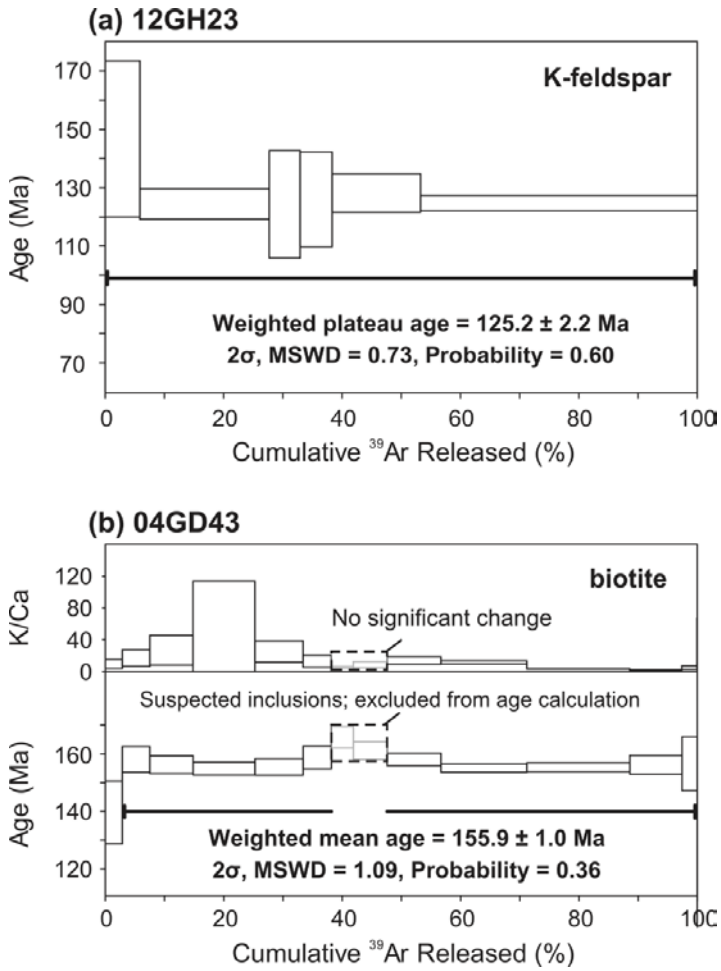

Figure 6.3 K-feldspar and biotite ^{40}Ar/^{39}Ar age spectra showing plateau or weighted-mean ages and K/Ca ratios.

MSWD—mean square of weighted deviates. Step-heating data bars are displayed at the 2σ confidence interval.

A K-feldspar multi-grain package from the Fuxi granite (12GH23) yielded a plateau age of 125.2 ± 2.2 Ma (2σ, MSWD=0.73; P=0.60), covering all 6 incremental heating steps (**Figure 6.3a**). The plateau age is interpreted to date the Ar isotopic closure of K-feldspar (150–350 °C; Lovera et al., 1989) at ca. 125 Ma.

Mengdong granite (04GD43) biotite multi-grain package yielded an age spectrum that included primarily concordant steps (88% of total ^{39}Ar released), with the exception of the first younger step (3% of ^{39}Ar released) and two slightly older steps (9% of ^{39}Ar released) in the middle of the spectrum (**Table C2; Figure 6.3b**). These steps were not associated with a variation in K/Ca ratio of the gas released (**Figure 6.3b**) and seemed to be only associated with variation of ^{40}Ar* from the biotite. The most reasonable explanation is therefore considered to be the cracking of fluid inclusions, releasing minor quantities of excess Ar in the middle of the experiment. Strictly speaking, this sample did not form a plateau age, but the behaviour of the two middle steps does not seem to affect the rest of the age spectrum. As such, the weighted mean age of 155.9 ± 1.0 Ma (MSWD=1. 09; P=0.36) given by the concordant steps is an meaningful age for the cooling of the biotite below its Ar closure temperature (300 ± 50 °C; Harrison et al., 1985).

6.3.3 ZHe ages

ZHe ages measured for all samples ranged from 152 to 115 Ma (**Table 6.2**; **Table C3**). ZHe ages (152–142 Ma) from Lower Jurassic sandstones (10JXLN04, 12GH22-1 and 09SC03-1) were 30–40 Myr younger than the depositional ages, implying a post-depositional heating. Syn- and pre-depositional ZHe ages were found in two sandstones (12GH22-1 and 09SC03-1; **Figure 6.4a**), possibly recording either cooling in the source areas or a cooling during deposition that was not obscured by later events. The ZHe mean ages of granites were clearly younger (35–300 Ma; **Table 6.2**) than their corresponding magmatic ages (**Table 6.2**). Therefore the ZHe ages are reset ages and indicate a post-emplacement heating event that exceeded 180 ± 20°C (Reiners et al., 2004; Guenthner et al., 2013).

Table 6.2 Table showing all new data from Shaoguan-Longnan region.

Sample #.	Lithology	Stratigraphic / Magmatic	Ages (Ma) $^{40}Ar/^{39}Ar$	ZHe	AFT	AHe	VR (%)
10JXLN04		185–174		152	72		
12GH22-1	sandstone	201–185		148	38/109	35	
09SC03-1		201–185		142	40/122	36	
12GH22-2	coal						1.88
12GH23		438	125 (K-feldspar)	130	69	34	
12GH24		442		139	62	37	
04GD43	granite	231	156 (biotite)	124	37	37	
2KGN38-1		189		115		33	
12GH15		162		126	39	38	

Data supporting **Figures 6.2–7** and **Table 6.2** are available in Appendices **Tables C1–5**. ZHe=zircon (U-Th-Sm)/He; AFT=apatite fission track; AHe=apatite (U-Th-Sm)/He; VR=vitrinite reflectance.

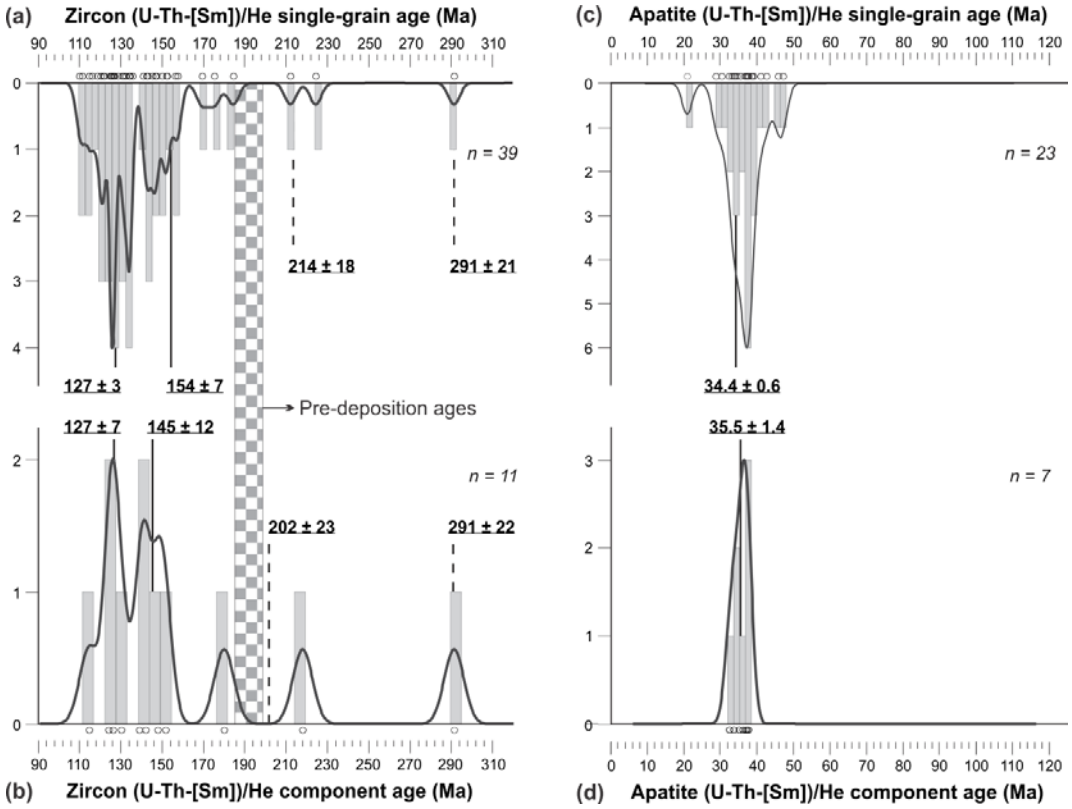

Figure 6.4 Histograms of apatite and zircon (U-Th-Sm)/He ages from Shaoguan-Longnan area. Plotted data are available in Tables 6 and 7. The black line is a kernel density estimation (KDE) calculated by DensityPlotter (Vermeesch, 2012). The bin sizes and bandwidths of **Figure 6.4a–d** are 3.78 and 1.67 Myr, 5.3 and 3.7 Myr, 1.6 and 1.4 Myr, and 1.6 and 1.5 Myr, respectively. Major age components were calculated with the implied mixed population determination tool. Black circles display the data points.

6.3.4 AFT and AHe ages

Apatite fission track ages were measured on three sedimentary and three granitic samples (**Table C4**) and were all significantly younger than the corresponding depositional or magmatic age (**Table 6.2**). The AFT ages therefore indicate a >110°C heating event (Gleadow and Duddy, 1981; Brandon et al., 1998) after the deposition or emplacement of the samples. Eocene (40 Ma and 38 Ma) and Late Cretaceous (122 Ma and 109 Ma) AFT age populations were identified in two sandstones that failed to pass the chi-square test (12GH22-1 and 09SC03-1) (**Figure 6.5**). The other samples passed the chi-square test and were considered to form a single age population (**Figure 6.5**) with AFT ages of Eocene (39 and 37 Ma) or Late Cretaceous–Paleocene (62 Ma, 69 Ma and 72 Ma; **Table 6.2**).

Two samples from the Fuxi granite (12GH23 and 12GH24) contained sufficient amount of horizontal confined tracks to obtain representative track length distribution (**Figure 6.5; Table C4**). They yielded identical mean track length (MTL) of 12.7 ± 1.6 μm. For all AFT samples, D_{par} values range broadly from 1.76 to 3.73 μm (**Table C4**). The dispersed D_{par} indicated a diverse compositional spectrum of measured apatite in terms of their F/Cl ratios, a factor that affects AFT annealing kinetics (Burtner et al., 1994; Donelick et al., 1999). Four samples with a single age component show a positive correlation between single-grain AFT ages and the corresponding D_{par} values (**Figure 6.5**).

Apatite (U-Th-Sm)/He ages were measured for most samples (except 10JXLN04 due to unsatisfactory grain quality) (**Table C5**; **Table 6.2**). The AHe age of each sample was younger than or similar to its AFT age (**Table 6.2**). AHe ages of all samples presented a tight Eocene age cluster (45–33 Ma; **Figure 6.4b**), implying an Eocene cooling through the AHe closure temperature of ~70°C (Ehlers and Farley, 2003).

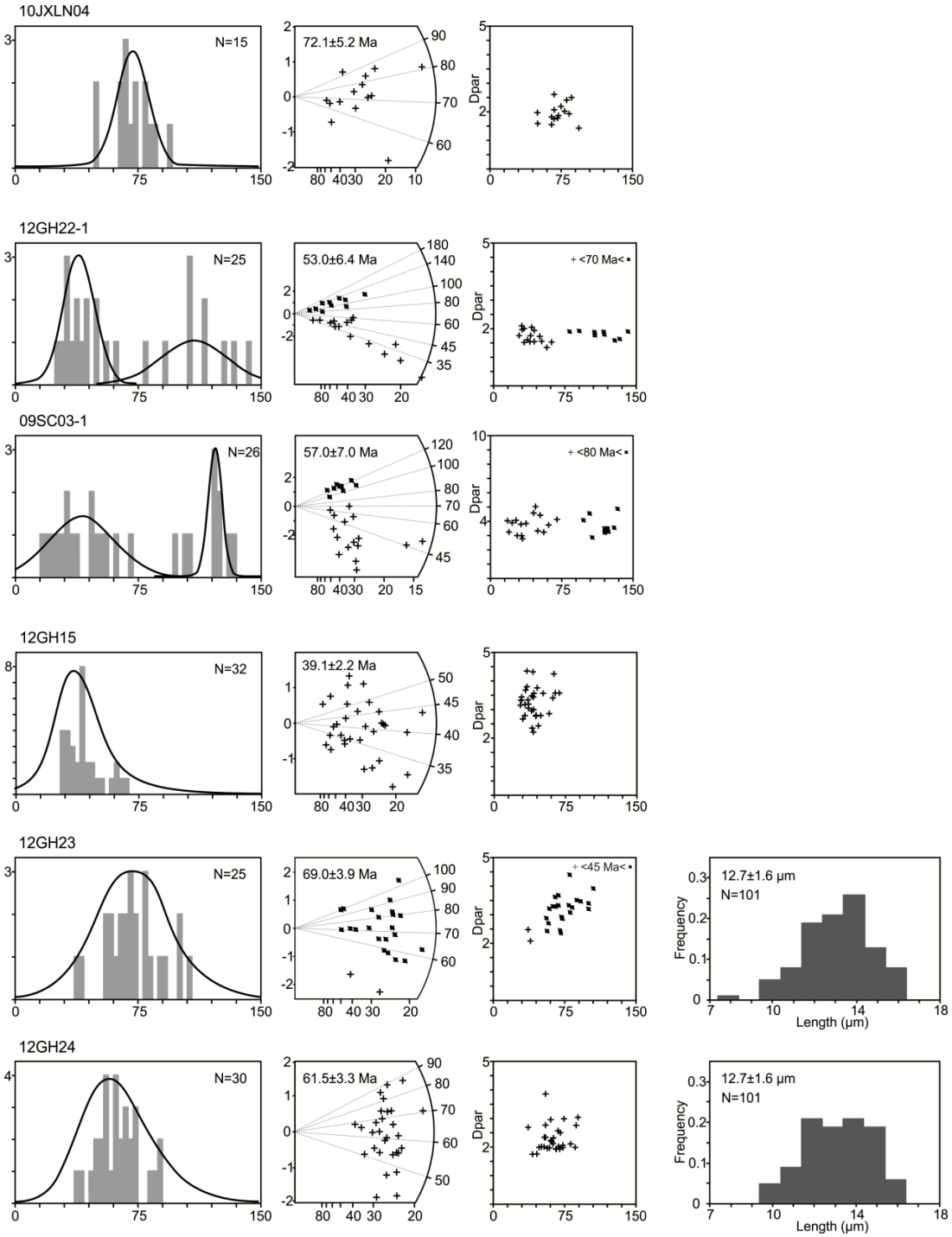

Figure 6.5 Apatite fission track single-grain age histograms, radial plots, AFT age vs. D_{par} plots and track lengths histogram.

Single-grain age histograms (y-axis: number of grains, x-axis: age in Ma). Radial plots (left-hand-axis: σ error, bottom axis: relative error in %, right-hand axis: age in Ma, top right are sample description and the total number of dated apatite grains, the black curve represents the age distribution of the identified age group, top left are apatite fission track central age ± 1σ error). D_{par} plots (y-axis: D_{par} values in μm, x-axis: age in Ma, top right are mean D_{par} value ± standard deviation). Fission track length distribution histogram (y-axis: frequency of tracks, x-axis: length in μm, top right are mean track length ± standard deviation and number of measured tracks).

6.3.5 VR data

VR value was measured one Lower Jurassic coal sample (12GH22-2). The measured maximum VR ranged from 1.690 % to 2.336 % and averaged at 1.883 % (**Figure 6.6; Table C6**), suggesting maximum temperatures of 180–200°C according to the EASY %R_o model (Sweeney and Burnham, 1990).

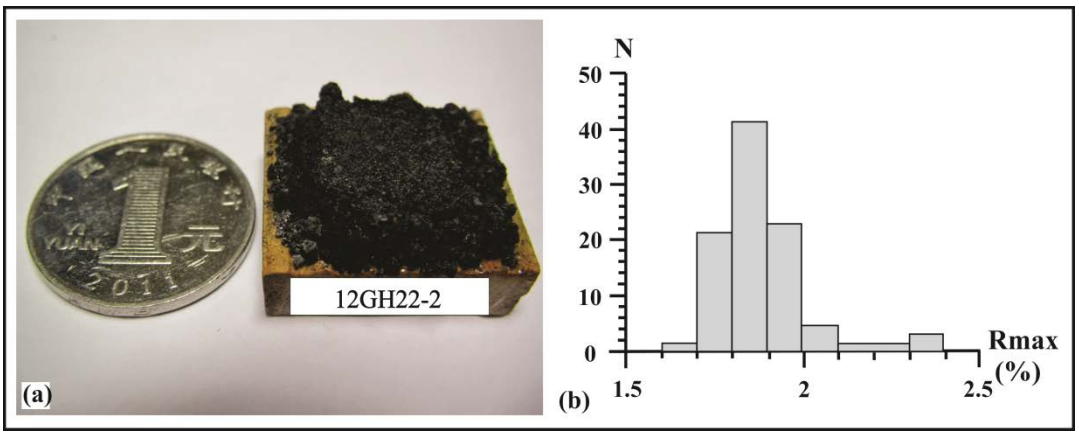

Figure 6.6 (a) Mount of coal sample 12GH22-2 and (b) the histogram of vitrinite reflectance data of the sample.

6.4 Discussion

6.4.1 Late Jurassic thermal resetting

Silurian granites could provide materials for Middle Devonian strata according to the detrital zircon U-Pb age distribution in the Shaoguan-Longnan region (Xu et al., 2005). This indicates that the Silurian granite (e.g. Fuxi granite, 12GH23) was exhumed to the surface soon after emplacement (**Figure 6.7**). That the Early Silurian Fuxi granite had exhumed to the surface by the Early Devonian is also supported by the observation that it is directly overlain by the Lower–Middle Devonian (D_{1-2}) strata (**Figure 6.8a**). The D_{1-2} strata was unconformably overlain by Lower Jurassic (J_1) strata (**Figure 6.8a**). This indicates that the Fuxi granite was exhumed to shallow depths by the Early Jurassic. This conclusion is in accordance with the exposure soon after emplacement. However, the thick strata from Devonian to Early Cretaceous

ruled out a long-term exposure of the Fuxi granite. A heating event after the Devonian exposure and before the pre-Early Jurassic exposure is a more realistic scenario (12GH23; **Figure 6.7**). K-feldspar $^{40}Ar/^{39}Ar$ and ZHe age of Fuxi granite (12GH23; **Figure 6.7**) imply that the granite was cooled to > 200°C at ca. 125 Ma. A heating event occurred between the Early Jurassic near-surface exposure and Early Cretaceous cooling (**Figure 6.7**). Similarly, the Lower Jurassic Keshubei granite was unconformably overlain by Upper Jurassic strata (**Figure 6.8b**) indicating that the intrusion had been exhumed during the Late Jurassic (2KGN38-1; **Figure 6.7**). In order to explain the data, a heating event is required before the Keshubei granite cooled thought the ZHe system closure temperature (**Figure 6.7**).

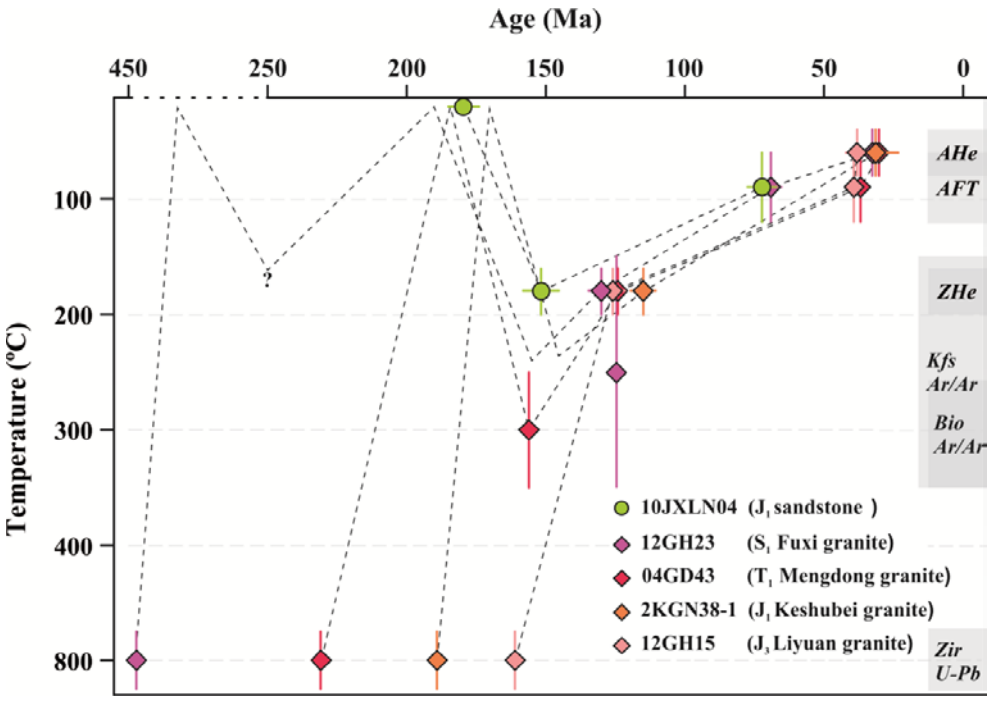

Figure 6.7 Time-temperature trajectories constructed with data generated in this study.
The trajectories of sedimentary samples start at the depositional ages at the assumed annual mean temperature of 20 ± 3°C, and those of granites start at the time defined by zircon U-Pb ages at 800 ± 100°C. All trajectories end at 0 Ma and 20 ± 3°C. The y-axis (temperature) of curves is determined by the characteristic closure temperature of each thermometer: 60 ± 20°C for apatite (U-Th-Sm)/He (AHe) (Wolf et al., 1998; Farley, 2000); 90 ± 30°C for apatite fission track (AFT) (Wagner and Van den Haute, 1992); 180 ± 20°C for zircon (U-Th-Sm)/He (ZHe) (Reiners et al., 2004; Guenthner et al., 2013); 240 ± 30°C for zircon fission track (ZFT) (Hurford, 1986; Brandon et al., 1998); 300 ± 50°C (Harrison et al., 1985) for biotite $^{40}Ar/^{39}Ar$ (Bio Ar/Ar) , and 150–350°C (Lovera et al., 1989) for K-feldspar $^{40}Ar/^{39}Ar$ (Kfs Ar/Ar), respectively. The x-axis (time) is controlled by measured AHe, AFT, ZHe, ZFT, BioAr, and KfsAr ages. Data-point error bars are displayed at 2σ confidence interval.

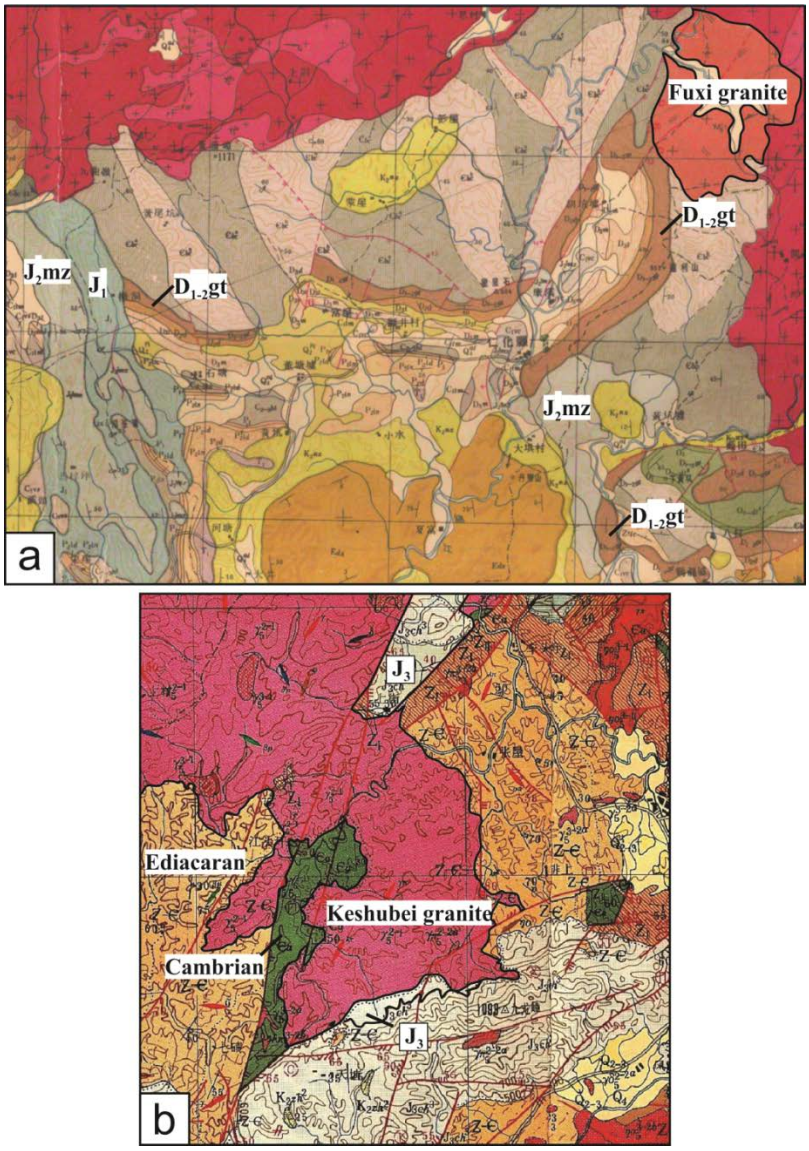

Figure 6.8 Geological maps showing (a) the Fuxi granite and (b) the Keshubei granite and surrounding strata, from JXBGMR (1969, 1973).

The exhumation of the Fuxi and Keshubei granites demonstrates that Jurassic exhumation occurred in both the west and east of the Shaoguan-Longnan region (**Figure 6.1**). Middle Jurassic strata is only restricted to very few exposures (GDBGMR, 1965). This may also imply an exhumation-dominant environment. The Mengdong granite should have undergone a similar exhumation process in the Jurassic, although the direct contact between the Lower Triassic Mengdong granite and Jurassic strata is missing (JXBGMR, 1969). If the Mengdong granite did exhume to a shallow position in the Jurassic (04GD43; **Figure 6.7**), the Late Jurassic biotite

$^{40}Ar/^{39}Ar$ ages (156 Ma) of sample 04GD43 was generated by a >300°C reheating event. In addition, the $^{40}Ar/^{39}Ar$ age of Mengdong granite is much younger (by 75 Myr) than the U-Pb age. It is very unlikely that this age relationship was produced through monotonic magmatic cooling because plutons usually cooled rapidly. The interpreted resetting of the BtAr, KfsAr and ZHe systems in granitic samples is consistent with the Late Jurassic resetting of ZHe ages in the Lower Jurassic sandstones. A Late Jurassic thermal resetting is thus proposed for the study area.

6.4.2 Late Cretaceous–Eocene cooling

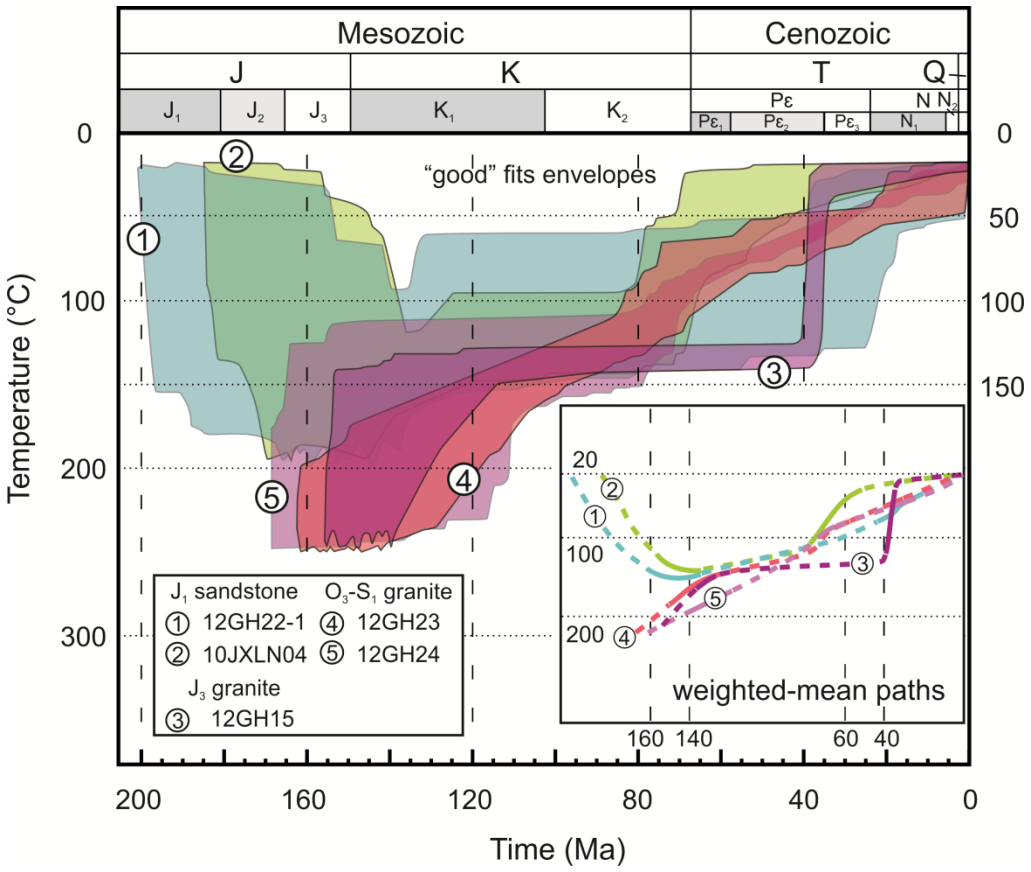

Figure 6.9 (a) Modelled good or acceptable fits shown as envelopes, and (b) weighted-mean paths of representative samples in this study.

To get a higher resolution low-temperature thermal history (<250°C) after the

Late Jurassic thermal resetting, five samples with multi-thermochronometry data were inversely-modelled by HeFTy (v1.81) software, initial conditions of the modelling give in caption of **Figure 6.9** (Ketcham, 2005). Early Jurassic sandstones, once deposited, experienced continuous heating during a thermal maximum during the Late Jurassic to almost 200°C (**Figure 6.9**). The VR data from the Lower Jurassic coal sample (12GH22-2) suggests a maximum post-depositional temperature of 180–200°C, supporting the inverse modelling result. It is inferred that the Lower Jurassic strata did not undergo any higher temperature re-heating after the Late Jurassic thermal maximum. This speculation is tested by the modelling results. Lower Jurassic sandstones cooled to <150°C during the Early Cretaceous and quiescent thermal conditions persisted until the Late Cretaceous–Paleogene when a stage of rapid cooling (7.5°C/Myr) occurred. Granites display a similar cooling pattern during the Cretaceous–Cenozoic, although some granites are prominently subjected to a Eocene cooling (i.e. 12GH15; **Figure 6.9**). All samples cooled to <50°C by the Late Eocene (**Figure 6.9**).

6.4.3 Tectonic drivers of the thermal history

The cooling of the Silurian granites after intrusion to surface conditions is very likely caused by exhumation during the Early Paleozoic orogenic exhumation (Li et al., 2010; Section 2.2). Early Mesozoic orogenic exhumation (**Section 2.3.1**) could explain the Pre-Early Jurassic exhumation of older plutons (e.g. Fuxi granite). The Late Jurassic thermal resetting temporally coincides with extensive magmatism during the Late Jurassic when magma upwelled after the delamination of the subducting Paleo-Pacific flat-slab (Li and Li, 2007; Section 2.3.1). Almost static thermal conditions in the study area during most of the Cretaceous fits with a long-term lithospheric rebounding in the SE SCB (Li and Li, 2007). The Late Cretaceous–Paleocene and Eocene rapid cooling events are likely related to episodic continental rifting (Zhou et al., 1995; Shi et al., 2011), as evidenced by Late Cretaceous (ca. 67 Ma; Zhao et al., 1991; ca. 96 Ma; Shu et al., 2004) and Eocene basalts (JXBGMR, 1970) deposited in NE-striking Nanxiong basin (**Figure 6.1**). Since the Late Cretaceous, the granitic plutons could have been reasonably rapidly exhumed as a rift

shoulder while the adjacent (Nanxiong) rift basin was subjected to subsidence and rift-related volcanism. Modelling result suggests post-Jurassic erosion of up to 4 km, assuming a geothermal gradient of 30°C/km and surface temperature of 20°C. The erosion may have led to the extensive exposure of Mesozoic magmatic rocks in SE SCB.

6.5 Conclusions

Our new thermochronological data provide novel insight into the tectonothermal evolution of Shaoguan-Longnan area. Late Jurassic biotite $^{40}Ar/^{39}Ar$ ages obtained from Upper Triassic granite demonstrate the occurrence of a thermal peak in the Late Jurassic. This peak is related to the prior regional emplacement of Upper Jurassic intrusions generated in an extensional setting, consistent with the predicted effects arising from delamination of a flat-subducted Paleo-Pacific slab. ZFT and ZHe data record protracted cooling through a 270–160°C temperature window during the Cretaceous. Late Mesozoic cooling is in accord with the prediction of regional uplift and exhumation arising from foundering of the paleo-Pacific flat-slab and consequent lithospheric rebound. The rapid cooling in Late Cretaceous and Eocene is consistent with Cenozoic rifting across the SE SCB.

Chapter 7 Thermochronological record of tectonic events in Hunan province

7.1 Geological setting

Hunan province is located in the northwest of the SE SCB (**Figure 7.1a**). NE-striking faults are distributed across the whole area of Hunan (**Figure 7.1b**). In contrast to areas to the southeast (e.g. Shaoguan-Longnan, Daxi and Meizhou), Jurassic intrusions are sporadically distributed and evidence of Cretaceous magmatism is rare in Hunan. Instead, numerous Triassic granitic intrusive bodies have been reported (Sun, 2006; Mao et al., 2013a; Qiu et al., 2014). There are two major mountain ranges in Hunan – the Wuling Mountains in the north and the Xuefeng Mountains in the central part of Hunan (**Figure 7.2**), separated by the Anhua-Xupu fault (**Figure 7.2**).

The depositional environment in the Hengyang-Zixing-Daoxian region (to the south of Xuefeng Mountains), before the Middle Jurassic was similar to that of the northern Guangdong region (**Chapters 5 and 6**). Ediacaran to Lower Silurian slates are unconformably overlain by Middle Devonian to Lower Triassic sandstone, shale and limestone (HNBGMR, 1974). Upper Triassic and Lower Jurassic sandstones formed in a swamp environment, along with black shale and coal seams that unconformably overlie Lower Triassic strata (HNBGMR, 1984; Yan et al., 2011). In contrast to the Shaoguan-Longnan and Daxi regions, the Middle–Upper Jurassic clastic strata in southern Hunan lacked volcanic input and were conformably deposited upon Lower Jurassic strata (HNBGMR, 1970, 1974). Lower Cretaceous mudstone marlstone and fine sandstone uncomfortably overlay pre-Cretaceous strata with a coarse clastic layer at the base (HNBGMR, 1984). Eocene and Quaternary conglomerate and glacial boulder clays were deposited over an unconformity (HNBGMR, 1974).

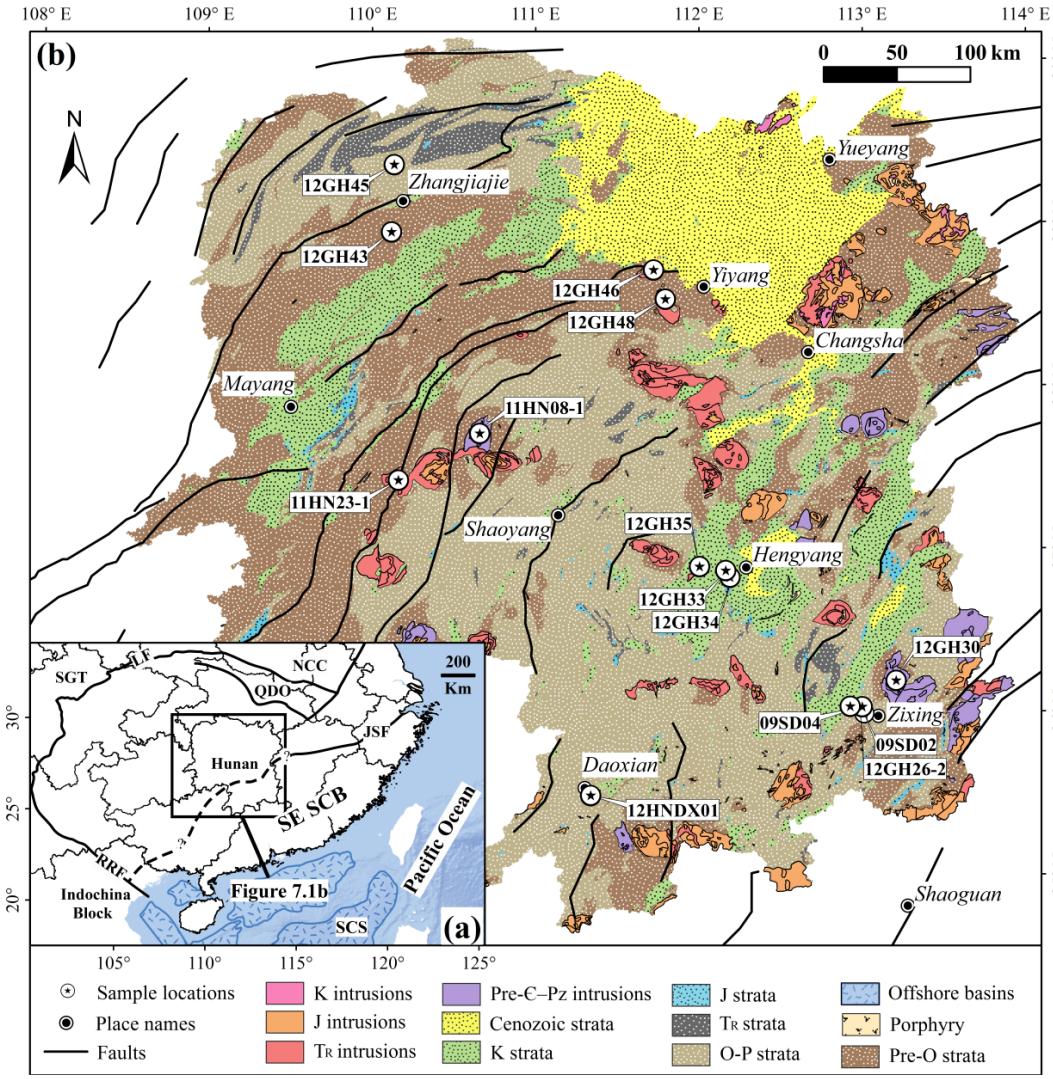

Figure 7.1 (a) Tectonic map of SCB-West Pacific region showing the extent of Figure 7.1b, and (b) simplified geological map of Hunan province showing sample locations, compiled from 1:20,0000 geological maps.

Divisions of geologic time are after (Walker et al., 2012) and symbols of geologic periods are after (GNCUSGS, 2010). The black in **Figure 7.1a** represents the extent of **Figure 7.1b.** LF—Longmenshan Fault, JSF—Jiang-Shao Fault, NCC—North China Craton, QDO—Qinling-Dabie Orogen, RRF—Red River Fault, SCS—South China Sea, SGT—Songpan-Ganzi Terrane.

A large Cenozoic sedimentary basin exists in northeast Hunan (**Figure 7.1b;** Yiyang basin in **Figure 7.2**), where Eocene shale and siltstone were deposited directly on Precambrian and Paleozoic strata (HNBGMR, 1975, 1976). Two large Cretaceous clastic basins distribute in the northeast direction, with the Mayang basin in the northwest and the Hengyang basin in the southeast (**Figure 7.1b; Figure 7.2**).

Ediacaran and Lower Paleozoic strata are widely exposed in northern Hunan whereas Upper Paleozoic (Ordovician–Permian) strata now cover large areas of central and southern Hunan (**Figure 7.1b**).

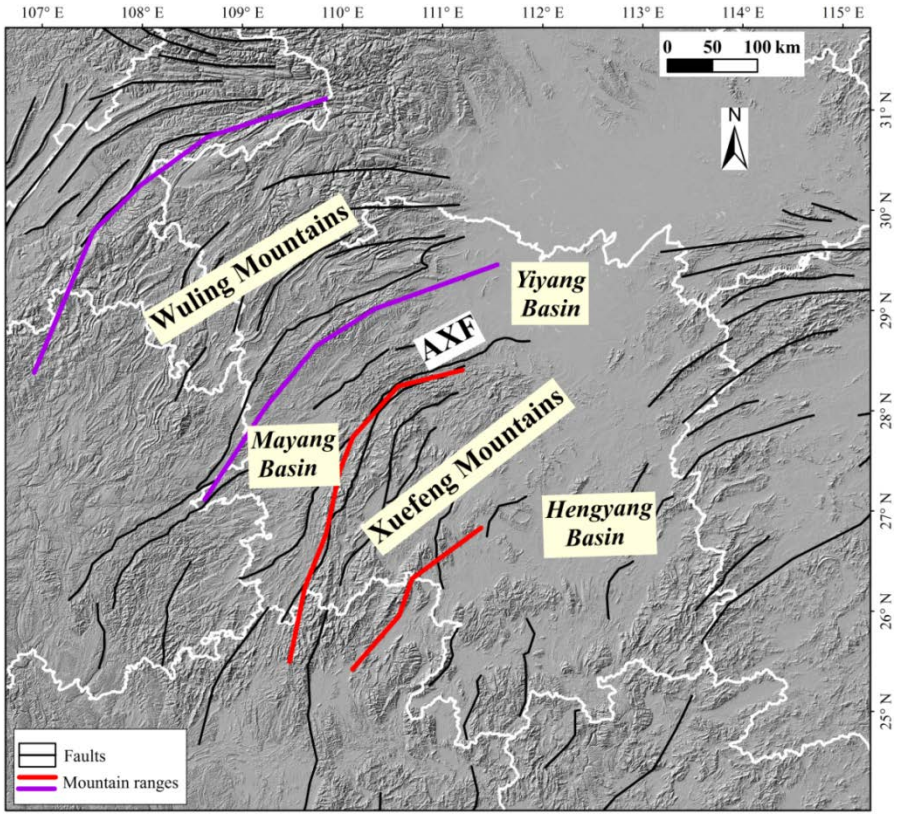

Figure 7.2 The digital elevation map (NASA EODIS database) of the Hunan province showing NE-striking mountain ranges. AXF=Anhua-Xupu fault.

7.2 Sampling

Seven sedimentary and six granitic samples were collected from southeast to northwest Hunan (**Table 7.1; Figure 7.1**). In southern Hunan, Upper Triassic–Middle Jurassic sandstones (12HNDX01, 09SD04 and 09SD02) were collected in order to investigate the thermal history of the post-Middle Triassic orogeny (**Figure 7.1**). One granodiorite sample (12GH30; Penggongmiao granodiorite) of proposed Early Paleozoic age (HNBGMR, 1970) was collected for complimentary geo-/thermo-chronological investigations (**Figure 7.1**). One Upper Triassic (12GH26-2) coal was

collected for VR measurement, to reveal the maximum paleo-temperature since the deposition. Further north in Hengyang, one Upper Jurassic sandstone sample, one Lower Jurassic (12GH34) coal sample and one granitic sample from the Jilongjie body were collected (**Table 7.1; Figure 7.1**). The Jilongjie granite was considered to emplace either in Triassic (Sun, 2006) or Jurassic (HNBGMR, 1974) without reliable magmatic ages being reported. Four pre-Jurassic granitic rocks were collected from the Xuefeng Mountains (11HN08-1, 11HN23-1, 12GH46 and 12GH48). One Middle Devonian sandstone and one Ediacaran sandstone were collected from the Wuling Mountains for thermal history reconstruction and comparison with samples from the Xuefeng Mountains, Hengyang basin and southern Hunan. Zircon U-Pb dating was applied on all six granitic samples to determine magmatic ages.

Table 7.1 Hunan sample information.

Sample No.	Litholotgy	Stratigraphic/ Formation Age	Latitude N (°)[a]	Longitude E (°)[a]	Location
12HNDX01	sandstone	J_2	25.480	111.637	Daoxian
09SD04	sandstone	J_1	26.022	113.285	
12GH26-2	coal	T_3	26.020	113.300	Zixing
09SD02	sandstone	T_3	26.019	113.299	
12GH30	granodiorite	Early Paleozoic?	26.182	113.445	*Penggongmiao*[b]
12GH33	sandstone	J_3	26.824	112.512	Hengyang
12GH34	coal	J_1	26.816	112.503	
12GH35	granite	Early Paleozoic?	26.843	112.236	*Jilongjie*
12GH45	sandstone	D_2	29.348	110.434	Zhangjiajie
12GH43	sandstone	Z	28.935	110.417	
11HN08-1	granite	Early Paleozoic?	27.712	110.949	*Baimashan*
11HN23-1	granite	Triassic?	27.460	110.459	*Baimashan*
12GH46	granodiorite	Early Paleozoic?	28.707	111.996	*Yanbaqiao*
12GH48	granite	Early Paleozoic?	28.523	112.083	*Taojiang*

[a]Coordinate system: WGS84.
[b]Names of granitic rocks in Chinese literatures are shown in *Italic*.

7.3 Results and interpretation

7.3.1 U-Pb ages

Sample 12GH30 showed concentric oscillatory zoning of magmatic origin

(**Figure 7.3a**). Fifteen spots analysed for this sample yielded a concordia age of 442.9 ± 2.8 Ma (MSWD=3.1; P=0.079, 95% conf.), and an indistinguishable weighted mean $^{206}Pb/^{238}U$ age of 443.4 ± 2.1 Ma (MSWD=1.4; P=0.13; 2σ; **Figure 7.3a; Table D1**). The new zircon U-Pb ages provide an accurate Early Silurian magmatic age for the Penggongmiao granodiorite.

Zircons from the 12GH35 were euhedral with concentric oscillatory zoning visible in CL images, implying a magmatic-origin (**Figure 7.3b**). A total of eighteen spots were analysed, yielding Th/U ratios of 0.18–0.80, and U and Th concentrations from 680 to 2215 pm and 320 to 1331 ppm, respectively (**Table D1**). The analyses form a single, well-defined concordia age of 427.4 ± 3.4 Ma (MSWD=0.1; P=0.75; 95% conf.), and an identical weighted mean $^{206}Pb/^{238}U$ age of 427.5 ± 2.6 Ma (MSWD=1.6; P=0.068; 2σ; **Figure 7.3b**). The results suggest a Late Silurian crystallization age for the Jilongjie granite, which is different from the previously proposed Mesozoic ages (HNBGMR, 1974; Sun, 2006).

Zircons from sample 12GH46 were euhedral (**Figure 7.3c**) and were relatively low in U content (mostly 222–700 ppm; **Table D1**). The magmatic-origin of analysed zircons was indicated by well-developed concentric oscillatory zoning (**Figure 7.3d**). Seventeen analysed spots gave a weighted mean $^{206}Pb/^{238}U$ age of 217.4 ± 1.1 Ma (MSWD=1.2; P=0.23; 2σ; **Figure 7.3c**). Our new zircon U-Pb ages provide a reliable Middle Triassic magmatic age for the Yanbaqiao granodiorite, which is much younger than the previously suggested Early Paleozoic age (HNBGMR, 1976; Sun, 2006).

Zircons from sample 12GH48 were euhedral to sub-euhedral. Concentric oscillatory zoning of magmatic origin was observed in the CL images of most crystals (**Figure 7.3d**). A total of twenty spots were analysed on different magmatic zircon grains, yielding Th/U ratios of 0.15–0.53 (**Table D1**). The analyses form a single, concordant group yielding a concordia age of 219.9 ± 1.7 Ma (MSWD=3.7; P=0.055; 95% conf.), and an indistinguishable weighted mean $^{206}Pb/^{238}U$ age of 220.1 ± 1.3 Ma (MSWD=1.3; P=0.18; 2σ; **Figure 7.3d**). The results suggest a Middle Triassic crystallization age for the Taojiang granite, much younger than the previously proposed Early Paleozoic age (HNBGMR, 1976; Sun, 2006).

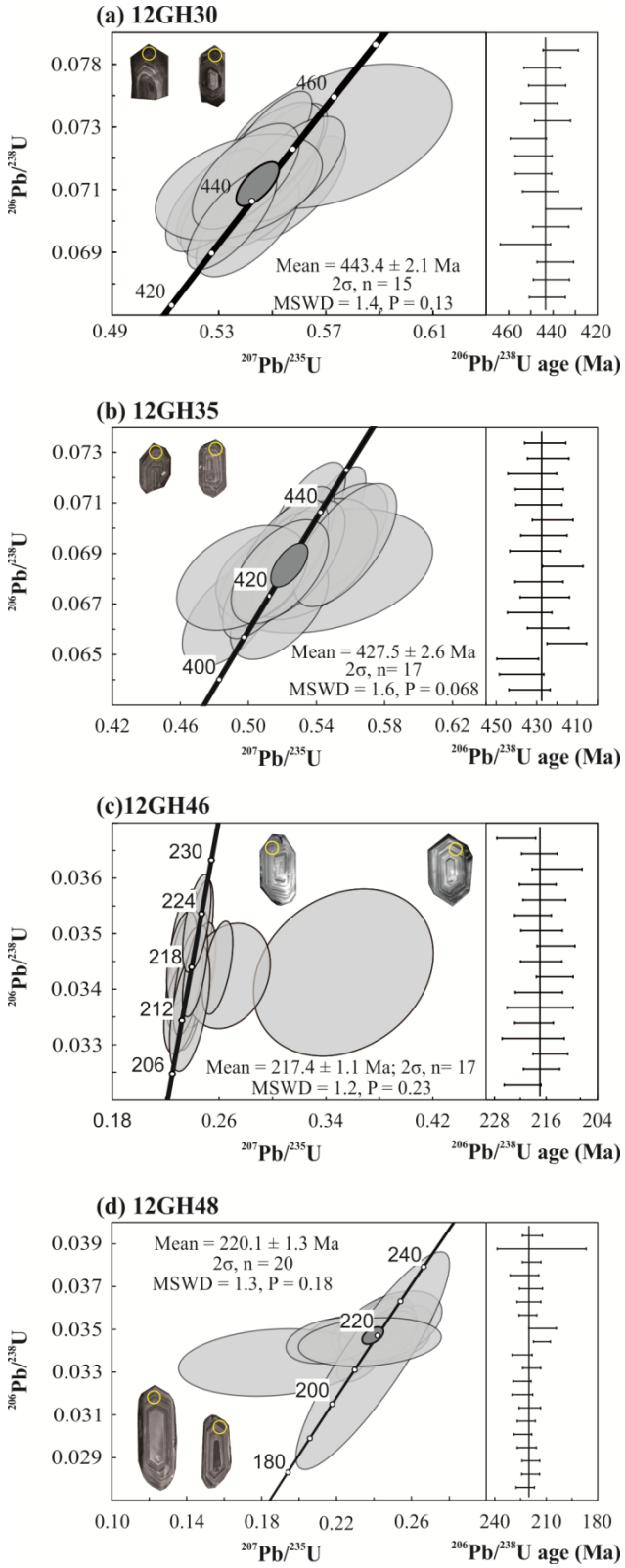

Figure 7.3 Zircon U-Pb concordia diagrams and weighted mean plots.

Analysed spots of ~30 μm diameter are shown as yellow circles on the CL images. Error ellipses in the concordia diagrams and dashes in the weighted-mean plots are displayed at the 2σ confidence interval. MSWD=mean square of weighted deviates. n=number of analysed spots.

7.3.2 $^{40}Ar/^{39}Ar$ ages

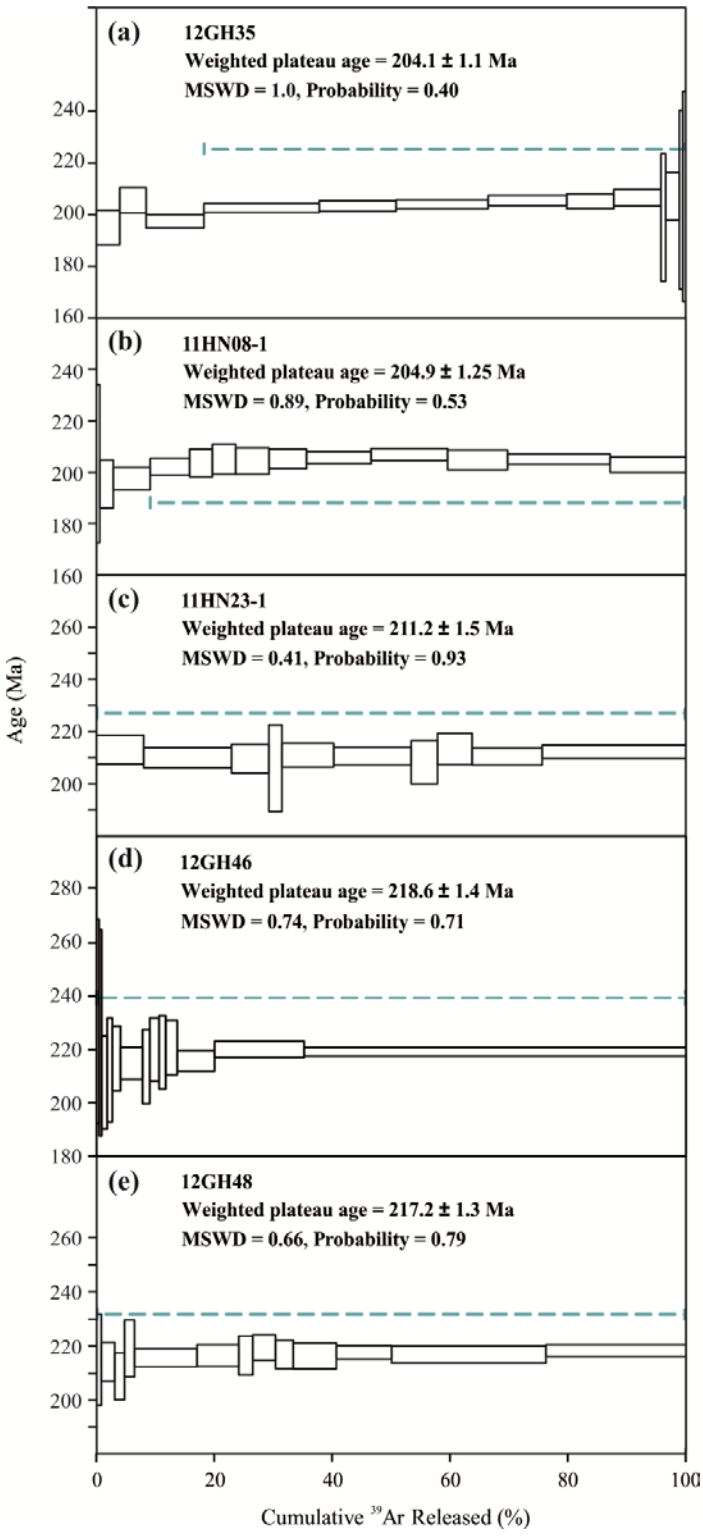

Figure 7.4 Biotite $^{40}Ar/^{39}Ar$ age spectra showing weighted plateau ages of five granitic samples from Hunan province.

MSWD=mean square of weighted deviates. Step-heating data bars are displayed at the 2σ confidence interval.

Single-grains of biotite from five granitic samples were step-heated by laser to get the timing of closure of the BtAr system. The five samples were of Late Silurian (12H35 and 11HN08-1) or Middle Triassic (11HN23-1, 12GH46 and 12GH48) magmatic age (**Section 7.3.1**). Ten to thirteen concordant steps were successfully conducted for each sample (**Table D2; Figure 7.4**). All five samples gave a plateau ages forming a narrow Middle Triassic range from 218.6 to 214.1 Ma (**Figure 7.4**). The good reproducibility of BtAr age constrain a Middle Triassic closure of the BtAr system (300 ± 50 ℃; Harrison et al., 1985).

7.3.3 ZFT ages

Table 7.2 Compilation of all new data from Hunan province.

Sample #.	Age ± 2σ (Ma)						VR (%)
	U/Pb	$^{40}Ar/^{39}Ar$	ZFT	ZHe	AFT	AHe	
12HNDX01	J2			253 ± 19		53.3 ± 9.4	
09SD04	J1			245 ± 27			
12GH26-2	T3						1.329 ± 0.073
09SD02	T3			220 ± 24			
12GH33	J3		126.6 ± 12.8	86.4 ± 5.7			
12GH34	J1						3.897± 0.171
12GH43	Z		341.0 ± 54.4	176 ± 15			
12GH45	D2		184.0 ± 23.6				
12GH30	443.4 ± 2.1			132 ± 11	51.6 ± 5.4	44.3 ± 5.8	
12GH35	427.5 ± 2.6	204.1 ± 1.1		44.9 ± 3.9	30.2 ± 4.2		
11HN08-1	~410[a]	204.9 ± 1.2		102.8 ± 7.7	51.6 ± 5.6		
11HN23-1	~217[a]	211.2 ± 1.5		149 ± 11	50.4 ± 5.8		
12GH46	217.4 ± 1.1	218.6 ± 1.4		122.8 ± 9.5	89.0 ± 12		
12GH48	220.1 ± 1.3	217.2 ± 1.3		95.1 ± 7.0	93.8 ± 10		

[a]Personal communication with W.X. Li.

Data supporting **Table 7.2** are available in Appendices **Tables D1–6**.

Twenty-five single-grain ZFT ages were measured on each of the three samples; 12GH43, 12GH45 and 12GH33 (**Table D3**). All three sample passed the chi-square

test with a >99.5% probability (**Table D3**) and, therefore, were considered to represent one age population. A Devonian–Carboniferous ZFT central age of 341.0 ± 54.4 Ma was given by the Ediacaran sandstone (12GH43) (**Table 7.2**). A Late Triassic–Early Jurassic central age of 184.0 ± 23.6 Ma was yielded by the Middle Devonian sandstone (12GH45), and an Early Cretaceous age (126.6 ± 12.8.8 Ma) was obtained on the Late Jurassic sandstone (12GH33) (**Table 7.2**). The ZFT ages of all three samples are clearly younger than the corresponding depositional ages (by >20 Ma) suggesting a post-depositional thermal resetting.

7.3.4 ZHe ages

ZHe ages were measured on eleven samples (**Table 7.2; Table D4**). The measured mean ZHe ages covered a wide range from 253 ± 19 Ma to 44.9 ± 3.9 Ma (**Table 7.2**). Three Lower Triassic–Middle Jurassic sandstones from southern Hunan yielded un-reset ZHe ages that were older (12HNDX01 and 09SD04) than, or (09SD02) identical to, the stratigraphic ages, whereas a Lower Silurian granodiorite (12GH30) from the south give Early Cretaceous mean ZHe age of 132 ± 11 Ma (**Table 7.2**). The Upper Jurassic sandstone (12GH33) from central Hunan had a reset Late Cretaceous ZHe age (ca. 86 Ma) whereas the Upper Silurian (11HN08-1) and Middle Triassic (11HN23-1, 12GH46 and 12GH48) intrusions from central Hunan gave Late Jurassic to mid-Cretaceous (149–95 Ma) mean ZHe ages (**Table 7.2**). The Eocene ZHe age from the Upper Silurian granite (12GH35) did not fit with the Late Jurassic to mid-Cretaceous age cluster (**Table 7.2**). In northern Hunan, the Ediacaran sandstone (12GH43) yielded a reset Jurassic ZHe age (176 ± 15 Ma; **Table 7.2**), much older than ages obtained from central and southern Hunan.

7.3.5 AFT and AHe data

Three apatite samples (12GH30, 11HN08-1 and 11HN23-1) contained enough tracks for length measurement (**Figure 7.5**). The mean track lengths of the three samples are relatively short (12.97 ± 1.60 μm, 12.72 ± 1.65 μm and 12.38 ± 1.45 μm), indicating substantial annealing of initial tracks (~16 μm).

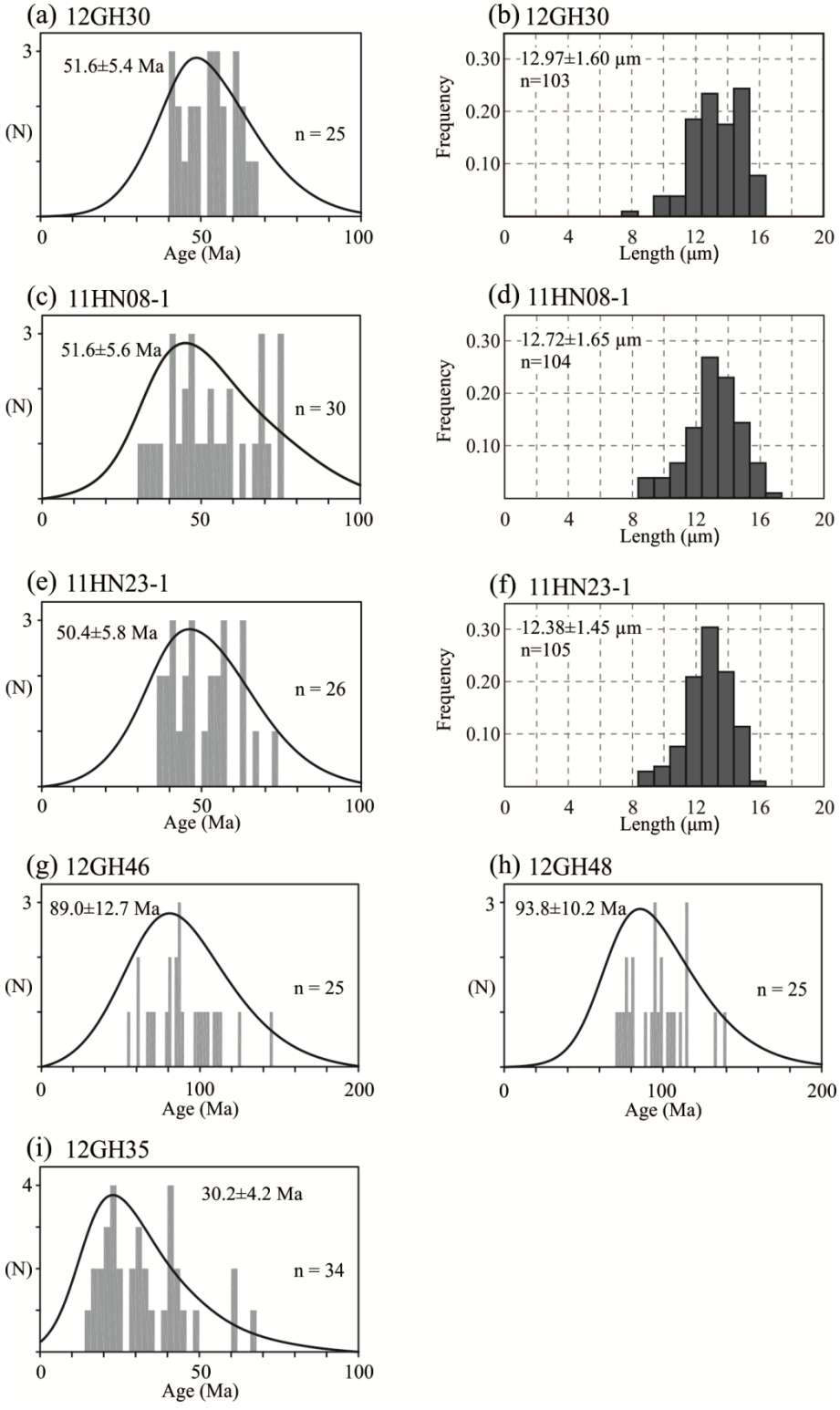

Figure 7.5 Apatite fission track single-grain age and track length distribution histograms.
Single-grain age histograms: y-axis shows number of grains; x-axis shows age in Ma; black curve shows the linear age spectrum with AFT age ± 2σ error labelled next to it; middle right is the number of counted grains. Fission track length distribution histograms (b and h): y-axis shows frequency of tracks; x-axis shows length in μm; top left are mean track length ± standard deviation and number of measured tracks.

AFT ages were measured on six samples that all passed the chi-square test (**Table D3; Figure 7.5**). Three groups of ages could be identified from the mean AFT ages of six samples; Late Cretaceous, Early Eocene and Early Oligocene (**Table 7.2**). The Late Cretaceous age group comprised AFT ages (89 ± 12 and 94 ± 10 Ma; **Table 7.2**) of two Middle Triassic intrusions (12GH46 and 12GH48, respectively). The Early Eocene age group consisted of mean AFT ages of a Lower Silurian granodiorite (12GH30; 52 ± 5 Ma), an Upper Silurian granite (11HN08-1; 52 ± 6 Ma) and a Middle Triassic granite (11HN23-1; 50 ± 6 Ma; **Table 7.2**). The Upper Silurian granite (12GH35) had ZHe ages much younger than other samples and also yielded a younger mean AFT age of 30 ± 4 Ma. The Upper Jurassic sandstone (12HNDX01) and Lower Silurian granodiorite (12GH30) gave Paleocene–Eocene mean AHe ages (59.3 ± 6.8 Ma and 48.9 ± 5.6, respectively, **Table D5**). Both AFT and AHe ages from all measured samples are interpreted to be reset ages.

7.3.6 VR data

For the Upper Triassic coal (12GH26-2), reflectance of forty vitrinite macerals were measured and the values ranged from 1.182% to 1.484% (**Table D6**). The mean value and its standard deviation were 1.329% and 0.073%. The mean VR value of 1.329% ± 0.073% was used for forward modelling of the maximum post-depositional temperature using the Easy%R_o model (Sweeney and Burnham, 1990) and HeFTy modelling program (Ketcham, 2005). The maximum post-depositional temperature was constrained to 160 ± 5°C.

Sixty VR measurements of Lower Jurassic coal (12GH34) ranged from 3.654% to 4.355%, with a mean value of 3.897% and a standard deviation of 0.171% (**Table D6**). The mean VR value was used for forward modelling and the modelled maximum post-depositional temperature of 12GH34 was 260 ± 10°C.

7.3.7 Modelling of thermal history

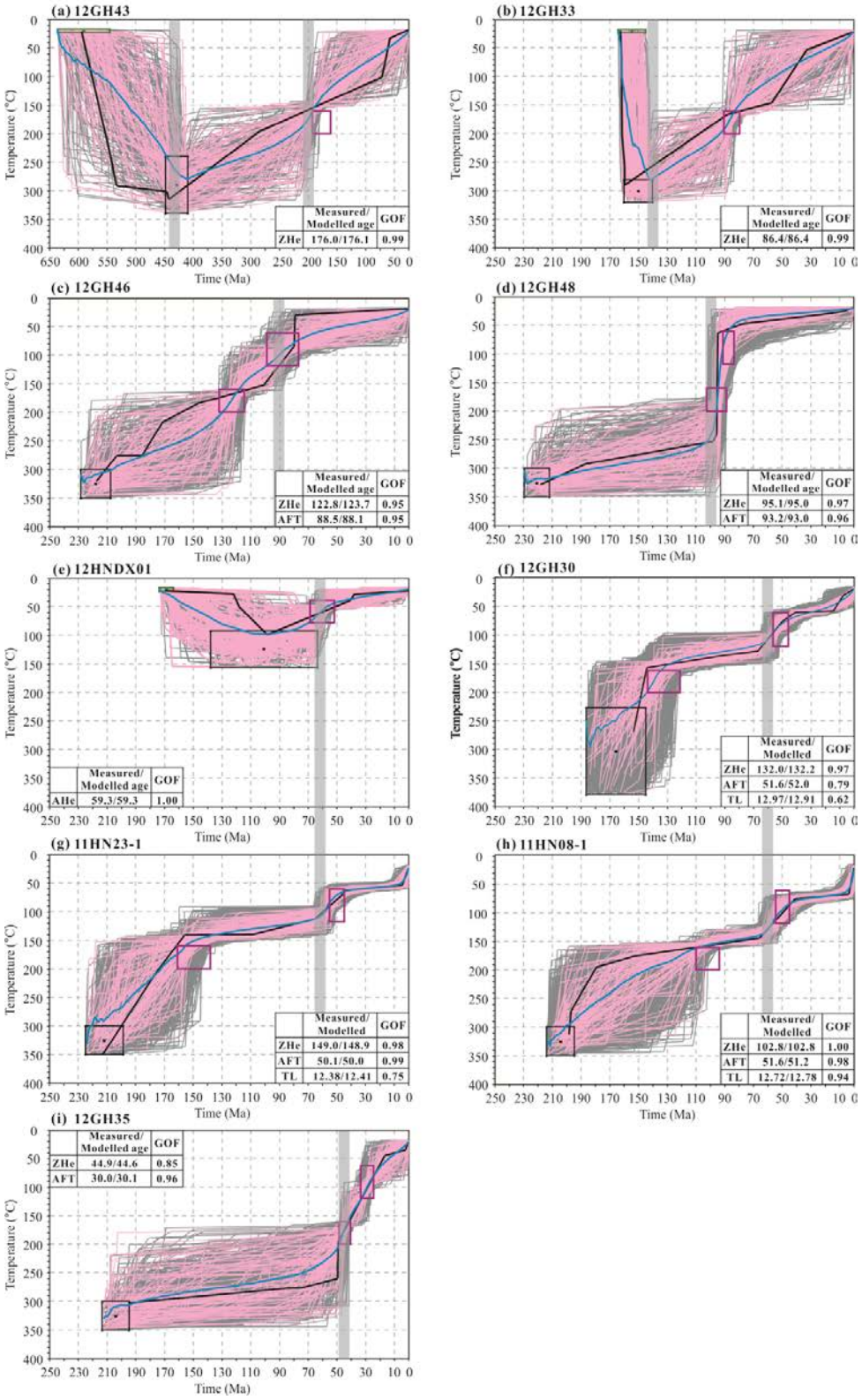

Figure 7.6 Modelled good and acceptable fits of representative samples from Hunan province. Green and black boxes represent the modelling starting points for sedimentary and granitic samples. Input data included the AFT, ZHe, and AHe ages, shown as purple boxes. Good fits were shown as pink curves and acceptable fits were shown as grey curves.

The Ediacaran sandstone from northern Hunan (12GH43) experienced heating to ~300°C at ca. 420 Ma and cooled through ~150°C at ca. 200 Ma (**Figure 7.6a**). The Upper Jurassic sandstone in central Hunan experienced similar post-depositional heating to ~300°C in the Early Cretaceous (ca. 140 Ma) and cooled through ~150°C at ca. 90 Ma (**Figure 7.6b**). Exhumation at ca. 90 Ma is also revealed by two intrusions from northern Hunan (**Figure 7.6 c** and **d**). The Middle Jurassic sandstone (12HNDX01) in southern Hunan sustained low post-depositional heating no higher than 150°C (**Figure 7.6e**). This sample cooled to below 100°C by ca. 60 Ma (**Figure 7.6e**). The ca. 60 Ma cooling is also shown by samples 12GH30, 11HN23-1 and 11HN08-1 after a 150–100°C thermal plateau began in the Early Cretaceous (12GH30 and 11HN23-1 at 140 Ma) and by sample 11HN08-1 at 110 Ma (**Figure 7.6 f–g**). Sample 12GH35 shows episodic Cenozoic cooling at ca. 50 Ma and ca. 30 Ma (**Figure 7.6i**).

7.4 Discussion

7.4.1 Late Triassic orogenic uplift in northern Hunan

Early Jurassic ZHe ages (ca. 176 Ma; **Table 7.2**) from the Ediacaran sandstone (12GH43) in Northern Hunan (**Figure 7.1**) result from Late Triassic cooling from ~300°C to 150°C (**Figure 7.6a**). The sample is located within Wuling Mountains (**Figure 7.2**), away from Paleozoic and Mesozoic magmatic zones (>180 km; **Figure 7.1**; **Figure 7.7**) so the Late Triassic cooling is unlikely magmatic-related. About 180 km to the southeast, Late Triassic (220–210 Ma) granitic intrusions (e.g. samples 12GH46, 12GH48, 11HN23-1; **Figure 7.7**) represent the syn-orogenic magmatism while the front of a flat-subducted oceanic slab was approaching (Li and Li, 2007). In addition to the syn-orogenic magmatism, the ongoing orogeny also led to orogenic thrusting and uplift of the overriding lithosphere (Li and Li, 2007). SE-striking thrusts parallel to the paleo-subduction trench (present Taiwan-Japan zone) are well developed in Hunan from the southeast to the northwest (**Figure 7.1** and Figure 2 in Li and Li (2007)). The Late Triassic uplift is reflected in synchronous cooling observed in sample 12GH43 (***a*** in **Figure 7.8**). Similarly, the ca. 184 Ma ZFT age of

the Devonian sandstone (12GH45) further north is also related with cooling due to the Late Triassic orgenic uplift. The absence of post-Late Triassic magmatism in northern Hunan prevents the orogenic uplift cooling from being obscured by younger magmatic heating. Whereas in southeastern areas, e.g. areas close to Shaoguan-Longnan, Daxi and Meizhou, the cooling signal of the Triassic orogenic uplift was very likely lost due to extensive Jurassic–Cretaceous magmatic overprint.

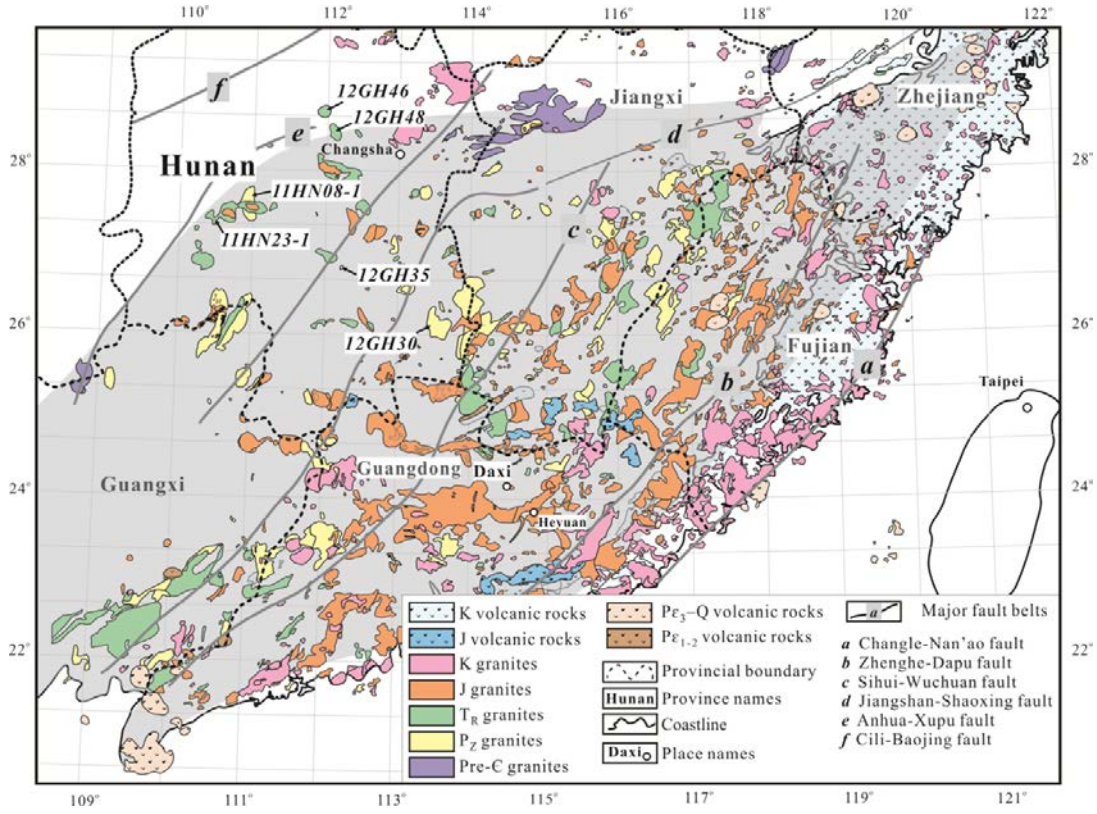

Figure 7.7 Distribution of magmatic rocks in Hunan and nearby regions highlighting the regional extent of the Early Paleozoic Wuyi-Yunkai orogeny (grey shaded), modified from Sun (2006) and Li et al. (2010).

Late Triassic thrusts in southern Hunan result from a subduction-induced orogeny (Li and Li, 2007). Syn-orogenic Upper Triassic–Lower Jurassic sandstones from Zixing (09SD02 and 09SD04) and the Middle Jurassic sandstone from Daoxian (11HNDX01) yielded un-reset ZHe ages (**Table 7.2**), indicating that the post depositional temperature did not exceed the zircon PRZ (200–160°C). The low

temperature setting in southern Hunan is supported by the lack of thick strata where overburden thickness did not lead to increased temperatures. For instance, the Late Triassic–Early Jurassic strata in Zixing is no thicker than 1.5 km thickness, upon which Middle Jurassic strata conformably deposited (HNBGMR, 1970).

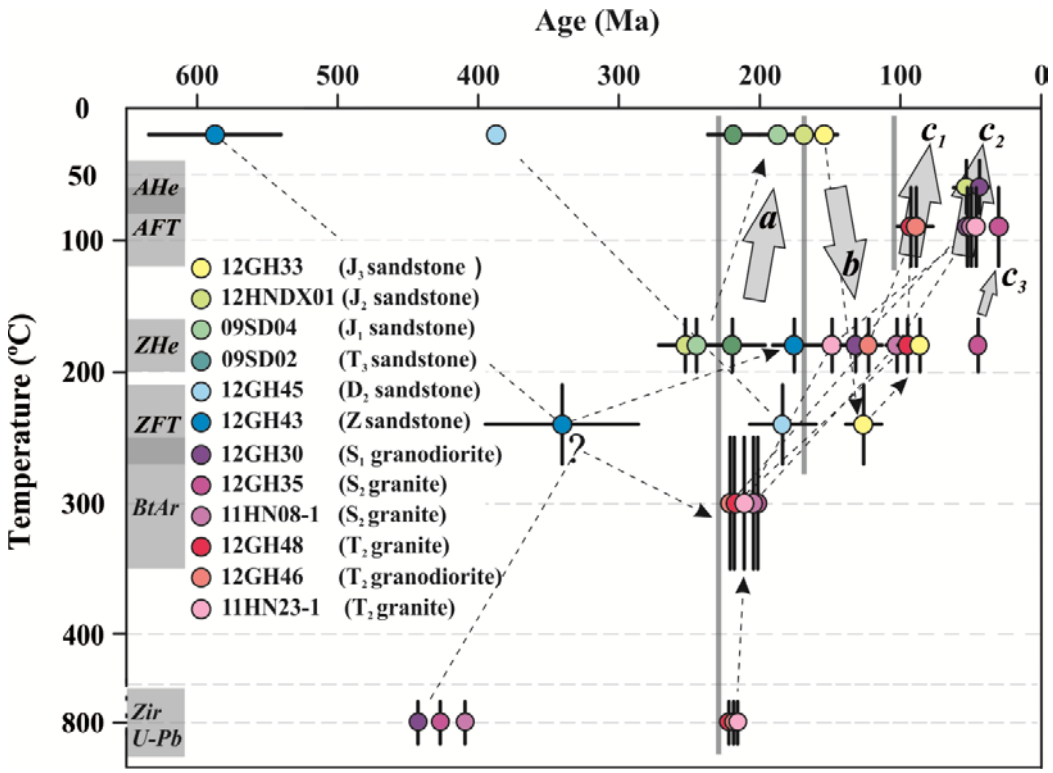

Figure 7.8 Time-temperature trajectories constructed with data generated in this study.
The trajectories of sedimentary samples start at the depositional ages at the assumed annual mean temperature of 20 ± 3°C, and those of granites start at the time defined by zircon U-Pb ages at 800 ± 100°C. All trajectories end at 0 Ma and 20 ± 3°C. The y-axis (temperature) of curves is determined by the characteristic closure temperature of each thermometer. The x-axis (time) is controlled by measured AHe, AFT, ZHe, BtAr, and U-Pb ages. Data-point error bars are displayed at 2σ confidence interval.

The ca. 420 Ma thermal peak identified by sample 12GH43 (**Figure 7.6a**) temporally coincides with syn-orogenic magmatism of the Early Paleozoic Wuyi-Yunkai orogeny (**Section 2.2.1**). For sample 12GH43, the nearest syn-Wuyi-Yunkai Silurian intrusion is represented by sample 11HN08-1 (**Figure 7.1**), defining the inland margin of the Wuyi-Yunkai orogen (**Figure 7.7**). Sample 11HN08-1 is,

however, far from sample 12GH43 (~150 km to the southeast; **Figure 7.1**) and the intrusion is unlikely to have imparted heat to 12GH43 by normal magmatic convective heating. Whether syn-Wuyi-Yunkai magmatism extended further to the northwest and whether it was able to generate a ~300°C thermal peak in northern Hunan is not yet clear.

7.4.2 Local Early Cretaceous burial heating?

Upper Jurassic sandstone (12GH33) yielded reset Early Cretaceous ZFT ages and thermal inverse modelling revealed an Early Cretaceous heating event (***b*** in **Figure 7.8**). This heating is well constrained to 250–300°C by local VR data (12GH34), and is supported by inverse modelling results (**Figure 7.6b**). Cretaceous magmatism has not been reported in the study area (**Figure 7.7**), so the Early Cretaceous heating is best explained by heat generated from the blanketing effort of the Lower Cretaceous strata.

7.4.3 Upper Cretaceous extensional exhumation

Upper Cretaceous (ca. 90 Ma) cooling (c_1 in **Figure 4.9**) is recorded by two Middle Triassic granitic samples (12GH46 and 12GH48) along the southern margin of the Cenozoic basin (**Figure 7.1; Figure 7.8 c** and **d**). Absence of Upper Palaeozoic and Lower Mesozoic strata (HNBGMR, 1976) implies significant erosion. Thick Upper Cretaceous clastic sequences (>1 km) with low maturation deposited in pull-apart basins (HNBGMR, 1984). Relatively speaking, the Middle Triassic granites and their Lower Palaeozoic country rocks would have uplifted to a higher elevation and would thus have suffered from erosion and cooling accompanying the formation of Upper Cretaceous extensional basins.

7.4.4 Cenozoic episodic rifting

Modelling results show a ca. 60 Ma rapid cooling in four samples (**Figure 7.6**

e–h; c_2 in **Figure 7.8**). Sample 12GH35 demonstrates rapid cooling at ca. 45 Ma and ca. 30 Ma (**Figure 7.6i;** c_3 in **Figure 7.8**). The three Eocene cooling stages are comparable to synchronous cooling in other part of SE SCB (**Chapters 4–6**), related to Cenozoic rifting. The new AFT and AHe data from Hunan suggests that the Cenozoic rifting occurred in vast areas of the SE SCB, reaching the Xuefeng Mountains but not the Wuling Mountains (**Figure 7.2**).

7.5 Conclusions

This Chapter presents a comprehensive new thermochronological dataset for representative strata and intrusions from the southeast to the northwest of the Hunan province. Forward analysis and modelling of the dataset were combined to investigate the thermal history of Hunan province, northwest of the SE SCB. Flat-subducted paleo-Pacific oceanic plates reached the northwest end of the province and generated Late Triassic orogenic uplift cooling. Apart from possible Early Cretaceous burial heating, Hunan province was dominated by gentle extensional cooling until the Late Cretaceous. Sagging of extensional basins during the Late Cretaceous induced increases in cooling rates in relatively uplifted ranges in northeast Hunan. Extension and rifting activated episodic rapid cooling at the location of the present Xuefeng Mountains and in southern Hunan, in the Early Paleogene, Middle Eocene and Early Oligocene.

Chapter 8 Thermal history of the SE SCB and its tectonic drivers: A synthesis

This study provides a comprehensive thermochronological database for the SE SCB that spans a temperature range of 400–40°C. Ages recording higher temperature events (400–300°C) are determined by MsAr and BtAr methods. ZHe ages cover the intermediate temperature events (200–160°C) and AFT and AHe methods are sensitive to the lowest temperature processes (<100°C).

Late Triassic MsAr and BtAr ages in the northwest (220–200 Ma) are clearly older than the Late Jurassic ages from the southeast (165–155 Ma; **Figure 8.1a**). One Early Jurassic age from the Shibei granite in Daxi is distinct from the Late Jurassic age cluster in the southeast (**Figure 8.1a**). Forty-one ZHe ages range from 253 Ma to 75 Ma (**Figure 8.1b**) while four ZHe ages are pre-Middle Jurassic (253, 245, 220 and 176 Ma). The remaining ZHe ages range from the Late Jurassic (152 Ma) to the Late Cretaceous (75 Ma). Key features to note are that the four pre-Middle Jurassic ages are all from the northwest (Hunan) and that the southeast is dominated by Cretaceous ages (**Figure 8.1b**). The majority of AFT ages cluster at 70–30 Ma, with two older ages (90 Ma) from samples in the northwest (**Figure 8.1c**). Similar to AFT ages, AHe ages form a relatively tight Late Cretaceous–Eocene cluster of 70–30 Ma (**Figure 8.1d**).

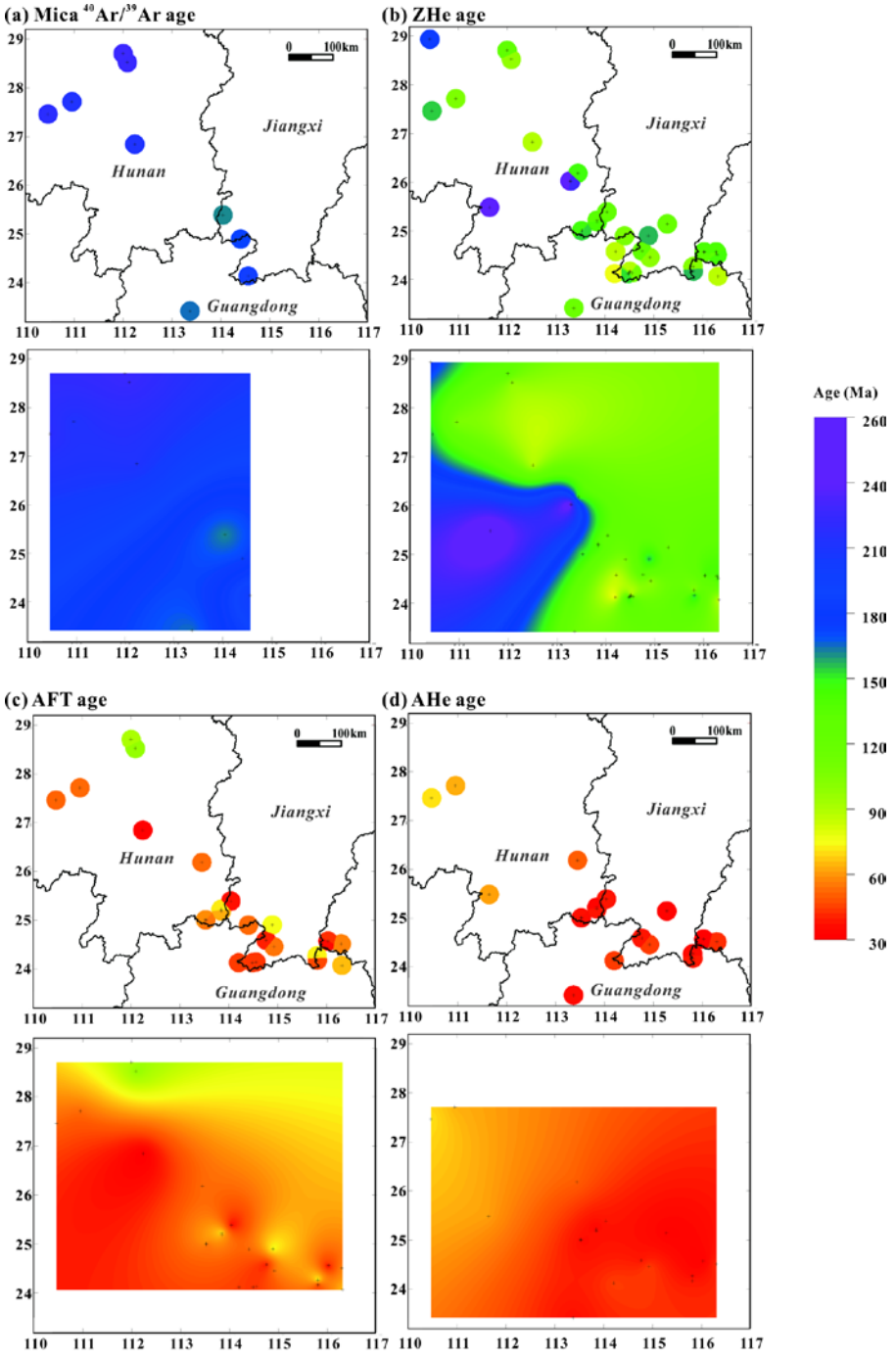

Figure 8.1 Database containing new mica $^{40}Ar/^{39}Ar$, ZHe, AFT and ZHe ages of SE SCB from this study.

X-axis is longitude in degree and y-axis is latitude in degree. Mica $^{40}Ar/^{39}Ar$ ages refer to muscovite and biotite $^{40}Ar/^{39}Ar$ ages. Ages are expressed in Ma as circles where age values are indicated by the colour of circles. Errors are not shown. Pattern of ages was obtained by interpolation and smoothing of the dataset and errors are not included. Existing data points are expressed as black crossings in interpolated maps. Note that linking between areas without data points is a result of interpolation. The maps purely show spatial distribution of ages and general trends whereby geology and faults are ignored. This figure was generated by using Golden Software Surfer (v8.0). Gridding methods were Kriging for interpolated maps and Nearest Neighbor for data point plots.

Time-temperature trajectories were extracted from both forward and inverse modelling of data from representative sedimentary and intrusive samples from Hunan, Shaoguan-Longnan, Daxi and Meizhou (**Figure 8.2**). A Precambrian sandstone in Hunan records rapid cooling related to orogenic uplift and related erosion during the Late Triassic. While the front of the subducting oceanic slab was generating orogenic uplift in the northwest, southeast regions, overriding the middle oceanic slab, were starting to sag and receiving sediment, and evolving into a shallow-marine basin during the Late Triassic and Early Jurassic (Liu and Xu, 1994) (**Figure 8.3**). The orogenic uplift is interpreted to be a result of the approach of the flat-subducted paleo-Pacific oceanic plateau from the southeast and the sagging basin resulted from the gravitational pull of the eclogitized oceanic flat slab (**Figure 8.3**) (Li and Li, 2007). Significant magmatic-dominated reheating occurred first in Daxi in the Middle Jurassic and generated a thermal peak of ~300°C. Subsequently, in the Late Jurassic, a thermal peak of 250–300°C developed in both Shaoguan-Longnan and Meizhou, to the northwest and east of Daxi, respectively (**Figure 8.2**). The voluminous Middle–Late Jurassic magmatism was related to the delamination and eventual break-off the eclogite paleo-Pacific slab (Li and Li, 2007). That the Daxi area was the first influenced by slab break-off is consistent with this area serving as the depocentre of the Late Triassic–Early Jurassic sagging basin, where the highest degree of eclogite facies metamorphism is expected. Nearby areas (e.g. Shaoguan-Longnan and Meizhou) were subsequently influenced by delamination-related magmatic heating as slab tearing continued (**Figure 8.3**).

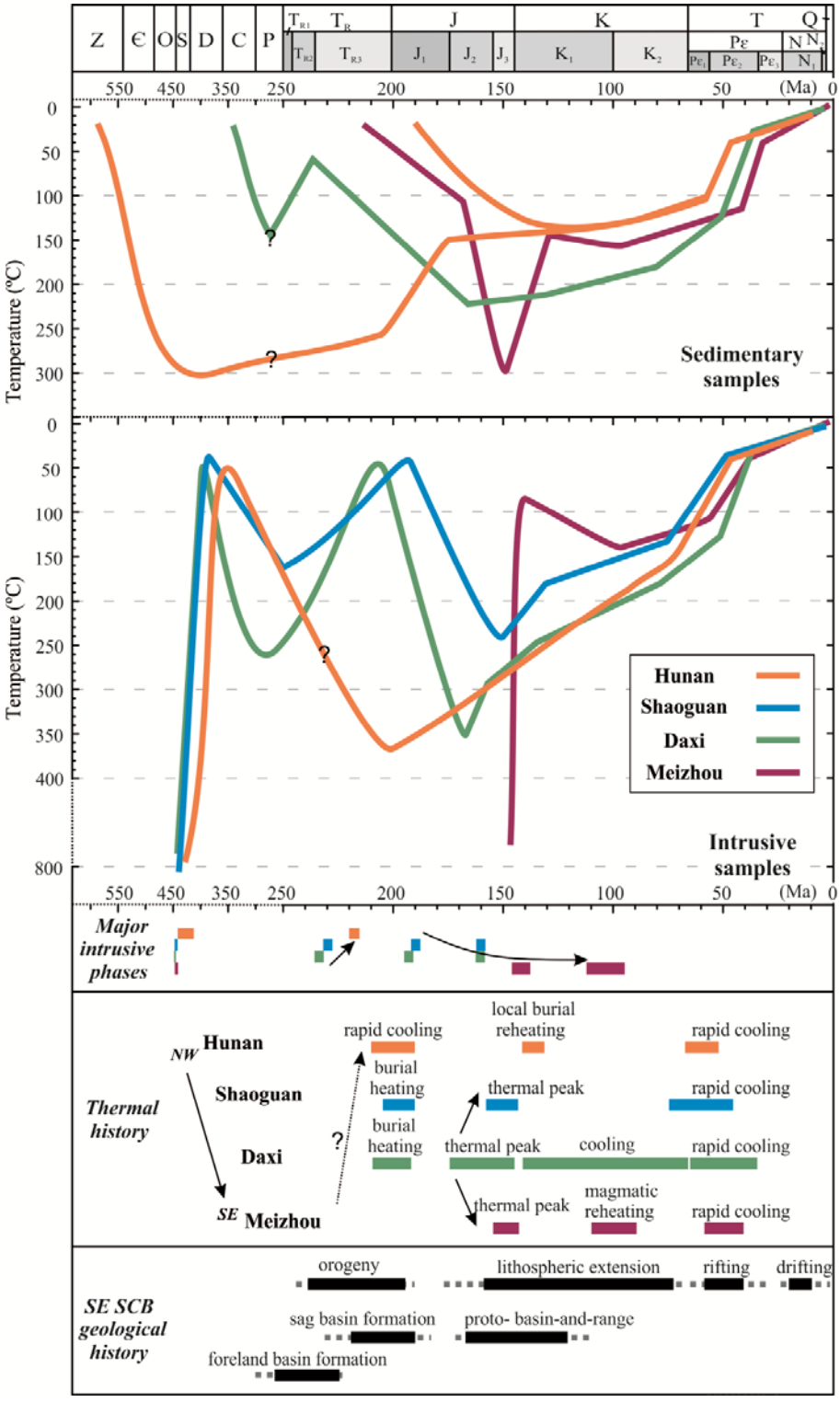

Figure 8.2 Modelled time-temperature paths and major phases of intrusive magmatism of Hunan, Shaoguan-Longnan, Daxi and Meizhou, and interpreted thermal and geological history of the SE SCB.

Arrows illustrate spatial and temporal trends. Black bars represent the major phases of geological processes and the grey dashed bars show the possible timing of initiation and termination of those processes.

The SE SCB was subjected to slow exhumational cooling during the Cretaceous (**Figure 8.2**). The relatively quiescent, low temperature (200–100°C) conditions reflect long-term thermal relaxation after Middle–Late Jurassic magmatic reheating. Nevertheless, a mid-Cretaceous magmatic reheating episode was identified in the Meizhou area (**Figure 8.2**). Protracted, slow cooling observed in the SE SCB during the Cretaceous correlates well with proposed continental lithospheric rebounding, when the gradational pull from the previously underlying flat slab abated (Li and Li, 2007). During the Cretaceous, the remaining paleo-Pacific oceanic slab started to retreat southeastward, generating intensive Cretaceous volcanic and intrusive magmatism in the southeastern and coastal regions (**Figure 8.2; Figure 8.3**) (Li and Li, 2007; Meng et al., 2012), accounting for the magmatic reheating recorded in the Meizhou area in this work. The Pacific subduction zone had migrated to the south of the present continental margin of SCB by ~90 Ma (**Figure 8.3**) (Lapierre et al., 1997; Li et al., 2012).

Conspicuous rapid cooling from ~150°C to surface temperatures is recorded in most study areas. The rapid cooling started as early as in the latest Cretaceous and lasted until the late Eocene (**Figure 8.2**), temporally coinciding with a recognized rifting event in the SE SCB (Ren et al., 2002; Zhu et al., 2004; Yan et al., 2009b; Zhou et al., 2009). Rifting has been linked to the rollback of the subducting western Pacific oceanic plates that ultimately led to the opening of the South China Sea (**Figure 8.3**) (Northrup et al., 1995; Li et al., 2012; Lester et al., 2014).

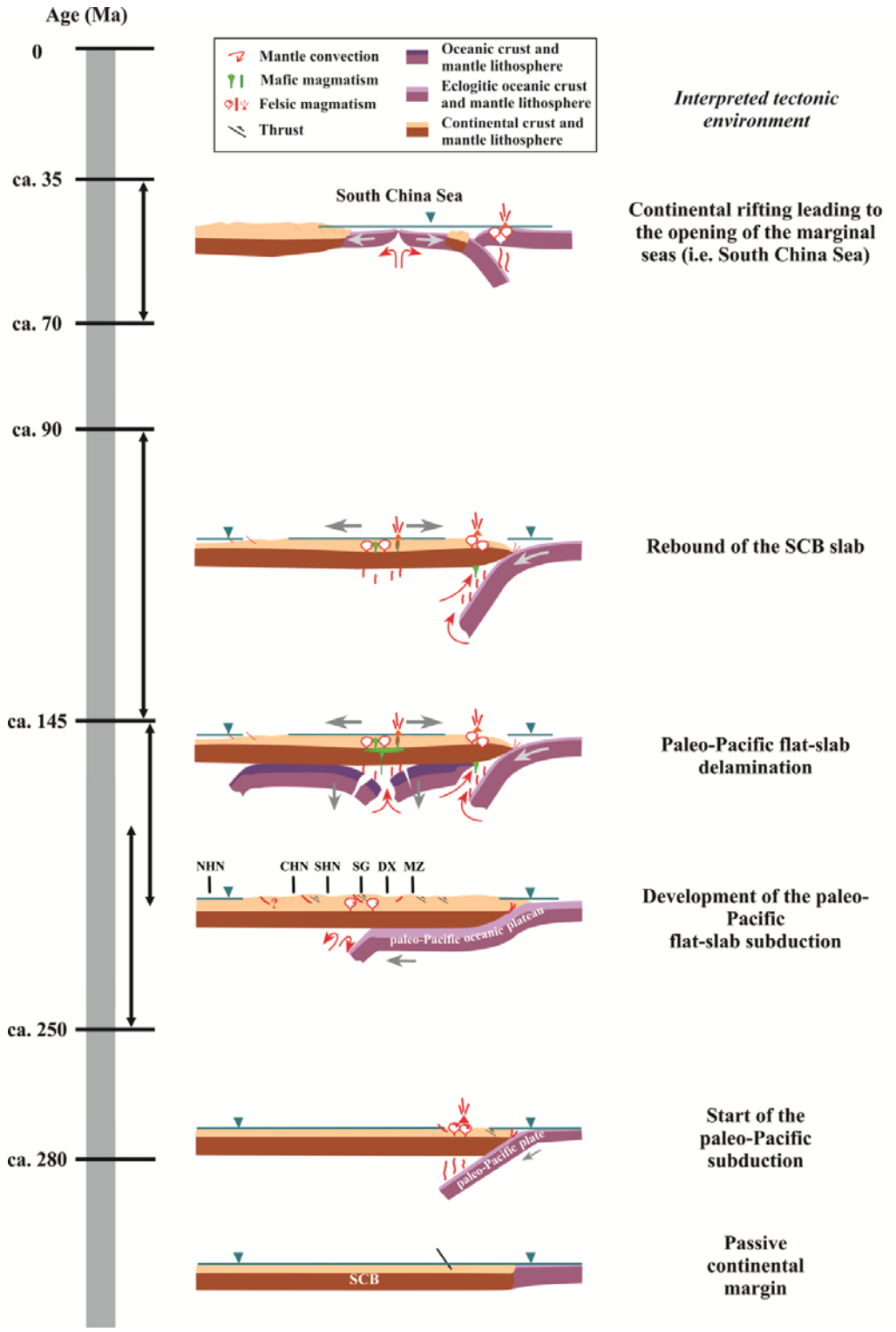

Figure 8.3 Schematic diagram showing the tectonic evolution of SE SCB, modified from Li and Li (2007) and Li et al. (2012).

NHN=northern Hunan; CHN=central Hunan; SHN=southern Hunan; SG=Shaoguan-Longnan; DX=Daxi; MZ=Meizhou.

Bibliography

Antia, D. D. J. (1986). Kinetic method for modeling vitrinite reflectance. *Geology, 14*(7), 606-608.

Armagnac, C., Bucci, J., Kendall, C., and Lerche, I. (1989). Estimating the thickness of sediment removed at an unconformity using vitrinite reflectance data. *Thermal history of sedimentary basins: methods and case histories: New York, Springer-Verlag*, 217-238.

Bao, Z. W., Zhao, Z. H., and Xiong, X. L. (2000). Geochemistry of Ejinao alkali syenite and its geodynamic significance. *Geochimica, 29*(5), 462-468 (in Chinese with English abstract).

Barbarand, J., Carter, A., Wood, I., and Hurford, T. (2003). Compositional and structural control of fission-track annealing in apatite. *Chemical Geology, 198*(1-2), 107-137.

Barker, C. E. (1989). Temperature and time in the thermal maturation of sedimentary organic matter. *Thermal history of basins: methods and case histories: Berlin, Springer-Verlag*, 74-98.

Barker, C. and Pawlewicz, M. (1986). The correlation of vitrinite reflectance with maximum temperature in humic organic matter. *Paleogeothermics*, 79-93.

Bhandari, N., Bhat, S. G., Lal, D., Rajagopalan, G., Tamhane, A. S., and Venkatavaradan, V. S. (1971). Fission fragment tracks in apatite: recordable track lengths. *Earth and Planetary Science Letters, 13*(1), 191-199.

Black, L. P., Kamo, S. L., Allen, C. M., Davis, D. W., Aleinikoff, J. N., Valley, J. W., . . . Foudoulis, C. . (2004). Improved $^{206}Pb/^{238}U$ microprobe geochronology by the monitoring of a trace-element-related matrix effect; SHRIMP, ID-TIMS, ELA-ICP-MS and oxygen isotope documentation for a series of zircon standards. *Chemical Geology, 205*(1–2), 115-140.

Bowring, S. A., Schoene, B., Crowley, J. L., Ramezani, J., and Condon, D. J. (2006). High-precision U-Pb zircon geochronology and the stratigraphic record: Progress and promise. *Paleontological Society Papers, 12*, 25-43.

Brandon, M. T., Roden-Tice, M. K., and Garver, J. I. (1998). Late Cenozoic exhumation of the Cascadia accretionary wedge in the Olympic Mountains, northwest Washington State. *Geological Society of America Bulletin, 110*(8), 985-1009.

Brenier, R., Mugnier, J., and Mirica, E. (1999). XPS study of amorphous zirconium oxide films prepared by sol–gel. *Applied Surface Science, 143*(1–4), 85-91.

Brown, R. W., Beucher, R., Roper, S., Persano, C., Stuart, F., and Fitzgerald, P. (2013). Natural age dispersion arising from the analysis of broken crystals, Part I. Theoretical basis and implications for the apatite (U-Th)/He thermochronometer. *Geochimica et Cosmochimica Acta, 122*, 478-497.

Burnham, A. K. and Sweeney, J. J. (1989). A chemical kinetic model of vitrinite maturation and reflectance. *Geochimica et Cosmochimica Acta, 53*(10), 2649-2657.

Burtner, R. L., Nigrini, A. , and Donelick, R. A. (1994). Thermochronology of Lower Cretaceous source rocks in the Idaho-Wyoming thrust belt. *AAPG bulletin, 78*(10), 1613-1636.

Cande, S. C. and Kent, D. V. (1992). A new geomagnetic polarity time scale for the Late Cretaceous and Cenozoic. *Journal of Geophysical Research: Solid Earth, 97*(B10), 13917-13951.

Carlson, W. D. (1990). Mechanisms and kinetics of apatite fission-track annealing. *American Mineralogist;(United States), 75*

Chan, L. S., Shen, W., and Pubellier, M. (2010). Polyphase rifting of greater Pearl River Delta region (South China): Evidence for possible rapid changes in regional stress configuration. *Journal of Structural Geology, 32*(6), 746-754.

Charvet, J. (2013). The Neoproterozoic–Early Paleozoic tectonic evolution of the South China Block: An overview. *Journal of Asian Earth Sciences, 74*(0), 198-209.

Charvet, J., Lapierre, H., and Yu, Y. W. (1994). Geodynamic significance of the Mesozoic volcanism of southeastern China. *Journal of Southeast Asian Earth Sciences, 9*(4), 387-396.

Charvet, J., Shu, L. S., Shi, Y. S., Guo, L. Z., and Faure, M. . (1996). The building of south China: collision of Yangzi and Cathaysia blocks, problems and tentative answers. *Journal of Southeast Asian Earth Sciences, 13*(3), 223-235.

Chen, C. H., Lee, C. Y., and Shinjo, R. I. (2008). Was there Jurassic paleo-Pacific subduction in South China?: Constraints from $^{40}Ar/^{39}Ar$ dating, elemental and Sr-Nd-Pb isotopic geochemistry of the Mesozoic basalts. *Lithos, 106*(1), 83-92.

Chen, P. R. , Zhou, X. M., Zhang, W. L., Li, H. M., Fan, C. F., Sun, T., . . . Zhang, M. (2005). Petrogenesis and significance of early Yanshanian syenite-granite complex in eastern Nanling Range. *Science China Earth Sciences, 48*(7), 912-924.

Chen, P. R., Hua, R. M., Zhang, B. T., Lu, J. J., and Fan, C. F. (2002a). Early Yanshanian post-orogenic granitoids in the Nanling region. *Science China Earth Sciences, 45*(8), 755-768.

Chen, W. S., Yang, H. C., Wang, X., and Huang, H. (2002b). Tectonic setting and exhumation history of the Pingtan–Dongshan Metamorphic Belt along the coastal area, Fujian Province, Southeast China. *Journal of Asian Earth Sciences, 20*(7), 829-840.

Cherniak, D. J. and Watson, E. B. (2003). Diffusion in zircon. *Reviews in Mineralogy and Geochemistry, 53*(1), 113.

Chung, S. L., Cheng, H., Jahn, B. M., O'Reilly, S. Y., and Zhu, B. Q. (1997). Major and trace element, and Sr-Nd isotope constraints on the origin of Paleogene volcanism in South China prior to the South China Sea opening. *Lithos, 40*(2), 203-220.

Compston, W. , Williams, I. S., and Mayer, C. (1984). U-Pb geochronology of zircons form lunar Breccia 73217 using a sensitive high mass-resolution ion microprobe. *Journal of Geophysical Research, 89*(S02), B525-B534.

Crowley, K. D., Cameron, M., and Schaefer, R. L. (1991). Experimental studies of annealing of etched fission tracks in fluorapatite. *Geochimica et Cosmochimica Acta, 55*(5), 1449-1465.

Cui, S. Q. and Li, J. R. (1983). On the Indosinian Orogeny along the Chinese western Pacific belt. *Acta Geologica Sinica, 57*(1), 51-61 (in Chinese).

Dalrymple, G. B., Alexander, E. C., Lanphere, M. A., and Kraker, G. P. (1981). Irradiation of samples for $^{40}Ar/^{39}Ar$ dating using the Geological Survey TRIGA reactor. . *US Geol. Surv. Prof. Paper. 1176,*

Danišık, M., Kuhlemann, J., Dunkl, I., Székely, B., and Frisch, W. (2007). Burial and exhumation of Corsica (France) in the light of fission track data. *Tectonics, 26*(1), 1-24.

Danišík, M., Shane, P., Schmitt, A. K., Hogg, A., Santos, G. M., Storm, S., . . . Lindsay, J. M. (2012). Re-anchoring the late Pleistocene tephrochronology of New Zealand based on concordant radiocarbon ages and combined $^{238}U/^{230}Th$ disequilibrium and (U–Th)/He zircon ages. *Earth and Planetary Science Letters, 349*, 240-250.

Deng, F. L. (1987). Isotopic geochronology of Southern Zhugangshan complex granite. *Geochimica,*(2), 141-152 (in Chinese).

Deng, P., Ren, J. S., Ling, H. F., Shen, W. Z. , Sun, L. Q., Zhu, B., and Tan, Z. Z. (2012). SHRIMP zircon U-Pb ages and tectonic implications for Indosinian granitoids of southern Zhuguangshan granitic composite, South China. *Chinese Science Bulletin, 57*(13), 1542-1552.

Deng, P., Shu, L. S., Yu, X. Q., Wang, B., Tan, Z. Z., and Sun, Y. (2004). Early-Middle Jurassic basins and features of igneous rocks in the Western Fujian-Southern Jiangxi region. *Acta Petrologica Sinica, 20*(3), 521-532.

Donelick, R. A., Ketcham, R. A., and Carlson, W. D. (1999). Variability of apatite fission-track annealing kinetics: II. Crystallographic orientation effects. *American Mineralogist, 84*(9), 1224-1234.

Donelick, R. A., O'Sullivan, P. B., and Ketcham, R. A. (2005). Apatite fission-track analysis. *Reviews in Mineralogy and Geochemistry, 58*(1), 49.

Duddy, I. R., Green, P. F., and Laslett, G. M. (1988). Thermal annealing of fission tracks in apatite 3. Variable temperature behaviour. *Chemical Geology: Isotope Geoscience section, 73*(1), 25-38.

Dunkl, I. (2002). TRACKKEY: A Windows program for calculation and graphical presentation of fission track data. *Computers & Geosciences, 28*(1), 3-12.

Dunkl, I., Di Giulio, A., and Kuhlemann, J. (2001). Combination of single-grain fission-track chronology and morphological analysis of detrital zircon crystals in provenance studies: Sources of the macigno formation (Apennines, Italy). *Journal of sedimentary research, 71*(4), 516-525.

Dunkl, I. and Székely, B. (2003). *Component analysis with visualization of fitting — Popshare, a freeware program for evaluation of mixed geochronological data.* Paper presented at the EGS-AGU-EUG Joint Assembly

Eaton, G. P. (1982). The Basin and Range province: Origin and tectonic significance. *Annual Review of Earth and Planetary Sciences, 10*, 409-440.

Ehlers, T. A. and Farley, K. A. (2003). Apatite (U-Th)/He thermochronometry: methods and applications to problems in tectonic and surface processes. *Earth and Planetary Science Letters, 206*(1), 1-14.

Evans, N. J., Byrne, J. P., Keegan, J. T., and Dotter, L. E. (2005a). Determination of uranium and thorium in zircon, apatite, and fluorite: Application to laser (U-Th)/He thermochronology. *Journal of Analytical Chemistry, 60*(12), 1159-1165.

Evans, N. J., Wilson, N. S. F., Cline, J. S., McInnes, B. I. A., and Byrne, J. (2005b). Fluorite (U–Th)/He thermochronology: Constraints on the low temperature history of Yucca Mountain, Nevada. *Applied Geochemistry, 20*(6), 1099-1105.

Fan, Q. C. and Hooper, P. R. (1991). The Cenozoic basaltic rocks of eastern China: petrology and chemical composition. *Journal of petrology, 32*(4), 765-810.

Farley, K. A. (2000). Helium diffusion from apatite: General behavior as illustrated by Durango fluorapatite. *Journal of Geophysical Research: Solid Earth, 105*(B2), 2903-2914.

Farley, K. A. (2002). (U-Th)/He dating: Techniques, calibrations, and applications. *Reviews in Mineralogy and Geochemistry, 47*(1), 819.

Farley, K. A., Wolf, R. A., and Silver, L. T. (1996). The effects of long alpha-stopping distances on (U-Th)/He ages. *Geochimica et Cosmochimica Acta, 60*(21), 4223-4229.

FJBGMR, Fujian Bureau of Geology and Mineral Resources. (1985). *Regional geology of Fujian Province, People's Republic of China*. Beijing: Geological Publishing House, 671 PP.

Fleischer, R. L. and Price, P. B. . (1964). Techniques for geological dating of minerals by chemical etching of fission fragment tracks. *Geochimica et Cosmochimica Acta, 28*(10), 1705-1714.

Fleischer, R. L., Price, P. B., and Walker, R. M. (1975). *Nuclear tracks in solids: principles and applications*. Berkeley, California: University of California Press, 626 PP.

Flower, M. F. J., Russo, R. M., Tamaki, K., and Hoang, N. (2001). Mantle contamination and the Izu-Bonin-Mariana (IBM) 'high-tide mark': evidence for mantle extrusion caused by Tethyan closure. *Tectonophysics, 333*(1), 9-34.

Flowers, R. M., Ketcham, R. A., Shuster, D. L., and Farley, K. A. (2009). Apatite (U-Th)/He thermochronometry using a radiation damage accumulation and annealing model. *Geochimica Et Cosmochimica Acta, 73*(8), 2347-2365.

Gaiduk, P. I., Komarov, F. F., and Wesch, W. (2000). Damage evolution in crystalline InP during irradiation with swift Xe ions. *Nuclear Instruments and Methods in Physics Research Section B: Beam Interactions with Materials and Atoms, 164*, 377-383.

Gallagher, K., Brown, R. , and Johnson, C. . (1998). Fission track analysis and its applications to geological problems. *Annu. Rev. Earth Planet., 26*, 519-572.

Gao, S. and Zhang, B. R. (1990). The discovery of Archean TTG gneisses in northern Yangtze craton and their implications. *Earth Science, 15*, 675-679.

Gautheron, C., Barbarand, J., Ketcham, R. A., Tassan-Got, L., van der Beek, P., Pagel, M., . . . Fialin, M. (2013). Chemical influence on α-recoil damage annealing in apatite: Implications for (U–Th)/He dating. *Chemical Geology, 351*, 257-267.

Gautheron, C., Tassan-Got, L., Barbarand, J., and Pagel, M. (2009). Effect of alpha-damage annealing on apatite (U-Th)/He thermochronology. *Chemical Geology, 266*(3-4), 157-170.

GDBGMR. (1962). Regional geological investigation report of 1:200,000 Shaoguan sheet (G-49-30).

GDBGMR. (1965). Regional geological investigation report of 1:200,000 Lianping sheet (G-50-31).

GDBGMR. (1970). Regional geological investigation report of 1:200,000 Xingning (G-50-32).

GDBGMR. (1971). Regional geological investigation report of 1:200,000 Meixian (G-50-33).

GDBGMR, Guangdong Bureau of Geology and Mineral Resources. (1988). *Regional geology of Guangdong Province, People's Republic of China*. Beijing: Geological Publishing House, 941 PP.

Geng, H. Y., Xu, X. S., O'Reilly, S. Y., Zhao, M., and Sun, T. (2006). Cretaceous volcanic-intrusive magmatism in western Guangdong and its geological significance. *Science China Earth Sciences, 49*(7), 696-713.

Gilder, S. A., Keller, G. R., Luo, M., and Goodell, P. C. (1991). Timing and spatial distribution of rifting in China. *Tectonophysics, 197*(2), 225-243.

Gleadow, A. J. W. (2007). *Fission track dating methods: principles and techniques.* The University of Melbourne (pp. 74).

Gleadow, A. J. W. and Duddy, I. R. (1981). A natural long-term track annealing experiment for apatite. *Nuclear Tracks, 5*(1), 169-174.

GNCUSGS, Geologic Names Committee of the U.S. Geological Survey. (2010). Divisions of geologic time–major chronostratigraphic and geochronologic units. *US Geol Surv Fact Sheet 2010-3059,*

Gong, J. F. and Chen, Y. J. (2014). Evidence of lateral asthenosphere flow beneath the South China craton driven by both Pacific plate subduction and the India-Eurasia continental collision. *Terra Nova, 26*(1), 55-63.

Goodell, P. C., Gilder, S., and Fang, X. (1991). A preliminary description of the Gan-Hang failed rift, southeastern China. *Tectonophysics, 197*(2), 245-255.

Green, P. F. (1981). A new look at statistics in fission-track dating. *Nuclear tracks, 5*(1-2), 77-86.

Green, P. F., Duddy, I. R., Gleadow, A. J. W., Tingate, P. R., and Laslett, G. M. (1986). Thermal annealing of fission tracks in apatite: 1. A qualitative description. *Chemical Geology: Isotope Geoscience section, 59*, 237-253.

Green, P. F., Duddy, I. R., Laslett, G. M., Hegarty, K. A., Gleadow, A. J. W., and Lovering, J. F. (1989). Thermal annealing of fission tracks in apatite 4. Quantitative modelling techniques and extension to geological timescales. *Chemical Geology: Isotope Geoscience section, 79*(2), 155-182.

Greentree, M. R. and Li, Z. X. (2008). The oldest known rocks in south-western China: SHRIMP U-Pb magmatic crystallisation age and detrital provenance analysis of the Paleoproterozoic Dahongshan Group. *Journal of Asian Earth Sciences, 33*(5), 289-302.

Gu, L. X., Khin, Z., Hu, W. X., Zhang, K. J., Ni, P., He, J. X., . . . Lin, C. M. . (2007). Distinctive features of Late Palaeozoic massive sulphide deposits in South China. *Ore Geology Reviews, 31*(1), 107-138.

Guenthner, W. R., Reiners, P. W., Ketcham, R. A., Nasdala, L., and Giester, G. (2013). Helium diffusion in natural zircon: Radiation damage, anisotropy, and the interpretation of zircon (U-Th)/He thermochronology. *American Journal of Science, 313*(3), 145-198.

Hames, W. E. and Bowring, S. A. (1994). An empirical evaluation of the argon diffusion geometry in muscovite. *Earth and Planetary Science Letters, 124*(1), 161-169.

Harrison, T. M., Duncan, I., and McDougall, I. (1985). Diffusion of ^{40}Ar in biotite: Temperature, pressure and compositional effects. *Geochimica et Cosmochimica Acta, 49*(11), 2461-2468.

Hasebe, N., Tagami, T., and Nishimura, S. (1994). Towards zircon fission-track thermochronology: Reference framework for confined track length measurements. *Chemical Geology, 112*(1-2), 169-178.

He, Z. Y., Xu, X. S., and Niu, Y. L. (2010). Petrogenesis and tectonic significance of a Mesozoic granite-syenite-gabbro association from inland South China. *Lithos, 119*(3), 621-641.

Hearn, T. M., Wang, S. Y. , Ni, J. F., Xu, Z. H., Yu, Y. X. , and Zhang, X. D. (2004). Uppermost mantle velocities beneath China and surrounding regions. *Journal of Geophysical Research: Solid Earth (1978-2012), 109*(B11), 1-11.

HNBGMR. (1970). Regional geological investigation report of 1:200,000 Yongxing sheet (G-49-18).

HNBGMR. (1974). Regional geological investigation report of 1:200,000 Hengyang sheet (G-49-11).

HNBGMR. (1975). Regional geological investigation report of 1:200,000 Changsha sheet (H-49-35).

HNBGMR. (1976). Regional geological investigation report of 1:200,000 Yuanjiang sheet (H-49-29).

HNBGMR, Hunan Bureau of Geology and Mineral Resources. (1984). *Regional geology of Hunan Province, People's Republic of China*. Beijing: Geological Publishing House, 719 PP.

Hourigan, J. K., Reiners, P. W., and Brandon, M. T. (2005). U-Th zonation-dependent alpha-ejection in (U-Th)/He chronometry. *Geochimica et Cosmochimica Acta, 69*(13), 3349-3365.

House, M. A. , Wernicke, B. P., Farley, K. A., and Dumitru, T. A. (1997). Cenozoic thermal evolution of the central Sierra Nevada, California, from (UTh)/He thermochronometry. *Earth and Planetary Science Letters, 151*(3), 167-179.

Hu, R. Z. and Zhou, M. F. (2012). Multiple Mesozoic mineralization events in South China—an introduction to the thematic issue. *Mineralium Deposita, 47*(6), 579-588.

Huang, J. S. and Liao, Y. S. (2008). Investigation on the form reason and geological characteristics of the Silver-Antimony ore in Songxi of Meixian in Guangdong Province. *Geology and Mineral Resources of South China, 1*, 008.

Huang, X. L., Niu, Y. L., Xu, Y. G., Ma, J. L., Qiu, H. N., and Zhong, J. W. (2013). Geochronology and geochemistry of Cenozoic basalts from eastern Guangdong, SE China: constraints on the lithosphere evolution beneath the

northern margin of the South China Sea. *Contributions to Mineralogy and Petrology, 165*(3), 437-455.

Humayun, M. and Clayton, R. N. (1995). Precise determination of the isotopic composition of potassium: Application to terrestrial rocks and lunar soils. *Geochimica et cosmochimica acta, 59*(10), 2115-2130.

Hurford, A. J. (1986). Cooling and uplift patterns in the Lepontine Alps South Central Switzerland and an age of vertical movement on the Insubric fault line. *Contributions to mineralogy and petrology, 92*(4), 413-427.

Hurford, A. J. (1990a). International union of geological sciences subcommission on geochronology recommendation for the standardization of fission track dating calibration and data reporting. *Nuclear tracks and radiation measurements, 17*(3), 233-236.

Hurford, A. J. (1990b). Standardization of fission track dating calibration: recommendation by the Fission Track Working Group of the I.U.G.S. Subcommission on Geochronology. *Chemical Geology: Isotope Geoscience section, 80*(2), 171-178.

Hurford, A. J. and Green, P. F. (1982). A users' guide to fission track dating calibration. *Earth and Planetary Science Letters, 59*(2), 343-354.

Hurford, A. J. and Green, P. F. (1983). The zeta age calibration of fission-track dating. *Chemical Geology, 41*, 285-317.

Ireland, T. R. and Williams, I. S. (2003). Considerations in zircon geochronology by SIMS. *Reviews in Mineralogy and Geochemistry, 53*(1), 215-241.

Jaffey, A. H., Flynn, K. F., Glendenin, L. E., Bentley, W. C., and Essling, A. M. (1971). Precision measurement of half-lives and specific activities of ^{235}U and ^{238}U. *Physical Review C, 4*(5), 1889.

Ji, S. C., Wang, Q., and Salisbury, M. H. (2009). Composition and tectonic evolution of the Chinese continental crust constrained by Poisson's ratio. *Tectonophysics, 463*(1), 15-30.

Jiang, S. Y., Yang, J. H., Ling, H. F., Chen, Y. Q., Feng, H. Z. , Zhao, K. D., and Ni, P. (2007). Extreme enrichment of polymetallic Ni–Mo–PGE–Au in Lower Cambrian black shales of South China: An Os isotope and PGE geochemical investigation. *Palaeogeography, Palaeoclimatology, Palaeoecology, 254*(1), 217-228.

Jiang, Y. H., Jiang, S. Y. , Dai, B. Z. , Liao, S. Y. , Zhao, K. D. , and Ling, H. F. . (2009). Middle to late Jurassic felsic and mafic magmatism in southern Hunan province, southeast China: Implications for a continental arc to rifting. *Lithos, 107*(3), 185-204.

Jiao, W. F., Wu, Y. B., Yang, S. H., Peng, M., and Wang, J. (2009). The oldest basement rock in the Yangtze Craton revealed by zircon U-Pb age and Hf

isotope composition. *Science in China Series D: Earth Sciences, 52*(9), 1393-1399.

Jones, C. H., Wernicke, B. P., Farmer, G. L., Walker, J. D., Coleman, D. S., McKenna, L. W., and Perry, F. V. (1992). Variations across and along a major continental rift: An interdisciplinary study of the Basin and Range Province, western USA. *Tectonophysics, 213*(1), 57-96.

Jourdan, F., Frew, A., Joly, A., Mayers, C., and Evans, N. J. (2014). WA1ms: A ~2.61 Ga muscovite standard for $^{40}Ar/^{39}Ar$ dating. *Geochimica et Cosmochimica Acta, 141*, 113-126.

Jourdan, F., Moynier, F., Koeberl, C., and Eroglu, S. (2011). $^{40}Ar/^{39}Ar$ age of the Lonar crater and consequence for the geochronology of planetary impacts. *Geology, 39*(7), 671.

Jourdan, F., Verati, C., and Féraud, G. (2006). Intercalibration of the Hb3gr $^{40}Ar/^{39}Ar$ dating standard. *Chemical Geology, 231*(3), 177-189.

JXBGMR. (1969). Regional geological investigation report of 1:200,000 Ganzhou sheet (G-50-19).

JXBGMR. (1970). Regional geological investigation report of 1:200,000 Longnan sheet (G-50-25).

JXBGMR. (1973). Regional geological investigation report of 1:200,000 Xunwu sheet (G-50-26).

JXBGMR, Jiangxi Bureau of Geology and Mineral Resources. (1984). *Regional geology of Jiangxi Province, People's Republic of China*. Beijing: Geological Publishing House, 921 PP.

Ketcham, R. A. (2005). Forward and inverse modeling of low-temperature thermochronometry data. *Reviews in Mineralogy and Geochemistry, 58*(1), 275.

Ketcham, R. A. (2014). HeFTy manual (Version 1.8.3). The University of Texas at Austin.

Ketcham, R. A., Carter, A., Donelick, R. A., Barbarand, J. , and Hurford, A. J. (2007). Improved modeling of fission-track annealing in apatite. *American Mineralogist, 92*(5), 799-810.

Ketcham, R. A., Donelick, R. A., Balestrieri, M. L., and Zattin, M. (2009). Reproducibility of apatite fission-track length data and thermal history reconstruction. *Earth and Planetary Science Letters, 284*(3-4), 504-515.

Ketcham, R. A., Donelick, R. A., and Donelick, M. B. (2000). AFTSolve: A program for multi-kinetic modeling of apatite fission-track data. *Geological Materials Research, 2*(1), 1-32.

Kohn, B. P., Osadetz, K. G., and Bezys, R. K. (1995). Apatite fission-track dating of two crater structures in the Canadian Williston basin. *Bulletin of canadian petroleum geology, 43*(1), 54-64.

Koppers, A. A. P. (2002). ArArCALC — software for $^{40}Ar/^{39}Ar$ age calculations. *Computers & Geosciences, 28*(5), 605-619.

Lal, D., Rajan, R. S., and Tamhane, A. S. (1969). Chemical composition of nuclei of Z > 22 in cosmic rays using meteoritic minerals as detectors. *Nature, 221*, 33-37.

Lapierre, H., Jahn, B. M., Charvet, J., and Yu, Y. W. (1997). Mesozoic felsic arc magmatism and continental olivine tholeiites in Zhejiang Province and their relationship with the tectonic activity in southeastern China. *Tectonophysics, 274*(4), 321-338.

Larter, S. (1988). Some pragmatic perspectives in source rock geochemistry. *Marine and petroleum geology, 5*(3), 194-204.

Laslett, G. M. and Galbraith, R. F. (1996). Statistical modelling of thermal annealing of fission tracks in apatite. *Geochimica et Cosmochimica Acta, 60*(24), 5117-5131.

Laslett, G. M., Green, P. F., Duddy, I. R., and Gleadow, A. J. W. (1987). Thermal annealing of fission tracks in apatite 2. A quantitative analysis. *Chemical Geology: Isotope Geoscience section, 65*(1), 1-13.

Laughland, M. M. and Underwood, M. B. (1993). Vitrinite reflectance and estimates of paleotemperature within the upper Shimanto Group, Muroto Peninsula, Shikoku, Japan. *Special papers-Geological Society of America*, 25-25.

Lerche, I, Yarzab, R. F., and Kendall, C. . (1984). Determination of paleoheat flux from vitrinite reflectance data. *AAPG Bulletin, 68*(11), 1704-1717.

Lester, R, Van Avendonk, H. J. A., McIntosh, K., Lavier, L., Liu, C. S., Wang, T. K., and Wu, F. (2014). Rifting and magmatism in the northeastern South China Sea from wide-angle tomography and seismic reflection imaging. *Journal of Geophysical Research: Solid Earth, 119*(3), 2305-2323.

Li, C. A. and Zou, H. P. . (2011). The Ar-Ar Age of the Nanxiong Fault Zone in Guangdong Province and Their Geological Significance. *Acta Scientiarum Naturalium University Sunyatseni, 50*(1), 129-137 (in Chinese with English abstract).

Li, J. H., Zhang, Y. Q., Dong, S. W., and Johnston, S. T. (2014a). Cretaceous tectonic evolution of South China: A preliminary synthesis. *Earth-Science Reviews, 134*, 98-136.

Li, W. X. and Li, X. H. (2003). Adakitic granites within the NE Jiangxi ophiolites, South China: geochemical and Nd isotopic evidence. *Precambrian Research, 122*(1), 29-44.

Li, W. X., Li, X. H., Li, Z. X., and Lou, F. S. (2008a). Obduction-type granites within the NE Jiangxi Ophiolite: Implications for the final amalgamation between the Yangtze and Cathaysia Blocks. *Gondwana Research, 13*(3), 288-301.

Li, X. H. (1997). Timing of the Cathaysia Block formation: constraints from SHRIMP U–Pb zircon geochronology. *Episodes, 20*(3), 188-192.

Li, X. H. (2000). Cretaceous magmatism and lithospheric extension in Southeast China. *Journal of Asian Earth Sciences, 18*(3), 293-305.

Li, X. H., Chen, Z., Liu, D. Y., and Li, W. X. (2003). Jurassic gabbro-granite-syenite suites from Southern Jiangxi province, SE China: Age, origin, and tectonic significance. *International Geology Review, 45*(10), 898-921.

Li, X. H., Chung, S. L., Zhou, H., Lo, C. H., Liu, Y., and Chen, C. H. (2004a). Jurassic intraplate magmatism in southern Hunan-eastern Guangxi: $^{40}Ar/^{39}Ar$ dating, geochemistry, Sr-Nd isotopes and implications for the tectonic evolution of SE China. *Geological Society, London, Special Publications, 226*(1), 193-215.

Li, X. H., Li, W. X., Li, Z. X., Lo, C. H., Wang, J., Ye, M. F., and Yang, Y. H. (2009a). Amalgamation between the Yangtze and Cathaysia Blocks in South China: Constraints from SHRIMP U-Pb zircon ages, geochemistry and Nd-Hf isotopes of the Shuangxiwu volcanic rocks. *Precambrian Research, 174*(1), 117-128.

Li, X. H., Li, Z. X. , Zhou, H. W., Liu, Y., and Kinny, P. D. (2002a). U-Pb zircon geochronology, geochemistry and Nd isotopic study of Neoproterozoic bimodal volcanic rocks in the Kangdian Rift of South China: Implications for the initial rifting of Rodinia. *Precambrian Research, 113*(1), 135-154.

Li, X. H., Li, Z. X., and Li, W. X. (2014b). Detrital zircon U–Pb age and Hf isotope constrains on the generation and reworking of Precambrian continental crust in the Cathaysia Block, South China: A synthesis. *Gondwana Research, 25*(3), 1202-1215.

Li, X. H., Li, Z. X., Li, W. X., Liu, Y., Yuan, C., Wei, G. J., and Qi, C. S. (2007a). U-Pb zircon, geochemical and Sr-Nd-Hf isotopic constraints on age and origin of Jurassic I- and A-type granites from central Guangdong, SE China: A major igneous event in response to foundering of a subducted flat-slab? *Lithos, 96*(1), 186-204.

Li, X. H., Li, Z. X., Li, W. X., Wang, X. C., and Gao, Y. Y. (2013). Revisiting the "C-type adakites" of the Lower Yangtze River Belt, central eastern China: In-situ zircon Hf–O isotope and geochemical constraints. *Chemical Geology, 345*, 1-15.

Li, X. H., Li, Z. X., Li, W. X., and Wang, Y. J. (2006). Initiation of the Indosinian Orogeny in South China: evidence for a Permian magmatic arc on Hainan Island. *The Journal of Geology, 114*(3), 341-353.

Li, X. H., Liu, D. Y., Sun, M., Li, W. X., Liang, X. R., and Y., LIiu. (2004b). Precise Sm-Nd and U-Pb isotopic dating of the supergiant Shizhuyuan polymetallic deposit and its host granite, SE China. *Geological Magazine, 141*(2), 225-231.

Li, X. H., Liu, Y., Li, Q. L., Guo, C. H., and Chamberlain, K. R. (2009b). Precise determination of Phanerozoic zircon Pb/Pb age by multicollector SIMS without external standardization. *Geochemistry, Geophysics, Geosystems, 10*(4), Q04010.

Li, X. H., Wang, Y. X., Zhao, Z. H., Chen, D. F., and Zhang, H. (1998). SHRIMP U-Pb zircon geochronology for amphibolite from the Precambrian basement in SW Zhejiang and NW Fujian province. *Geochimica, 27*(4), 327-334.

Li, X. H., Zhou, H. W., Liu, Y., Li, J. Y., Chen, Z. H., Yu, J. S., and Gui, X. T. (2000). Mesozoic shoshonitic intrusives in the Yangchun Basin, western Guangdong, and their tectonic significance: I. Petrology and isotope geochronology. *Geochimica, 29*(6), 513-520 (in Chinese with English abstract).

Li, X. M., Wang, Y. J., Tan, K. X., and Peng, T. P. (2005a). Meso-Cenozoic uplifting and exhumation on Yunkaidashan: Evidence from fission track thermochronology. *Chinese Science Bulletin, 50*(9), 903-909.

Li, X., Qi, C., Liu, Y., Liang, X., Tu, X., Xie, L., and Yang, Y. (2005b). Petrogenesis of the Neoproterozoic bimodal volcanic rocks along the western margin of the Yangtze Block: new constraints from Hf isotopes and Fe/Mn ratios. *Chinese Science Bulletin, 50*(21), 2481-2486.

Li, X. Y., Zheng, J. P. , Ma, Q., Xiong, Q., Griffin, W. L., and Lu, J. G. (2014c). From enriched to depleted mantle: Evidence from Cretaceous lamprophyres and Paleogene basaltic rocks in eastern and central Guangxi Province, western Cathaysia block of South China. *Lithos, 184*, 300-313.

Li, Z. X. (1998). Tectonic history of the major East Asian lithospheric blocks since the Mid-Proterozoic — a synthesis. *Mantle Dynamics and Plate Interactions in East Asia, 27*, 221–243.

Li, Z. X. , Wartho, J. A., Occhipinti, S., Zhang, C. L., Li, X. H., Wang, J., and Bao, C. M. (2007b). Early history of the eastern Sibao Orogen (South China) during the assembly of Rodinia: New mica $^{40}Ar/^{39}Ar$ dating and SHRIMP U-Pb detrital zircon provenance constraints. *Precambrian Research, 159*(1), 79-94.

Li, Z. X., Bogdanova, S. V., Collins, A. S., Davidson, A., De Waele, B., Ernst, R. E., . . . Vernikovsky, V. (2008b). Assembly, configuration, and break-up history of Rodinia: A synthesis. *Precambrian Research, 160*(1), 179-210.

Li, Z. X., Chen, H. L., Li, X. H., and Zhang, F. Q. (2014d). *Tectonics of the South China Block Interpreting the rock record*. Beijing: Science Press, 144 PP.

Li, Z. X., Li, X .H., Wartho, J. A., Clark, C., Li, W. X., Zhang, C. L., and Bao, C. M. (2010). Magmatic and metamorphic events during the early Paleozoic Wuyi-Yunkai orogeny, southeastern South China: New age constraints and pressure-temperature conditions. *Geological Society of America Bulletin, 122*(5), 772-793.

Li, Z. X. and Li, X. H. (2007). Formation of the 1300-km-wide intracontinental orogen and postorogenic magmatic province in Mesozoic South China: A flat-slab subduction model. *Geology, 35*(2), 179-182.

Li, Z. X., Li, X. H. , Li, W. X., and Ding, S. J. (2008c). Was Cathaysia part of Proterozoic Laurentia? – new data from Hainan Island, south China. *Terra Nova, 20*(2), 154-164.

Li, Z. X., Li, X. H., Chung, S. L., Lo, C. H., Xu, X., and Li, W. X. (2012). Magmatic switch-on and switch-off along the South China continental margin since the Permian: Transition from an Andean-type to a Western Pacific-type plate boundary. *Tectonophysics, 532*, 271-290.

Li, Z. X., Li, X. H., Kinny, P. D., and Wang, J. (1999). The breakup of Rodinia: did it start with a mantle plume beneath South China? *Earth and Planetary Science Letters, 173*(3), 171-181.

Li, Z. X., Li, X. H., Zhou, H. W., and Kinny, P. D. (2002b). Grenvillian continental collision in south China: New SHRIMP U-Pb zircon results and implications for the configuration of Rodinia. *Geology, 30*(2), 163-166.

Lin, W., Wang, Q. C., and Chen, K. (2008). Phanerozoic tectonics of south China block: New insights from the polyphase deformation in the Yunkai massif. *Tectonics, 27*(6), 1-16.

Liu, B. J. and Xu, X. S. (1994). *Altas of Lithofacies and Palaeogeography of South China*. Beijing: Science Press, 188 PP.

Liu, M., Cui, X., and Liu, F. (2004). Cenozoic rifting and volcanism in eastern China: a mantle dynamic link to the Indo-Asian collision? *Tectonophysics, 393*(1), 29-42.

Lovera, O. M, Richter, F. M., and Harrison, T. M. (1989). The $^{40}Ar/^{39}Ar$ thermochronometry for slowly cooled samples having a distribution of diffusion domain sizes. *Journal of Geophysical Research, 94*(B12), 17917-17935.

Ludwig, K. R. (2009). *Squid 2: a user's manual*. Berkeley Geochronology Center, Berkeley, California. (pp. 100).

Ludwig, K. R. (2012). *User's manual for Isoplot: a geochronological toolkit for microsoft excel (Berkeley Geochronology Center Special Publication No. 5).* Berkeley Geochronology Center, Berkeley, California. (pp. 75).

Ma, J. L., Wei, G. J., Xu, Y. G., Long, W. G., and Sun, W. D. (2007). Mobilization and re-distribution of major and trace elements during extreme weathering of

basalt in Hainan Island, South China. *Geochimica et Cosmochimica Acta, 71*(13), 3223-3237.

Mao, J. R., Ye, H. M., Liu, K., Li, Z. L., Takahashi, Y., Zhao, X. L., and Kee, W. S. (2013a). The Indosinian collision–extension event between the South China Block and the Palaeo-Pacific plate: Evidence from Indosinian alkaline granitic rocks in Dashuang, eastern Zhejiang, South China. *Lithos, 172*, 81-97.

Mao, J. W., Cheng, Y. B., Chen, M. H., and Franco, P. . (2013b). Major types and time–space distribution of Mesozoic ore deposits in South China and their geodynamic settings. *Mineralium Deposita, 48*(3), 267-294.

Mao, J. W., Pirajno, F. , and Cook, N. . (2011). Mesozoic metallogeny in East China and corresponding geodynamic settings—an introduction to the special issue. *Ore Geology Reviews, 43*(1), 1-7.

McDougall, I. and Harrison, T. M. (1999). *Geochronology and Thermochronology by the $^{40}Ar/^{39}Ar$ Method*. New York: Oxford University Press, PP.

McDowell, F. W., McIntosh, W. C., and Farley, K. A. (2005). A precise ^{40}Ar-^{39}Ar reference age for the Durango apatite (U–Th)/He and fission-track dating standard. *Chemical Geology, 214*(3), 249-263.

Meng, L. F., Li, Z. X., Chen, H. L., Li, X. H., and Wang, X. C. (2012). Geochronological and geochemical results from Mesozoic basalts in southern South China Block support the flat-slab subduction model. *Lithos, 132*, 127-140.

Merrihue, C. and Turner, G. (1966). Potassium-argon dating by activation with fast neutrons. *Journal of Geophysical Research, 71*(11), 2852-2857.

Metcalfe, I. (2011). Palaeozoic–Mesozoic history of SE Asia. *Geological Society, London, Special Publications, 355*(1), 7-35.

Middleton, M. F. (1982). Tectonic history from vitrinite reflectance. *Geophysical Journal of the Royal Astronomical Society, 68*(1), 121-132.

Molnar, P. and Tapponnier, P. (1975). Cenozoic tectonics of Asia: Effects of a continental collision. *Science, 189*(4201), 419-426.

Muffler, L. J. P. and White, D. E. (1969). Active metamorphism of upper Cenozoic sediments in the Salton Sea geothermal field and the Salton Trough, southeastern California. *Geological Society of America Bulletin, 80*(2), 157-182.

Mukhopadhyay, P. K. and Dow, W. G. (1994). *Vitrinite reflectance as a maturity parameter* (Vol. 570): American Chemical Society, PP.

Naeser, C. W. (1969). Etching fission tracks in zircons. *Science, 165*(3891), 388.

Naeser, N. D. (1992). *Miocene Cooling in the Southwestern Powder River Basin, Wyoming: Preliminary Evidence from Apatite Fission-track Analysis* (Vol.

B1917-O): US Department of the Interior, US Geological Survey, O1-O17 PP.

Nasdala, L., Hofmeister, W., Norberg, N., Martinson, J. M., Corfu, F., Dörr, W., . . . Reiners, P. W. (2008). Zircon M257-a Homogeneous Natural Reference Material for the Ion Microprobe U-Pb Analysis of Zircon. *Geostandards and Geoanalytical Research, 32*(3), 247-265.

Nelson, D. R. (2001). Compilation of geochronology data, 2000. Western Australia Geological Survey. *2001/2*

Northrup, C. J., Royden, L. H., and Burchfiel, B. C. (1995). Motion of the Pacific plate relative to Eurasia and its potential relation to Cenozoic extension along the eastern margin of Eurasia. *Geology, 23*(8), 719-722.

Pang, C. J. (2014). *Basin Record of Mesozoic Tectonic Events in Southeast South China.* Doctor of Philosophy; Curtin University, 259 PP.

Pang, C. J. , Krapež, B. , Li, Z. X. , Xu, Y. G. , Liu, H. Q. , and Cao, J. (2014). Stratigraphic evolution of a Late Triassic to Early Jurassic intracontinental basin in southeastern South China: A consequence of flat-slab subduction? *Sedimentary Geology, 302*, 44-63.

Parrish, R. R. and Noble, S. R. (2003). Zircon U-Th-Pb geochronology by isotope dilution—thermal ionization mass spectrometry (ID-TIMS). *Reviews in mineralogy and geochemistry, 53*(1), 183-213.

Peng, B. X., Wang, Y. J., Fan, W. M., Peng, T. P., and Liang, X. Q. (2006). LA-ICPMS zircon U-Pb dating for three Indosinian granitic plutons from central Hunan and western Guangdong provinces and its petrogenetic implications. *Acta Geologica Sinica-English Edition, 80*(5), 660-669.

Peter, W. R. and Todd, A. E. (Eds.). (2005). *Low-temperature thermochronology: Techniques, interpretations, and application.* (Vols. 58): Mineralogical Society of America Geochemical Society.

Price, L. C. (1983). Geologic time as a parameter in organic metamorphism and vitrinite reflectance as an absolute paleogeothermometer. *Journal of Petroleum Geology, 6*(1), 5-37.

Price, P. B. and Walker, R. M. (1962a). Chemical etching of charged-particle tracks in solids. *Journal of applied physics, 33*(12), 3407-3412.

Price, P. B. and Walker, R. M. (1962b). Observation of fossil particle tracks in natural micas. *Nature, 196*(4856), 732-734.

Price, P. B. and Walker, R. M. (1963). Fossil tracks of chanrged particles in mica and the age of minerals. *Journal of Geophysical Research, 68*(16), Medium: X; Size: Pages: 4847-4862.

Qian, L., Bai, Q., Xiong, C., Wu, J., Xu, M., He, D., and Wang, S. (1987). *Mesozoic Coal-bearing Sequences in South China*. Beijing (in Chinese with English abstract): China Coal Industry Publishing House, 322 PP.

Qiu, L., Yan, D. P., Zhou, M. F., Arndt, N. T., Tang, S. L., and Qi, L. (2014). Geochronology and geochemistry of the Late Triassic Longtan pluton in South China: termination of the crustal melting and Indosinian orogenesis. *International Journal of Earth Sciences, 103*(3), 649-666.

Qiu, Y. M., Gao, S., McNaughton, N. J., Groves, D. I., and Ling, W. L. (2000). First evidence of >3.2 Ga continental crust in the Yangtze craton of south China and its implications for Archean crustal evolution and Phanerozoic tectonics. *Geology, 28*(1), 11-14.

Rahn, M. K., Brandon, M. T., Batt, G. E., and Garver, J. I. (2004). A zero-damage model for fission-track annealing in zircon. *American Mineralogist, 89*(4), 473-484.

Reiners, P. W. and Farley, K. A. (2001). Influence of crystal size on apatite (U-Th)/He thermochronology: an example from the Bighorn Mountains, Wyoming. *Earth and Planetary Science Letters, 188*(3), 413-420.

Reiners, P. W., Farley, K. A., and Hickes, H. J. (2002). He diffusion and (U-Th)/He thermochronometry of zircon: initial results from Fish Canyon Tuff and Gold Butte. *Tectonophysics, 349*(1), 297-308.

Reiners, P. W., Spell, T. L., Nicolescu, S., and Zanetti, K. A. (2004). Zircon (U-Th)/He thermochronometry: He diffusion and comparisons with $^{40}Ar/^{39}Ar$ dating. *Geochimica et Cosmochimica Acta, 68*(8), 1857-1887.

Ren, J. S. (1991). On the Geotectonics of Southern China. *Acta Geologica Sinica-English Edition, 4*(2), 111-136.

Ren, J. Y., Tamaki, K, Li, S. T., and Junxia, Z. . (2002). Late Mesozoic and Cenozoic rifting and its dynamic setting in Eastern China and adjacent areas. *Tectonophysics, 344*(3), 175-205.

Renne, P. R. (2006, October 21). *Progress and challenges in K-Ar and $^{40}Ar/^{39}Ar$ geochronology*. Geochronology: Emerging Opportunities, Paleontological Society Short Course, (12). Paleontological Society Papers, Philadelphia, PA.

Renne, P. R., Balco, G., Ludwig, K. R., Mundil, R., and Min, K. (2011). Response to the comment by W.H. Schwarz et al. on "Joint determination of ^{40}K decay constants and $^{40}Ar^{*}/^{40}K$ for the Fish Canyon sanidine standard, and improved accuracy for $^{40}Ar/^{39}Ar$ geochronology" by P.R. Renne et al. (2010). *Geochimica et Cosmochimica Acta, 75*(17), 5097-5100.

Renne, P. R., Sharp, W. D., Deino, A. L., Orsi, G., and Civetta, L. (1997). $^{40}Ar/^{39}Ar$ dating into the historical realm: calibration against Pliny the Younger. *Science, 277*(5330), 1279-1280.

Ritter, U. . (1984). The influence of time and temperature on vitrinite reflectance. *Organic Geochemistry, 6*, 473-480.

Rutherford, E (1905). *Present problems in radioactivity. Popular Science (May).* (pp. 1-34).

Seton, M., Müller, R. D., Zahirovic, S., Gaina, C., Torsvik, T., Shephard, G., . . . Chandler, M. (2012). Global continental and ocean basin reconstructions since 200 Ma. *Earth-Science Reviews, 113*(3), 212-270.

Shi, H. C., Shi, X. B., Yang, X. Q., and Jiang, H. Y. (2013). The Exhumation Process of Mufushan Granite in Jiangnan Uplift Since Cenozoic: Evidence from Low-Temperature Thermochronology. *Chinese Journal of Geophysics, 56*(3), 273-286.

Shi, H. and Li, C. F. (2012). Mesozoic and early Cenozoic tectonic convergence-to-rifting transition prior to opening of the South China Sea. *International Geology Review, 54*(15), 1801-1828.

Shi, X. B., Kohn, B, Spencer, S, Guo, X. W., Li, Y.M., Yang, X. Q., . . . Gleadow, A. (2011). Cenozoic denudation history of southern Hainan Island, South China Sea: Constraints from low temperature thermochronology. *Tectonophysics, 504*(1), 100-115.

Shu, L. S. and Charvet, J. (1996). Kinematics and geochronology of the proterozoic Dongxiang-Shexian ductile shear zone: With HP metamorphism and ophiolitic melange (Jiangnan region, south China). *Tectonophysics, 267*(1-4), 291-302.

Shu, L. S., Deng, P., Wang, B., Tan, Z. Z., Yu, X. Q., and Sun, Y. (2004). Lithology, kinematics and geochronology related to Late Mesozoic basin-mountain evolution in the Nanxiong-Zhuguang area, South China. *Science China Earth Sciences, 47*(8), 673-688.

Shu, L. S., Faure, M. , Wang, B., Zhou, X. M., and Song, B. (2008). Late Palaeozoic–Early Mesozoic geological features of South China: Response to the Indosinian collision events in Southeast Asia. *Comptes Rendus Geoscience, 340*(2), 151-165.

Shu, L. S., Zhou, X. M., Deng, P., Wang, B., Jiang, S. Y., Yu, J. H., and Zhao, X. X. (2009). Mesozoic tectonic evolution of the Southeast China Block: New insights from basin analysis. *Journal of Asian Earth Sciences, 34*(3), 376-391.

Shuster, D. L. and Farley, K. A. (2009). The influence of artificial radiation damage and thermal annealing on helium diffusion kinetics in apatite. *Geochimica et Cosmochimica Acta, 73*(1), 183-196.

Shuster, D. L., Flowers, R. M., and Farley, K. A. (2006). The influence of natural radiation damage on helium diffusion kinetics in apatite. *Earth and Planetary Science Letters, 249*(3), 148-161.

Silk, E. C. H. and Barnes, R. S. (1959). Examination of fission fragment tracks with an electron microscope. *Phil. Mag., 4*(44), 970-972.

Sláma, J., Kosler, J., Condon, D. J., Crowley, J. L., Gerdes, A., Hanchar, J. M., . . . Norberg, N. (2008). Plešovice zircon A new natural reference material for U-Pb and Hf isotopic microanalysis. *Chemical Geology, 249*, 1-35.

Spiegel, C., Kohn, B., Belton, D., Berner, Z., and Gleadow, A. (2009). Apatite (U-Th-Sm)/He thermochronology of rapidly cooled samples: The effect of He implantation. *Earth and Planetary Science Letters, 285*(1), 105-114.

Stern, R. A. (2001). *A new isotopic and trace-element standard for the ion microprobe: preliminary thermal ionization mass spectrometry (TIMS) U-Pb and electron-microprobe data* (Radiogenic Age and Isotopic Studies: Report 14).

Sun, J. S. (1991). Cenozoic volcanic activity in the northern South China Sea and Guangdong coastal area. *Marine Geology & Quaternary Geology, 11*(3), 45.

Sun, M., Chen, N., Zhao, G., Wilde, S. A., Ye, K., Guo, J., . . . Yuan, C. (2008). U-Pb Zircon and Sm-Nd isotopic study of the huangtuling granulite, dabie-sulu belt, China: Implication for the paleoproterozoic tectonic history of the yangtze craton. *American Journal of Science, 308*(4), 469-483.

Sun, T. (2006). A new map showing the distribution of granites in South China and its explanatory notes. *Geological Bulletin of China, 25*(3), 332-335 (in Chinese with English abstract).

Sweeney, J. J. and Burnham, A. K. (1990). Evaluation of a simple model of vitrinite reflectance based on chemical kinetics. *AAPG Bulletin, 74*(10), 1559-1570.

Swindle, T. D., Isachsen, C. E., Weirich, J. R., and Kring, D. A. (2009). ^{40}Ar-^{39}Ar ages of H-chondrite impact melt breccias. *Meteoritics & Planetary Science, 44*(5), 747-762.

Tagami, T. (2005). Zircon fission-track thermochronology and applications to fault studies. *Reviews in Mineralogy and Geochemistry, 58*(1), 95-122.

Tagami, T. and O'Sullivan, P. B. (2005). Fundamentals of fission-track thermochronology. *Reviews in Mineralogy and Geochemistry, 58*(1), 19.

Tagami, T., Carter, A., and Hurford, A. J. (1996). Natural long-term annealing of the zircon fission-track system in Vienna Basin deep borehole samples: constraints upon the partial annealing zone and closure temperature. *Chemical Geology, 130*(1-2), 147-157.

Tagami, T., Galbraith, R. F., Yamada, R., and Laslett, G. M. (1998). Revised annealing kinetics of fission tracks in zircon and geological implications.

Tagami, T. and Shimada, C. (1996). Natural long-term annealing of the zircon fission track system around a granitic pluton. *J. Geophys. Res., 101*(B4), 8245-8255.

Tang, D. L. K., Seward, D, Wilson, C. J. N., Sewell, R. J., Carter, A. , and Paul, B. T. (2014). Thermotectonic history of SE China since the Late Mesozoic: insights from detailed thermochronological studies of Hong Kong. *Journal of the Geological Society, 171*(4), 591-604.

Tao, J. H. (2012). *Indosinian Granites in Central Hunan Province and Southern Jiangxi Province:Geochronology, Petrogenesis and Tectonic implications.* Ph.D. thesis Chinese Academy of Sciences: Guangzhou Institute of Geochemistry, Guangzhou, 188 PP.

Taylor, B. and Hayes, D. E. (1983). Origin and history of the South China Sea basin. *Geophysical Monograph Series, 27*, 23-56.

Tetley, N. , McDougall, I. , and Heydegger, H. R. (1980). Thermal neutron interferences in the $^{40}Ar/^{39}Ar$ dating technique. *Journal of Geophysical Research, 85*(B12), 7201-7205.

Vermeesch, P. (2012). On the visualisation of detrital age distributions. *Chemical Geology, 312*, 190-194.

Wagner, G. A. (1979). Correction and interpretation of fission track ages. *Lectures in isotope geology. Berlin, Springer*, 170-177.

Wagner, G. A., Hejl, E., and Van Den Haute, P. (1994). The KTB fission-track project: Methodical aspects and geological implications. *Radiation Measurements, 23*(1), 95-101.

Wagner, G. A. and Van den Haute, P. (1992). *Fission-Track Dating*. Stuttgart: Enke, 285 PP.

Walker, J. D., Geissman, J. W., Bowring, S. A., and Babcock, L. E. (2012). Geologic Time Scale v. 4.0: Geological Society of America.

Wan, Y., Liu, D., Wilde, S.A., Cao, J., Chen, B., Dong, C., . . . Du, L. (2010). Evolution of the Yunkai Terrane, South China: Evidence from SHRIMP zircon U–Pb dating, geochemistry and Nd isotope. *Journal of Asian Earth Sciences, 37*(2), 140-153.

Wang, F. , Chen, H. L., Batt, G. E., Lin, X. B., Gong, J. F., Gong, G. H., . . . Jourdan, F. (2015). Tectonothermal history of the NE Jiangshan–Shaoxing suture zone: Evidence from 40Ar/39Ar and fission-track thermochronology in the Chencai region. *Precambrian Research, 264*, 192-203.

Wang, J. and Li, Z. X. (2003). History of Neoproterozoic rift basins in South China: implications for Rodinia break-up. *Precambrian Research, 122*(1), 141-158.

Wang, K. L., Chung, S. L., Lo, Y. M., Lo, C. H., Yang, H. J., Shinjo, R., . . . Huang, S. T. (2012). Age and geochemical characteristics of Paleogene basalts drilled from western Taiwan: Records of initial rifting at the southeastern Eurasian continental margin. *Lithos, 155*, 426-441.

Wang, Q, Li, J. W., Jian, P., Zhao, Z. H., Xiong, X. L., Bao, Z. W., . . . Ma, J. L. (2005). Alkaline syenites in eastern Cathaysia (South China): link to Permian-Triassic transtension. *Earth and Planetary Science Letters, 230*(3), 339-354.

Wang, Q, Xu, J. F., Jian, P., Bao, Z. W., Zhao, Z. H., Li, C. F., . . . Ma, J. L. (2006). Petrogenesis of adakitic porphyries in an extensional tectonic setting, Dexing, South China: Implications for the genesis of porphyry copper mineralization. *Journal of Petrology, 47*(1), 119-144.

Wang, X. C. , Li, Z. X. , Li, X. H. , Li, Q. L. , and Zhang, Q. R. . (2011). Geochemical and Hf–Nd isotope data of Nanhua rift sedimentary and volcaniclastic rocks indicate a Neoproterozoic continental flood basalt provenance. *Lithos, 127*(3), 427-440.

Wang, X., Chen, J., and Luo, D. (2008a). Study on petrogenesis of zircons from the Danzhu granodiorite and its geological implications. *Geological Review, 54*(3), 387-398.

Wang, Y. H., Wang, S. C., and Kang, T. S. (1994). Zircon and apatite fission track analysis of Litian thrust belt in Southwest Fujian, China. *Chinese Science Bulletin, 39*(14), 1205-1209.

Wang, Y. J., Fan, W. M., Cawood, P. A., and Li, S. Z. (2008b). Sr-Nd-Pb isotopic constraints on multiple mantle domains for Mesozoic mafic rocks beneath the South China Block hinterland. *Lithos, 106*(3), 297-308.

Wang, Y. J., Fan, W. M., Guo, F., Peng, T. P., and Li, C. W. (2003). Geochemistry of Mesozoic mafic rocks adjacent to the Chenzhou-Linwu fault, South China: Implications for the lithospheric boundary between the Yangtze and Cathaysia blocks. *International Geology Review, 45*(3), 263-286.

Wang, Y. J., Fan, W. M., Sun, M., Liang, X. Q., Zhang, Y. H., and Peng, T. P. (2007). Geochronological, geochemical and geothermal constraints on petrogenesis of the Indosinian peraluminous granites in the South China Block: A case study in the Hunan Province. *Lithos, 96*(3), 475-502.

Wang, Y. J., Fan, W. M., Zhang, G. W., and Zhang, Y. H. (2013). Phanerozoic tectonics of the South China Block: Key observations and controversies. *Gondwana Research, 23*(4), 1273-1305.

Waples, D. W. (1980). Time and temperature in petroleum formation: application of Lopatin's method to petroleum exploration. *AAPG Bulletin, 64*(6), 916-926.

Williams, I. S. (1998). U-Th-Pb geochronology by ion microprobe. *Reviews in Economic Geology, 7*(1), 1-35.

Winter, J. D. (2010). *Principles of igneous and metamorphic petrology* (Vol. 2): Prentice Hall New York, 720 PP.

Wolf, R. A., Farley, K. A., and Kass, D. M. (1998). Modeling of the temperature sensitivity of the apatite (U-Th)/He thermochronometer. *Chemical Geology, 148*(1), 105-114.

Wolf, R. A., Farley, K. A., and Silver, L. T. (1996). Helium diffusion and low-temperature thermochronometry of apatite. *Geochimica et Cosmochimica Acta, 60*(21), 4231-4240.

Wolfe, M. R. and Stockli, D. F. (2010). Zircon (U-Th)/He thermochronometry in the KTB drill hole, Germany, and its implications for bulk He diffusion kinetics in zircon. *Earth and Planetary Science Letters, 295*(1), 69-82.

Wong, J., Sun, M., Xing, G. F., Li, X. H., Zhao, G. C., Wong, K., . . . Wu, F. Y. (2009). Geochemical and zircon U–Pb and Hf isotopic study of the Baijuhuajian metaluminous A-type granite: Extension at 125–100 Ma and its tectonic significance for South China. *Lithos, 112*(3), 289-305.

Wood, D. A. (1988). Relationships between thermal maturity indices calculated using Arrhenius equation and Lopatin method: implications for petroleum exploration. *AAPG Bulletin, 72*(2), 115-134.

Wu, F. Y., Zhang, Y. B., Yang, J. H., Xie, L. W., and Yang, Y. H. (2008). Zircon U–Pb and Hf isotopic constraints on the Early Archean crustal evolution in Anshan of the North China Craton. *Precambrian Research, 167*(3), 339-362.

Wu, Y. B. and Zheng, Y. F. (2004). Genesis of zircon and its constraints on interpretation of U-Pb age. *Chinese Science Bulletin, 49*(15), 1554-1569.

Wu, Y., Gao, S., Zhang, H., Zheng, J., Liu, X., Wang, H., . . . Yuan, H. (2012). Geochemistry and zircon U–Pb geochronology of Paleoproterozoic arc related granitoid in the Northwestern Yangtze Block and its geological implications. *Precambrian Research, 200*, 26-37.

Xia, Y., Xu, X., and Zhu, K. Y. (2012). Paleoproterozoic S-and A-type granites in southwestern Zhejiang: Magmatism, metamorphism and implications for the crustal evolution of the Cathaysia basement. *Precambrian Research, 216*, 177-207.

Xiang, H., Zhang, L., Zhou, H. W., Zhong, Z. Q., Zeng, W., Liu, R., and Jin, S. (2008). U-Pb zircon geochronology and Hf isotope study of metamorphosed basic-ultrabasic rocks from metamorphic basement in southwestern Zhejiang: The response of the Cathaysia Block to Indosinian orogenic event. *Science in China Series D-Earth Sciences, 51*(6), 788-800.

Xu, X. S. , Zhang, M., Zhu, K. Y., Chen, X. M., and He, Z. Y. (2012). hydrothermal fluid leaching. *Lithos, 150*, 256-267.

Xu, X. S., O'Reilly, S. Y., Griffin, W. L., Deng, P., and Pearson, N. J. (2005). Relict Proterozoic basement in the Nanling Mountains (SE China) and its tectonothermal overprinting. *Tectonics, 24*(2), 1-16.

Xu, X. S., O'Reilly, S. Y., Griffin, W. L., Wang, X. L., Pearson, N. J., and He, Z. Y. (2007). The crust of Cathaysia: Age, assembly and reworking of two terranes. *Precambrian Research, 158*(1), 51-78.

Yamada, R., Tagami, T., Nishimura, S., and Ito, H. (1995). Annealing kinetics of fission tracks in zircon: an experimental study. *Chemical Geology, 122*(1), 249-258.

Yan, Y., Carter, A., Xia, B., Ge, L., Brichau, S., and Hu, X. Q. . (2009a). A fission-track and (U-Th)/He thermochronometric study of the northern margin of the South China Sea: An example of a complex passive margin. *Tectonophysics, 474*(3), 584-594.

Yan, Y., Hu, X. Q. , Lin, G. , and Xia, B. (2009b). Denudation history of South China block and sediment supply to northern margin of the South China Sea. *Journal of China University of Geosciences, 20*(1), 57-65.

Yan, Y., Hu, X. Q., Lin, G., Santosh, M., and Chan, L. S. . (2011). Sedimentary provenance of the Hengyang and Mayang basins, SE China, and implications for the Mesozoic topographic change in South China Craton: Evidence from detrital zircon geochronology. *Journal of Asian Earth Sciences, 41*(6), 494-503.

Yang, D. S., Li, X. H., Li, W. X. , Liang, X. Q., Long, W. G. , and Xiong, X. L. (2010). U-Pb and ^{40}Ar-^{39}Ar geochronology of the Baiyunshan gneiss (central Guangdong, south China): constraints on the timing of early Palaeozoic and Mesozoic tectonothermal events in the Wuyun (Wuyi-Yunkai) Orogen. *Geological Magazine, 147*(4), 481-496.

Ye, H. M., Mao, J. R. , Zhao, X. L. , Liu, K. , and Chen, D. D. . (2013). Revisiting Early–Middle Jurassic igneous activity in the Nanling Mountains, South China: Geochemistry and implications for regional geodynamics. *Journal of Asian Earth Sciences, 72*, 108-117.

Ye, H., Zhang, B. T., and Mao, F. Y. (1987). The Cenozoic tectonic evolution of the Great North China: two types of rifting and crustal necking in the Great North China and their tectonic implications. *Tectonophysics, 133*(3), 217-227.

Yu, J. H., O'Reilly, S. Y., Zhou, M. F., Griffin, W. L., and Wang, L. J. (2012). U–Pb geochronology and Hf–Nd isotopic geochemistry of the Badu Complex, Southeastern China: Implications for the Precambrian crustal evolution and paleogeography of the Cathaysia Block. *Precambrian Research, 222*, 424-449.

Yu, J. H., Wang, L., O'Reilly, S. Y., Griffin, W. L., Zhang, M., Li, C., and Shu, L. (2009). A Paleoproterozoic orogeny recorded in a long-lived cratonic remnant (Wuyishan terrane), eastern Cathaysia Block, China. *Precambrian Research, 174*(3), 347-363.

Yu, J. H., Xu, X. S., O'Reilly, S. Y., Griffin, W. L., and Zhang, M. (2003). Granulite xenoliths from Cenozoic Basalts in SE China provide geochemical

fingerprints to distinguish lower crust terranes from the North and South China tectonic blocks. *Lithos, 67*(1), 77-102.

Yu, X. Q., Wu, G. G., Zhao, X. X., Gao, J. F., Di, Y. J., Zheng, Y., . . . Qiu, J. T. (2010). The Early Jurassic tectono-magmatic events in southern Jiangxi and northern Guangdong provinces, SE China: Constraints from the SHRIMP zircon U-Pb dating. *Journal of Asian Earth Sciences, 39*(5), 408-422.

Yue, H. Y., Shu, L. S., Wang, J. F., and Zhang, J. (1998). Mechanism for the Wugongshan granite in Wugongshan Mountain, South China in the Mesozoic. *Geotectonica et Metallogenia, 22*(3), 227-233

Zaun, P. E. and Wagner, G. A. (1982). Fission-track stability in zircons under geological conditions. *Nuclear Tracks and Radiation Measurements, 10*(3), 303-307.

Zaw, K., Peters, S. G., Cromie, P., Burrett, C., and Hou, Z. Q. (2007). Nature, diversity of deposit types and metallogenic relations of South China. *Ore Geology Reviews, 31*(1), 3-47.

Zeitler, P. K., Herczeg, A. L., McDougall, I., and Honda, M. (1987). U-Th-He dating of apatite: A potential thermochronometer. *Geochimica et Cosmochimica Acta, 51*(10), 2865-2868.

Zeng, Q. D., Liu, J. M., Qin, K. Z., Fan, H. R., Chu, S. X., Wang, Y. B., and Zhou, L. L. (2013). Types, characteristics, and time–space distribution of molybdenum deposits in China. *International Geology Review, 55*(11), 1-48.

Zhai, M. G. (2013). The main old lands in China and assembly of Chinese unified continent. *Science China Earth Sciences, 56*(11), 1829-1852.

Zhang, S. H., Jiang, G. Q., and Han, Y. G. (2008). The age of the Nantuo Formation and Nantuo glaciation in South China. *Terra Nova, 20*(4), 289-294.

Zhang, Z. J., Badal, J., Li, Y. K., Chen, Y., Yang, L. Q., and Teng, J. W. (2005). Crust–upper mantle seismic velocity structure across Southeastern China. *Tectonophysics, 395*(1), 137-157.

Zhang, Z., Zhang, G., Tang, S., and Wang, J. (2001). On the age of metamorphic rocks of the Yudongzi Group and the Archean crystalline basement of the Qinling orogen. *Acta Geologica Sinica, 75*(2), 198-204.

Zhao, G. C. and Cawood, P. A. (1999). Tectonothermal evolution of the Mayuan Assemblage in the Cathaysia Block: Implications for Neoproterozoic collision-related assembly of the South China Craton. *American Journal of Science, 299*(4), 309.

Zhao, G. C. and Cawood, P. A. (2012). Precambrian geology of China. *Precambrian Research, 222*, 13-54.

Zhao, K. D., Jiang, S. Y., Sun, T., Chen, W. F., Ling, H. F. , and Chen, P. R. (2013). Zircon U-Pb dating, trace element and Sr-Nd-Hf isotope geochemistry of

Paleozoic granites in the Miao'ershan-Yuechengling batholith, South China: Implication for petrogenesis and tectonic-magmatic evolution. *Journal of Asian Earth Sciences, 74*(0), 244-264.

Zhao, Z. K., Ye, J, Li, H. M., Zhao, Z. H., and Yan, Z. (1991). Extinction of the dinosaurs across the Cretaceous-Tertiary boundary in Nanxiong Basin, Guandong Province. *Vertebrata Palasiatica, 29*(1), 1-20.

Zheng, J. P., Griffin, W. L., Li, L. S., O'Reilly, S. Y., Pearson, N. J., Tang, H. Y., . . . Su, Y. P. (2011). Highly evolved Archean basement beneath the western Cathaysia Block, South China. *Geochimica et Cosmochimica Acta, 75*(1), 242-255.

Zheng, Y. F. , Xiao, W. J., and Zhao, G. C. (2013). Introduction to tectonics of China. *Gondwana Research, 23*(4), 1189-1206.

Zhou, D., Ru, K., and Chen, H. (1995). Kinematics of Cenozoic extension on the South China Sea continental margin and its implications for the tectonic evolution of the region. *Tectonophysics, 251*(1), 161-177.

Zhou, H. M., Xiao, L., Dong, Y. X., Wang, C. Z., Wang, F. Z., and Ni, P. Z. (2009). Geochemical and geochronological study of the Sanshui basin bimodal volcanic rock suite, China: implications for basin dynamics in southeastern China. *Journal of Asian Earth Sciences, 34*(2), 178-189.

Zhou, T. F., Yuan, F., Yue, S. C., Liu, X. D., Zhang, X., and Fan, Y. (2007). Geochemistry and evolution of ore-forming fluids of the Yueshan Cu–Au skarn- and vein-type deposits, Anhui Province, South China. *Ore Geology Reviews, 31*(1), 279-303.

Zhou, X. M. and Li, W. X. (2000). Origin of Late Mesozoic igneous rocks in Southeastern China: implications for lithosphere subduction and underplating of mafic magmas. *Tectonophysics, 326*(3), 269-287.

Zhou, X. M., Sun, T., Shen, W. Z., Shu, L. S., and Niu, Y. L. (2006). Petrogenesis of Mesozoic granitoids and volcanic rocks in South China: A response to tectonic evolution. *Episodes, 29*(1), 26-33.

Zhou, Z. Y., Guo, T. L., Xu, C. H., and Yang, F. L. (2005). Fission track analysis on Mesozoic strata in the Shiwandashan basin, Guangxi province and its geological significance. *Acta Geologica Sinica, 79*(3), 395-401 (in Chinese).

Zhu, B. Q., Wang, H. F. , Chen, Y. W., Chang, X. Y. , Hu, Y. G. , and Xie, J. (2004). Geochronological and geochemical constraint on the Cenozoic extension of Cathaysian lithosphere and tectonic evolution of the border sea basins in East Asia. *Journal of Asian Earth Sciences, 24*(2), 163-175.

Zhu, B. Q., Wang, H. F., Mao, C. X., Zhu, N. J., Huang, R. S., Peng, J. H., and Pu, Z. P. (1991). Geochronology and Nd-Sr-Pb isotopic evidence for mantle source in the ancient subduction zone beneath Sanshui basin, China. *Ceochimica, 20*(1), 27-32 (in Chinese with English abstract).

Zoback, M. L. , Anderson, R. E., and Thompson, G. A. (1981). Cainozoic Evolution of the State of Stress and Style of Tectonism of the Basin and Range Province of the Western United States. *Philosophical Transactions of the Royal Society of London. Series A, Mathematical and Physical Sciences, 300*(1454), 407-434.

Zoback, M. L. and Thompson, G. A. (1978). Basin and Range rifting in northern Nevada: Clues from a mid-Miocene rift and its subsequent offsets. *Geology, 6*(2), 111-116.

Appendices

Appendix A. Sample information and data from Chapter 4: Meizhou

Table A1. Meizhou sample information.

Sample No.	Lithology	Stratigraphic/ magmatic age	GPS (°)[a]
11GDMX06	sandstone	J_2	24.510, 116.297
12GH12-1	shale	J_1	24.561, 116.271
12GH11-1	sandstone	T_3	24.570, 116.274
10GDJL04	tuff	J_1	24.560, 116.024
09SC24-2	sandstone	T_3	24.568, 116.027
09SC23	sandstone	T_3	24.570, 116.028
12GH09	coal	P_2	24.533, 116.162
12GH02-2	porphyry	K_1	24.266, 115.804
12GH08	granite	K_1	24.065, 116.313
12GH13	porphyry	J_3	24.543, 116.275
12GH02-1	granodiorite	S_1	24.266, 115.804
12GH01	granodiorite	S_1	24.168, 115.809

[a]Coordinate system: WGS84.

Table A2. Zircon SHRIMP U-Pb data.

Spot #	U (ppm)	Th (ppm)	Th/U	$^{206}Pb_c$ [a] (%)	Isotopic ratios						Ages (Ma)					
					$^{207}Pb^*/^{206}Pb^*$	1σ (%)	$^{207}Pb^*/^{235}U$	1σ (%)	$^{206}Pb^*/^{238}U$	1σ (%)	$t_{207/206}$	1σ	$t_{207/235}$	1σ	$t_{206/238}$	1σ
12GH01																
1	521	222	0.43	0.08	0.0562	1.4	0.5620	2.3	0.0725	1.8	462	32	453	8	451	8
2	610	242	0.40	-0.02	0.0567	1.0	0.5480	2.4	0.0701	2.2	480	22	444	9	437	9
3	525	213	0.41	0.03	0.0554	1.2	0.5200	2.2	0.0681	1.8	428	27	425	8	424	7
4	656	286	0.44	0.06	0.0564	1.2	0.5600	2.2	0.0720	1.8	470	27	452	8	448	8
5	489	200	0.41	2.62	0.0612	4.7	0.6060	5.0	0.0719	1.9	646	101	481	19	448	8
6	534	228	0.43	0.00	0.0561	1.1	0.5370	2.1	0.0694	1.8	457	24	436	7	433	8
7	541	191	0.35	0.08	0.0564	1.5	0.5520	2.4	0.0710	1.8	469	33	446	9	442	8
8	662	448	0.68	1.10	0.0567	3.1	0.5450	3.6	0.0697	1.8	481	69	442	13	435	8
9	378	148	0.39	0.05	0.0553	1.5	0.5440	2.4	0.0714	1.9	425	33	441	9	444	8
10	496	196	0.40	-0.03	0.0566	1.2	0.5450	2.2	0.0698	1.8	477	26	442	8	435	8
11	641	272	0.42	0.03	0.0565	1.2	0.5470	2.1	0.0701	1.8	474	26	443	8	437	8
12	551	232	0.42	0.13	0.0560	1.5	0.5220	2.3	0.0676	1.8	451	33	426	8	422	7
13	685	288	0.42	0.07	0.0555	1.4	0.5570	2.3	0.0729	1.8	432	30	450	8	453	8
14	608	250	0.41	0.00	0.0555	1.0	0.5240	2.1	0.0685	1.8	432	23	428	7	427	7
													Mean age		**437.9**	**4.2 (2σ)**
12GH02-1																
1	569	302	0.53	-0.17	0.0570	1.7	0.5520	2.9	0.0701	2.3	493	38	446	10	437	10
2	414	320	0.77	-0.36	0.0579	2.5	0.5570	3.4	0.0697	2.4	527	54	450	12	435	10
3	276	209	0.76	0.36	0.0529	3.4	0.5010	4.2	0.0687	2.4	325	77	412	14	429	10
4	467	496	1.06	0.10	0.0549	1.8	0.5330	3.0	0.0704	2.4	409	40	434	11	438	10

5	433	447	1.03	0.16	0.0552	1.9	0.5290	3.1	0.0694	2.4	422	43	431	11	432	10
6	314	179	0.57	-0.08	0.0561	3.1	0.5350	4.9	0.0692	3.8	457	69	435	17	431	16
7	464	441	0.95	0.15	0.0557	1.8	0.5270	3.0	0.0686	2.4	442	41	430	11	428	10
8	359	306	0.85	-0.25	0.0574	2.3	0.5480	3.3	0.0693	2.4	506	50	444	12	432	10
9	505	508	1.01	0.00	0.0542	1.3	0.5200	2.7	0.0696	2.4	378	29	425	9	434	10
10	278	299	1.08	0.00	0.0576	1.7	0.5550	3.0	0.0699	2.4	515	38	448	11	436	10
11	413	485	1.17	0.18	0.0545	2.1	0.5300	3.2	0.0705	2.4	392	48	432	11	439	10
12	309	381	1.23	0.07	0.0540	1.9	0.5110	3.1	0.0686	2.4	373	43	419	11	428	10
13	151	159	1.05	-1.05	0.0620	5.5	0.6060	6.1	0.0709	2.5	674	118	481	23	441	11
14	369	201	0.54	-0.12	0.0574	1.9	0.5540	3.0	0.0700	2.4	506	41	448	11	436	10
15	346	234	0.68	-0.25	0.0558	2.3	0.5360	3.3	0.0697	2.4	444	52	436	12	434	10
16	321	197	0.61	-0.14	0.0561	2.2	0.5380	3.2	0.0695	2.4	458	48	437	11	433	10
17	294	313	1.06	-0.07	0.0570	1.9	0.5530	3.1	0.0703	2.4	491	42	447	11	438	10
													concordia age		**434.3**	**4.8 (2σ)**
													Mean age		**434.2**	**5.0 (2σ)**
12GH13																
1	935	246	0.26	0.07	0.0509	2.0	0.1630	3.0	0.0233	2.3	236	45	153	4	148	3
2	430	404	0.94	0.16	0.0489	3.6	0.1530	4.3	0.0227	2.4	144	85	145	6	144	3
3	287	150	0.52	0.24	0.0480	5.1	0.1490	5.8	0.0226	2.7	98	122	141	8	144	4
4	293	132	0.45	-1.49	0.0597	8.3	0.1950	8.7	0.0237	2.5	592	180	181	14	151	4
5	539	261	0.48	-0.24	0.0513	3.4	0.1630	4.1	0.0230	2.3	254	78	153	6	147	3
6	395	205	0.52	0.57	0.0466	6.4	0.1460	6.9	0.0227	2.5	31	153	138	9	144	4
7	1537	537	0.35	0.08	0.0484	1.6	0.1620	3.7	0.0242	3.3	119	38	152	5	154	5
8	1906	557	0.29	-0.14	0.0503	1.6	0.1620	2.8	0.0233	2.3	207	36	152	4	149	3
9	343	112	0.33	-0.41	0.0498	5.4	0.1570	5.9	0.0228	2.4	185	125	148	8	146	3
10	909	557	0.61	-0.27	0.0518	3.8	0.1630	4.5	0.0229	2.5	276	87	153	6	146	4

11	521	284	0.55	0.68	0.0447	5.6	0.1450	7.9	0.0235	5.6	-73	137	137	10	150	8
12	747	426	0.57	-0.09	0.0493	2.3	0.1560	3.8	0.0230	3.0	162	55	147	5	146	4
13	414	168	0.41	0.47	0.0458	5.5	0.1440	6.2	0.0227	2.9	-12	133	137	8	145	4
14	307	154	0.50	0.00	0.0485	3.0	0.1520	3.8	0.0227	2.4	121	70	144	5	145	3
15	825	320	0.39	-0.21	0.0506	2.2	0.1650	3.2	0.0236	2.4	223	50	155	5	151	4
16	759	277	0.36	-0.13	0.0497	2.2	0.1570	3.3	0.0230	2.5	179	52	148	5	146	4
17	370	133	0.36	-0.51	0.0550	4.9	0.1750	5.4	0.0230	2.4	412	109	164	8	147	3
18	268	130	0.49	-1.11	0.0571	7.2	0.1810	7.6	0.0229	2.4	496	159	169	12	146	3
													Mean age		**146.8**	**1.8 (2σ)**
12GH08																
1	432	310	0.72	-1.16	0.0608	6.0	0.1870	7.0	0.0223	3.5	631	129	174	11	142	5
2	69	39	0.57	-2.09	0.0667	17.6	0.2050	18.5	0.0223	5.4	828	368	189	32	142	8
3	1146	901	0.79	-0.06	0.0487	1.9	0.1480	3.0	0.0220	2.3	135	45	140	4	140	3
4	88	42	0.48	1.41	0.0406	21.3	0.1160	21.5	0.0208	3.4	-313	545	111	23	133	4
5	395	199	0.50	0.18	0.0491	4.1	0.1450	4.7	0.0214	2.4	151	95	137	6	137	3
6	475	312	0.66	0.29	0.0465	4.3	0.1370	5.1	0.0215	2.7	22	104	130	6	137	4
7	559	233	0.42	-0.14	0.0489	3.2	0.1490	4.0	0.0221	2.3	142	75	141	5	141	3
8	455	349	0.77	-0.43	0.0515	4.4	0.1570	5.0	0.0221	2.3	263	101	148	7	141	3
9	608	418	0.69	-0.23	0.0523	3.2	0.1580	4.0	0.0219	2.3	300	73	149	6	140	3
10	339	196	0.58	0.41	0.0475	5.7	0.1400	6.2	0.0215	2.4	72	136	133	8	137	3
11	113	84	0.74	1.91	0.0331	28.7	0.0930	28.9	0.0204	3.3	-870	826	90	25	130	4
12	404	162	0.40	-0.16	0.0496	3.6	0.1490	4.3	0.0218	2.3	178	84	141	6	139	3
13	384	150	0.39	-0.74	0.0535	6.0	0.1600	6.4	0.0217	2.4	351	135	151	9	139	3
14	1129	1007	0.89	0.00	0.0492	1.5	0.1490	2.7	0.0220	2.3	156	35	141	4	140	3
15	522	379	0.73	0.84	0.0412	7.3	0.1200	7.7	0.0212	2.5	-273	186	115	8	135	3
16	1023	973	0.95	0.00	0.0488	1.7	0.1470	3.1	0.0218	2.5	140	41	139	4	139	3
17	464	242	0.52	-0.47	0.0525	4.7	0.1550	5.3	0.0214	2.4	306	107	146	7	137	3

18	503	228	0.45	0.00	0.0503	2.6	0.1520	3.5	0.0219	2.4	211	59	144	5	140	3
19	667	334	0.50	0.25	0.0461	3.9	0.1360	4.6	0.0214	2.3	1	95	129	6	136	3
20	754	681	0.90	0.00	0.0480	2.0	0.1460	3.1	0.0221	2.3	100	48	138	4	141	3
													concordia age		**138.2**	**1.6 (2σ)**
													Mean age		**138.3**	**1.6 (2σ)**

[a] Pb_c and Pb^* indicate the common and radiogenic portions.

Table A3. K-feldspar $^{40}Ar/^{39}Ar$ data of sample 12GH08.

Sample (mineral)	Heating step #.	Temp.(°C)	^{36}Ar (Volt)	1σ (%)	^{37}Ar (Volt)	1σ (%)	^{38}Ar (Volt)	1σ (%)	^{39}Ar (Volt)	1σ (%)	^{40}Ar (Volt)	1σ (%)	40Ar* (%)	$39Ar_K$ (%)	Age (Ma)	2σ
12GH08	1.1	62.0	1.12E-04	9.1	5.75E-04	862.5	2.86E-05	21.2	7.85E-04	1.9	4.69E-02	0.3	28.59	0.10	102.65	46.0
	1.2	64.0	3.59E-04	3.5	2.51E-03	219.1	2.22E-04	7.6	1.10E-02	0.8	2.60E-01	0.1	58.62	1.36	83.70	4.3
	1.3	66.0	2.35E-04	5.7	2.49E-04	1889.7	1.67E-04	7.9	1.04E-02	0.8	2.21E-01	0.2	68.19	1.29	87.28	4.8
	1.4	68.0	3.14E-04	5.0	1.71E-03	284.1	2.34E-04	2.8	1.19E-02	0.6	2.67E-01	0.2	64.76	1.47	87.71	4.8
	1.5	70.0	1.17E-05	79.8	2.57E-03	188.2	3.70E-05	16.1	2.85E-03	1.1	4.76E-02	0.3	92.23	0.35	92.67	11.7
	1.6	71.0	4.44E-04	3.0	3.04E-03	172.9	2.86E-04	3.6	1.63E-02	0.7	3.62E-01	0.1	63.31	2.01	85.03	3.1
	1.7	72.0	1.64E-04	7.9	7.97E-04	594.6	1.95E-04	4.0	1.27E-02	0.6	2.33E-01	0.1	79.00	1.58	86.97	3.7
	1.8	**73.0**	**2.28E-04**	**6.6**	**3.77E-03**	**125.9**	**2.26E-04**	**3.7**	**1.54E-02**	**0.6**	**2.80E-01**	**0.1**	**75.54**	**1.90**	**83.22**	**3.7**[a]
	1.9	**79.0**	**4.28E-04**	**3.1**	**1.82E-03**	**264.6**	**3.94E-04**	**4.4**	**2.31E-02**	**0.6**	**4.43E-01**	**0.2**	**71.08**	**2.85**	**82.33**	**2.3**
	1.10	**80.0**	**4.07E-04**	**3.2**	**2.06E-03**	**228.0**	**3.72E-04**	**4.5**	**2.39E-02**	**0.5**	**4.46E-01**	**0.1**	**72.66**	**2.96**	**81.70**	**2.1**
	1.11	**80.0**	**8.37E-04**	**3.5**	**3.62E-04**	**1364.4**	**7.87E-04**	**2.2**	**4.93E-02**	**0.4**	**9.04E-01**	**0.1**	**72.34**	**6.10**	**80.15**	**2.2**
	1.12	**81.0**	**1.72E-03**	**2.2**	**6.12E-04**	**764.4**	**2.04E-03**	**2.0**	**1.38E-01**	**0.4**	**2.39E+00**	**0.0**	**78.48**	**17.01**	**82.35**	**1.1**
	1.13	**81.0**	**2.19E-03**	**2.0**	**5.77E-03**	**84.9**	**2.93E-03**	**1.3**	**1.98E-01**	**0.4**	**3.37E+00**	**0.0**	**80.53**	**24.50**	**82.67**	**1.0**
	1.14	**82.0**	**1.71E-03**	**1.7**	**4.84E-03**	**101.4**	**2.39E-03**	**1.7**	**1.61E-01**	**0.4**	**2.74E+00**	**0.0**	**81.35**	**19.88**	**83.57**	**0.9**
	1.15	**82.0**	**8.16E-04**	**3.4**	**7.51E-03**	**64.6**	**1.11E-03**	**2.5**	**7.46E-02**	**0.4**	**1.27E+00**	**0.0**	**80.76**	**9.22**	**83.10**	**1.5**
	2.1	**59.0**	**1.13E-04**	**9.8**	**8.11E-05**	**214.5**	**9.32E-05**	**8.6**	**5.68E-03**	**0.9**	**1.12E-01**	**0.2**	**70.08**	**0.70**	**83.78**	**7.1**
	2.2	**63.0**	**3.86E-05**	**17.8**	**3.65E-05**	**482.7**	**3.90E-05**	**18.1**	**2.67E-03**	**1.7**	**4.68E-02**	**0.2**	**75.37**	**0.33**	**79.79**	**9.5**
	2.3	**68.0**	**1.34E-04**	**9.6**	**3.54E-05**	**480.6**	**1.08E-04**	**9.1**	**6.71E-03**	**0.7**	**1.32E-01**	**0.1**	**69.62**	**0.83**	**82.63**	**6.9**
	2.4	**60.0**	**2.27E-04**	**5.3**	**2.50E-04**	**49.6**	**2.35E-04**	**3.3**	**1.58E-02**	**0.6**	**2.80E-01**	**0.1**	**75.77**	**1.95**	**81.38**	**2.8**
	2.5	**65.0**	**2.08E-04**	**5.7**	**2.88E-04**	**47.5**	**4.20E-04**	**3.4**	**2.94E-02**	**0.5**	**4.69E-01**	**0.1**	**86.73**	**3.63**	**83.47**	**1.6**
	J=0.00341900 ± 0.22%				**FCs=28.294 ± 0.13% Ma**				**Laser**				**Plateau age**		**82.78 ± 0.56 Ma**	

[a]Analyses shown in bold were included in plateau or mean age calculation.

Correction factors for interfering isotopes	
$(^{39}Ar/^{37}Ar)_C$	0.000706 ± 7% (1σ)
[a] $(^{36}Ar/^{37}Ar)_C$	0.000281 ± 3% (1σ)
[a] $(^{40}Ar/^{39}Ar)_K$	0.000676 ± 10% (1σ)
Reactor and radiation hours	
USGS TRIGA Reactor (USA) for 40 hours	

Table A4. Zircon (U-Th-Sm)/He data.

Sample #.	N_c[a]	^{238}U (ng)	+/- (%)	^{232}Th (ng)	+/- (%)	^{147}Sm (ng)	+/- (%)	eU (ppm)	He (ncc)	+/- (%)	Th/U	Raw age (Ma)	1σ (Ma)	F_T	Cor. age (Ma)	1σ (Ma)	Mean (Ma)	2σ (Ma)
11GDMX06	1	0.29	2.3	0.26	2.0	0.00	49.9	141.6	4.319	1.2	0.89	101.0	2.3	0.67	**149.7**	**11.0**[b]		
	2	0.91	1.9	0.44	1.5	0.00	33.7	342.6	12.37	1.2	0.48	99.9	2.0	0.69	**144.0**	**10.5**		
	3	0.98	1.9	0.43	1.5	0.01	76.6	273.0	14.76	1.2	0.43	110.9	2.3	0.74	**150.2**	**11.0**		
	4	1.42	1.8	0.27	1.5	0.01	53.2	660.7	16.14	1.2	0.19	88.9	1.9	0.68	**131.5**	**9.6**		
	5	1.61	1.8	0.34	1.5	0.01	21.0	472.0	19.91	1.2	0.21	96.3	2.0	0.72	**134.2**	**9.8**		
																	141.0	**9.2**
12GH11-1	1	1.71	1.9	0.64	1.5	0.00	9.6	506.7	21.05	1.3	0.4	92.2	2.0	0.69	**133.7**	**9.8**		
	2	2.16	1.9	1.13	1.5	0.00	14.0	716.0	29.89	1.3	0.5	100.6	2.2	0.71	**141.6**	**10.4**		
	3	3.85	1.9	0.89	1.5	0.00	17.2	1198.8	46	1.3	0.2	92.5	2.1	0.7	**132.1**	**9.7**		
	4	1.27	2.0	0.51	1.5	0.00	15.3	638.2	16.38	1.3	0.4	96.1	2.1	0.73	**131.7**	**9.7**		
	5	2.29	2.0	0.27	1.5	0.00	17.2	1037.7	28.91	1.3	0.1	100.0	2.4	0.68	**147.0**	**10.9**		
																	136.7	**9.0**
10GDJL04	1	0.16	2.7	0.13	3.8			319.8	1.54	2.5	0.83	68.5	4.1	0.57	**119.6**	**9.3**		
	2	0.16	2.7	0.13	3.8			547.1	1.672	1.9	0.85	73.6	4.3	0.5	**143.5**	**10.9**		
	3	0.21	2.7	0.16	3.8			388.1	2.336	2.1	0.78	78.5	4.3	0.57	**134.8**	**10.4**		
																	131	**12**
09SC24-2	1	0.35	2.4	0.26	1.5	0.00	32.4	512.0	4.704	1.3	0.8	94.4	2.3	0.77	**122.6**	**9.1**		
	2	0.58	1.9	0.31	1.5	0.00	24.8	895.7	8.192	1.3	0.5	101.9	2.2	0.81	**125.8**	**9.2**		
	3	1.32	5.0	0.44	1.5	0.00	15.4	2012.4	15.75	1.3	0.3	90.6	4.4	0.78	**116.1**	**9.9**		
	4	0.78	1.9	0.56	1.5	0.00	9.3	1094.9	11.82	1.3	0.7	105.7	2.2	0.81	**130.4**	**9.5**		
	5	1.07	2.0	0.24	1.5	0.00	26.6	1092.5	10.67	1.3	0.2	77.6	1.8	0.69	**112.4**	**8.3**		
																	121.1	**8.2**
09SC23	1	0.54	2.7	0.71	3.8			327.7	8.84	1.3	1.37	103.1	3.6	0.72	**141.2**	**10.5**		
	2	1.21	2.7	0.68	3.8			687.8	15.88	2.5	0.58	95.1	4.7	0.69	**135.1**	**10.6**		
	3	1.61	2.7	0.72	3.8			623.5	22.27	2.5	0.46	102.7	4.8	0.74	**137.3**	**10.7**		
																	138	**12**

12GH02-2	1	0.21	0.0	0.38	0.0	0.02	0.0	359.1	1.977	0.0	1.79	54.4	1.1	0.53	**103.4**	**7.5**	
	2	0.24	0.0	0.37	0.0	0.00	0.0	304.4	2.249	0.0	1.54	56.6	1.1	0.58	**97.7**	**7.1**	
	3	0.30	0.0	0.50	0.0	0.00	0.0	381.2	3.123	0.0	1.62	60.8	1.2	0.59	**103.6**	**7.5**	
	4	0.13	0.0	0.24	0.0	0.00	0.0	251.0	1.1	0.0	1.78	47.2	0.9	0.49	**95.8**	**7.0**	
	5	0.16	0.0	0.45	0.0	0.00	0.0	347.5	1.738	0.0	2.69	52.9	1.0	0.53	**99.4**	**7.2**	
																	99.8	**6.5**
12GH08	1	0.61	2.9	0.57	4.0	0.02	23.4	227.3	5.656	1.2	0.93	62.5	1.7	0.73	**86.1**	**6.5**	
	2	0.74	2.9	0.50	4.0	0.01	23.2	277.5	5.662	1.2	0.68	54.3	1.5	0.71	**76.0**	**5.7**	
	3	1.87	2.9	1.29	4.0	0.01	13.6	593.4	17.22	1.2	0.68	64.7	1.8	0.73	**88.7**	**6.7**	
	4	1.31	2.9	0.81	4.0	0.01	20.6	862.0	10.73	1.2	0.61	58.4	1.7	0.64	**91.6**	**6.9**	
	5	0.95	2.9	0.60	4.0	0.01	28.9	439.3	7.55	1.2	0.63	56.7	1.6	0.71	**80.1**	**6.1**	
	6	1.28	2.9	1.06	4.0	0.00	32.5	801.1	10.56	1.2	0.82	56.5	1.6	0.67	**83.9**	**6.3**	
																	83.7	**5.2**
12GH13	1	0.70	3.0	0.46	4.0	0.00	33.1	347.8	8.151	1.2	0.66	82.8	2.4	0.69	**120.8**	**9.1**	
	2	0.67	3.0	0.45	4.0	0.00	17.3	362.4	8.4	1.2	0.67	88.2	2.5	0.68	**130.5**	**9.9**	
	3	0.38	2.9	0.26	4.0	0.00	40.1	261.5	4.242	1.2	0.68	79.6	2.3	0.62	**129.3**	**9.8**	
	4	0.92	2.9	0.89	4.0	0.02	14.7	449.0	11.32	1.2	0.96	81.7	2.2	0.69	**117.8**	**8.9**	
	5	0.94	3.0	0.77	4.0	0.00	19.1	333.3	13	1.2	0.81	94.5	2.7	0.71	**133.2**	**10.0**	
	6	0.63	3.0	0.51	4.0	0.01	25.3	292.1	8.351	1.2	0.81	91.5	2.6	0.66	**137.8**	**10.4**	
																	127.5	**7.9**
12GH02-1	1	2.82	2.9	2.33	4.0	0.00	24.8	9306.6	42.05	1.2	0.82	101.9	2.8	0.77	**132.3**	**10.0**	
	2	2.65	3.0	2.30	4.0	0.01	24.1	8016.6	35.2	1.2	0.86	90.1	2.5	0.78	**115.8**	**8.7**	
	3	1.52	3.0	1.47	4.0	0.01	26.2	5513.3	24.4	1.2	0.96	106.9	3.0	0.71	**150.4**	**11.3**	
	4	1.31	3.1	0.99	4.0	0.01	27.2	5626.4	17.97	1.2	0.75	95.1	2.8	0.74	**127.8**	**9.7**	
																	129.3	**9.8**
	1	2.01	1.8	1.47	1.4	0.00	16.0	612.3	37.38	1.3	0.73	129.2	2.7	0.74	174.5	12.7		
12GH01	2	2.68	1.8	2.76	1.4	0.03	12.9	711.8	46.56	1.3	1.02	113.9	2.3	0.76	**150.4**	**10.9**		
	3	1.78	1.8	1.58	1.4	0.00	10.2	927.6	27	1.3	0.88	102.2	2.1	0.65	**156.4**	**11.4**		
	4	1.88	1.8	1.57	1.4	0.01	12.2	677.9	29.26	1.3	0.83	106.2	2.2	0.72	**147.9**	**10.8**		
																	151	**13**

[a] N_c = number of dated apatite or zircon crystals; +/- = analytical errors of individual measurements; ng = nanogram; He = ^{4}He in ncc at STP; ncc = nanocubic centimetre; TAU = total analytical uncertainty; F_T = alpha recoil correction factor after Farley et al. (1996).
[b] Analyses shown in bold were included in mean age calculation.

Table A5. Apatite fission track data.

Sample #.	N	ρ_S	N_s	ρ_i	N_i	ρ_d	N_d	Age (Ma)		P(χ2) (%)	D_{par} (μm)		N(L)	TL (μm)	
								Central	±2σ		Mean	s.d.		Mean	s.d.
11GDMX06	25	7.181	415	14.759	853	7.259	2484	55.3	7.0	99.26	1.85	0.5	103	12.54	1.7
09SC24-2	22	8.398	314	26.049	974	3.675	2484	34.3	4.8	44.63	3.89	0.7			
09SC23	30	10.007	755	23.911	1804	6.321	2484	41.4	4.4	28.92	3.66	1.4			
12GH08	25	3.039	231	4.473	340	5.598	2484	63.5	11	98.96	3.40	0.8			
12GH02-1	40	8.524	813	11.429	1090	5.877	2484	70.8	9.0	1.30	3.78	0.60			
12GH01	25	5.054	507	12.731	1277	7.308	2484	45.5	5.4	46.75	2.78	1.01	102	12.62	1.57

[a]N = number of dated apatite or zircon crystals; ρ_S (ρ_i) = spontaneous (induced) track densities (×10^5 tracks/cm^2); N_s (N_i) = number of counted spontaneous (induced) tracks; ρ_d = dosimeter track density (×10^5 tracks/cm^2); N_d = number of tracks counted on dosimeter; P(χ^2) = probability obtaining chi-square value for n degree of freedom (where n = number of crystals); D_{par} = average etch pit diameter of fission tracks; s.d. = standard deviation; NL = number of horizontal confined tracks measured. TL = horizontal confined track length. Glass dosimeter CN-5 was used. Zeta value was 314.59 ± 3.29.

Table A6. Apatite (U-Th-Sm)/He data.

Sample #.	N_c [a]	^{238}U (ng)	+/- (%)	^{232}Th (ng)	+/- (%)	^{147}Sm (ng)	+/- (%)	eU (ppm)	He (ncc)	+/- (%)	Th/U	Raw age (Ma)	1σ (Ma)	F_T	Cor. age (Ma)	1σ (Ma)	Mean (Ma)	2σ (Ma)
11GDMX06	1	0.03	4.3	0.16	4.1	0.03	1.6	16.1	0.21	1.2	4.7	24.4	0.8	0.72	**33.8**	**2.6**[b]		
	2	0.02	4.3	0.21	4.1	0.08	1.2	15.8	0.23	1.2	9.4	26.1	0.9	0.74	**35.3**	**2.7**		
	3	0.21	4.2	0.20	4.1	0.18	0.8	55.9	1.13	1.2	1.0	36.3	1.3	0.76	**47.9**	**3.8**		
	4	0.05	4.3	0.21	4.1	0.18	0.9	36.6	0.45	1.2	4.4	37.5	1.2	0.69	**54.7**	**4.2**		
	5	0.01	4.4	0.11	4.1	0.05	1.6	18.8	0.10	1.2	12.7	23.7	0.8	0.62	**38.0**	**3.0**		
	6	0.14	4.3	0.36	4.1	0.19	0.9	62.4	0.87	1.2	2.6	31.8	1.0	0.73	**43.5**	**3.4**		
	7	0.10	4.3	0.23	4.1	0.13	0.8	45.2	0.50	1.2	2.4	27.2	0.9	0.72	**37.8**	**2.9**	**(RadialPlotter)**	
																	41	**5**
09SC24-2	1	0.00	4.8	0.21	4.1	0.04	1.8	11.8	0.15	1.2	145.9	24.3	1.0	0.72	**33.8**	**2.7**		
	2	0.03	4.3	0.32	4.1	0.07	1.4	58.0	0.27	1.2	9.8	20.6	0.7	0.60	**34.5**	**2.7**		
	3	0.04	4.3	0.08	4.1	0.03	1.7	19.6	0.40	1.2	2.0	56.6	1.9	0.71	79.5	6.2		
	4	0.03	4.3	0.16	4.1	0.09	1.1	35.6	0.11	1.2	5.8	13.4	0.4	0.66	**20.4**	**1.6**		
	5	0.00	4.5	0.08	4.1	0.07	1.2	14.5	0.07	1.2	17.4	25.9	0.9	0.59	**43.7**	**3.4**		
	6	0.04	4.3	0.03	4.1	0.03	2.3	19.2	0.25	1.2	0.7	48.5	1.9	0.68	71.8	5.8	**(RadialPlotter)**	
																	31.9	**8.8**
12GH02-1	1	0.14	4.3	0.20	4.1	0.07	1.5		0.67	1.2	1.1	31.3	1.2	0.73	**42.9**	**3.4**		
	2	0.06	4.3	0.00	4.1	0.03	2.4		0.20	1.2	0.7	24.1	0.9	0.63	**38.3**	**3.1**		
	3	0.08	4.3	0.10	4.1	0.05	2.2		0.30	1.2	0.9	27.1	1.0	0.66	**41.1**	**3.3**		
	4	0.07	4.3	0.10	4.1	0.04	2.7		0.21	1.2	0.8	19.8	0.8	0.60	**33.0**	**2.6**		
	5	0.08	4.3	0.10	4.1	0.03	2.6		0.24	1.2	0.8	21.2	0.8	0.61	**34.8**	**2.8**		
	6	0.12	4.3	0.10	4.1	0.05	2.3		0.49	1.2	1.0	26.2	1.0	0.71	**36.9**	**2.9**		
	7	0.05	4.3	0.00	4.1	0.04	1.8		0.15	1.2	0.6	21.8	0.9	0.68	**32.1**	**2.6**		

	8	0.08	4.3	0.10	4.1	0.05	2.0		0.26	1.2	0.9	21	0.8	0.61	**34.5**	**2.7**		
	9	0.07	4.4	0.00	4.1	0.03	2.6		0.20	1.2	0.7	21	0.8	0.64	**32.8**	**2.6**		
	10	0.10	4.3	0.10	4.1	0.05	1.7		0.32	1.2	0.9	22.1	0.8	0.66	**33.4**	**2.7**		
																	35.4	**1.8**
12GH01	1	0.10	4.3	0.23	4.1	0.01	2.3	34.1	0.56	1.2	2.3	30.4	1.0	0.73	**41.6**	**3.2**		
	2	0.33	4.2	0.70	4.1	0.06	1.4	38.8	1.71	1.2	2.1	28.4	0.9	0.81	**35.0**	**2.7**		
	3	0.21	4.2	0.45	4.1	0.03	1.8	49.6	1.08	1.2	2.2	28.4	0.9	0.76	**37.2**	**2.9**		
	4	0.17	4.2	0.29	4.1	0.02	2.1	52.3	0.83	1.2	1.7	28.9	1.0	0.75	**38.3**	**3.0**		
	5	0.14	4.3	0.21	4.1	0.02	2.2	42.0	0.61	1.2	1.5	26.6	0.9	0.73	**36.3**	**2.8**		
	6	0.15	4.3	0.39	4.1	0.03	1.9	29.2	0.88	1.2	2.5	29.9	1.0	0.78	**38.4**	**3.0**		
	7	0.22	4.2	0.52	4.1	0.02	2.3	90.0	1.19	1.2	2.4	28.9	1.0	0.74	**39.2**	**3.0**		
																	37.8	**2.2**

[a] N_c = number of dated apatite or zircon crystals; +/- = analytical errors of individual measurements; ng = nanogram; He = ^{4}He in ncc at STP; ncc = nanocubic centimetre; TAU = total analytical uncertainty; F_T = alpha recoil correction factor after Farley et al. (1996).
[b] Analyses shown in bold were included in mean age calculation.

Table A7. Vitrinite reflectance data.

Sample: 12GH12-1	
wave length:	546
Measured Object:	50
Reflectivity type:	Ro
Measure Condition:	Oil
Refractive index of oil:	1.518
Standard Sample:	3.11
Measurement #.	Data
1	3.871
2	3.939
3	3.943
4	3.973
5	3.976
6	4.045
7	4.066
8	4.130
9	4.158
10	4.181
11	4.189
12	4.212
13	4.214
14	4.315
15	4.328
16	4.329
17	4.552
18	4.576
19	4.666
20	4.712

Sample: 12GH09	
wave length:	546
Measured Object:	50
Reflectivity type:	Ro
Measure Condition:	Oil
Refractive index of oil:	1.518
Standard Sample:	0.904
Measurement #.	Data
1	1.810
2	1.872
3	1.879
4	2.276
5	2.290
6	2.301
7	2.387
8	2.414
9	2.423
10	2.553
11	2.952
12	3.104

Appendix B. Data from Chapter 5: Daxi

Table B1. Zircon SHRIMP U-Pb data.

Spot #	U (ppm)	Th (ppm)	Th/U	$^{206}Pb_c$ [a] (%)	Isotopic ratios						Ages (Ma)					
					$^{207}Pb^*/^{206}Pb^*$	1σ (%)	$^{207}Pb^*/^{235}U$	1σ (%)	$^{206}Pb^*/^{238}U$	1σ (%)	$t_{207/206}$	1σ	$t_{207/235}$	1σ	$t_{206/238}$	1σ
12GH14-1	1085	740	0.70	0.07	0.0551	1.0	0.5545	3.6	0.0730	3.5	416	22	448	13	454	15
12GH14-2	1530	849	0.57	0.12	0.0548	1.0	0.5261	5.9	0.0697	5.9	403	23	429	21	434	25
12GH14-3	1051	543	0.53	-0.03	0.0559	0.9	0.5625	2.8	0.0729	2.7	450	19	453	10	454	12
12GH14-4	670	317	0.49	-0.03	0.0557	1.2	0.5499	2.9	0.0715	2.7	442	26	445	11	445	12
12GH14-5	754	374	0.51	-0.04	0.0562	1.0	0.5496	2.9	0.0710	2.7	459	22	445	10	442	11
12GH14-6	974	488	0.52	-0.12	0.0564	1.1	0.5526	2.9	0.0710	2.7	469	24	447	10	442	11
12GH14-7	950	595	0.65	-0.03	0.0559	3.3	0.5462	4.3	0.0709	2.7	448	74	443	15	441	11
12GH14-8	823	492	0.62	0.07	0.0552	1.1	0.5394	2.9	0.0709	2.7	419	25	438	10	442	11
12GH14-9	1416	892	0.65	0.01	0.0554	0.7	0.5558	3.8	0.0727	3.8	430	15	449	14	452	16
12GH14-10	912	470	0.53	-0.04	0.0562	0.9	0.5560	2.8	0.0717	2.7	462	20	449	10	446	12
12GH14-11	1181	741	0.65	-0.04	0.0551	0.8	0.5456	3.5	0.0718	3.4	417	19	442	12	447	15
12GH14-12	692	383	0.57	0.18	0.0565	1.4	0.5660	3.0	0.0727	2.7	471	30	455	11	452	12
12GH14-13	811	436	0.56	0.20	0.0540	1.4	0.5141	3.0	0.0690	2.7	373	30	421	10	430	11
12GH14-14	541	310	0.59	-0.16	0.0568	1.5	0.5449	3.1	0.0696	2.7	484	33	442	11	434	11
12GH14-15	636	395	0.64	0.11	0.0547	1.3	0.5349	3.0	0.0709	2.7	402	30	435	11	441	11
12GH14-16	748	437	0.60	0.00	0.0547	0.9	0.5357	2.8	0.0711	2.7	398	21	436	10	443	11
12GH14-17	826	522	0.65	0.00	0.0559	0.8	0.5388	2.8	0.0699	2.7	449	18	438	10	436	11
12GH14-18	1192	617	0.53	0.04	0.0556	0.8	0.5436	2.8	0.0710	2.7	435	18	441	10	442	11
												Concordia age			**440.7**	**4.3(2σ)**

[a] Pb_c and Pb^* indicate the common and radiogenic portions.

Table B2. $^{40}Ar/^{39}Ar$ data.

Sample (mineral)	Step #.	Power (W)/ Temp (°C)	^{36}Ar (Volt)	1σ (%)	^{37}Ar (Volt)	1σ (%)	^{38}Ar (Volt)	1σ (%)	^{39}Ar (Volt)	1σ (%)	^{40}Ar (Volt)	1σ (%)	40Ar* (%)	$39Ar_K$ (%)	Age (Ma)	2σ
12GH19-1 (biotite)	1	62.0	6.89E-05	13.0	1.93E-03	65.3	5.90E-05	13.2	2.58E-03	1.6	4.48E-02	0.4	53.79	0.61	56.76	12.6
	2	64.0	4.20E-04	3.6	2.05E-03	70.1	1.83E-04	3.8	6.05E-03	0.6	2.24E-01	0.1	43.97	1.42	98.11	8.8
	3	66.0	4.00E-04	4.5	1.56E-04	825.3	3.04E-04	3.4	1.26E-02	0.5	4.01E-01	0.1	70.21	2.95	133.62	5.1
	4	67.0	2.22E-04	6.5	1.33E-03	104.4	3.27E-04	1.8	1.44E-02	0.5	4.78E-01	0.1	86.12	3.37	169.15	3.8
	5	68.0	1.60E-04	7.3	1.13E-03	148.2	7.14E-04	2.0	3.51E-02	0.5	1.18E+00	0.1	95.98	8.26	189.27	2.1
	6	**68.5**	**9.27E-05**	**11.3**	**2.47E-05**	**4461.3**	**7.83E-04**	**2.6**	3.90E-02	**0.5**	**1.30E+00**	**0.0**	**97.87**	**9.16**	**191.49[a]**	**2.1**
	7	**69.0**	**8.74E-05**	**12.1**	**4.12E-04**	**292.6**	**7.64E-04**	**1.9**	3.75E-02	**0.5**	**1.26E+00**	**0.1**	**97.93**	**8.80**	**192.36**	**1.9**
	8	**69.5**	**8.77E-05**	**15.5**	**4.15E-04**	**318.7**	**6.54E-04**	**3.5**	3.10E-02	**0.6**	**1.06E+00**	**0.0**	**97.52**	**7.29**	**194.30**	**2.6**
	9	**70.0**	**1.04E-04**	**15.2**	**2.32E-03**	**55.9**	**7.24E-04**	**1.5**	3.54E-02	**0.4**	**1.21E+00**	**0.2**	**97.44**	**8.33**	**194.83**	**2.2**
	10	**70.5**	**1.04E-04**	**11.4**	**5.45E-04**	**261.5**	**7.45E-04**	**1.0**	3.63E-02	**0.4**	**1.22E+00**	**0.1**	**97.45**	**8.54**	**192.32**	**2.0**
	11	**71.0**	**1.30E-04**	**10.1**	**1.06E-03**	**143.1**	**1.23E-03**	**2.3**	6.12E-02	**0.4**	**2.04E+00**	**0.0**	**98.10**	**14.38**	**191.73**	**1.6**
	12	71.5	1.25E-04	8.2	6.91E-05	2119.0	1.06E-03	1.4	5.42E-02	0.4	1.87E+00	0.0	98.00	12.74	197.32	1.7
	13	72.0	1.28E-04	8.3	8.46E-04	147.2	7.19E-04	2.0	3.63E-02	0.4	1.19E+00	0.1	96.79	8.52	186.23	1.8
	14	80.0	2.38E-04	5.8	6.14E-04	177.0	3.57E-04	3.2	1.54E-02	0.5	5.67E-01	0.1	87.45	3.62	188.86	3.5
	15	82.0	5.33E-04	3.0	1.13E-03	124.4	2.69E-04	5.8	8.55E-03	0.7	4.32E-01	0.1	63.11	2.01	186.84	6.6
	J=0.00341900 ± 0.22%				**FCs=28.294 ± 0.13% Ma**			**Laser**						**Weighted mini plateau age**		**192.6 ± 1.2 Ma**
11GG10-1 (muscovite)	1	58.7	6.75E-05	11.7	4.53E-05	191.3	2.92E-05	25.7	1.48E-03	1.7	5.91E-02	0.3	65.92	1.54	155.34	18.8
	2	59.1	4.28E-05	23.2	1.11E-05	772.3	4.46E-05	18.7	2.47E-03	1.4	8.68E-02	0.3	85.28	2.57	175.48	14.2
	3	59.6	1.41E-04	6.5	2.37E-05	418.8	7.92E-05	10.4	4.00E-03	0.7	1.68E-01	0.1	74.90	4.15	183.88	8.0
	4	60.1	6.47E-05	10.9	5.35E-05	184.9	5.86E-05	11.4	3.86E-03	0.9	1.37E-01	0.1	85.85	4.01	178.14	6.8
	5	61.0	4.59E-05	18.2	4.59E-05	205.5	1.04E-04	7.7	6.77E-03	0.7	2.17E-01	0.1	93.70	7.03	176.30	4.8
	6	**62.0**	**7.42E-05**	**9.4**	**5.25E-05**	**205.6**	**1.92E-04**	**4.1**	**1.31E-02**	**0.6**	**3.98E-01**	**0.1**	**94.43**	**13.58**	**168.83**	**2.6**

	7	**63.0**	**8.33E-05**	**13.1**	**7.83E-05**	**107.9**	**1.48E-04**	**7.3**	**1.14E-02**	**0.8**	**3.46E-01**	**0.1**	**92.80**	**11.80**	**166.20**	**4.1**
	8	**64.0**	**2.38E-05**	**33.0**	**1.20E-05**	**782.9**	**7.09E-04**	**2.6**	**5.33E-02**	**0.4**	**1.51E+00**	**0.0**	**99.53**	**55.31**	**166.21**	**1.4**
	J=0.00341900 ± 0.22%			**FCs=28.294 ± 0.13% Ma**			**Laser**						**Weighted plateau age**		**166.7 ± 1.6 Ma**	
09SC02-1 (muscovite)	1	57.1	4.08E-05	15.9	4.14E-05	482.6	7.40E-06	89.4	3.53E-04	3.0	2.83E-02	0.5	57.00	0.14	261.96	60.3
	2	57.5	1.67E-05	36.8	8.66E-05	233.9	1.50E-05	39.4	8.63E-04	1.4	3.65E-02	0.4	86.38	0.34	211.96	24.0
	3	58.0	7.60E-06	80.0	6.19E-05	339.0	2.08E-05	34.6	1.95E-03	2.3	8.58E-02	0.2	97.37	0.76	245.91	14.7
	4	58.3	5.02E-05	14.1	1.64E-04	129.1	7.41E-05	11.5	5.43E-03	0.6	2.65E-01	0.1	94.34	2.12	262.87	5.1
	5	58.7	4.32E-05	17.2	1.01E-04	200.8	1.50E-04	7.0	1.03E-02	0.7	5.08E-01	0.1	97.46	4.02	273.24	4.4
	6	59.1	3.70E-05	21.6	1.08E-04	197.7	3.48E-04	3.9	2.76E-02	0.4	1.29E+00	0.1	99.14	10.73	264.26	2.3
	7	59.6	8.75E-05	10.2	8.00E-05	265.2	9.55E-04	2.2	7.22E-02	0.4	2.84E+00	0.0	99.08	28.11	225.50	1.6
	8	60.1	2.48E-05	29.0	1.26E-04	167.7	5.97E-04	2.1	4.56E-02	0.4	1.35E+00	0.1	99.45	17.76	173.32	1.5
	9	61.0	1.16E-05	58.6	2.34E-04	87.1	1.53E-04	10.0	1.21E-02	0.5	3.50E-01	0.1	99.02	4.70	168.70	2.4
	10	62.0	6.00E-07	1102.0	2.54E-04	84.0	9.07E-05	12.2	6.70E-03	0.6	1.93E-01	0.1	100.10	2.61	169.20	3.8
	11	63.0	2.80E-06	228.8	2.76E-04	73.9	5.71E-05	14.2	4.17E-03	1.9	1.22E-01	0.1	99.32	1.62	169.96	8.0
	12	66.0	1.20E-06	484.2	3.35E-04	60.6	1.27E-05	53.7	1.35E-03	1.8	3.90E-02	0.2	100.98	0.53	171.13	15.5
	J=0.00341900 ± 0.22%			**FCs=28.294 ± 0.13% Ma**			**Laser**						**Age constrain**		**< ~ 169 Ma**	
08FG-1 (biotite)	1	550	2.57E-04	6.1	6.79E-04	2.8	4.42E-04	4.1	2.57E-02	0.3	1.89E-01	0.1	73.31	2.87	76.35	7.1
	2	**600**	**2.48E-04**	**4.2**	**4.04E-04**	**3.0**	**4.90E-04**	**2.4**	**3.21E-02**	**0.3**	**3.86E-01**	**0.1**	**88.46**	**3.59**	**158.24**	**4.6**
	3	**650**	**2.04E-04**	**8.9**	**4.40E-04**	**2.6**	**9.68E-04**	**3.1**	**6.88E-02**	**0.3**	**7.50E-01**	**0.1**	**96.08**	**7.70**	**160.03**	**3.1**
	4	**700**	**1.81E-04**	**3.3**	**4.62E-04**	**2.2**	**1.47E-03**	**1.8**	**1.05E-01**	**0.1**	**1.10E+00**	**0.1**	**98.09**	**11.74**	**158.66**	**1.5**
	5	**750**	**1.23E-04**	**7.5**	**4.27E-04**	**1.9**	**1.17E-03**	**2.5**	**8.57E-02**	**0.2**	**8.95E-01**	**0.1**	**99.73**	**9.59**	**159.43**	**2.0**
	6	**800**	**1.21E-04**	**5.0**	**4.45E-04**	**4.6**	**7.96E-04**	**2.2**	**5.60E-02**	**0.4**	**5.92E-01**	**0.1**	**99.97**	**6.26**	**159.09**	**2.6**
	7	850	1.11E-04	9.2	4.96E-04	3.8	5.77E-04	2.1	4.03E-02	0.3	4.50E-01	0.1	99.99	4.51	164.64	2.2
	8	900	1.30E-04	5.6	5.28E-04	3.3	6.08E-04	2.1	4.19E-02	0.3	4.75E-01	0.1	99.92	4.68	167.13	3.2
	9	**950**	**1.40E-04**	**6.7**	**5.88E-04**	**2.9**	**8.74E-04**	**2.2**	**6.20E-02**	**0.3**	**6.70E-01**	**0.1**	**99.63**	**6.93**	**161.75**	**2.5**
	10	**1000**	**1.39E-04**	**5.5**	**7.04E-04**	**2.9**	**1.92E-03**	**1.7**	**1.42E-01**	**0.2**	**1.47E+00**	**0.1**	**99.93**	**15.91**	**159.54**	**1.5**
	11	**1050**	**1.77E-04**	**7.2**	**8.08E-04**	**3.0**	**1.92E-03**	**1.0**	**1.42E-01**	**0.2**	**1.47E+00**	**0.0**	**99.21**	**15.94**	**158.47**	**1.6**
	12	**1100**	**2.63E-04**	**4.1**	**1.64E-03**	**1.9**	**1.15E-03**	**1.6**	**8.32E-02**	**0.2**	**9.03E-01**	**0.1**	**95.98**	**9.31**	**158.39**	**2.1**
	13	**1200**	**1.79E-04**	**2.8**	**5.05E-04**	**3.4**	**1.39E-04**	**5.8**	**8.01E-03**	**0.9**	**1.23E-01**	**0.2**	**90.99**	**0.89**	**157.87**	**14.3**
	14	1300	1.96E-04	4.5	4.15E-04	3.7	5.10E-05	15.5	5.30E-04	2.8	4.94E-02	0.2	20.03	0.06	48.46	274.4

15	1400	2.06E-04	5.2	4.20E-04	4.1	4.60E-05	11.3	9.40E-05	5.6	5.47E-02	0.3	0.00	0.01	0.00	0.0
J=0.0091360 ± 0.21%			**FCs=28.030 ± 0.28% Ma**			**Furnace**							**Weighted mean age**		**159.2 ± 0.9 Ma**

[a]Analyses shown in bold were included in plateau or mean age calculation.

12GH19-1, 11GG10-1. 09SC02-1		08FG-1	
Correction factors for interfering isotopes			
$(^{39}Ar/^{37}Ar)_{Ca}$	0.000706 ± 7% (1σ)	$(^{39}Ar/^{37}Ar)_{Ca}$	0.00073 ± 11% (1σ)
$(^{36}Ar/^{37}Ar)_{Ca}$	0.000281 ± 3% (1σ)	$(^{36}Ar/^{37}Ar)_{Ca}$	0.000282 ± 1% (1σ)
$(^{40}Ar/^{39}Ar)_{K}$	0.000676 ± 10% (1σ)	$(^{40}Ar/^{39}Ar)_{K}$	0.000676 ± 10% (1σ)
Reactor and radiation hours			
USGS TRIGA Reactor (USA) for 40 hours		McMaster University Reactor (Canada) for 25 hours	

Table B3. Apatite and zircon fission track data.

Sample #.	N	ρ_S	N_s	ρ_i	N_i	ρ_d	N_d	Central age (Ma)		$P(\chi^2)$	D_{par} (μm)		NL	TL (μm)	
								Age	1σ	(%)	Mean	s.d.		Mean	s.d.
						Apatite									
10GDDX32-1	15	2.349	107	5.686	259	6.469	2484	42.1	5.1	65.9	1.8	0.3			
12GH14	25	8.098	624	16.520	1273	6.864	2484	52.7	2.8	80.6	2.2	0.3	97.0	13.3	1.3
11GG10-1	25	7.282	577	15.762	1249	7.061	2484	51.1	2.8	99.9	1.8	0.2			
12GH19-1	25	3.145	171	8.092	440	6.962	2484	42.4	3.9	86.2	3.3	0.7			
09SC11-1	25	2.095	174	4.745	394	6.271	2484	43.4	4.1	99.8	1.6	0.2			
						Zircon									
09DX02	25	237.092	2250	206.322	1958	13.645	4932	95	3.5	84.5					
12GH20	25	157.926	1169	104.834	776	11.861	4878	108.1	5.5	78.4					
12GH14	25	176.566	1374	144.183	1122	13.714	4878	101.6	4.6	57.7					
12GH19-1	25	186.968	1313	126.022	885	13.441	4878	120.5	5.8	67.4					
09SC11-1	25	154.110	1053	145.182	992	10.809	4932	69.7	3.8	21.6					

[a]N = number of dated apatite or zircon crystals; ρ_S (ρ_i) = spontaneous (induced) track densities ($\times 10^5$ tracks/cm^2); N_s (N_i) = number of counted spontaneous (induced) tracks; ρ_d = dosimeter track density ($\times 10^5$ tracks/cm^2); N_d = number of tracks counted on dosimeter; $P(\chi^2)$ = probability obtaining chi-square value for n degree of freedom (where n = number of crystals); D_{par} = average etch pit diameter of fission tracks; s.d. = standard deviation; NL = number of horizontal confined tracks measured. TL = horizontal confined track length. Glass dosimeter CN-5 for apatite samples and CN-1 for zircon samples, and zeta value of 314.59 ± 3.29 for apatites and 121.01 ± 1.73 for zircons.

Table B4. Apatite and zircon (U-Th-Sm)/He data.

Sample #.	N_c[a]	^{238}U (ng)	+/- (%)	^{232}Th (ng)	+/- (%)	^{147}Sm (ng)	+/- (%)	eU (ppm)	He (ncc)	+/- (%)	TAU (%)	Th/U	Raw age (Ma)	1σ (Ma)	F_T	Cor. age (Ma)	1σ (Ma)	Mean (Ma)	2σ (Ma)
										Apatite									
12GH14	1	0.06	5.9	0.1	5.8	0.04	1.8	70.9	0.3	1.5	4.6	2.00	25.6	1.2	0.63	**40.6**	**3.4**[b]		
	2	0.04	4.4	0.1	4.1	0.02	3.1	75.5	0.2	1.5	3.6	2.01	24.0	0.9	0.53	**45.6**	**3.6**		
	3	0.03	4.3	0.1	4.1	0.03	2.2	44.1	0.1	1.5	3.4	2.80	23.5	0.8	0.54	**43.1**	**3.4**		
																		43.0	**4.0**
08FG-1	1	0.00	3.9	0.1	3.7	/	/	25.0	0.2	2.3	3.5	3.82	21.3	0.7	0.70	**31.9**	**2.5**		
	2	0.10	3.9	0.3	3.7	/	/	40.5	0.4	2.8	3.9	4.13	24.6	0.9	0.70	**37.0**	**3.0**		
	3	0.00	3.9	0.1	3.8	/	/	34.4	0.2	2.2	3.5	4.16	25.8	0.9	0.60	**40.8**	**3.2**		
																		35.8	**3.3**
09SC11-1	1	0.03	4.4	0.1	4.1	0.16	1.0	42.7	0.2	1.4	3.2	4.03	25.3	0.8	0.59	**43.2**	**3.3**		
	2	0.02	4.3	0.1	4.1	0.17	0.9	33.9	0.1		1.4	3.33	25.6	0.8	0.54	**47.7**	**3.7**		
	3	0.09	4.3	0.3	4.1	0.42	0.6	75.8	0.5	1.3	3.2	3.79	24.8	0.8	0.65	**37.9**	**2.9**		
	4	0.04	4.3	0.2	4.1	0.16	1.0	66.6	0.2	1.3	3.2	4.66	24.9	0.8	0.58	**43.3**	**3.3**		
	5	0.02	4.3	0.1	4.1	0.15	0.9	53.0	0.1	1.4	3.2	3.93	22.3	0.7	0.48	**46.7**	**3.6**		
																		43.2	**3.0**
										Zircon									
10GDDX34	1	0.5	2.0	0.31	1.5	0.005	39.5	204.0	7.6	1.2	2.1	0.60	107.5	2.3	0.70	**152.9**	**11.2**		
	2	0.7	2.1	0.30	1.5	0.001	15.4	502.7	8.1	1.2	2.3	0.43	86.9	2.0	0.64	**134.8**	**9.9**		
	3	1.2	2.2	0.37	1.5	0.003	27.6	909.0	14.5	1.2	2.4	0.30	91.0	2.1	0.64	**142.1**	**10.5**		
	4	0.2	2.0	0.08	1.6	0.008	75.4	160.2	3.4	1.2	2.2	0.33	106.0	2.3	0.65	**162.9**	**12.0**		
																		147	**11**
10GDDX32-1	1	0.2	2.0	0.32	1.5	0.007	11.2	99.4	3.2	1.2	1.9	1.35	83.3	1.6	0.69	**120.1**	**8.7**		
	2	1.0	2.0	0.34	1.5	0.004	25.4	285.3	14.0	1.2	2.2	0.34	106.4	2.3	0.72	**147.5**	**10.8**		
	3	0.2	2.1	0.23	1.5	0.009	54.1	160.0	3.1	1.2	2.1	0.98	86.6	1.8	0.64	**135.4**	**9.9**		
	4	0.4	2.0	0.19	1.5	0.008	63.3	321.1	5.4	1.2	2.2	0.44	94.7	2.1	0.64	**147.8**	**10.8**		
	5	0.5	2.0	0.35	1.5	0.006	38.7	430.7	6.6	1.2	2.1	0.72	96.0	2.0	0.63	**151.3**	**11.0**		
																		138.3	**9.1**

09DX08	1	1.9	2.0	0.95	1.5	0.009	34.3	953.2	21.1	1.2	2.2	0.50	81.1	1.8	0.68	**119.3**	**8.7**	
	2	0.5	2.0	0.28	1.5	0.002	11.8	276.1	6.2	1.2	2.2	0.57	92.1	2.0	0.66	**139.8**	**10.2**	
	3	0.6	2.0	0.47	1.5	0.003	15.2	290.1	7.8	1.2	2.1	0.82	94.2	2.0	0.67	**140.6**	**10.3**	
																	132	**11**
09DX02	1	0.8	1.8	0.14	1.5	0.001	12.5	612.3	6.0	1.2	2.1	0.18	60.1	1.3	0.63	**95.0**	**6.9**	
	2	0.5	1.8	0.18	1.5	0.002	35.6	684.7	4.4	1.2	2.1	0.33	61.6	1.3	0.55	**111.4**	**8.1**	
	3	0.7	1.8	0.11	1.5	0.000	27.8	816.0	5.1	1.2	2.1	0.16	57.2	1.2	0.54	**105.3**	**7.7**	
																	103.0	**8.7**
10GDDX01-2	1	0.4	2.6	0.30	2.2	0.007	8.5	168.9	3.8	1.2	2.5	0.73	64.4	1.6	0.67	**96.5**	**7.2**	
	2	1.4	2.1	0.44	1.5	0.003	12.7	371.0	13.1	1.2	2.3	0.30	69.1	1.6	0.75	**92.2**	**6.8**	
	3	0.2	2.1	0.05	1.8	0.001	17.4	32.5	1.7	1.2	2.4	0.22	61.1	1.5	0.79	**77.3**	**5.7**	
	4	1.0	2.0	0.38	1.5	0.002	21.0	277.5	7.4	1.2	2.2	0.37	55.4	1.2	0.75	**74.1**	**5.4**	
	5	0.5	2.0	0.26	1.5	0.002	10.4	270.5	4.1	1.2	2.2	0.51	59.8	1.3	0.65	**91.6**	**6.7**	
																	85.8	**8.2**
12GH20	1	2.2	2.0	0.64	1.5	0.005	20.7	402.1	16.7	1.2	2.2	0.29	59.1	1.3	0.75	**78.5**	**5.8**	
	2	0.3	2.0	0.22	1.5	0.003	38.6	141.9	2.4	1.2	2.1	0.70	55.0	1.1	0.70	**78.9**	**5.8**	
	3	1.5	2.0	0.32	1.5	0.003	15.5	541.8	12.8	1.2	2.2	0.22	68.3	1.5	0.70	**97.2**	**7.1**	
	4	1.1	2.0	0.51	1.5	0.005	29.9	282.6	10.2	1.2	2.1	0.47	69.6	1.5	0.74	**94.0**	**6.9**	
																	85.5	**6.3**
12GH14	1	1.3	3.0	0.68	4.0	0.003	37.6	715.9	12.2	1.2	2.9	0.50	66.3	1.9	0.69	**96.2**	**7.3**	
	2	1.1	2.9	0.56	4.0	0.001	36.7	666.9	9.8	1.2	2.9	0.51	65.9	1.9	0.68	**97.1**	**7.4**	
	3	0.7	2.9	0.33	4.0	0.001	26.1	552.8	5.9	1.2	2.9	0.46	61.7	1.8	0.64	**95.6**	**7.3**	
	4	0.9	3.0	0.47	4.0	0.001	40.7	677.4	8.1	1.2	2.9	0.50	63.4	1.9	0.65	**96.9**	**7.3**	
	5	1.1	3.0	0.52	4.0	0.004	40.4	603.0	9.4	1.2	2.9	0.49	65.4	1.9	0.67	**97.3**	**7.4**	
																	96.6	**6.6**
11GG10-1	1	0.8	2.0	0.20	1.5	0.001	12.9	502.2	7.3	1.2	2.2	0.25	70.8	1.6	0.65	**108.9**	**8.0**	
	2	1.3	2.0	0.24	1.5	0.002	13.0	807.8	12.6	1.2	2.2	0.18	76.4	1.7	0.66	**115.7**	**8.5**	
	3	3.0	2.0	0.58	1.5	0.012	28.7	1011.9	27.4	1.2	2.2	0.19	71.2	1.6	0.70	**101.4**	**7.4**	
	4	2.9	2.0	0.68	1.5	0.021	48.1	839.9	26.4	1.2	2.2	0.23	70.7	1.6	0.74	**94.9**	**7.0**	
	5	3.3	2.0	0.95	1.5	0.012	10.7	1029.6	31.7	1.2	2.2	0.29	73.8	1.6	0.74	**99.5**	**7.3**	
																	103.1	**6.8**
09SC02-1	1	2.4	1.8	0.19	1.5	0.011	30.2	2385.1	14.0	1.3	2.2	0.08	46.9	1.0	0.59	**79.3**	**5.8**	
	2	1.1	1.8	0.30	1.5	0.008	35.9	1319.1	6.1	1.3	2.1	0.28	44.4	0.9	0.56	**78.7**	**5.8**	
	3	1.9	1.9	0.52	1.4	0.007	43.5	2128.1	11.6	1.3	2.2	0.28	47.9	1.0	0.57	**84.6**	**6.2**	

	4	0.3	1.8	0.03	2.0	0.000	17.3	569.3	1.7	1.3	2.2	0.11	49.6	1.1	0.50	**99.7**	**7.3**	
																		84.1	**6.2**
12GH19-1	1	0.9	1.8	0.38	1.5	0.004	39.3	552.3	10.0	1.3	2.1	0.42	82.7	1.8	0.63	**85.0**	**13.5**		
	2	1.8	1.8	0.60	1.4	0.002	8.6	1252.4	19.5	1.3	2.2	0.33	81.6	1.8	0.63	**129.4**	**13.2**		
	3	3.2	1.8	0.74	1.4	0.011	32.9	1516.6	30.6	1.2	2.1	0.23	73.8	1.5	0.66	**111.5**	**11.4**		
																		109	**15**
08FG-1	1	9.2	4.1	4.13	4.1	/	/	1663.5	95.8	2.5	4.5	0.45	81.8	3.6	0.74	**111.2**	**9.2**		
	2	7.1	4.1	2.70	4.1	/	/	1936.7	73.4	2.5	4.5	0.38	83.1	3.7	0.74	**112.3**	**9.4**		
	3	3.7	4.1	2.17	4.1	/	/	966.4	41.1	2.5	4.4	0.59	85.6	3.7	0.73	**118.0**	**9.8**		
	4	8.8	4.1	6.50	4.1	/	/	1922.8	84.5	2.5	4.4	0.74	71.4	3.0	0.65	**109.0**	**9.0**		
	5	5.8	4.1	2.29	4.1	/	/	1501.7	52.8	2.5	4.5	0.40	73.2	3.2	0.69	**106.5**	**8.9**		
																		111.1	**8.3**
09SC11-1	1	0.6	1.8	0.37	1.5	0.005	44.8	640.6	4.1	1.2	2.0	0.57	46.3	0.9	0.58	**79.8**	**5.8**		
	2	0.2	1.9	0.11	1.5	0.007	45.5	387.9	1.2	1.2	2.0	0.52	41.1	0.8	0.51	**79.9**	**5.8**		
	3	1.1	1.8	0.60	1.4	0.003	17.4	442.1	7.2	1.2	2.0	0.54	47.3	1.0	0.70	**67.7**	**4.9**		
																		74.8	**6.3**

[a] N_c = number of dated apatite or zircon crystals; +/- = analytical errors of individual measurements; ng = nanogram; He = ^{4}He in ncc at STP; ncc = nanocubic centimetre; TAU = total analytical uncertainty; F_T = alpha recoil correction factor after Farley et al. (1996).

[b] Analyses shown in bold were included in mean age calculation.

Appendix C. Data from Chapter 6: Shaoguan-Longnan

Table C1. Zircon SHRIMP U-Pb data.

Spot #	U (ppm)	Th (ppm)	Th/U	$^{206}Pb_c$ [a] (%)	Isotopic ratios						Ages (Ma)					
					$^{207}Pb^*/^{206}Pb^*$	1σ (%)	$^{207}Pb^*/^{235}U$	1σ (%)	$^{206}Pb^*/^{238}U$	1σ (%)	$t_{207/206}$	1σ	$t_{207/235}$	1σ	$t_{206/238}$	1σ
12GH15																
12GH15-1	938	338	0.37	-0.25	0.0517	6.3	0.1802	6.8	0.0253	2.7	272	144	168	11	161	4
12GH15-2	846	358	0.44	0.14	0.0497	2.3	0.1715	3.5	0.0250	2.7	183	54	161	5	159	4
12GH15-3	1055	415	0.41	-0.15	0.0512	1.9	0.1803	3.3	0.0255	2.7	251	43	168	5	163	4
12GH15-4	1165	1389	1.23	-0.33	0.0527	7.2	0.1840	7.7	0.0253	2.7	317	164	171	12	161	4
12GH15-5	519	225	0.45	-0.88	0.0559	4.5	0.1956	5.7	0.0254	3.6	449	99	181	10	162	6
12GH15-6	3028	825	0.28	-0.07	0.0494	1.0	0.1815	2.8	0.0267	2.7	165	23	169	4	170	4
12GH15-7	1004	375	0.39	1.24	0.0585	3.7	0.2056	4.9	0.0255	3.3	548	81	190	9	162	5
													Concordia age		**162.1**	**2.7 (2σ)**
12GH23																
12GH23-1	354	176	0.52	0.05	0.0546	1.6	0.5250	1.9	0.0698	1.1	394	36	428	7	435	5
12GH23-2	510	174	0.35	-0.07	0.0566	1.3	0.5420	1.7	0.0694	1.0	477	30	440	6	432	4
12GH23-3	434	193	0.46	0.04	0.0555	1.4	0.5440	1.7	0.0711	1.0	434	31	441	6	443	4
12GH23-4	577	181	0.32	-0.14	0.0574	1.4	0.5570	1.7	0.0703	1.0	509	30	450	6	438	4
12GH23-5	882	270	0.32	-0.14	0.0578	1.1	0.5680	1.6	0.0712	1.1	522	24	457	6	444	5
12GH23-6	506	241	0.49	0.03	0.0556	1.3	0.5370	1.6	0.0701	1.0	437	28	436	6	437	4
12GH23-7	542	181	0.35	0.10	0.0549	2.4	0.5330	2.6	0.0705	1.0	407	54	434	9	439	4

12GH23-8	949	358	0.39	0.37	0.0543	1.7	0.5250	1.9	0.0701	1.0	383	37	428	7	437	4
12GH23-9	433	209	0.50	0.04	0.0553	1.4	0.5320	1.7	0.0698	1.0	422	31	433	6	435	4
12GH23-10	354	188	0.55	0.10	0.0557	1.8	0.5330	2.1	0.0694	1.1	440	40	434	7	433	5
12GH23-11	390	207	0.55	-0.13	0.0575	1.7	0.5620	2.0	0.0708	1.1	512	37	453	7	441	5
12GH23-12	422	159	0.39	0.00	0.0556	1.3	0.5340	1.7	0.0697	1.1	437	29	434	6	434	4
12GH23-13	575	216	0.39	0.00	0.0559	1.1	0.5460	1.5	0.0709	1.0	447	24	442	5	442	4
12GH23-14	589	300	0.53	0.06	0.0564	1.3	0.5480	1.8	0.0706	1.2	466	29	444	6	440	5
12GH23-15	384	217	0.58	-0.13	0.0575	1.7	0.5570	2.0	0.0703	1.1	512	37	450	7	438	5
12GH23-16	606	258	0.44	0.06	0.0555	1.2	0.5450	1.6	0.0712	1.0	432	28	442	6	444	4
12GH23-17	514	209	0.42	0.11	0.0557	1.5	0.5380	1.8	0.0701	1.0	440	33	437	6	437	4
12GH23-18	725	266	0.38	0.13	0.0551	1.2	0.5390	1.9	0.0709	1.4	417	28	438	7	442	6
													Concordia age		**438.1**	**2.1 (2σ)**
12GH24																
12GH24-1	587	173	0.31	-0.06	0.0570	1.2	0.5550	1.6	0.0705	1.0	493	27	448	6	439	4
12GH24-2	413	230	0.58	-0.08	0.0554	1.5	0.5490	2.0	0.0719	1.3	427	33	444	7	447	6
12GH24-3	665	204	0.32	0.07	0.0559	1.2	0.5390	1.5	0.0699	1.0	449	26	438	5	436	4
12GH24-4	726	269	0.38	0.17	0.0558	1.4	0.5370	1.7	0.0699	1.0	443	30	436	6	435	4
12GH24-5	235	125	0.55	0.00	0.0567	1.6	0.5450	2.0	0.0697	1.1	479	36	442	7	434	5
12GH24-6	663	188	0.29	0.17	0.0548	1.3	0.5450	1.6	0.0721	1.0	405	29	442	6	449	4
12GH24-7	557	333	0.62	0.35	0.0552	1.8	0.5300	2.1	0.0696	1.0	420	41	432	7	434	4
12GH24-8	415	302	0.75	-0.08	0.0564	1.5	0.5500	2.1	0.0706	1.5	469	34	445	8	440	6
12GH24-9	904	547	0.63	-0.04	0.0566	0.9	0.5580	1.3	0.0715	1.0	478	20	450	5	445	4
12GH24-10	765	211	0.29	-0.02	0.0568	1.0	0.5570	1.4	0.0710	1.0	486	21	450	5	442	4
12GH24-11	617	167	0.28	-0.11	0.0565	1.3	0.5600	1.6	0.0718	1.0	473	28	452	6	447	4
12GH24-12	589	196	0.34	0.06	0.0561	1.2	0.5490	1.6	0.0709	1.0	457	28	444	6	442	4
12GH24-13	573	258	0.47	0.32	0.0544	1.7	0.5350	2.0	0.0713	1.0	387	39	435	7	444	4

12GH24-14	822	272	0.34	0.15	0.0547	1.2	0.5380	1.7	0.0714	1.2	400	27	437	6	444	5
12GH24-15	720	395	0.57	-0.05	0.0570	1.6	0.5570	1.9	0.0709	1.0	491	35	450	7	442	4
12GH24-16	701	234	0.35	0.09	0.0544	1.2	0.5450	1.5	0.0728	1.0	386	27	442	5	453	4
12GH24-17	464	166	0.37	0.11	0.0546	1.5	0.5340	1.9	0.0710	1.1	395	35	434	7	442	4
													Concordia age		**442.2**	**2.8 (2σ)**

[a]Pb_c and Pb^* indicate the common and radiogenic portions.

Table C2. $^{40}Ar/^{39}Ar$ data.

Sample #. (mineral)	Step #.	Power (W)/ Temp .(°C)	^{36}Ar (Volt)	1σ (%)	^{37}Ar (Volt)	1σ (%)	^{38}Ar (Volt)	1σ (%)	^{39}Ar (Volt)	1σ (%)	^{40}Ar (Volt)	1σ (%)	$^{40}Ar^*$ (%)	$^{39}Ar_K$ (%)	Age (Ma)	2σ
12GH23 (K-feldspar)	**1**	**57.5**	**7.71E-05**	**14.3**	**1.66E-05**	**923.4**	**3.69E-05**	**15.8**	**1.45E-03**	**2.1**	**5.89E-02**	**0.2**	**60.94**	**5.85**	**146.75**	**26.66**[a]
	2	**57.7**	**3.24E-05**	**22.1**	**1.92E-05**	**739.3**	**7.26E-05**	**8.9**	**5.41E-03**	**1.0**	**1.23E-01**	**0.1**	**92.11**	**21.86**	**124.39**	**5.19**
	3	**58.1**	**4.30E-06**	**157.5**	**6.53E-05**	**211.1**	**1.66E-05**	**32.5**	**1.29E-03**	**1.2**	**2.83E-02**	**0.4**	**95.44**	**5.22**	**124.30**	**18.41**
	4	**60.5**	**5.60E-06**	**111.2**	**1.02E-04**	**124.9**	**1.93E-05**	**25.5**	**1.34E-03**	**1.1**	**3.00E-02**	**0.5**	**94.40**	**5.41**	**125.99**	**16.26**
	5	**62.0**	**1.21E-05**	**53.3**	**6.40E-05**	**232.6**	**4.15E-05**	**17.6**	**3.69E-03**	**1.1**	**8.33E-02**	**0.2**	**95.67**	**14.93**	**128.18**	**6.60**
	6	**67.0**	**7.77E-05**	**8.8**	**3.00E-06**	**4731.9**	**1.75E-04**	**4.3**	**1.16E-02**	**0.6**	**2.66E-01**	**0.1**	**91.26**	**46.73**	**124.69**	**2.60**
	J=0.00341900 ± 0.22%[b]				FCs=28.294 ± 0.13% Ma				Laser						Weighted plateau age	125.2 ± 2.2
04GD43 (Biotite)	**1**	**550.0**	**4.60E-04**	**4.7**	**4.63E-04**	**3.6**	**3.48E-04**	**2.8**	**2.01E-02**	**0.3**	**3.05E-01**	**0.2**	**63.04**	**2.86**	**139.62**	**10.91**
	2	**600.0**	**2.41E-04**	**5.2**	**4.59E-04**	**2.9**	**4.59E-04**	**1.7**	**3.27E-02**	**0.3**	**3.91E-01**	**0.1**	**89.44**	**4.65**	**158.11**	**4.45**
	3	**650.0**	**2.39E-04**	**5.7**	**4.61E-04**	**3.9**	**6.77E-04**	**2.3**	**5.14E-02**	**0.1**	**5.71E-01**	**0.1**	**93.16**	**7.31**	**156.27**	**3.06**
	4	**700.0**	**2.25E-04**	**5.9**	**4.39E-04**	**4.5**	**1.03E-03**	**2.9**	**7.35E-02**	**0.1**	**7.79E-01**	**0.0**	**95.63**	**10.45**	**154.88**	**2.23**
	5	**750.0**	**2.07E-04**	**6.6**	**4.80E-04**	**3.0**	**7.77E-04**	**3.0**	**5.73E-02**	**0.2**	**6.17E-01**	**0.0**	**95.45**	**8.15**	**155.48**	**2.83**
	6	**800.0**	**1.53E-04**	**6.7**	**4.93E-04**	**4.5**	**4.35E-04**	**1.7**	**3.35E-02**	**0.4**	**3.73E-01**	**0.0**	**97.13**	**4.76**	**158.72**	**3.92**
	7	850.0	1.59E-04	3.1	5.97E-04	2.4	3.74E-04	1.8	2.62E-02	0.3	3.15E-01	0.1	96.17	3.73	165.80	3.77
	8	900.0	1.79E-04	4.9	5.76E-04	5.4	5.06E-04	2.1	4.00E-02	0.2	4.53E-01	0.0	96.23	5.69	161.15	3.08
	9	**950.0**	**1.45E-04**	**6.4**	**5.83E-04**	**4.0**	**8.54E-04**	**3.3**	**6.41E-02**	**0.2**	**6.77E-01**	**0.0**	**99.23**	**9.11**	**158.11**	**2.16**
	10	**1000.0**	**1.74E-04**	**3.1**	**7.53E-04**	**2.6**	**1.28E-03**	**1.4**	**1.02E-01**	**0.2**	**1.04E+00**	**0.0**	**98.77**	**14.49**	**155.15**	**1.46**
	11	**1050.0**	**1.78E-04**	**6.4**	**1.80E-03**	**0.7**	**1.60E-03**	**1.0**	**1.22E-01**	**0.1**	**1.25E+00**	**0.0**	**99.05**	**17.40**	**155.37**	**1.53**
	12	**1100.0**	**2.54E-04**	**6.8**	**1.57E-03**	**2.4**	**8.39E-04**	**3.3**	**6.19E-02**	**0.2**	**6.77E-01**	**0.1**	**95.05**	**8.80**	**156.22**	**3.26**
	13	**1200.0**	**1.79E-04**	**7.9**	**5.41E-04**	**3.5**	**2.50E-04**	**4.4**	**1.81E-02**	**0.5**	**2.20E-01**	**0.1**	**97.75**	**2.57**	**156.60**	**9.39**
	14	**1300.0**	**1.80E-04**	**3.4**	**4.01E-04**	**3.1**	**4.40E-05**	**12.5**	**2.97E-04**	**5.3**	**4.36E-02**	**0.2**	**0.00**	**0.04**	**0.00**	**0.00**
	15	**1400.0**	**1.71E-04**	**7.0**	**3.96E-04**	**2.9**	**4.40E-05**	**14.6**	**5.90E-05**	**14.6**	**4.53E-02**	**0.2**	**0.00**	**0.00**	**0.00**	**0.00**

	J=0.0091360 ± 0.21%	FCs=28.030 ± 0.28% Ma	Furnace	Weighted mean age	155.9 ± 1.0

[a]Analyses shown in bold were included in plateau or mean age calculation.

12GH23		04GD43	
Correction factors for interfering isotopes			
$(^{39}Ar/^{37}Ar)_{Ca}$	0.000706 ± 7% (1σ)	$(^{39}Ar/^{37}Ar)_{Ca}$	0.00073 ± 11% (1σ)
$(^{36}Ar/^{37}Ar)_{Ca}$	0.000281 ± 3% (1σ)	$(^{36}Ar/^{37}Ar)_{Ca}$	0.000282 ± 1% (1σ)
$(^{40}Ar/^{39}Ar)_{K}$	0.000676 ± 10% (1σ)	$(^{40}Ar/^{39}Ar)_{K}$	0.000676 ± 10% (1σ)
Reactor and radiation hours			
USGS TRIGA Reactor (USA) for 40 hours		McMaster University Reactor (Canada) for 25 hours	

Table C3. Zircon (U-Th-Sm)/He data.

Sample #.	N_c[a]	^{238}U (ng)	+/- (%)	^{232}Th (ng)	+/- (%)	^{147}Sm (ng)	+/- (%)	eU (ppm)	He (ncc)	+/- (%)	TAU (%)	Th/U	Raw age (Ma)	±1σ (Ma)	Ft	Cor. age (Ma)	±1σ (Ma)	Mean age (Ma)	±2σ (Ma)	He dose (α/g)
10JXLN04	1	0.6	1.8	0.2	1.5	0.010	32.9	645.5	7.3	1.2	2.1	0.30	89.5	1.8	0.59	**152.1**	**11.1**[b]			1.9E+17
	2	0.3	1.8	0.3	1.5	0.004	30.4	263.2	3.9	1.2	1.9	0.91	92.3	1.8	0.62	**150.0**	**10.9**			8.0E+16
	3	1.0	1.9	0.5	1.4	0.017	36.2	479.1	14.8	1.2	2.1	0.50	106.5	2.2	0.68	**157.7**	**11.5**			1.7E+17
	4	0.3	1.8	0.2	1.5	0.004	31.1	213.1	4.5	1.2	2.0	0.63	98.2	2.0	0.67	**147.2**	**10.7**			6.9E+16
	5	0.4	1.8	0.3	1.4	0.013	32.6	317.4	6.0	1.2	1.9	0.82	96.9	1.9	0.64	**152.3**	**11.1**			1.0E+17
																		151.7	**9.9**	
12GH22-1	1	2.5	2.0	0.9	1.5	0.026	4.5	177.1	59.6	1.2	2.2	0.37	176.1	3.8	0.83	212.1	15.5			1.0E+17
	2	1.1	2.0	0.7	1.5	0.020	5.0	150.3	27.9	1.2	2.1	0.62	177.8	3.8	0.79	224.3	16.4			8.9E+16
	3	0.4	2.0	0.6	1.5	0.005	15.2	76.3	8.4	1.2	1.9	1.52	122.8	2.4	0.78	**156.5**	**11.4**			3.1E+16
	4	0.5	2.0	0.2	1.5	0.008	36.7	202.9	6.8	1.2	2.2	0.37	101.4	2.2	0.71	**142.6**	**10.5**			6.8E+16
	5	0.5	2.0	0.4	1.5	0.013	49.3	159.1	7.9	1.2	2.0	0.84	107.4	2.2	0.73	**146.7**	**10.7**			5.6E+16
																		148	**12**	
																		218	23	
09SC03-1	1	2.7	2.0	1.7	1.5	0.012	9.2	132.3	57.6	1.2	2.1	0.64	150.0	3.1	0.86	*175.3*	*12.8*			6.6E+16
	2	1.5	2.0	1.0	1.5	0.009	35.5	71.6	24.9	1.2	2.1	0.66	120.9	2.5	0.86	**140.9**	**10.3**			2.9E+16
	3	1.3	2.0	0.7	1.5	0.008	7.6	111.6	20.6	1.2	2.1	0.55	117.3	2.5	0.82	**143.0**	**10.5**			4.3E+16
	4	1.6	2.0	1.4	1.5	0.012	39.7	137.3	35.5	1.2	2.0	0.86	151.5	3.1	0.82	*184.4*	*13.4*			6.9E+16
	5	0.5	2.0	1.0	1.5	0.007	16.3	134.4	20.3	1.2	1.9	1.91	221.5	4.1	0.76	291.3	21.1			9.9E+16
																		142	**15**	
																		180	*19*	
																		291.3	21.1	
12GH23	1	0.9	2.3	0.5	2.0	0.003	34.3	586.2	10.2	1.3	2.4	0.58	84.8	2.0	0.65	**130.7**	**9.7**			1.6E+17
	2	1.3	1.8	0.8	1.4	0.007	34.5	559.5	16.7	1.3	2.0	0.60	91.3	1.9	0.68	**134.0**	**9.8**			1.7E+17
	3	1.0	1.8	0.6	1.4	0.039	38.0	692.7	11.7	1.3	2.1	0.56	85.1	1.8	0.65	**131.3**	**9.6**			1.9E+17
	4	1.2	1.8	0.5	1.4	0.005	43.9	772.2	13.4	1.3	2.1	0.45	83.4	1.7	0.66	**126.9**	**9.3**			2.1E+17
	5	3.0	1.8	1.2	1.4	0.009	35.9	909.9	36.3	1.3	2.1	0.41	90.3	1.9	0.70	**128.5**	**9.4**			2.7E+17
																		130.2	**8.5**	
12GH24	1	0.7	1.8	0.4	1.4	0.007	33.5	339.8	9.4	1.3	2.1	0.59	92.1	1.9	0.68	**134.5**	**9.8**			1.0E+17

	2	0.3	1.8	0.1	1.5	0.001	34.3	336.0	3.0	1.3	2.1	0.54	80.3	1.7	0.55	**145.3**	**10.6**			8.9E+16
	3	0.6	2.0	0.3	1.5	0.002	10.5	402.8	7.0	1.3	2.2	0.40	82.2	1.8	0.65	**125.6**	**9.2**			1.1E+17
	4	0.5	1.8	0.2	1.5	0.006	43.5	457.7	5.8	1.3	2.1	0.47	81.7	1.7	0.61	**134.1**	**9.8**			1.2E+17
	5	0.4	1.8	0.3	1.5	0.002	12.7	287.4	6.5	1.3	2.1	0.63	105.9	2.2	0.63	**169.3**	**12.4**			1.0E+17
																		139.0	**9.1**	
04GD43	1	3.8	4.1	2.9	4.1			501.3	50.0	2.5	3.5	0.78	97.5	4.1	0.80	**122.0**	**10.0**			1.2E+17
	2	21.0	4.4	5.9	4.2			1845	254.5	2.5	4.1	0.28	99.2	4.7	0.79	**126.1**	**10.7**			7.7E+17
	3	4.4	4.1	4.0	4.1			506.1	61.1	2.5	3.5	0.9	97.6	4.1	0.80	**121.4**	**10.0**			1.4E+17
	4	11.1	4.1	3.7	4.1			1541	143.5	2.5	3.9	0.33	104.2	4.7	0.83	**125.3**	**10.5**			3.6E+17
	5	5.1	4.1	3.3	4.1			952.9	61.8	2.5	3.6	0.64	91.7	3.9	0.72	**126.6**	**10.5**			2.1E+17
																		124.2	**9.2**	
2KGN38-1	1	2.4	4.8	1.6	4.7			518.6	21.5	2.5	4.2	0.65	68.4	3.3	0.61	**111.3**	**9.5**			1.1E+17
	2	3.0	4.8	1.5	4.4			786.7	33.2	2.5	4.3	0.51	85.7	4.1	0.72	**118.7**	**10.2**			2.1E+17
	3	3.7	4.8	1.9	4.3			708.8	36.2	2.5	4.3	0.51	77.0	3.7	0.70	**109.9**	**9.4**			1.7E+17
	4	2.2	4.8	1.1	4.4			675.9	25.8	2.5	4.3	0.48	91.2	4.4	0.76	**120.3**	**10.3**			1.9E+17
	5	0.6	4.1	0.5	4.2			252.6	6.7	1.3	3.5	0.84	80.5	2.9	0.70	**114.6**	**9.1**			6.3E+16
																		114.7	**8.7**	
12GH15	1	1.6	1.8	0.7	1.4	0.002	19.5	1072	13.1	1.3	2.1	0.42	59.9	1.3	0.62	**97.1**	**7.1**			2.1E+17
	2	1.7	1.8	0.5	1.4	0.003	64.3	1034.7	19.3	1.3	2.2	0.31	86.7	1.9	0.64	**135.6**	**9.9**			3.0E+17
	3	1.9	1.8	0.5	1.4	0.001	20.2	1114.7	19.2	1.3	2.2	0.27	76.4	1.7	0.66	**116.0**	**8.5**			2.8E+17
	4	1.4	1.8	0.5	1.5	0.001	24.0	1261.5	14.7	1.3	2.2	0.32	77.7	1.7	0.59	**132.4**	**9.7**			3.2E+17
	5	2.9	1.8	0.9	1.4	0.005	42.2	1227.8	32.2	1.3	2.2	0.32	85.7	1.8	0.69	**124.7**	**9.1**			3.5E+17
																		126.2	**9.3**	

[a] N_c = number of dated apatite or zircon crystals; +/- = analytical errors of individual measurements; ng = nanogram; He = ^{4}He in ncc at STP; ncc = nanocubic centimetre; TAU = total analytical uncertainty; F_T = alpha recoil correction factor after Farley et al. (1996).
[b] Analyses shown in bold were included in mean age calculation.

Table C4. Apatite fission track data.

Sample #.	N	ρ_S	N_s	ρ_i	N_i	ρ_d	N_d	Central age (Ma)		P(χ2)	C1	±1σ	C2	±1σ	C1	D_{par} (μm)		N(L)	TL (μm)	
								Age	±1σ	(%)	(Ma)				(%)	Mean	s.d.		Mean	s.d.
					Apatite															
10JXLN014	15	2.349	107	5.686	259	6.469	2484	72.1	5.2	95.21						1.97	0.35			
12GH22-1	25	2.231	289	5.697	738	6.814	2484	53.0	6.4	0.02	38.0	9.6	109.0	20.0	59.0	1.76	0.20			
09SC03-1	26	4.082	425	9.442	983	7.160	2484	57.0	7.0	0.00	40.2	19.9	121.6	4.3	68.4	3.73	0.62			
12GH23	25	8.344	624	12.142	908	6.419	2484	69.0	3.9	74.92						3.12	0.53	101	12.7	1.58
12GH24	30	4.460	673	7.966	1202	7.012	2484	61.5	3.3	91.72						2.30	0.47	101	12.6	1.64
04GD43	20	34.170	152	4.005	1297	16.110	3076	36.6	3.2	94.88						/				
12GH15	32	4.808	543	12.663	1430	6.568	2484	39.1	2.2	98.13						3.26	0.53			

[a]N = number of dated apatite or zircon crystals; ρ_S (ρ_i) = spontaneous (induced) track densities ($\times 10^5$ tracks/cm^2); N_s (N_i) = number of counted spontaneous (induced) tracks; ρ_d = dosimeter track density ($\times 10^5$ tracks/cm^2); N_d = number of tracks counted on dosimeter; P(χ^2) = probability obtaining chi-square value for n degree of freedom (where n = number of crystals); D_{par} = average etch pit diameter of fission tracks; s.d. = standard deviation; NL = number of horizontal confined tracks measured. TL = horizontal confined track length. Glass dosimeter CN-5 was used. Zeta value of 389.3 ± 5.0 for apatite sample 04GD43 and 314.59 ± 3.29 for other apatite samples.

Table C5. Apatite (U-Th-Sm)/He data.

Sample #.	N_c[a]	^{238}U (ng)	+/- (%)	^{232}Th (ng)	+/- (%)	^{147}Sm (ng)	+/- (%)	eU (ppm)	He (ncc)	+/- (%)	TAU (%)	Th/U	Raw age (Ma)	±1σ (Ma)	Ft	Cor. age (Ma)	±1σ (Ma)	Mean (Ma)	±2σ (Ma)
12GH22-1	1	0.101	4.2	0.482	4.1	0.027	1.9	30.1	0.9	1.2	3.2	4.8	33.3	1.1	0.78	**42.7**	**3.3**[b]		
	2	0.176	4.2	0.405	4.1	0.080	1.1	31.6	1.0	1.2	3.3	2.3	29.1	1.0	0.82	**35.5**	**2.8**		
	3	0.000	129.0	0.145	4.1	0.016	2.4	4.9	0.1	1.2	4.2	1144.2	23.4	1.0	0.79	29.5	2.4		
	4	0.004	4.6	0.174	4.1	0.080	1.2	7.1	0.1	1.2	3.8	40.3	15.7	0.6	0.75	**21.0**	**1.7**		
	5	0.002	4.7	0.031	4.1	0.023	2.0	1.7	0.0	1.2	3.5	15.0	35.2	1.2	0.74	**47.3**	**3.7**	**(RadialPlotter)**	
																		35.1	**11.0**
09SC03-1	1	0.002	4.6	0.032	4.1	0.017	2.4	3.1	0.1	1.2	3.5	14.0	70.1	2.4	0.69	102.0	8.0		
	3	0.008	4.4	0.144	4.1	0.041	1.3	6.8	0.1	1.2	3.6	18.9	26.2	0.9	0.79	**33.3**	**2.6**		
	4	0.091	4.3	0.005	5.0	0.021	1.9	55.8	0.3	1.2	4.3	0.1	28.9	1.3	0.70	**41.2**	**3.4**		
	5	0.001	18.0	0.021	4.2	0.006	4.4	1.1	0.0	1.2	4.3	34.9	66.8	2.9	0.73	91.6	7.5		
	6	0.003	12.2	0.004	1.3	0.001	12.4	1.1	0.0	1.2	9.1	1.6	42.7	3.9	0.71	60.0	6.9		
																		36.2	**4.1**
12GH23	1	0.101	4.3	0.214	4.1	0.077	1.2	53.3	0.4	1.2	3.4	2.1	19.2	0.6	0.66	**28.9**	**2.2**		
	2	0.143	4.3	0.278	4.1	0.090	1.3	49.8	0.7	1.2	3.4	1.9	28.1	1.0	0.73	**38.6**	**3.0**		
	3	0.056	4.3	0.168	4.1	0.087	1.1	17.4	0.3	1.2	3.2	3.0	25.8	0.8	0.75	**34.6**	**2.7**		
	4	0.153	4.2	0.348	4.1	0.140	0.8	30.3	0.8	1.2	3.3	2.3	27.9	0.9	0.79	**35.5**	**2.7**		
	5	0.117	4.2	0.266	4.1	0.097	1.0	45.1	0.5	1.2	3.3	2.3	24.6	0.8	0.72	**34.0**	**2.6**		
																		33.7	**2.3**
12GH24	1	0.067	4.4	0.181	4.1	0.096	1.8	36.7	0.3	1.4	3.4	2.7	25.7	0.9	0.68	**37.5**	**2.9**		
	2	0.049	4.3	0.131	4.1	0.121	1.1	35.5	0.2	1.3	3.3	2.7	22.4	0.7	0.66	**33.8**	**2.6**		
	3	0.037	4.3	0.085	4.1	0.055	1.9	37.4	0.2	1.3	3.4	2.3	23.9	0.8	0.64	**37.3**	**2.9**		
	4	0.042	4.5	0.096	4.1	0.060	1.8	33.9	0.2	1.3	3.5	2.3	24.2	0.8	0.64	**37.8**	**3.0**		
	5	0.034	4.3	0.095	4.1	0.073	1.3	23.3	0.2	1.3	3.3	2.8	25.9	0.9	0.66	**39.1**	**3.0**		
																		36.9	**2.6**
04GD43	1	0.228	3.9	1.300	3.7			64.4	2.2	2.0	3.4	5.7	35.1	1.2	0.74	47.4	3.7		
	2	0.052	3.9	0.265	3.8			69.7	0.3	2.7	3.8	5.1	24.7	0.9	0.67	**36.9**	**2.9**		
	3	0.141	3.9	0.543	3.7			67.0	1.0	2.0	3.4	3.9	32.6	1.1	0.71	**45.9**	**3.6**		
	4	0.051	3.9	0.314	3.7			78.9	0.5	2.7	3.8	6.2	32.4	1.2	0.68	47.6	3.8		
	5	0.179	3.9	0.527	3.7			130.9	0.7	2.3	3.6	2.9	20.1	0.7	0.66	**30.5**	**2.4**	**(RadialPlotter)**	

																		37.2	**7.2**
2KGN38-1	1	0.002	4.0	0.021	3.8			4.7	0.0	9.5	9.9	9.1	48.0	4.8	0.62	77.4	9.4		
	2	0.005	3.9	0.009	4.1			7.2	0.0	8.5	9	1.8	54.9	5.0	0.58	94.7	###		
	3	0.014	4.1	0.055	4.1			18.3	0.2	2.1	3.6	3.8	52.9	1.9	0.62	85.3	6.7		
	4	0.014	4.0	0.075	4.1			25.7	0.1	3.3	4.4	5.5	32.3	1.4	0.59	54.7	4.5		
	5	0.034	4.0	0.130	4.2			44.7	0.2	3.4	4.5	3.9	19.5	0.9	0.60	**32.5**	**2.7**		
																		32.5	**5.4**
12GH15	1	0.045	4.8	0.137	4.1	0.082	2.3	65.3	0.2	1.5	3.6	3.0	21.6	0.8	0.58	**37.3**	**2.9**		
	2	0.046	4.8	0.137	4.1	0.073	2.1	66.0	0.2	1.5	3.6	2.9	21.4	0.8	0.58	**36.9**	**2.9**		
	3	0.027	4.5	0.098	4.1	0.066	1.8	55.4	0.1	1.5	3.4	3.5	19.9	0.7	0.51	**38.7**	**3.0**		
																		37.6	**3.4**

[a]N_c = number of dated apatite or zircon crystals; +/- = analytical errors of individual measurements; ng = nanogram; He = ^{4}He in ncc at STP; ncc = nanocubic centimetre; TAU = total analytical uncertainty; F_T = alpha recoil correction factor after Farley et al. (1996).
[b]Analyses shown in bold were included in mean age calculation.

Table C6. Vitrinite reflectance data.

Sample: 12GH22-2					
wave length:	546		Measure Condition:		Oil
Measured Object:	50		Refractive index of oil:		1.518
Reflectivity type:	Ro		Standard Sample:		0.904
Measurement #.	Data	Measurement #.	Data	Measurement #.	Data
1	1.69	21	1.816	41	1.906
2	1.723	22	1.817	42	1.914
3	1.743	23	1.821	43	1.915
4	1.748	24	1.823	44	1.921
5	1.752	25	1.828	45	1.935
6	1.757	26	1.83	46	1.941
7	1.759	27	1.835	47	1.942
8	1.759	28	1.838	48	1.945
9	1.763	29	1.845	49	1.953
10	1.767	30	1.846	50	1.956
11	1.77	31	1.85	51	1.966
12	1.774	32	1.851	52	1.987
13	1.779	33	1.852	53	1.993
14	1.78	34	1.865	54	2.023
15	1.804	35	1.869	55	2.023
16	1.805	36	1.878	56	2.097
17	1.807	37	1.892	57	2.163
18	1.809	38	1.898	58	2.259
19	1.809	39	1.899	59	2.333
20	1.813	40	1.901	60	2.338

Appendix D. Data from Chapter 7: Hunan

Table D1. Zircon SHRIMP U-Pb data.

Spot #.	U (ppm)	Th (ppm)	Th/U	$^{206}Pb_c$ [a] (%)	Isotopic ratios						Ages (Ma)					
					$^{207}Pb^*/^{206}Pb^*$	1σ (%)	$^{207}Pb^*/^{235}U$	1σ (%)	$^{206}Pb^*/^{238}U$	1σ (%)	$t_{207/206}$	1σ	$t_{207/235}$	1σ	$t_{206/238}$	1σ
12GH30																
1	1319	339	0.26	0.00	0.0570	1.0	0.5590	1.4	0.0711	0.9	493	21	451	5	443	4
2	1440	194	0.13	-0.01	0.0546	1.0	0.5320	1.4	0.0708	1.0	394	23	433	5	441	4
3	906	128	0.14	0.03	0.0552	1.3	0.5360	1.6	0.0705	1.0	421	28	436	6	439	4
4	476	331	0.70	0.00	0.0574	2.7	0.5750	3.0	0.0727	1.3	505	59	461	11	452	6
5	1457	93	0.06	0.04	0.0561	1.0	0.5480	1.4	0.0708	0.9	458	23	444	5	441	4
6	1097	190	0.17	0.02	0.0562	1.1	0.5410	1.5	0.0699	1.0	458	25	439	5	435	4
7	1490	558	0.37	0.02	0.0558	0.9	0.5510	1.3	0.0716	0.9	444	20	446	5	446	4
8	1438	339	0.24	0.05	0.0556	1.0	0.5520	1.4	0.0721	0.9	435	22	446	5	449	4
9	983	196	0.20	0.06	0.0552	1.2	0.5490	1.5	0.0721	1.0	420	27	444	5	449	4
10	2147	234	0.11	0.01	0.0549	0.8	0.5480	1.2	0.0725	0.9	406	18	444	4	451	4
11	1265	343	0.27	-0.01	0.0543	1.1	0.5290	1.4	0.0707	1.0	382	24	431	5	440	4
12	1095	163	0.15	0.01	0.0564	1.1	0.5570	1.5	0.0717	1.0	469	24	450	5	446	4
13	857	141	0.16	-0.05	0.0548	2.2	0.5380	2.4	0.0711	1.0	406	48	437	9	443	4
14	1033	193	0.19	0.00	0.0548	1.2	0.5400	1.5	0.0714	1.0	406	26	438	5	445	4
15	1636	301	0.18	0.02	0.0554	0.9	0.5350	1.3	0.0701	0.9	427	19	435	5	437.0	4
													concordia age		**442.9**	**2.8 (2σ)**
													Mean age		**443.4**	**2.1 (2σ)**
12GH35																

1	1149	677	0.59	0.14	0.0557	1.6	0.5340	2.0	0.0696	1.2	440	36	434	7	434	5
2	2215	399	0.18	0.10	0.0564	1.1	0.5460	1.7	0.0702	1.3	469	24	442	6	437	5
3	1564	858	0.55	0.00	0.0549	1.3	0.5340	1.7	0.0705	1.2	410	28	434	6	439	5
4	1134	488	0.43	0.32	0.0532	1.9	0.4880	2.3	0.0665	1.2	338	43	404	8	415	5
5	680	322	0.47	0.03	0.0546	2.0	0.5120	2.3	0.0680	1.2	395	44	420	8	424	5
6	1479	697	0.47	0.42	0.0575	1.8	0.5520	2.2	0.0696	1.3	513	40	446	8	433	5
7	980	530	0.54	1.15	0.0578	4.6	0.5450	4.8	0.0683	1.5	523	100	442	17	426	6
8	1659	1331	0.80	2.42	0.0566	3.0	0.5030	3.3	0.0645	1.3	477	67	414	11	403	5
9	761	395	0.52	0.00	0.0564	2.8	0.5350	3.1	0.0688	1.4	469	61	435	11	429	6
10	754	320	0.42	-0.06	0.0562	1.9	0.5180	2.3	0.0668	1.2	461	42	424	8	417	5
11	1245	719	0.58	0.07	0.0550	1.5	0.5240	2.1	0.0691	1.5	411	33	428	7	431	6
12	1020	578	0.57	0.05	0.0549	1.7	0.5180	2.2	0.0684	1.4	410	37	424	8	426	6
13	941	439	0.47	0.00	0.0545	1.4	0.5080	1.9	0.0677	1.2	391	32	417	6	422	5
14	1195	633	0.53	0.16	0.0558	1.6	0.5290	2.1	0.0688	1.4	445	36	431	7	429	6
15	995	587	0.59	0.05	0.0548	1.7	0.5190	2.2	0.0688	1.4	402	37	424	8	429	6
16	1020	460	0.45	-0.05	0.0583	1.7	0.5570	2.2	0.0693	1.4	539	37	450	8	432	6
17	895	448	0.50	0.71	0.0529	2.9	0.4960	3.2	0.0680	1.2	325	66	409	11	424	5
18	986	571	0.58	0.17	0.0551	1.9	0.5190	2.3	0.0683	1.2	415	42	424	8	426	5
													concordia age		**427.4**	**3.4 (2σ)**
													Mean age		**427.5**	**2.6 (2σ)**
12GH46																
1	494	257	0.52	0.05	0.0486	1.6	0.2340	1.9	0.0350	1.0	127	37	213	4	221	2
2	510	301	0.59	-0.08	0.0500	1.6	0.2360	1.9	0.0342	1.0	196	37	215	4	217	2
3	837	604	0.72	0.02	0.0508	1.0	0.2380	1.4	0.0339	1.0	232	24	217	3	215	2
4	605	425	0.70	-0.17	0.0507	1.7	0.2420	2.4	0.0346	1.7	227	39	220	5	219	4
5	981	923	0.94	-0.07	0.0509	1.1	0.2420	1.5	0.0345	1.0	237	25	220	3	219	2
6	270	233	0.86	1.45	0.0747	7.6	0.3530	7.8	0.0343	1.8	1060	153	307	21	217	4

7	433	269	0.62	0.14	0.0493	1.9	0.2340	2.3	0.0343	1.3	163	46	213	4	218	3
8	372	218	0.59	0.00	0.0512	1.5	0.2380	1.8	0.0338	1.0	248	34	217	4	214	2
9	689	475	0.69	-0.19	0.0520	1.6	0.2450	2.0	0.0343	1.1	284	37	223	4	217	2
10	296	272	0.92	0.08	0.0499	2.1	0.2320	2.4	0.0337	1.0	192	49	212	5	214	2
11	222	148	0.67	-0.72	0.0565	4.7	0.2670	4.9	0.0342	1.1	471	105	240	10	217	2
12	547	269	0.49	0.12	0.0487	1.7	0.2320	2.0	0.0346	1.0	132	41	212	4	219	2
13	603	426	0.71	-0.08	0.0503	1.6	0.2370	1.9	0.0341	1.2	208	36	216	4	216	2
14	709	417	0.59	-0.16	0.0546	1.5	0.2590	1.8	0.0344	1.0	395	34	234	4	218	2
15	548	278	0.51	-0.25	0.0513	2.2	0.2380	2.6	0.0337	1.4	253	51	217	5	213	3
16	687	738	1.07	-0.03	0.0511	1.3	0.2420	1.6	0.0343	1.0	246	29	220	3	218	2
17	414	258	0.62	0.00	0.0501	1.5	0.2430	1.8	0.0352	1.0	202	34	221	4	223	2
													Mean age		**217.4**	**1.1 (2σ)**
12GH48																
1	785	265	0.34	-0.09	0.0526	2.4	0.2540	2.7	0.0351	1.2	310	56	230	6	222	3
2	866	174	0.20	0.22	0.0458	2.9	0.2180	3.2	0.0346	1.2	-13	71	200	6	219	3
3	1135	227	0.20	-0.13	0.0512	1.9	0.2440	2.3	0.0346	1.2	252	44	222	5	219	3
4	1761	381	0.22	0.19	0.0487	2.7	0.2340	3.0	0.0349	1.3	132	64	213	6	221	3
5	1867	466	0.25	0.13	0.0490	1.7	0.2380	2.0	0.0353	1.2	147	39	217	4	224	3
6	1114	277	0.25	0.08	0.0496	1.9	0.2390	2.3	0.0350	1.2	178	44	218	5	222	3
7	995	195	0.20	0.04	0.0508	2.1	0.2430	2.6	0.0346	1.4	234	49	221	5	220	3
8	1592	633	0.40	0.02	0.0492	1.8	0.2400	2.3	0.0353	1.4	160	42	218	5	224	3
9	1211	347	0.29	-0.06	0.0497	2.0	0.2420	2.3	0.0354	1.2	181	46	220	5	224	3
10	746	175	0.23	-0.05	0.0514	4.1	0.2440	4.3	0.0345	1.2	257	94	222	9	218	3
11	859	239	0.28	-0.04	0.0502	2.3	0.2450	2.7	0.0354	1.3	204	53	223	5	224	3
12	1935	300	0.16	0.05	0.0503	1.8	0.2320	2.2	0.0335	1.2	208	42	212	4	213	2
13	331	104	0.31	1.63	0.0403	10.9	0.1860	11.1	0.0335	1.9	-331	280	173	18	212	4
14	1350	331	0.25	0.00	0.0513	2.7	0.2460	2.9	0.0348	1.2	252	61	223	6	221	3

15	1087	337	0.31	0.11	0.0514	2.3	0.2460	2.8	0.0347	1.6	257	53	223	6	220	3
16	917	184	0.20	-0.09	0.0516	2.4	0.2460	2.9	0.0345	1.6	267	55	223	6	219	3
17	550	219	0.40	-0.46	0.0514	4.1	0.2490	4.5	0.0352	1.9	257	94	226	9	223	4
18	588	205	0.35	0.43	0.0457	4.4	0.2170	4.5	0.0345	1.3	-18	106	199	8	218	3
19	525	282	0.54	-0.21	0.0518	3.3	0.2390	7.0	0.0335	6.2	275	75	218	14	213	13
20	318	134	0.42	0.13	0.0501	6.4	0.2380	6.6	0.0344	1.4	201	149	217	13	218	3
													concordia age		**219.9**	**1.7 (2σ)**
													Mean age		**220.1**	**1.3 (2σ)**

[a]Pb_c and Pb^* indicate the common and radiogenic portions.

Table D2. $^{40}Ar/^{39}Ar$ data.

Sample (mineral)	Heating step #.	Temp. (°C)	^{36}Ar (Volt)	1σ (%)	^{37}Ar (Volt)	1σ (%)	^{38}Ar (Volt)	1σ (%)	^{39}Ar (Volt)	1σ (%)	^{40}Ar (Volt)	1σ (%)	40Ar* (%)	$39Ar_K$ (%)	Age (Ma)	2σ
12GH46 (Biotite)	1	56°C	3.30E-06	228.4	6.13E-05	154.8	8.80E-06	61.8	6.83E-04	3.3	2.82E-02	0.4	96.54	0.42	230.53	38.4[a]
	2	57°C	4.00E-07	2127.0	2.02E-05	480.0	6.70E-06	82.7	7.35E-04	1.9	2.86E-02	0.4	100.42	0.45	226.24	38.7
	3	57°C	1.31E-05	58.2	2.43E-05	377.1	2.54E-05	34.8	1.50E-03	1.3	5.74E-02	0.3	93.19	0.92	207.61	17.4
	4	57°C	8.40E-06	94.8	2.10E-06	4729.4	2.63E-05	22.5	1.47E-03	2.0	5.61E-02	0.2	95.53	0.90	212.34	19.5
	5	57°C	3.20E-06	243.6	1.90E-05	582.6	2.82E-05	21.3	2.25E-03	1.0	8.52E-02	0.3	98.86	1.39	216.66	12.2
	6	57°C	3.02E-05	29.0	1.84E-04	51.6	8.66E-05	7.4	6.06E-03	0.9	2.33E-01	0.1	96.14	3.72	214.79	6.0
	7	57°C	8.70E-06	86.7	7.85E-05	121.4	3.69E-05	19.2	1.96E-03	1.4	7.47E-02	0.2	96.52	1.20	213.57	13.9
	8	57°C	5.90E-06	145.8	2.00E-06	4706.8	4.44E-05	11.9	2.59E-03	1.1	1.00E-01	0.2	98.23	1.59	219.92	11.9
	9	57°C	9.90E-06	75.7	4.70E-06	2592.5	3.34E-05	16.9	1.85E-03	0.9	7.29E-02	0.1	95.95	1.14	218.93	13.7
	10	57°C	7.40E-06	124.6	3.43E-05	297.6	4.67E-05	15.8	3.18E-03	1.0	1.23E-01	0.1	98.21	1.95	220.67	10.3
	11	57°C	4.38E-05	20.3	2.33E-04	46.0	1.31E-04	9.8	1.03E-02	0.6	3.96E-01	0.1	96.69	6.32	215.74	3.7
	12	58°C	6.00E-05	15.4	5.29E-04	26.1	3.43E-04	2.3	2.47E-02	0.7	9.59E-01	0.1	98.13	15.21	220.15	3.0
	13	60°C	8.86E-05	15.2	2.60E-03	5.0	1.44E-03	1.9	1.05E-01	0.4	4.01E+00	0.0	99.34	64.78	219.13	1.6
	J=0.00341900 0.22%				FCs=28.294 0.13% Ma			Laser					Plateau age		218.6 ± 1.4 Ma	
12GH48 (Biotite)	1	56°C	5.30E-06	107.6	7.07E-05	184.2	1.96E-05	24.3	1.17E-03	1.4	4.50E-02	0.18	96.49	0.78	215.0	16.9
	2	56°C	1.24E-05	53.2	9.88E-05	124.7	5.08E-05	7.3	3.44E-03	0.8	1.31E-01	0.1	97.17	2.28	214.33	7.1
	3	57°C	9.80E-06	60.9	1.51E-05	837.6	4.45E-05	9.4	2.53E-03	1.0	9.39E-02	0.2	96.87	1.68	208.83	8.7
	4	57°C	3.90E-06	147.5	1.97E-05	648.5	3.26E-05	17.7	2.54E-03	1.7	9.71E-02	0.7	98.80	1.68	219.16	10.4
	5	57°C	4.01E-05	22.9	5.13E-05	269.8	2.03E-04	4.8	1.60E-02	0.7	6.08E-01	0.0	98.03	10.61	215.74	3.3
	6	57°C	2.71E-05	30.0	1.42E-04	85.2	1.44E-04	3.8	1.07E-02	0.8	4.07E-01	0.1	98.02	7.08	216.61	4.0
	7	57°C	1.45E-05	40.9	1.66E-04	76.0	5.54E-05	11.8	3.59E-03	1.2	1.38E-01	0.1	96.88	2.38	216.56	7.2

	8	**57°C**	**7.60E-06**	**81.6**	**7.43E-05**	**174.3**	**8.21E-05**	**7.6**	**5.84E-03**	**0.8**	**2.23E-01**	**0.1**	**98.99**	**3.87**	**219.42**	**4.7**
	9	**57°C**	**7.40E-06**	**88.6**	**9.32E-05**	**131.5**	**6.59E-05**	**6.5**	**4.53E-03**	**0.6**	**1.72E-01**	**0.1**	**98.71**	**3.00**	**216.96**	**5.3**
	10	**57°C**	**1.00E-05**	**70.4**	**5.95E-05**	**206.9**	**1.29E-04**	**4.2**	**1.10E-02**	**0.9**	**4.15E-01**	**0.6**	**99.28**	**7.31**	**216.39**	**4.8**
	11	**57°C**	**1.07E-05**	**52.8**	**1.50E-04**	**83.3**	**2.09E-04**	**3.9**	**1.42E-02**	**0.5**	**5.35E-01**	**0.0**	**99.40**	**9.38**	**217.75**	**2.5**
	12	**58°C**	**2.64E-05**	**31.3**	**6.52E-04**	**19.5**	**5.30E-04**	**4.2**	**3.95E-02**	**0.7**	**1.49E+00**	**0.3**	**99.47**	**26.19**	**216.89**	**3.2**
	13	**60°C**	**1.32E-05**	**56.5**	**4.29E-04**	**29.3**	**4.83E-04**	**2.6**	**3.59E-02**	**0.5**	**1.36E+00**	**0.1**	**99.71**	**23.77**	**218.35**	**2.2**
	J=0.00341900 0.22%			**FCs=28.294 0.13% Ma**				**Laser**					**Plateau age**		**217.2 ± 1.3 Ma**	
11HN23-1 (Biotite)	**1**	**57°C**	**2.12E-05**	**39.5**	**3.40E-06**	**2834.8**	**7.19E-05**	**9.2**	**6.14E-03**	**0.8**	**2.32E-01**	**0.1**	**97.27**	**8.00**	**213.13**	**5.5**
	3	**57°C**	**2.55E-05**	**33.7**	**5.78E-05**	**141.3**	**1.50E-04**	**8.5**	**1.14E-02**	**0.8**	**4.21E-01**	**0.1**	**98.19**	**14.91**	**210.03**	**3.9**
	4	**57°C**	**4.30E-06**	**172.9**	**5.95E-05**	**129.2**	**6.60E-05**	**15.4**	**4.86E-03**	**0.6**	**1.76E-01**	**0.1**	**99.28**	**6.33**	**209.67**	**5.6**
	5	**57°C**	**2.30E-06**	**327.9**	**7.40E-06**	**1449.2**	**2.23E-05**	**26.5**	**1.71E-03**	**2.0**	**6.11E-02**	**0.1**	**98.87**	**2.22**	**206.02**	**16.5**
	6	**57°C**	**3.50E-06**	**229.3**	**2.51E-05**	**300.8**	**8.75E-05**	**7.3**	**6.74E-03**	**0.6**	**2.46E-01**	**0.1**	**99.58**	**8.78**	**210.97**	**4.6**
	7	**57°C**	**2.80E-06**	**274.6**	**9.81E-05**	**95.0**	**1.23E-04**	**6.3**	**1.01E-02**	**0.6**	**3.65E-01**	**0.1**	**100.23**	**13.15**	**210.67**	**3.5**
	8	**57°C**	**6.00E-07**	**1132.5**	**1.15E-05**	**762.9**	**3.39E-05**	**16.5**	**3.44E-03**	**1.0**	**1.23E-01**	**0.5**	**99.84**	**4.49**	**208.20**	**8.2**
	9	**57°C**	**2.80E-06**	**241.7**	**7.67E-05**	**97.9**	**6.42E-05**	**11.0**	**4.49E-03**	**0.8**	**1.64E-01**	**0.2**	**100.51**	**5.86**	**213.38**	**6.1**
	10	**58°C**	**8.00E-07**	**931.3**	**1.76E-04**	**60.8**	**1.14E-04**	**9.2**	**9.10E-03**	**0.5**	**3.30E-01**	**0.1**	**100.07**	**11.87**	**210.48**	**3.3**
	11	**60°C**	**6.70E-06**	**110.8**	**4.21E-04**	**25.3**	**2.44E-04**	**4.2**	**1.87E-02**	**0.5**	**6.86E-01**	**0.1**	**99.71**	**24.38**	**212.32**	**2.5**
	J=0.00341900 0.22%			**FCs=28.294 0.13% Ma**				**Laser**					**Plateau age**		**211.2 ± 1.5 Ma**	
11HN08-1 (Biotite)	1	56°C	8.60E-06	79.5	9.58E-05	154.5	7.30E-06	87.1	7.51E-04	1.9	2.88E-02	0.36	91.09	0.56	203.3	30.8
	2	57°C	7.02E-05	10.7	8.08E-05	201.8	5.48E-05	10.7	3.06E-03	1.3	1.24E-01	0.1	83.05	2.29	195.35	9.4
	3	57°C	7.29E-05	12.8	1.10E-04	135.5	9.65E-05	8.2	8.37E-03	0.6	3.05E-01	0.1	92.88	6.25	197.50	4.5
	4	**57°C**	**3.95E-05**	**16.4**	**9.10E-05**	**165.5**	**1.14E-04**	**8.8**	**8.98E-03**	**0.6**	**3.24E-01**	**0.1**	**96.35**	**6.71**	**202.22**	**3.3**
	5	**57°C**	**8.90E-06**	**77.3**	**8.30E-05**	**202.4**	**5.99E-05**	**12.7**	**5.16E-03**	**0.8**	**1.83E-01**	**0.2**	**98.55**	**3.85**	**203.53**	**5.4**
	6	**57°C**	**1.70E-06**	**353.8**	**8.34E-05**	**182.0**	**7.90E-05**	**10.0**	**5.29E-03**	**1.0**	**1.87E-01**	**0.5**	**99.72**	**3.95**	**205.13**	**5.9**
	7	**57°C**	**2.80E-06**	**296.9**	**1.10E-04**	**131.2**	**8.54E-05**	**10.6**	**7.58E-03**	**0.9**	**2.67E-01**	**0.1**	**99.69**	**5.66**	**204.39**	**5.1**

	8	**57°C**	**3.00E-07**	**2330.6**	**2.47E-04**	**61.8**	**1.19E-04**	**7.6**	**8.54E-03**	**0.6**	**3.01E-01**	**0.1**	**99.97**	**6.38**	**205.20**	**3.8**
	9	**57°C**	**4.30E-06**	**165.2**	**2.81E-04**	**52.4**	**1.91E-04**	**5.0**	**1.47E-02**	**0.5**	**5.17E-01**	**0.1**	**100.25**	**10.94**	**205.64**	**2.4**
	10	**57°C**	**3.00E-07**	**2737.0**	**4.87E-04**	**31.3**	**2.30E-04**	**5.4**	**1.74E-02**	**0.5**	**6.18E-01**	**0.0**	**100.02**	**12.98**	**206.90**	**2.4**
	11	**57°C**	**2.20E-06**	**286.9**	**7.40E-04**	**21.9**	**1.69E-04**	**6.3**	**1.37E-02**	**0.9**	**4.80E-01**	**0.1**	**100.15**	**10.19**	**204.77**	**3.8**
	12	**58°C**	**5.20E-06**	**148.4**	**2.12E-03**	**8.7**	**2.93E-04**	**5.9**	**2.33E-02**	**0.5**	**8.22E-01**	**0.0**	**99.83**	**17.38**	**205.10**	**2.1**
	13	**60°C**	**7.10E-06**	**128.7**	**3.35E-03**	**5.2**	**2.33E-04**	**4.2**	**1.72E-02**	**0.6**	**6.03E-01**	**0.1**	**99.69**	**12.87**	**202.98**	**3.0**
	J=0.00341900 0.22%			**FCs=28.294 0.13% Ma**				**Laser**					**Plateau age**		**204.9 ± 1.2 Ma**	
12GH35 (Biotite)	1	57°C	1.42E-04	7.1	3.90E-06	402.2	1.03E-04	6.3	5.90E-03	1.0	2.39E-01	0.07	82.31	3.97	195.0	6.7
	2	58°C	1.20E-04	7.2	1.21E-05	150.5	1.17E-04	4.7	6.66E-03	0.6	2.70E-01	0.2	86.75	4.49	205.54	4.9
	3	58°C	1.12E-04	8.1	3.14E-05	46.9	1.98E-04	5.5	1.45E-02	0.4	5.24E-01	0.1	93.62	9.78	197.42	2.6
	4	**58°C**	**6.18E-05**	**15.0**	**1.26E-05**	**121.7**	**3.65E-04**	**3.5**	**2.91E-02**	**0.3**	**1.03E+00**	**0.1**	**98.20**	**19.59**	**202.57**	**1.7**
	5	**58°C**	**9.80E-06**	**90.4**	**6.30E-06**	**262.8**	**2.69E-04**	**3.8**	**1.94E-02**	**0.3**	**6.77E-01**	**0.1**	**99.57**	**13.03**	**203.32**	**2.0**
	6	**58°C**	**8.10E-06**	**117.0**	**1.31E-05**	**128.3**	**2.85E-04**	**2.9**	**2.32E-02**	**0.3**	**8.12E-01**	**0.1**	**99.70**	**15.62**	**203.94**	**1.8**
	7	**59°C**	**1.56E-05**	**56.9**	**2.18E-05**	**76.1**	**2.67E-04**	**3.9**	**1.98E-02**	**0.3**	**7.02E-01**	**0.1**	**99.34**	**13.34**	**205.49**	**2.0**
	8	**59°C**	**1.34E-05**	**65.1**	**1.04E-05**	**148.4**	**1.61E-04**	**5.2**	**1.19E-02**	**0.4**	**4.21E-01**	**0.1**	**99.05**	**7.99**	**205.17**	**2.9**
	9	**59°C**	**1.70E-06**	**537.5**	**1.42E-05**	**112.5**	**1.65E-04**	**3.9**	**1.19E-02**	**0.5**	**4.19E-01**	**0.1**	**100.12**	**7.98**	**206.51**	**3.2**
	10	**59°C**	**2.00E-06**	**455.4**	**7.10E-06**	**249.7**	**1.34E-05**	**30.5**	**1.23E-03**	**1.2**	**4.23E-02**	**0.3**	**98.61**	**0.83**	**198.85**	**24.6**
	11	**59°C**	**3.10E-06**	**296.3**	**4.40E-06**	**399.8**	**4.78E-05**	**9.7**	**3.42E-03**	**0.7**	**1.22E-01**	**0.3**	**99.25**	**2.30**	**207.09**	**9.3**
	12	**60°C**	**2.50E-06**	**346.9**	**7.90E-06**	**203.2**	**1.27E-05**	**30.8**	**8.59E-04**	**2.1**	**3.10E-02**	**0.4**	**97.57**	**0.58**	**205.78**	**34.6**
	13	**61°C**	**1.90E-06**	**479.9**	**7.00E-07**	**2325.9**	**1.28E-05**	**33.3**	**7.51E-04**	**2.3**	**2.72E-02**	**0.4**	**97.94**	**0.51**	**206.97**	**40.6**
	J=0.00341900 0.22%			**Hb3gr=1081.000 0.11% Ma**				**Laser**					**Plateau age**		**204.1 ± 1.1 Ma**	

[a]Analyses shown in bold were included in plateau or mean age calculation.

Table D3. Zircon and apatite fission track data.

Sample #.	N	ρ_S	N_s	ρ_i	N_i	ρ_d	N_d	Age (Ma)		P(χ2) (%)	D_{par} (μm)		N(L)	TL (μm)	
								Central	±2σ		Mean	s.d.		Mean	s.d.
Zircon															
12GH33	25	178.282	1252	102.526	720	12.054	4932	126.6	12.8	99.55					
12GH43	25	164.91	939	35.827	204	12.469	4932	341.0	54.4	100					
12GH45	25	142.875	922	58.886	380	12.607	4932	184.0	23.6	99.98					
Apatite															
12GH30	25	6.897	701	13.967	1419	6.666	2484	51.6	5.4	99.43	1.83	0.3	103	12.97	1.60
12GH35	34	5.427	325	16.032	960	5.679	2484	30.2	4.2	44.37	2.64	0.5			
11HN08-1	30	6.921	645	12.662	1180	6.025	2484	51.6	5.6	71.16	1.76	0.3	104	12.72	1.65
11HN23-1	26	6.494	538	12.372	1025	6.123	2484	50.4	5.8	98.51	1.73	0.2	105	12.38	1.45
12GH46	25	9.203	455	9.567	473	5.926	2484	89.0	12.4	99.23	2.67	0.6			
12GH48	25	10.644	800	10.764	809	6.074	2484	93.8	10.2	95.54	3.60	0.9			

[a]N = number of dated apatite or zircon crystals; ρ_S (ρ_i) = spontaneous (induced) track densities ($\times 10^5$ tracks/cm^2); N_s (N_i) = number of counted spontaneous (induced) tracks; ρ_d = dosimeter track density ($\times 10^5$ tracks/cm^2); N_d = number of tracks counted on dosimeter; P(χ^2) = probability obtaining chi-square value for n degree of freedom (where n = number of crystals); D_{par} = average etch pit diameter of fission tracks; s.d. = standard deviation; NL = number of horizontal confined tracks measured. TL = horizontal confined track length. Glass dosimeter was CN-5 for apatite samples and CN-1 for zircon samples, and zeta value of 314.59 ± 3.29 for apatites and 121.01 ± 1.73 for zircons.

Table D4. Zircon (U-Th-Sm)/He data.

Sample #.	N_c[a]	^{238}U (ng)	+/- (%)	^{232}Th (ng)	+/- (%)	^{147}Sm (ng)	+/- (%)	eU (ppm)	He (ncc)	+/- (%)	Th/U	Raw age (Ma)	1σ (Ma)	F_T	Cor. age (Ma)	1σ (Ma)	Mean (Ma)	2σ (Ma)
12HNDX01	1	1.08	1.9	0.66	1.5	0.000	10.9	178.912	30.586	1.3	0.60	199.4	4.2	0.76	**262.4**	**19.2**[b]		
	2	2.75	2.6	1.01	1.5	0.000	9.3	501.052	66.107	1.3	0.40	179.1	4.8	0.73	**245.4**	**18.4**		
	3	4.23	2.0	0.80	1.5	0.000	15.7	645.476	104.095	1.3	0.20	190.3	4.3	0.76	**250.4**	**18.4**		
	4	5.09	1.9	1.11	1.5	0.000	7.4	636.836	135.984	1.3	0.20	205.0	4.5	0.80	**256.2**	**18.8**		
																	253	**19**
09SD04	1	1.83	2.7	1.02	3.8			508.9	51.08	2.5	0.58	202.5	9.0	0.77	**254.9**	**20.0**		
	2	1.01	2.7	0.55	3.8			430.4	34.081	2.5	0.56	245.2	11.3	0.74	319.6	25.1		
	3	0.56	2.7	0.28	3.8			379.8	12.824	2.5	0.52	168.6	8.4	0.69	**237.0**	**18.6**		
																	245	**27**
09SD02	1	3.37	2.7	0.32	3.8			908.9	71.082	2.5	0.10	169.6	7.8	0.78	**213.5**	**16.9**		
	2	0.73	2.7	1.00	3.8			172.8	21.728	2.5	1.42	184.9	7.7	0.80	**227.1**	**17.7**		
																	220	**24**
12GH33	1	0.32	2.0	0.17	1.5	0.004	25.1	57.9	2.582	1.2	0.53	59.1	1.3	0.78	**75.8**	**5.6**		
	2	0.64	2.0	0.33	1.5	0.002	9.7	44.7	6.889	1.2	0.52	78.4	1.7	0.84	**92.9**	**6.8**		
	3	2.44	2.1	0.47	1.5	0.012	35.1	356.9	21.987	1.2	0.19	70.5	1.6	0.78	**89.9**	**6.6**		
	4	1.86	2.1	1.12	1.5	0.004	17.1	202.6	21.002	1.2	0.60	80.8	1.8	0.82	**98.6**	**7.2**		
	5	1.60	2.0	0.74	1.5	0.004	22.3	119.2	14.902	1.2	0.46	68.7	1.5	0.84	**82.0**	**6.0**		
																	86.4	**5.7**
12GH43	1	0.40	2.0	0.19	1.5	0.000	24.7	178.196	7.322	1.3	0.50	134.6	3.0	0.75	**179.4**	**13.2**		
	2	0.75	2.4	0.60	1.5	0.000	12.1	307.802	15.296	1.3	0.80	139.7	3.4	0.76	**183.8**	**13.6**		
	3	0.65	1.9	0.34	1.5	0.000	18.2	373.875	10.547	1.3	0.50	117.2	2.5	0.70	**167.4**	**12.3**		
	4	0.69	1.9	0.81	1.5	0.000	7.4	299.077	9.486	1.3	1.20	88.4	1.8	0.66	134.0	9.8		

																	176	**15**
12GH30	1	1.39	3.3	0.24	1.6	0.000	19.6	1975.086	19.695	1.2	0.20	110.9	3.8	0.77	**144.0**	**11.2**		
	2	2.26	2.0	3.01	1.5	0.000	3.2	2782.87	30.19	1.2	1.30	83.2	1.6	0.75	110.9	8.1		
	3	2.00	2.0	0.32	1.5	0.000	27.5	1706.094	22.809	1.2	0.20	89.7	2.0	0.76	**118.0**	**8.7**		
	4	2.28	2.1	0.41	1.5	0.000	15.2	2024.917	32.293	1.2	0.20	110.9	2.6	0.79	**140.4**	**10.3**		
																	132	**11**
12GH35	1	2.65	3.3	2.61	1.5	0.000	10.9	1597.432	23.395	1.3	1.00	58.6	1.7	0.70	83.8	6.4		
	2	6.94	1.9	5.08	1.5	0.000	4.7	3065.171	27.798	1.3	0.70	28.0	0.6	0.65	**43.1**	**3.1**		
	3	4.02	3.7	3.65	1.5	0.000	6.7	3373.656	16.747	1.3	0.90	28.1	0.9	0.66	**42.6**	**3.3**		
	4	3.92	1.9	2.67	1.5	0.000	9.3	1884.942	28.341	1.3	0.70	51.0	1.1	0.69	73.9	5.4		
	5	4.43	2.0	4.03	1.5	0.000	9.9	2547.573	21.069	1.3	0.90	32.1	0.7	0.64	**50.4**	**3.7**		
																	44.9	**3.9**
11HN08-1	1	15.15	3.2	7.12	1.5	0.000	5.2	4700.186	170.812	1.3	0.50	82.9	2.7	0.79	**104.9**	**8.1**		
	2	12.87	1.9	3.07	1.5	0.000	5.5	5536.409	122.071	1.3	0.20	73.4	1.6	0.73	**100.5**	**7.4**		
	3	9.65	3.0	6.00	1.5	0.000	11.7	8944.256	83.766	1.3	0.60	62.0	1.8	0.67	**92.5**	**7.0**		
	4	12.13	1.9	6.68	1.5	0.000	6.4	3956.104	157.221	1.3	0.50	93.6	2.0	0.78	***120.0***	***8.8***		
																	102.8	**7.7**
11HN23-1	1	3.82	1.9	2.23	1.5	0.000	11.3	1494.529	57.409	1.3	0.60	107.5	2.3	0.70	**153.6**	**11.3**		
	2	3.18	2.1	2.33	1.5	0.000	15.0	2384.548	46.376	1.3	0.70	101.3	2.3	0.69	**146.8**	**10.8**		
	3	4.56	2.9	2.84	1.5	0.000	9.9	1229.31	66.74	1.3	0.60	104.0	3.0	0.71	**146.5**	**11.1**		
	4	5.11	1.9	2.40	1.5	0.000	25.4	1562.663	75.85	1.3	0.50	108.8	2.4	0.73	**149.0**	**10.9**		
																	149	**11**
12GH46	1	2.89	5.0	2.47	1.5	0.000	13.8	1721.252	40.937	1.3	0.80	96.3	4.2	0.81	**118.9**	**9.8**		
	2	3.61	3.9	3.67	1.5	0.000	10.1	1605.815	34.908	1.3	1.00	63.9	2.2	0.74	86.3	6.7		
	3	4.54	3.7	3.96	1.5	0.000	12.8	1572.603	61.747	1.3	0.90	92.2	3.1	0.78	**118.2**	**9.2**		
	4	2.78	3.5	2.54	1.5	0.000	11.7	1080.727	42.817	1.3	0.90	103.3	3.3	0.82	**126.0**	**9.7**		
	5	2.81	1.9	2.29	1.5	0.000	10.7	1299.511	41.52	1.3	0.80	101.2	2.1	0.79	**128.1**	**9.3**		

																122.8	**9.5**
12GH48	1	1.24	1.9	0.58	1.5	0.000	25.4	1511.861	13.858	1.2	0.50	81.9	1.7	0.79	**103.7**	**7.6**	
	2	1.36	1.9	0.81	1.5	0.000	15.0	1263.056	13.896	1.2	0.60	73.1	1.5	0.77	**94.9**	**6.9**	
	3	1.01	1.9	0.52	1.5	0.000	27.0	924.071	10.038	1.2	0.50	72.5	1.5	0.83	**87.3**	**6.4**	
	4	1.59	2.1	0.79	1.5	0.000	19.0	1994.743	17.174	1.2	0.50	79.0	1.8	0.81	**97.5**	**7.2**	
																95.1	**7.0**

[a] N_c = number of dated apatite or zircon crystals; +/- = analytical errors of individual measurements; ng = nanogram; He = ^{4}He in ncc at STP; ncc = nanocubic centimetre; TAU = total analytical uncertainty; F_T = alpha recoil correction factor after Farley et al. (1996).
[b] Analyses shown in bold were included in mean age calculation.

Table D5. Apatite (U-Th-Sm)/He data.

Sample #.	N_c[a]	^{238}U (ng)	+/- (%)	^{232}Th (ng)	+/- (%)	^{147}Sm (ng)	+/- (%)	He (ncc)	+/- (%)	Th/U	Raw age (Ma)	1σ (Ma)	F_T	Cor. age (Ma)	1σ (Ma)	Mean (Ma)	2σ (Ma)
12HNDX01	1	0.26	4.2	0.03	4.1	0.10	1.0	1.14	1.2	0.10	35.4	1.5	0.83	**42.9**	**3.5**[b]		
	2	0.13	4.3	0.04	4.1	0.29	0.8	0.83	1.2	0.34	49.6	2.0	0.83	**59.6**	**4.8**		
	3	0.10	4.3	0.03	4.1	0.17	0.9	0.63	1.2	0.34	49.1	2.0	0.83	**59.0**	**4.8**		
	4	0.14	4.3	0.01	4.4	0.05	1.2	0.39	1.2	0.07	22.3	1.0	0.83	26.8	2.2		
																53.3	**9.4**
12GH30	1	0.24	4.2	0.07	4.1	0.26	0.6	1.11	1.2	0.27	35.5	1.5	0.73	**48.9**	**4.0**		
	2	0.25	4.2	0.12	4.1	0.34	0.7	0.86	1.2	0.48	25.3	1.0	0.80	31.9	2.6		
	3	0.22	4.2	0.09	4.1	0.25	0.8	1.02	1.2	0.41	34.9	1.4	0.79	**44.4**	**3.6**		
	4	0.51	4.2	0.22	4.1	0.36	0.5	2.40	1.2	0.43	34.9	1.4	0.78	**44.5**	**3.6**		
	5	0.15	4.2	0.05	4.1	0.20	0.8	0.59	1.2	0.34	30.7	1.2	0.79	**38.8**	**3.1**		
	6	0.23	4.2	0.09	4.1	0.23	0.7	1.15	1.2	0.41	37.4	1.5	0.76	**49.0**	**4.0**		
	7	0.21	4.2	0.07	4.1	0.23	0.8	1.22	1.2	0.34	43.2	1.8	0.75	**57.2**	**4.6**		
	8	0.25	4.2	0.10	4.1	0.21	0.8	1.57	1.2	0.39	46.4	1.9	0.73	63.5	5.1		
	9	0.46	4.2	0.47	4.1	0.21	0.7	5.17	1.2	1.01	73.3	2.7	0.74	99.0	7.8	**(RadialPlotter)**	
																44.3	**5.8**

[a]N_c = number of dated apatite or zircon crystals; +/- = analytical errors of individual measurements; ng = nanogram; He = ^{4}He in ncc at STP; ncc = nanocubic centimetre; TAU = total analytical uncertainty; F_T = alpha recoil correction factor after Farley et al. (1996).
[b]Analyses shown in bold were included in mean age calculation.

Table D6. Vitrinite reflectance data.

Sample: 12GH26-2			
wave length:	546	Measure Condition:	Oil
Measured Object:	50	Refractive index of oil:	1.518
Reflectivity type:	Ro	Standard Sample:	0.904
Measurement #.	Data	Measurement #.	Data
1	1.182	21	1.315
2	1.233	22	1.316
3	1.240	23	1.317
4	1.246	24	1.318
5	1.251	25	1.318
6	1.257	26	1.318
7	1.262	27	1.326
8	1.263	28	1.345
9	1.275	29	1.354
10	1.278	30	1.358
11	1.278	31	1.389
12	1.283	32	1.392
13	1.295	33	1.397
14	1.304	34	1.404
15	1.309	35	1.423
16	1.311	36	1.453
17	1.311	37	1.455
18	1.311	38	1.462
19	1.312	39	1.484
20	1.314	40	1.484
Sample: 12GH34			
wave length:	546	Measure Condition:	Oil
Measured Object:	50	Refractive index of oil:	1.518
Reflectivity type:	Ro	Standard Sample:	3.11

Measurement #.	Data	Measurement #.	Data	Measurement #.	Data
1	3.654	21	3.814	41	3.935
2	3.654	22	3.815	42	3.950
3	3.663	23	3.817	43	3.967
4	3.673	24	3.821	44	3.997
5	3.673	25	3.824	45	4.021
6	3.680	26	3.825	46	4.033
7	3.693	27	3.833	47	4.033
8	3.716	28	3.834	48	4.057
9	3.734	29	3.847	49	4.086
10	3.738	30	3.853	50	4.091
11	3.749	31	3.854	51	4.092
12	3.755	32	3.856	52	4.109
13	3.757	33	3.862	53	4.121
14	3.760	34	3.870	54	4.154
15	3.766	35	3.876	55	4.175
16	3.769	36	3.879	56	4.182
17	3.775	37	3.907	57	4.207
18	3.800	38	3.926	58	4.228
19	3.803	39	3.931	59	4.242
20	3.809	40	3.932	60	4.355